Investigation of SiPM physics parameters down to cryogenic temperatures and for a bio-medical application

Andrii Nagai

université PARIS-SACLAY

UNIVERSITÉ PARIS SUD
Comprendre le monde, construire l'avenir

Investigation of SiPM Physics Parameters down to Cryogenic Temperatures and for a Bio-medical Application

Thèse de doctorat de l'Université Paris-Saclay
préparée à l'Université Paris-Sud

École doctorale n°576 Particules hadrons énergie et noyau : instrumentation, image, cosmos et simulation (PHENIICS)

Spécialité de doctorat: imagerie médicale et radioactivité

Thèse présentée et soutenue à Orsay, le 22 septembre 2016, par

Andrii NAGAI

Composition du Jury:

Achille Stocchi Professor, Paris-Sud University, director of Linear accelerator laboratory	Président
Gianmaria Collazuol Assistant professor, University of Padova, Department of Physics and Astronomy	Rapporteur
Christian Morel Professor, Aix-Marseille University, Department of Physics	Rapporteur
Adam Para Dr., Fermi National Accelerator Laboratory, Semiconductor depatment	Examinateur
Pascal Vincent Dr., Sorbonne University, Pierre and Marie Curie Campus, Laboratory of Nuclear Physics and High Energies	Examinateur
Nicoleta Dinu-Jaeger Dr., University of Côte d'Azur, Laboratoire ARTEMIS	Directeur de thèse

NNT : 2016SACLS552

Thèse de doctorat

Abstract

Silicon PhotoMultiplier (SiPM) detector has become a suitable visible light/photon detector for many applications like high energy physics and neutrino experiments, fluorescence detection, bio-photonics and medical imaging. The main advantages are coming from its compactness (i.e. Si wafers ~300 μm thickness), easily adjustable size (i.e. from single to hundreds of readout channels), low operating voltage (i.e. $V_{bias} < 80$ V), high gain (i.e. $G \sim 10^5 \div 10^7$), speed of response (i.e. tens of ps single photon timing resolution) and insensitivity to magnetic fields (i.e. confirmed up to 7 T).

To achieve the best performance for a given application, two important points should be addressed: (1) device physics parameters like gain G, breakdown voltage V_{BD}, signal shape, μcell capacitance $C_{\mu cell}$, quenching resistance R_q, dark count rate DCR (i.e. thermal rate, afterpulses, cross-talk), photon detection efficiency PDE, and their temperature T variation should be known and their impact on the measurement quality must be understood, and (2) SiPM device with the best adapted technological and geometrical parameters should be selected.

During my thesis I have performed studies on various SiPM devices of the same μcell size (50×50 μm^2) produced by two main manufacturers (i.e. Hamamatsu HPK and KETEK) and I directed my analysis to improve our knowledge in the field of both previously mentioned points.

The first part of my thesis was oriented to the studies of SiPM physics parameters as a function of temperature. Particularly, recent KETEK devices (year 2015) with different technological characteristics like p/n and n/p junctions, with and without trench technology, and different widths of epitaxial layer were studied in the temperature range from 308.15 K (+35 °C) down to 238.15 K (-35 °C). In addition, the Hamamatsu devices from 2011 production run as well as new devices from 2015 year, with improved technological characteristics inducing a reduced noise, were investigated in a wider temperature range from 318.15 K (+45 °C) down to 98.15 K (-175 °C).

For these purposes, I participated to the design, installation, commissioning and calibration of a cryogenic experimental setup dedicated to electrical, optical and temperature studies of SiPM devices. Also, I have developed an automatic analysis procedure able to handle in a short time an impressive quantity of experimental data (i.e. tens of Gb/device) and to give a precise and fast information on main SiPM parameters and their temperature dependence. In particular, a complete set of AC electrical parameters like gain G, breakdown voltage V_{BD}, microcell capacitance $C_{\mu cell}$, pulse shape, quenching resistance R_q, dark count rate DCR and optical cross-talk were calculated. Detector properties like photon detection efficiency PDE and associated Geiger triggering probability P_{Geiger} were also be evaluated.

I have also developed a physical model describing the DC I-V curves of SiPM detectors at different temperatures. The proposed model fits well the shape of IV curve in a very large currents range from 10^{-12} A up to 10^{-5} A over the full working range of various devices. Consequently, the IV model can be used as a simple and fast method for determination of SiPM parameters like breakdown voltage V_{BD}, the shape of Geiger triggering probability P_{Geiger} as a function of V_{bias} as well as the V_{bias} working range. The comparison of these parameters with those calculated from AC measurements and analyzed by the automatic procedure showed a good agreement.

The second part of my thesis was oriented to the study of SiPM devices and their physical parameters required to build a prototype of beta-sensitive intracerebral probe. Such probe is dedicated to measure the local concentration of radiolabeled molecules on awake and freely

moving animal and to study new animal models of human disorders (neurodegenerative diseases, tumor growth, and neuropsychiatric disorders). It is composed of small size, low-noise SiPM device coupled to a scintillating fiber and read-out by a dedicated miniaturized low-power consumption electronics. Three SiPM devices have been chosen as the most adapted for our application: two small KETEK devices of 0.5×0.5 mm^2 size (with and without optical trenches, specially developed by KETEK to fulfill our requirements) and a standard Hamamatsu device of 1.3×1.3 mm^2 size, all devices having 50×50 μm^2 μcell size. For each SiPM the gain G, dark count rate *DCR* and beta sensitivity were measured as a function of V_{bias} and temperature. The obtained results showed that the small field of view and newly developed structure of the KETEK devices allow a large decrease of the dark count rate *DCR*. However, this small field of view also leads to a reduced light collection due to the thickness of the epoxy protection resin on top of the SiPM and the acceptance angle of the fiber. Since the beta sensitivity represents a tradeoff between photon detection efficiency *PDE* and dark count rate *DCR*, KETEK SiPMs exhibit similar performances in comparison with the Hamamatsu device. Preliminary results demonstrate that the beta sensitivity of KETEK devices can be significantly improved by using focusing lens between the scintillating fiber and the SiPM or by reducing the thickness of its epoxy protection resin.

Résumé

Les Photomultiplicateurs Silicium (SiPM) sont devenus aujourd'hui des détecteurs de lumière visible, applicables dans de nombreux domaines comme la Physique des Hautes Énergies, les expériences Neutrinos, la détection de fluorescence, pour des applications de bio-photonique ou d'imagerie médicale. Les principaux avantages de ces composants tiennent dans leur compacité (épaisseur des plaquettes de Si ~300µm), une surface de détection ajustable (de un à plusieurs centaines de canaux de lecture), un fonctionnement à faible tension de polarisation (i.e. V_{bias} < 80 V), un gain élevé ($G \sim 10^5 \div 10^7$), une réponse rapide (quelques dizaines de picosecondes de résolution temporelle pour un photon), et une insensibilité aux champs magnétiques (jusqu'à 7 T).

Pour obtenir les meilleures performances pour une application donnée, il faut considérer deux points importants : (1) Les paramètres physiques comme le gain G, la tension de breakdown V_{BD}, la forme du signal, la capacité de la µ-cellule $C_{\mu cell}$, la résistance de quenching R_q, le ″dark count rate″ *DRC* (i.e. : bruit thermique, afterpulses, diaphonie entre cellules) ainsi que leurs variations en fonction de la température doivent être connus, mais également leur impact sur la qualité de la mesure doit être comprise; (2) Le composant SiPM doit être sélectionné sur certains critères technologiques et sur l'adéquation de ses paramètres géométriques à l'application.

Durant ma Thèse, j'ai étudié plusieurs types de SiPM de même taille de µ-cellule (50×50 µm^2) produits par deux sociétés (KETEK et HAMAMATSU), et j'ai concentré mes analyses sur l'amélioration de nos connaissances concernant les paramètres mentionnés précédemment.

La première partie de ma Thèse concerne l'étude des divers paramètres physiques des SiPM en fonction de température T. En particulier, des composants récents (2015) de KETEK ayant diverses caractéristiques technologiques comme des jonctions p/n ou n/p, avec ou sans ″trench″ entre cellules, différentes épaisseurs de couches épitaxiales, etc … ont été étudiés dans la gamme de T de 308.15 K (+35 °C) à 238.15 K (-35 °C). En plus, des composants Hamamatsu de production 2011, ainsi que de production 2015 avec des caractéristiques technologiques améliorées (faible bruit), ont été testés dans la gamme 318.15 K (+45 °C) à 98.15 K (-175 °C).

Pour ces études, j'ai participé à la conception, l'installation, la mise en service et la calibration d'un banc cryogénique destiné aux caractérisations électriques, optiques, et en température, des SiPM. J'ai développé une procédure d'analyse automatisée, capable de traiter en un temps très court une énorme quantité de données expérimentales (i.e. dizaines de Gb/détecteur), et de fournir une information rapide et précise sur les principaux paramètres et leur dépendance en T. En particulier, un set complet des paramètres électriques en AC, comme G, V_{BD}, $C_{\mu cell}$, forme du signal, R_q et *DCR* furent calculés. Des paramètres comme la *PDE* et la probabilité de triggering P_{Geiger} associée ont été également évalués.

J'ai développé un modèle physique décrivant les courbes IV en DC pour différentes T. Ce modèle proposé reproduit bien la forme de la courbe IV dans une large gamme de courants allant de 10^{-12} à 10^{-5} A sur toute la zone de fonctionnement des divers détecteurs. Ainsi, le modèle IV peut être utilisé comme un outil simple et rapide pour déterminer les paramètres du SiPM comme le V_{BD}, la forme de la courbe P_{Geiger} en fonction de V_{bias}, ainsi que la plage des

tensions de fonctionnement. La comparaison de ces paramètres avec ceux obtenus en mesure AC, et analysés par la procédure automatisée, sont en bonne concordance.

La seconde partie de ma Thèse a porté sur l'étude de composants SiPM spécialement adaptés à une application biomédicale. Il s'agit d'une sonde intracérébrale, sensible à l'émission β (N_β) de molécules marquées par un traceur radioactif, injectées dans le cerveau d'un animal vivant. Le but étant de construire un nouveau ″modèle animal″ de maladies humaines telles que les maladies neuro-dégénératives ou neuropsychiatriques et la croissance de tumeurs. Cette sonde se compose d'un SiPM de très petite taille, bas bruit, couplé à une fibre scintillante, suivie d'une électronique de lecture spécifique, miniaturisée, à faible consommation. Ces SiPM ont été choisis comme les plus adaptés à notre application : deux SiPM de KETEK de 0.5×0.5 mm^2 (spécialement développés par cette compagnie pour nos besoins), et un SiPM standard de 1.3×1.3 mm^2 de Hamamatsu, tous ayant des μ-cellules de 50×50 μm^2. Pour chaque composant, les paramètres *G*, *DCR* et la sensibilité β ont été mesurés en fonction de V_{bias} et *T*. Les résultats obtenus montrent que le faible champ de vue des nouvelles structures KETEK permet une bonne amélioration du *DCR*. Cependant ce faible champ de vue entraîne une perte de collection de lumière due à l'épaisseur de la couche de résine époxy de protection, et à l'angle d'acceptante de la fibre.

Comme la sensibilité β est un compromis entre le *PDE* et le *DCR*, les SiPM de KETEK montrent au final des performances voisines de celles de Hamamatsu. Les résultats préliminaires démontrent que la sensibilité β de KETEK peut être améliorée significativement en utilisant une lentille de focalisation entre la fibre scintillante et le SiPM, ou en diminuant l'épaisseur de la couche de résine époxy de protection.

Acknowledgements

First and foremost, I would like to express my sincere gratitude to my thesis advisor Nicoleta Dinu-Jaeger, You have been a tremendous mentor for me. It has been an honor and great opportunity to work with her. I appreciate all her contributions of time, ideas and funding to make my PhD experience productive. Without her guidance this dissertation would not have been possible. Nicoleta deserves very warm words for her patience in paying continuous attention to my scientific and nonscientific problems. I definitely can say that I caught a great opportunity to work with her as she is a good example of a successful physicist. Physicist who know how to manage the scientific work in all stages (e.g. planning and preparing the experiment, data taking, data analysis and presenting the results).

I would like to thank the reviewers Gianmaria Collazoul and Christian Morel who kindly agreed to spend part of their precious time and read this manuscript, their comments were very helpful and very much appreciated. Also, I would like to thank the rest of my thesis jury: Achille Stocchi, Adam Para and Pascal Vincent.

I would like to express my special appreciation and thanks to Adam Para. It is very hard to overestimate the importance of his advises and fruitful discussions during our meetings in Skype. His huge experience and knowledge in experimental physics and data analysis were extremely important and very much appreciated.

During my thesis I worked in collaboration with team from IMNC laboratory on a bio-medical application and therefore my sincere thanks also goes to IMNC laboratory: Laurent Menard, Laurent Pinot, Philippe Laniece, Marc-Antoine Verdier, Sara Spadola and many others.

Many thanks to LAL mechanical and infrastruction services for the precious help in designing and building the cryogenic set-up, as well as to SERDI/GRED group for providing lasers, measurement instruments and help in cabling. A special thanks is given to Hammoudi Nourredine from IPNO laboratory for his advises on calibration of the cryogenic set-up.

A lot of thanks to Jean-Jacques Jager for his patience, instruments and help with French language.

I would like to thank Sergey Barsuk for his useful advices and even more useful questions.

Also, I would like to thank Elias Khan, Fabien Cavalier, Christiane Eder, Sylvie Prandt and all other people who helped me to resolve all administrative problems and as a result bring this thesis to the end.

I would like to thank all my friends with whom I had wonderful discussions with a cup of coffee every day at 16h00. In particular to: Leonid, Iryna, Viacheslav, Sviatoslav, Illya and Maksym.

Last but not the least, I would like to thank my family. To my parents and my brother who are always near and support me in all my pursuits and decisions. To my best grandfather in the world. Every hour which has been spent with you gave me a huge boost of energy for next months.

Table of contents :

1. Introduction

Silicon PhotoMultiplier (SiPM) detector has become a suitable photon detector for many applications that would employ typically PMTs or MA-PMT. Thanks to its important advantages such as compactness (i.e. Si chips ~300 μm thickness), easily adjustable size (i.e. from single to hundreds of readout channels), low operating voltage (i.e. < 80 V), high gain (i.e. $10^5 – 10^7$), speed of response (i.e. tens of ps single photon timing resolution) and insensitivity to magnetic field (i.e. confirmed up to 7 T), the SiPM is used today in many applications like high energy physics [1] and neutrino experiments [2], fluorescence detection [3], and biophotonics [4] and medical applications [5] [6].

To achieve the best performances for a given application, two important points should be addressed:

- SiPM physics parameters like gain, breakdown voltage, signal shape, dark count rate (i.e. thermal rate, afterpulses, cross-talk), photon detection efficiency, and their temperature variation should be known, and their impact on the measurement quality should be understood;
- a SiPM device with the best adapted technological and geometrical parameters should be selected.

During my thesis I directed my work to improve our knowledge in the field of both previously mentioned points. More precisely, I performed studies on various SiPM devices of the same μcell size (50 × 50 μm^2), with different technological characteristics, produced by two main manufacturers (i.e. Hamamatsu HPK and KETEK) and I analyzed their parameters in a context of temperature and bias voltage variation and for a biomedical application.

An overview of SiPM physics and technology, as well as the present state of the art of its various physics parameters is given in the Chapter 2 “SiPM - state of the art”. In particular, static characteristics as forward and reverse current-voltage IV curves, dynamic characteristics as signal shape, gain, breakdown voltage, dark count rate, cross-talk and afterpulsing, and optical parameter as photon detection efficiency including quantum efficiency, geometrical fill factor and triggering probability are described in detail. Moreover, the present knowledge on their temperature dependence is also presented.

The main part of my thesis was oriented to the study of the physics parameters of various SiPM devices as a function of temperature and bias voltage, in dark and light conditions, and it is included in the Chapter 3 “Investigation of SiPM parameters down to cryogenic temperatures”. Particularly, I studied SiPM’s from 2015 production year runs with:

- different technological characteristics like p/n and n/p junctions, with and without trench technology, and different widths of epitaxial layer produced by KETEK company; these devices were tested in a temperature range from 308.15 K (+35 °C) down to 238.15 K (-35 °C).
- improved technological characteristics inducing a reduced noise produced by Hamamatsu company; these devices were tested in a wider temperature range from 318.15 K (+45 °C) down to 98.15 K (-175 °C); for calibration and comparison purposes, an old Hamamatsu device from 2011 production run was also tested in the same conditions.

In this context, the cryogenic setup developed at the Laboratory of Linear Accelerator (LAL) as well as various elements of particular relevance for our measurement like climatic chamber, electrical connections, light injection, temperature sensors, mechanical fixations, temperature

calibration etc… are described in detail in the Section 3.1 "Experimental setup" and Section 3.2 "Measured devices & measurements conditions".

The main physics results of the thesis are presented in the Sections 3.3 "Static characterizations" and 3.4 "Dynamic characterizations". In particular, the temperature dependence of forward and reverse IV characteristics allowing to calculate the quenching resistance and respectively the breakdown voltage are given in the Sections 3.3.1 and respectively 3.3.2. Moreover, the temperature and bias voltage dependence of various AC electrical parameters as gain, breakdown voltage, capacitance, signal amplitude, dark count rate, optical cross-talk and Geiger triggering probability are given in the Section 3.4.3.

Since the analysis of SiPM AC parameters in various temperature and bias voltage experimental conditions involved a huge amount of experimental data (tens of Gb/device), an automatic procedure able to handle these data in a very short time and to extract the parameters of interest was developed on ROOT data Analysis Framework and it is described in detail in the Section 3.4.1 "Automatic analysis procedure". In particular, the general waveform parameters and the procedure for baseline restoration are given in the Sections 3.4.1.a.1 "Waveform parameters" and respectively 3.4.1.a.2 "Baseline restoration". Various steps involved in the analysis of SiPM pulse analysis like pulse finding procedure, pulse template, pulses characteristics and identification, trains of pulses and template subtraction procedure are described in the Section 3.4.1.b, while the efficiency of the analysis procedure is related in the Section 3.4.1.c.

A fully new physical model describing the shape of reverse IV characteristics was developed and it is presented in the Section 3.5. This model allows fast calculation of three important SiPM parameters like breakdown voltage, working range and the shape of Geiger triggering probability. The results of these parameters extracted from experimental IV curves fitted by our model are presented in the Sections 3.5.1 (room temperature) and 3.5.2 (various temperatures).

The second and quite modest part of my thesis was oriented to the study of SiPM devices dedicated to a beta sensitive intra-cerebral probe and it is presented in the Chapter 4, "Investigation of SiPM parameters in a bio-medical context". A short introduction describing the detection principle and the limitations of previously developed beta probes is given in the Section 4.1 "Introduction". Details on the new miniaturized probe based on SiPM and its principle are presented in the Section 4.2. The selected SiPM devices selected (two small devices of 0.5×0.5 mm^2 specially developed by KETEK company at our request, and a standard Hamamatsu device of 1.3×1.3 mm^2) are presented in the Section 4.2.1 "SiPM devices for SONIM project". The experimental setup developed in collaboration with our colleagues from the laboratory of "Imagerie et Modelisation en Neurobiologie et Cancerologie" and dedicated to characterize the SiPM physics parameters of interest for this application (dark count rate, beta sensitivity) as well as the miniaturized dedicated read-out electronics developed at LAL are described in the Section 4.2.2 "Experimental setup". The test procedure and the obtained experimental results are given in the Section 4.2.3 "Test procedure" and 4.2.4 "Experimental results".

The manuscript of the thesis is finishing with the Section 5, "Summary of SiPM parameters investigations and perspectives" including the main results of the thesis and future perspectives.

2. SiPM - state of the art

In this Section, a review of various silicon devices developed up today and dedicated to visible light detection will be given. Primary, the technological structures and the light detection principle of the well-known Photodiode (PN or PIN), Avalanche Photodiode (APD) and Geiger-Mode Avalanche Photodiode (GM-APD) will be related. Then, the attention will be focused on the most recent silicon photon detector, the so-called Silicon PhotoMultiplier (SiPM), device to which my thesis studies were particularly dedicated. The SiPM technological structures, its static (e.g. forward and reverse current-voltage IV curves) and dynamic characteristics (e.g. signal shape, gain, breakdown voltage, dark count rate, cross-talk and afterpulsing) and photo-detection efficiency will be described in details. Since the temperature variation of many SiPM parameters is important for many applications, a particular attention to the temperature dependence of the SiPM parameters will be given. This overview is based on some reference publications, with the aim to learn what has been already known in the field before starting my PhD thesis and to motivate the choice of the work and futures studies I have performed during my thesis.

2.1. Precursors of SiPM – Photodiode, APD, GM-APD

For a better understanding of the main reasons for which the SiPM was developed as photon detector as well as for an easier transition to the physical phenomena's involved in the SiPM, a short review of its ancestors will be given below.

Photodiode

A photodiode device is using the functionality of reversed biased p-n junction to detect light. The cross section of a generic Si photodiode is presented in Figure 2.1 [7]. The p-type impurity is shallow diffused at the active surface of n-type Si substrate to form the p-n junction (typical thickness of the p-type layer is 1 μm or less). The contact pads are deposited, the positive electrode (anode) on the front of active area and the negative electrode (cathode) on the back side. To reduce the light loos due to light reflection the active area is passivated with an antireflection coating.

When the photons with an energy greater than bandgap energy E_g (E_{gSi} = 1.12 eV which corresponds to a wavelength of 1100 nm) strike a device, the valence band electrons are excited to the conduction band, leaving holes in their place in the valence band. Because of presence of internal electric field inside the junction, the electrons and holes drift in opposite directions to device electrodes. *The number of collected charges is proportional to the intensity of the incident light, and therefore a photodiode is a device with an internal gain of 1.*

Because of their simplicity, the photodiodes are used today in many applications, particularly where photomultipliers tubes are too bulky and delicate, or where high voltage is not possible to be applied or where insensitivity to magnetic fields is required. However, because of their lack of internal gain, the smallest detectable light flux should be at least ~ $10^8 \div 10^9$ photons/s.

In a first approximation, the photodiode current can be described by the Shockley ideal diode law:

$$I = I_s\left[\exp\left(\frac{V_j}{\eta V_T}\right)-1\right] \qquad 2.1$$

where I_s – is the reverse biased saturation current, V_j – is the voltage across the junction, V_T – is the thermal voltage ($V_T = kT/q$, where k – is the Boltzmann constant, T – is the temperature and q – is the elementary charge), η – is the ideality factor (has a value of 1 for the diffusion current and is approximately 2 for the recombination current).

The dark IV characteristic is presented by the curve (1) in Figure 2.2 [7]. However, when the light illuminates the photodiode, the curve (1) shifts by the amount of photocurrent I_{ph} which is proportional to the photon flux (curves (2) or (3)). Thus:

$$I = I_s\left[\exp\left(\frac{V_j}{\eta V_T}\right)-1\right] - I_{ph} \qquad 2.2$$

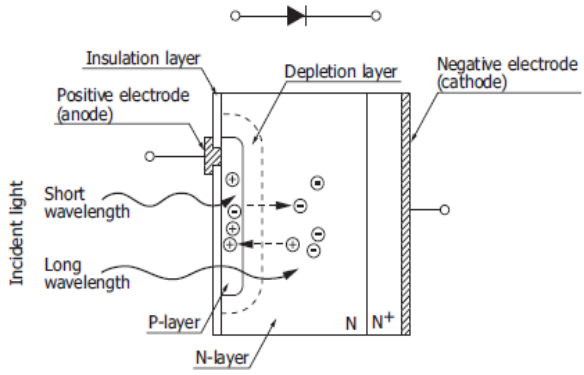

Figure 2.1 The cross section of generic Si photodiode [7]

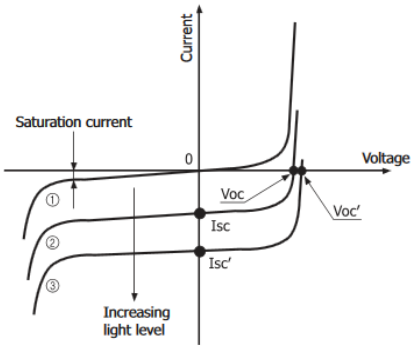

Figure 2.2 Current-voltage characteristic for a photodiode in dark (1) and light conditions (2) and (3) [7]

A photodiode can be operated either in photovoltaic mode (unbiased) or in photoconductive mode (few volts reverse biased voltage).

The photodiode optical performance is characterized by the responsivity R_λ and quantum efficiency QE. R_λ is the effectiveness of the conversion of the light power P_{opt} into electrical photodiode current I_{ph}:

$$R_\lambda = \frac{I_{ph}}{P_{opt}} \qquad 2.3$$

The R_λ varies with the incident light wavelength λ, applied bias voltage and temperature T. The R_λ as a function of λ for various photodiodes produced by Hamamatsu is presented in Figure 2.3 [7]. The photodiode QE is defined as the ratio between the incident photons to photons that contribute to photocurrent. It is connected to R_λ as:

$$QE = R_\lambda \cdot \frac{h \cdot c}{\lambda \cdot e^-} = 1240 \cdot \frac{R_\lambda}{\lambda} \qquad 2.4$$

where h – is the Plank constant, c – is the light speed in the vacuum, e^- – is the electron charge, R_λ – is the responsivity in A/W and λ – is the wavelength in nm. As can be observed in Figure 2.3 the QE has maximum of 65 ÷ 90% for an 800 ÷ 900nm wavelength range.

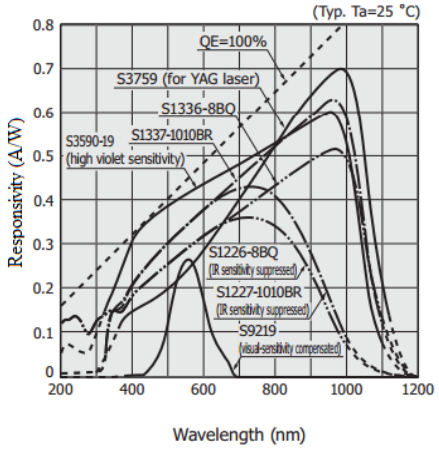

Figure 2.3 Rλ as a function of λ for various photodiodes produced by Hamamatsu [7]

The photodiode is considered linear if the I_{ph} increases linearly with the P_{opt}. The lower limit of linearity is limited by the noise dark current I_{tn}. The I_{tn} is the sum of the thermal noise (or Johnson noise) I_{Jn} and the shot noise I_{sn}:

$$I_{tn} = \sqrt{I_{Jn}^2 + I_{sn}^2} \qquad 2.5$$

The upper limit of photodiode linearity is limited by the diode series resistance and the load resistance.

The photodiode characteristics are affected by change in temperature. The most affected ones are: dark current, shunt resistance, and responsivity. The dark current is approximately double for every 8 ÷ 10 ^{0}C increases in temperature. The shunt resistance may double for every 6 ^{0}C decreases in temperature. The variation of responsivity is related to absorption coefficient which changes with temperature.

Avalanche Photodiode (APD)

An APD is also using the functionality of silicon p-n junction to detect light. The mechanism by which carriers are generated inside an APD is the same as in a photodiode, but the APD is different from a photodiode in that it has a functionality to multiply the generated internal current.

An APD is designed to work at higher reverse bias voltage (e.g. tens to hundreds of volts), which leads to an electrical field inside the p-n junction one order of magnitude higher than the photodiode (See Figure 2.4) and riches up to 10^5 V/cm. Therefore, if the electrical field is high enough, the primary generated carriers accelerate and gain enough energy to ionize the crystals lattice with the subsequent production of the secondary electron-hole pairs, phenomena called impact ionization. The secondary pairs will be accelerated and can multiply too. This

phenomena is called “avalanche multiplication” and it is used by APD if it is reverse biased at enough high voltage, approaching the breakdown voltage. The multiplication rate (number of generated charges) due to impact ionization is given by the equation:

$$M = \alpha_n \left| J_n \right| + \alpha_p \left| J_p \right| \qquad 2.6$$

where α_p, α_n – are the holes and electrons ionization rates respectively, J_p, J_n – are the hole and electron current densities.

The APD gain or multiplication rate M increases the internal photo-electric signal. Therefore, the output current is expressed as:

$$I_{APD} = M \cdot R_0(\lambda) \cdot P_{opt} \qquad 2.7$$

where $R_0(\lambda)$ – is the intrinsic responsivity of the APD at a gain $M = 1$, λ – is the wavelength, M – is the gain of the APD and P_{opt} – is the incident optical power. The gain of APD varies with applied reverse voltage V_{bias}. The gain-voltage curve of APD produced by Hamamatsu (S12023-05) is presented in Figure 2.5. The optimal gain depends in part on the excess noise factor F:

$$F = \frac{M^2 + \sigma_M^2}{M^2} \qquad 2.8$$

where σ_M – is the gain variation. *We can observe that APD's can reach gains of the order of 500 ÷ 1000, and therefore, with special designs, APD's may improve the signal-to-noise ratio with respect to Photodiode and increase the sensitivity by at least two orders of magnitude (e.g. photon flux of tens to hundreds of photons can be detected).*

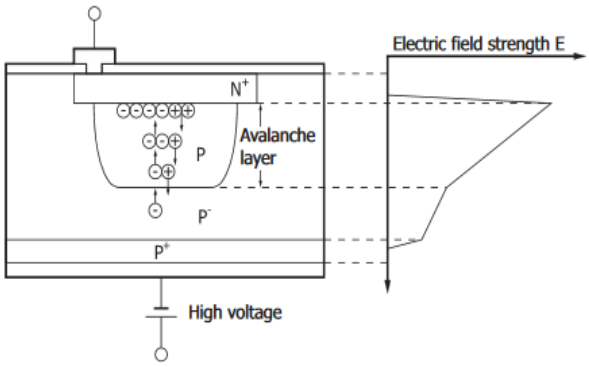

Figure 2.4 Schematic representation of an APD and internal electrical field [7]

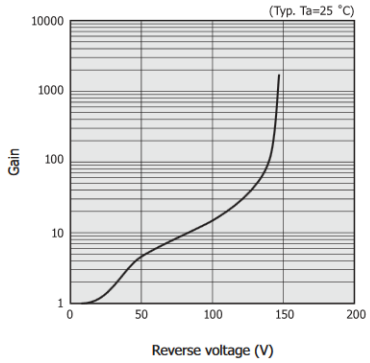

Figure 2.5 An APD (Hamamatsu S12023-05 device) gain as a function of reverse voltage [7]

The dark current for an APD can be described in a first approximation by the Shockley ideal diode law given by Eq. 2.1. But it gives only a qualitative agreement with reverse current-voltage IV characteristics of real device. The real APD device`s dark current $I_{diode\text{-}total}$ consists of the sum of surface leakage current $I_{surface}$ flowing through the interface between the p-n junction and Si oxide layer existing on the diode surface and the internal current I_{bulk} generated inside of the Si substrate multiplied by the multiplication factor M:

$$I_{diode-total} = I_{surface} + M \cdot I_{bulk} \qquad 2.9$$

The I_{bulk} flows in the avalanche region so it is multiplied by the APD gain M, whereas $I_{surface}$ doesn`t flow in the avalanche region and therefore is not multiplied. The contributions of $I_{surface}$ and I_{bulk} to the total $I_{diode-total}$ as a function of V_{bias} for a classical APD is presented in Figure 2.6 [7]. We can observe that the I_{bulk} increases much faster with respect to $I_{surface}$ with increasing V_{bias} due to increases of M, as was expected from Eq. 2.9.

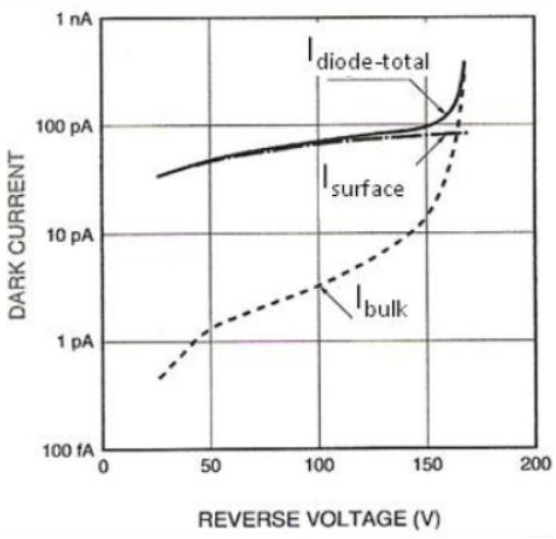

Figure 2.6 Dark current vs. reverse voltage for a classical APD device; the contributions of surface leakage current $I_{surface}$ and the bulk generated leakage current I_{bulk} are showed [7]

The APD characteristics, similar to photodiode`s, are affected by temperature changes. In particular, the APD gain variates with temperature with a temperature coefficient of:

$$\frac{1}{M}\frac{dM}{dT} = -2.2\%/^{0}C \qquad 2.10$$

Geiger Mode Avalanche Photodiode (GM-APD)

As we will see in the Section 2.2, the GM-APD represents the elementary cell of SiPM, therefore its structure and physical properties will be described in details in the following.

As its predecessors, the GM-APD structure is also based on a p-n junction, but it is designed in such a way that it works at reverse bias voltage exceeding the breakdown voltage and consequently, the electrical field inside the junction reaches high values of the orders of $3 \div 9 \times 10^5$V/cm. That means that each single carrier created by an incident photon gain enough energy to trigger an avalanche with a multiplication factor close to infinity ($M = \infty$). Such condition is called Geiger mode. Historically, the first GM-APD devices have been proposed by Haitz (Haitz, 1964, 1965) and McIntire (R. McIntyre, 1961, 1966) in their studies of micro-plasma instabilities. The proposed structures are quite different and they are presented in Figure 2.7.

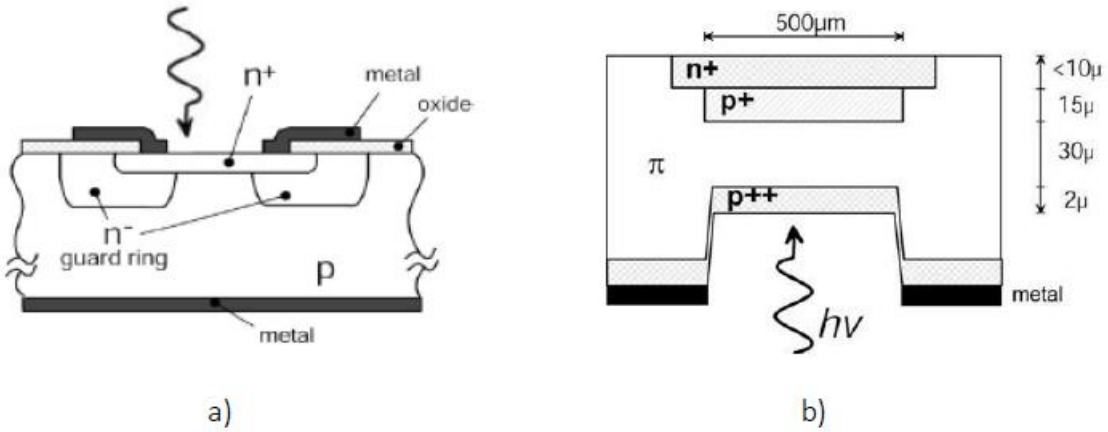

Figure 2.7 GM-APD devices proposed by Haitz, 1965 a) and McIntyre, 1966 b)

The first one shown in Figure 2.7 a) represents a so-called thin-junction GM-APD structure with an optical window on top side and an avalanche region (high electrical field) formed by the n^+ layer with the p-type substrate. An n^- guard ring is used to isolate and create a small, well defined avalanche region. Such kind of device has two main features: low breakdown voltage of 20 ÷ 50 V and small active area of 20 ÷ 100 µm in diameter.

The second one shown in Figure 2.7 b) represents a so-called thick-junction GM-APD structure with an optical absorption window on the bottom and the avalanche region formed by the n^+p^+ layer on the top. Typically, the avalanche region thickness extends more than 10 µm. Such kind of devices has three main features: breakdown voltage of 200 ÷ 500 V, wide active area of 100 ÷ 500 µm in diameter and high avalanche current of few tens of mA. These devices are delicate and costly, therefore not widely presented. The actual GM-APD devices are mainly based on the structure initially developed by Haitz.

Following the McIntyre (R. McIntyre, 1961) the operation of GM-APD can be qualitatively described as in Figure 2.8. In this representation the GM-APD is biased to V_{bias} above the breakdown voltage V_{BD}. It will stay in an OFF state (no current is flowing) until a carrier will trigger an avalanche what will bring the device into its ON state (current increases). Not every carrier in the depletion region will initiate an avalanche, therefore the probability to trigger an avalanche is characterized by the triggering probability P_{Geiger} (more details in chapter 2.2.4). To be able to detect next photon, the avalanche current must be turned off by using proper quenching mechanism, able to reduce the bias voltage to V_{BD} or below, and finally recharge it to initial V_{bias}.

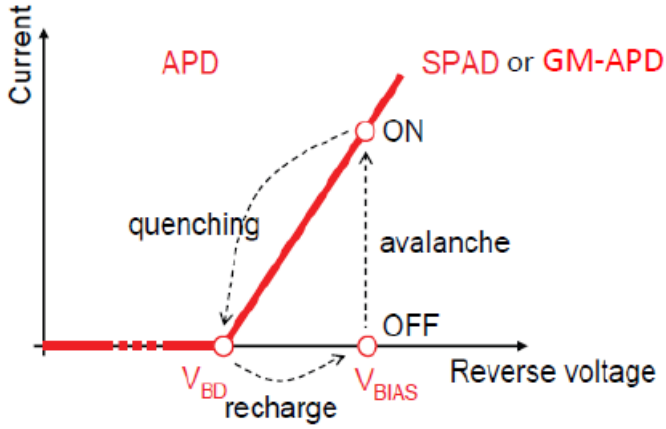

Figure 2.8 Qualitative description of the operating mechanism of GM-APD

Few different mechanisms can be used to quench the avalanche. The simplest one, the so-called passive quenching, is by using a high ohmic resistor (hundreds of kΩ) in series with the GM-APD [8] (See Figure 2.9 a)). Also, an active quenching mechanism presented in Figure 2.9 b), and composed by an active resistor made on MOS transistor controlled by fast trigger electronics [8] can be used.

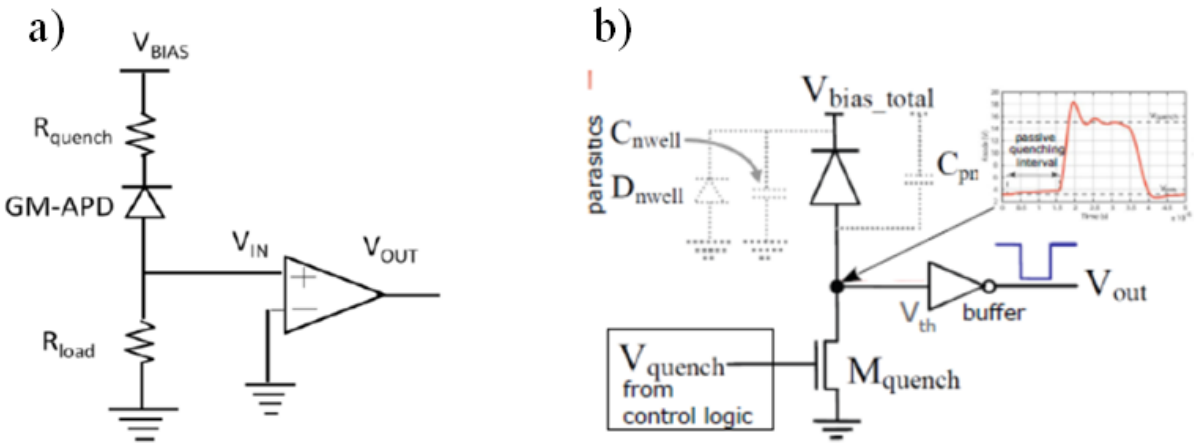

Figure 2.9 Schematic representation of GM-APD connected to passive a) and active b) quenching mechanism [8]

Since the quenching mechanism involved in SiPM µcells is the passive one, I will describe in more details the dynamic behavior of a GM-APD quenched by a quenching resistance. Starting from the electrical model developed by Haitz [9] and presented in Figure 2.10, the GM-APD can be presented as a diode resistance R_D and a capacitance C_D, connected in series to a quenching resistance R_Q (passive quenching mechanism). The switch S represents the GM-APD into its OFF state (before avalanche multiplication) and into its ON state (carrier triggers an avalanche). The time evolution of current I_D and voltage V_D across the GM-APD during the avalanche evolution are presented in Figure 2.11.

During the pre-avalanche state ($t < t_0$) the C_D is charged at $V_D = V_{bias} > V_{BD}$ and no current is flowing through the circuit. When a carrier triggers an avalanche ($t = t_0$), the new state of the GM-APD can be modeled by turning ON the switch S (the V_{BD} and R_D added to the circuit). Following Haitz [9] and Senitzky [10], at $t = t_0$ a very short current spike of $\sim 10^{-11}$ s occurs through the diode, with a maximum current of $(V_{bias} - V_{BD})/R_D$. In the same time, the C_D discharges exponentially from $V_D = V_{bias} - V_{BD}$ to V_{BD} through R_D with a time constant

$\tau_{discharge} = R_D \times C_D$. At $t = t_1$ when the C_D is discharged and V_D is reached to V_{BD}, the current flows to an asymptotic value of $(V_{bias} - V_{BD})/(R_D + R_Q)$. If the value of R_Q is big enough, it will let the I_D decreases to a level smaller than a critical value called I_{latch} and the avalanche will be quenched. The I_{latch} represents the current below which the population of the carriers is enough small that they will transit out of the high-field region without ionizing. The probability that the current is so low that statistical fluctuation brings the instantaneous number of carriers flowing through the high-field region to zero and consequently quenches the avalanche is called turn-off probability $P_{turn\text{-}off}$.

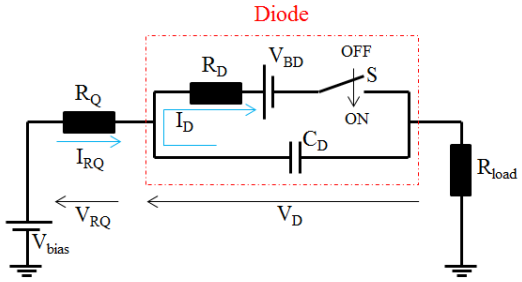

Figure 2.10 Equivalent circuit of a GM-APD [9]

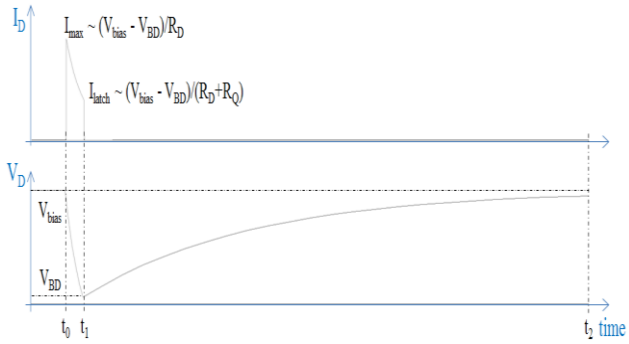

Figure 2.11 Time evolution of the avalanche current signal and the voltage across the GM-APD [9]

As the avalanche multiplication is quenched, the switch S is again in OFF position ($t > t_1$). The C_D which was discharged at V_{BD} (during the avalanche multiplication) starts the recharging to its normal state of V_{bias} through R_Q with a time constant $\tau_{recharge} = C_D \times R_Q$. The total recharge time, defined as the time needed to recharge the diode from 0 to 99% of the bias voltage is given as: $5 \times \tau_{recharge} = 5 \times C_D \times R_Q$. Since the $R_Q >> R_D$ the recharge time is much longer than the discharge: $\tau_{recharge} >> \tau_{discharge}$. During the time interval from t_1 to t_2 the device can work and detect a new photon, but since the C_D is not fully recharged the GM-APD gain will be limited by:

$$G(t) = G_{normal} \times \left[1 - \exp\left(-\frac{t}{\tau_{recharge}}\right)\right] \qquad 2.11$$

where $G(t)$ – is the GM-APD gain in $t_1 < t < t_2$, G_{normal} – normal device gain when the C_D is charged to V_{bias}. The G increases with increasing V_{bias} and can reach a typical gain of PMT`s ~10^6. The GM-APD will be operable with a normal gain only at $t > t_2$ therefore the device dead time t_{dead} is defined as:

$$t_{dead} = t_2 - t_0 \cong 5 \times \tau_{recharge} = 5 \times C_D \times R_Q \qquad 2.12$$

A typical t_{dead} of a GM-APD is in a range from few tens up to few hundreds of ns as a function of device R_Q and C_D.

As shown in this section, employing the avalanche breakdown mechanism the GM-APD becomes the first detector in silicon technology which provides high gain, comparable with that of the photomultiplier tubes. *Thanks to this property, the GM-APD allows the detection of single photon, reason for which it is also called single-photon avalanche photodiode (SPAD)* [11]. However, the t_{dead} limits the GM-APD dynamic range and it cannot provide proportional

information regarding the magnitude of an incoming photon flux. Therefore, to overcome this limitation, new devices called the SiPM`s were invented by Golovin and Sadygov [12] [13] and they will be presented in details in the following section.

2.2. SiPM physics and technology

2.2.1. Working principle

The SiPM structure is composed by a parallel array of μcells on a common silicon substrate, where each μcell is a GM-APD connected in series with a R_q. A top view to a commercial device of 1 × 1mm^2 total area with 400 μcells of 50 × 50 μm^2 size is presented in Figure 2.12. Two electrodes are shown on the top of the device, one is connected through a metallic grid to μcells and another one to the common substrate. A detailed cross-section of a typical device is presented in Figure 2.13. The μcells are shown, each of them being represented by a p-n junction built on a thin (1 ÷ 4 μm) epitaxial layer grown on a Si substrate. Individual R_q is connecting each μcell with the metal grid. The active area is covered by an antireflection coating to optimize the detection of light with a given wavelength.

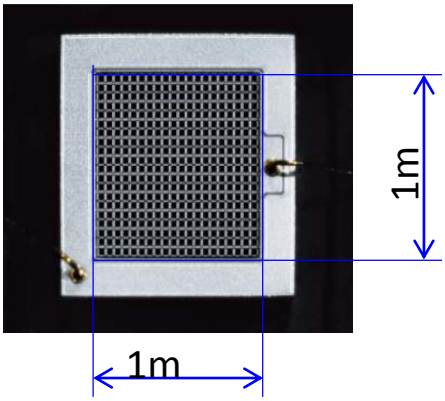

Figure 2.12 Picture of SiPM detector produced by Hamamatsu HPK, with a total area of 1x1 mm^2 and μcell of 50 × 50 μm^2; a metallic grid is connecting the μcells in parallel

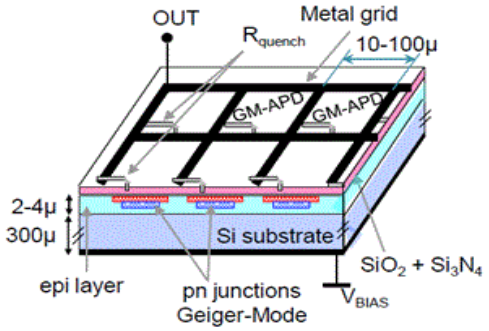

Figure 2.13 Schematic drawing of a typical SiPM device

To use the SiPM as a low light level detector an external amplifier should be connected to the device. An example of connection of the SiPM to an amplifier is presented in Figure 2.14 [7]. The 1 kΩ resistance and 0.1 μF capacitance serve as a low-pass filter that eliminates high frequency noise of the power supply. An oscilloscope connected to the amplifier`s output is the easiest way to observe the signals from the SiPM. An example of typical output SiPM signals coming from different μcells is presented in Figure 2.15. The situations where one, two and three fired μcells are shown. *Each μcell works as a digital device, and gives a standard output signal independent of the number of photons which fired the device (no information on light intensity). However, all μcells are connected together in parallel on a common load, producing an output signal which is the sum of signals from all fired μcells (the SiPM works as an analog device; it can measure the light intensity).*

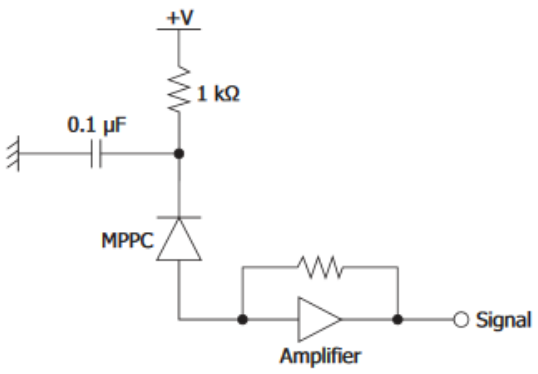

Figure 2.14 Example of connection of the SiPM to an amplifier [7]

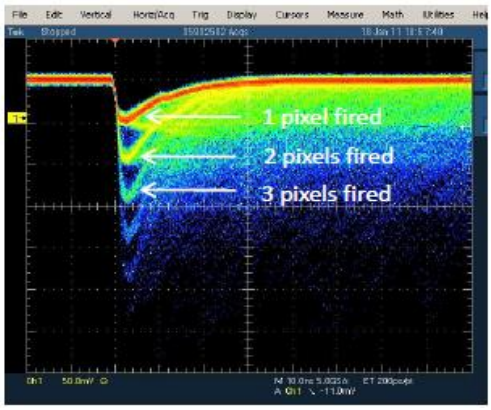

Figure 2.15 Typical output signals, We can distinguish a signal from single μcell, two, three and four fired μcell in the same time

The SiPM's presented today on the market can be classified in two main technological categories: (1) devices with n^+/p μcells build on p-type substrate, produced by FBK (e.g. RGB SiPMs) and SensL (e.g. M-series) and (2) devices with p^+/n μcells build on n-type substrate, produced by FBK (e.g. NUV SiPMs), Hamamatsu, KETEK, and SensL (e.g. B-series). The main difference of these two categories is that the first one is more sensitive to green light, whereas the second one is more sensitive to blue light (more details will be given in the Section 2.2.4 "Photon detection efficiency (PDE)" the two types of structures are schematically represented in Figure 2.16 a) and b) [14]. For both structures, device sizes of 1 × 1 mm^2, 2 × 2 mm^2, 3 × 3 mm^2 and 6 × 6 mm^2 with different μcell size from 10 μm to 100 μm are available. Small μcell size leads to a higher dynamic range at the expense of geometrical fill factor which leads to a decrease of photon detection efficiency (see Section 2.2.4 "Photon detection efficiency (PDE)").

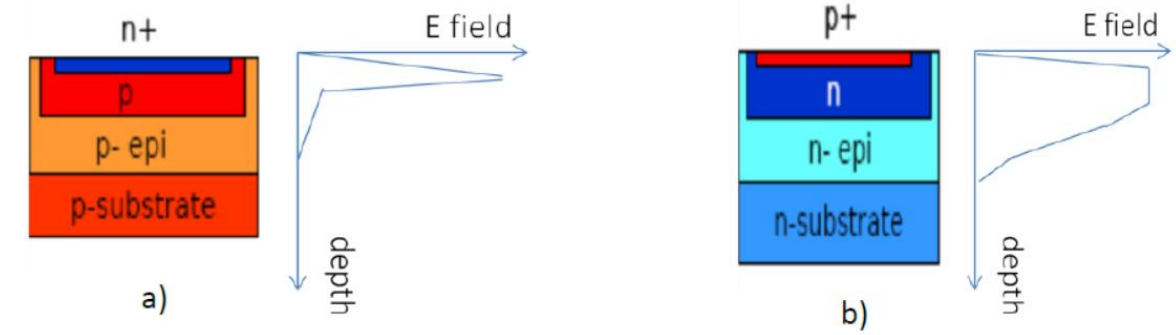

Figure 2.16 Schematic representation of two categories of SiPM μcells and the corresponding electrical field shape: a) FBK (RGB SiPMs) and SensL (M-series) devices (μcells of $n^+/p/p$-epi/p substrate); b) Hamamatsu devices (μcells of $p^+/n/n$-epi/n substrate) [14]

Besides the main difference in between these two categories mentioned previously, inside of a given category the SiPM parameters vary from one producer to another as well as from one device to another. Therefore, for a good selection of the most adapted device as well as for achieving the best performance to a given application, the most important SiPM parameters like gain, breakdown voltage, signal shape, dark count rate, and photon detection efficiency should be known. Majority of these parameters can be determined from dynamic measurements (the so-called AC tests), with an expenses of a quite complicate experimental setup (it requires an amplifier and a data acquisition system). However, a much faster and simpler static current-voltage measurements (so-called DC tests), requiring just a connection of the device to a source-

meter, can be used to easily measure parameters like breakdown voltage, device working range and quenching resistor R_q. Moreover, the reverse IV characteristic can be also used to determine the shape of the Geiger probability, one of the SiPM parameter which is not yet fully understood in our days.

I should mention here that the number of scientific publications reporting on the characterization of SiPM devices and on the analysis of their parameters increased exponentially since last 10 years and a detailed overview is almost impossible to be given in this short chapter of my thesis. However, a modest summary of SiPM parameters extracted from some reference publications will be given, showing that many physical phenomena related to this device are already known today, but still more work is required for a full understanding of some of them.

2.2.2. **Static characteristics**

2.2.2.a. Forward IV characteristic

The forward IV characteristics of various SiPM`s produced by Hamamatsu HPK, SensL, FBK and KETEK are presented in Figure 2.17 [15] and Figure 2.18 (A. Nagai, not published). Independent of device, we can observe that IV curve is characterized by a very small increase of the forward current with the V_{bias} up to a given V_{cr} (e.g. 0.6 V for Hamamatsu, KETEK and FBK devices; 6 V for SensL devices) and a much faster and linear increase of the current for V_{bias} exceeding V_{cr}.

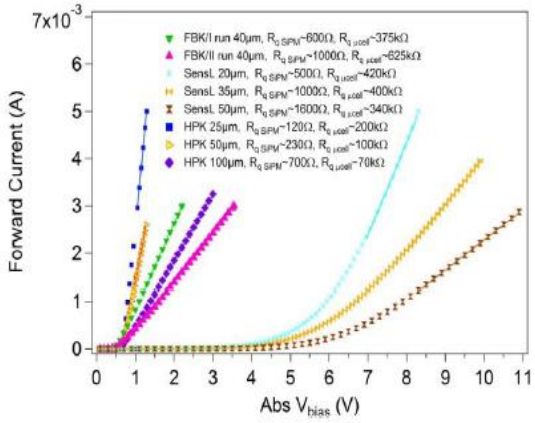

Figure 2.17 Forward static characteristics of the different SiPM`s produced by Hamamatsu HPK, SensL and FBK [15]

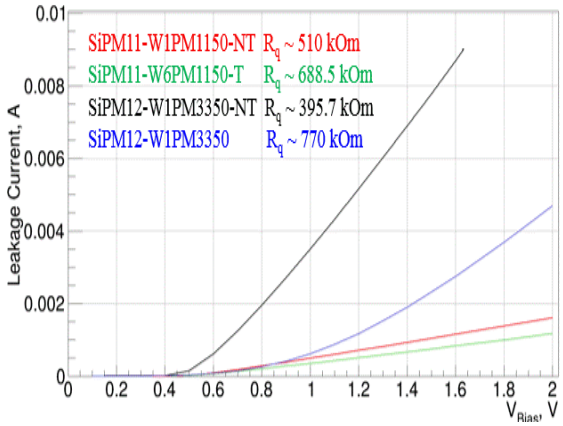

Figure 2.18 Forward static characteristics of the different SiPM`s produced by KETEK (A. Nagai, not published)

For a physical interpretation of these results, we can start from the ideal Shockley low and express the forward current flowing through a p-n diode as following by Eq. 2.1. From this equation the V_j can be expressed as:

$$V_j = \eta V_T \left[\ln\left(\frac{I}{I_s} + 1 \right) \right] \qquad 2.13$$

The voltage V_j is the difference between the applied voltage V_{bias} and the voltage drop across the neutral region and the ohmic contacts on the two sides of the junction IR_s:

$$V_j = V_{bias} - IR_s \qquad 2.14$$

Replacing V_j by V_{bias} in the Eq. 2.13, we obtain:

$$V_{Bias} = \eta V_T \left[\ln\left(\frac{I}{I_s} + 1 \right) \right] + IR_s \qquad 2.15$$

Since the SiPM is composed by a given number of μcell`s $N_{\mu cell}$, where each of μcell is presented as a diode (GM-APD) connected in series with a quenching resistor R_q, the Eq. 2.15 can be implemented for a single SiPM μcell by adding an additional voltage drop on quenching resistance R_q:

$$V_{Bias} = \eta V_T \left[\ln\left(\frac{I}{I_s} + 1 \right) \right] + IR_s + IR_q \qquad 2.16$$

or for full SiPM device with $N_{\mu cell}$, where each μcell is connected in parallel:

$$V_{Bias} = \eta V_T \left[\ln\left(\frac{I}{I_s} + 1 \right) \right] + I\frac{R_s}{N_{\mu cell}} + I \times \frac{R_q}{N_{\mu cell}} \qquad 2.17$$

The $I\frac{R_S}{N_{\mu cell}} + I\frac{R_q}{N_{\mu cell}}$ term remains negligible when I is small, however it dominates at high currents (I > 10 mA). As the result the $R_s + R_q$ of a SiPM can be calculated from linear fit ($I = a + b \times V_{bias}$, where a and b – are the fit free parameters) of the forward IV plots presented in Figures 2.18 and 2.19:

$$R_q \approx \left| R_q >> R_s \right| \approx R_q + R_s = \frac{N_{\mu cell}}{b} \qquad 2.18$$

where $N_{\mu cell}$ – is the number of the SiPM μcells. Consequently, R_q ranging from 70 kΩ for Hamamatsu HPK up to 770 kΩ for KETEK devices have be found.

2.2.2.b. Reverse IV characteristic

The reverse IV characteristics of different SiPM`s produced by Hamamatsu HPK, SensL, FBK and KETEK are presented in Figure 2.19 [15] and Figure 2.20 [16]. We can recognize the value of V_{BD} ~22.5 V for KETEK devices, the V_{BD} 28 ÷ 32 V for SensL and FBK devices and the V_{BD} ~69 V for the Hamamatsu devices. Independent of the device and producer, the shape of reverse IVs is characterized by two main zones:

- The pre-breakdown region corresponding to V_{bias} below V_{BD}; in this region, the current increases slowly with V_{bias}, being determined by free carriers of surface dark current (i.e. ionic impurities deposited on the surface during device fabrication) and bulk dark current (i.e. Shockley-Read-Hall (SRH) thermal carrier`s generated in the depleted region and carriers resulting from trap-assisted or band-to-band tunneling);
- The post-breakdown region, corresponding to V_{bias} exceeding V_{BD}; in this region, the current increases much faster with V_{bias}, being determined by Geiger discharges resulting from impact ionization of free carriers within depleted region (i.e. SRH

thermal generation and tunneling) and the associated effects (afterpulsing, cross-talk).

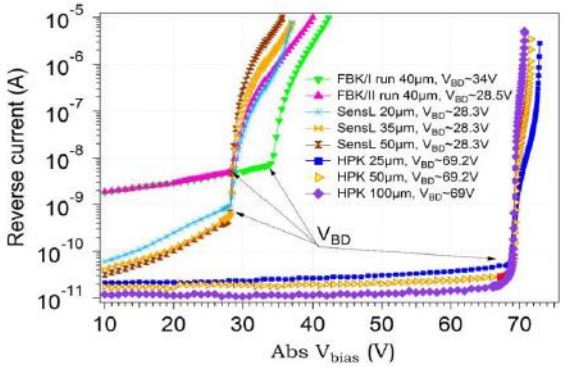

Figure 2.19 Reverse static characteristics of the different SiPM`s produced by Hamamatsu HPK, SensL and FBK [15]

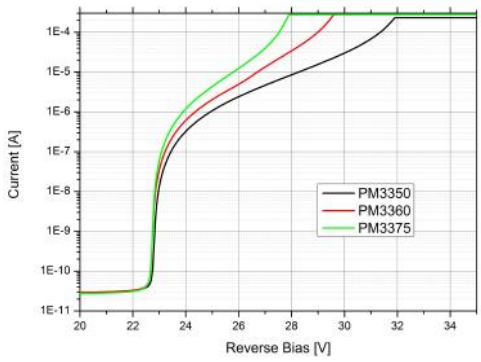

Figure 2.20 Reverse static characteristics of the three KETEK devices with different µcell sizes [16]

The reverse IV measurements can be used for fast V_{BD} calculation. Two main methods are presented in the literature: parabolic fit procedure discussed in [17] and inverse logarithmic derivative method shown in [18] and [19].

The first method described by Piemonte [17] approximates the reverse IV by a line in the pre-breakdown region and by a parabola in the post-breakdown region to determine the V_{BD} as a vertex of the parabolic fit. An example of parabolic fit procedure is presented in Figure 2.21 [17].

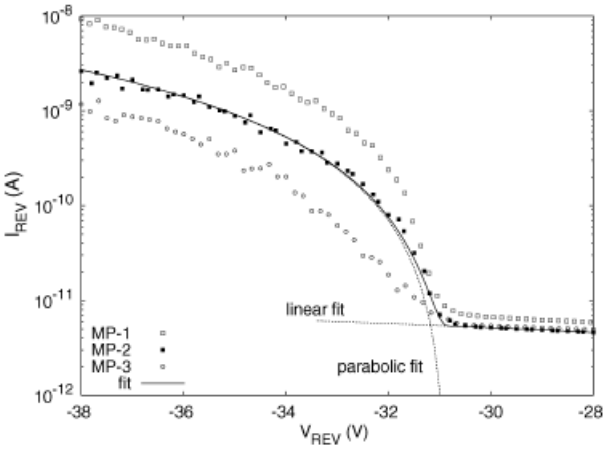

Figure 2.21 Example of the reverse IV characteristics and parabolic fit procedure for VBD determination [17]

The second method called the inverse logarithmic derivative method is also used to determine V_{BD} from reverse IV curves [18], [19]. In this method the few assumptions were done:

- When the SiPM is operating in dark environment, the main contribution to the measured current is done by the dark counts and their correlated noise (cross-talk and afterpulsing) (more details on these parameters can be found in the sections 2.2.3.d, 2.2.3.e, 2.2.3.f);
- Since the dark count rate and cross-talk probability show an approximately linear dependence on the bias voltage, and the SiPM gain increases linearly with the overvoltage (difference between bias voltage and breakdown voltage), the measured current was approximated as:

$$I = \alpha\left(V_{bias} - V_{BD}^{I}\right)^{n} \qquad 2.19$$

where I – is the measured reverse current, α and n – are the model constants which determine the shape of the reverse IV. Therefore the inverse logarithmic derivative of the Eq. 2.19:

$$\left[\frac{d\ln(I)}{dV}\right]^{-1} = \frac{V_{bias} - V_{BD}^{I}}{n} \qquad 2.20$$

which shows a linear increases after the V_{BD}. The V_{BD} was calculated as an intercept of the linear fit with the x axis. This method was used for two SiPM devices and presented in Figure 2.22 [19].

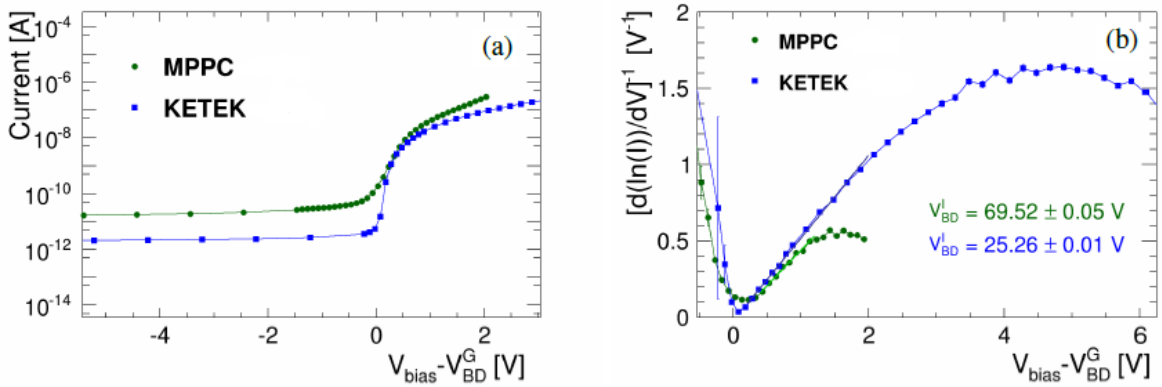

Figure 2.22 a) Reverse current and b) logarithmic derivative curves of the reverse IV measurements as a functions of the difference between the applied voltage V_{bias} and breakdown voltage calculated from AC measurements V^{G}_{BD} for of the Hamamatsu MPPC S10362-11-050P and KETEK (25µm pixel size and in total with 2304) devices [19]

The comparison between the breakdown voltage calculated from AC measurements V^{G}_{BD} (more details about this method will be given in the Section 2.2.3.b "*Gain (G)*") and breakdown voltage from the inversed logarithmic derivative method V^{I}_{BD} is presented in Table 2.1. We can observe that for both devices the V^{I}_{BD} shows in ~50 mV systematically higher value with respect to V^{G}_{BD}. The resulting V^{I}_{BD} depends on the relative magnitude of the avalanche-induced current and the parasitic currents [19].

Device	V^{G}_{BD} (V)	V^{I}_{BD} (V)
Hamamatsu	69.47±0.03	69.52±0.05
KETEK	25.22±0.01	25.26±0.01

Table 2.1 Comparison of the breakdown voltage calculated from AC measurements (V^{G}_{BD}) and inverse logarithmic derivative method (V^{I}_{BD}) [19]

For a better understanding of the systematical difference between the V_{BD} determined by different methods as well as to overcome the limitations of the presented calculation methods, deeper studies of physical mechanism determining the reverse IV shape are required. Therefore, one of the main aim of my thesis was the development of a physical model describing the shape of the IV curves over full working range of various SiPM`s. This model can be used to determine SiPM characteristics like V_{BD}, the shape of Geiger probability P_{Geiger} and the device working range. More details about P_{Geiger} will be given in the Section 2.2.4) "Photon detection efficiency (PDE)" and the developed model will be described in the Section 3.5 "Physical model of the reverse IV characteristic".

2.2.3. **Dynamic characteristics**

2.2.3.a. Signal shape

Even if the SiPM signal shape is slightly modified by used read-out electronics (see the Section 2.2.1 "Working principle"), it contains useful information like: amplitude and signal length (e.g. leading edge and falling edge). These parameters should be known to choose the read-out chain with the best adapted characteristics (input impedance, bandwidth, shaping time, gain, etc.).

Since each SiPM µcell is composed by a GM-APD connected in a series with R_q we can expect that SiPM signal shape is similar to GM-APD output signal. The dynamic behavior of a GM-APD was described in the Section 2.1 and it was shown that the GM-APD signal shape is characterized by a very fast leading edge (hundreds of ps) and a slow falling edge with an exponential decay (tens of ns.). However, it was found [20] that other passive (not fired) µcells and parasitic grid capacitance C_g affect the SiPM output signal shape.

The equivalent circuit of the SiPM [20] is presented in Figure 2.23. In this figure the fired µcell is presented as a GM-APD connected in series with R_q and parasitic quenching capacitance C_Q. All others µcells, as well as the parasitic grid capacitance C_g are connected in parallel with the fired µcell and contribute to the final signal shape. Following the Seifert [20] the SiPM signal rise time is characterized by a time constant:

$$\tau_{rise} \approx (C_D + C_Q) \times R_D \qquad 2.21$$

where C_D – is the capacitance of the reverse-biased diode, and R_D – is the diode series resistance, and C_Q – is the stray capacitance, associated to R_q.

The signal falling edge consists of two parts:

- Fast one characterized by a time constant:

$$\tau_{fall\ fast} \approx (C_D + C_Q) \times R_{load} \qquad 2.22$$

- Slow one characterized by a time constant:

$$\tau_{fall\ slow} \approx (C_D + C_Q) \times (R_{load} + R_q) \qquad 2.23$$

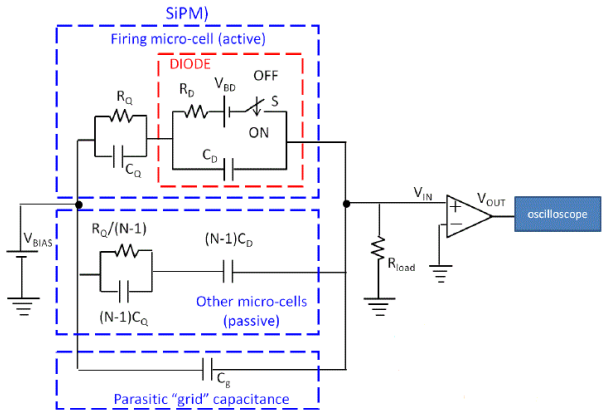

Figure 2.23 Equivalent circuit of the SiPM, with firing µcell, passive µcells and parasitic grid capacitance connected to load resistance and voltage amplifier [14]

A proper electrical model with well-known values of passive components can be used to simulate the signal shape from a given SiPM, this significantly simplifying the development of a dedicated amplifier. More details about the simulation of the SiPM signals can be found in the references: [21] [22] and [20].

Single SiPM signals measured at the output of a given amplifier (e.g. MITEQ, bandwidth = 500 MHz, gain = 45 dB) for SiPM devices produced by Hamamatsu HPK and FBK are presented in Figure 2.24 [15], by SensL devices are presented in the Figure 2.25 [15] and by KETEK devices in Figure 2.26. As expected from the electrical model presented above [20], we can observe that all devices show a fast leading edge with a time constant τ_{rise} ~2 ns and a falling edge composed by a fast time constant $\tau_{fall\ fast}$ ~0.5 ns (clearly seen for FBK and KETEK devices) and a slow time constant $\tau_{fall\ slow}$ in a range from 5 ns (Hamamatsu with 25 µm µcell size) to ~120 ns (SensL and KETEK devices). The total recovery time, calculated as ~5 × $\tau_{fall\ slow}$, corresponds to the time needed to recharge the µcell from 0 to 99% of the V_{bias}.

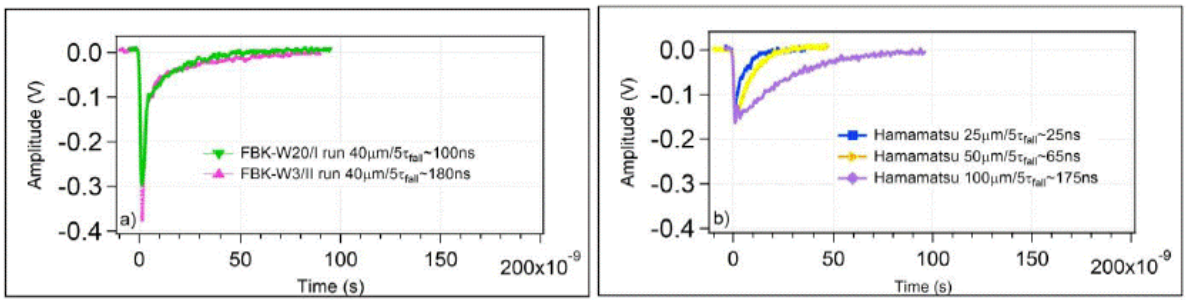

Figure 2.24 Single SiPM signals at the output of the amplifier produced by: a) FBK and b) Hamamatsu HPK [15]

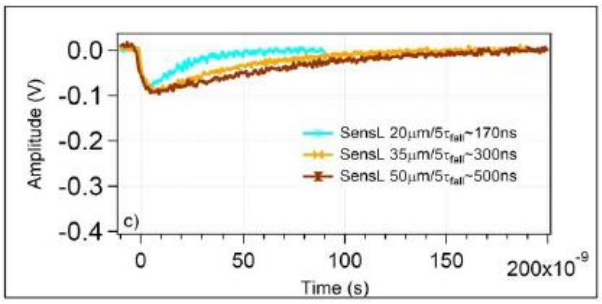

Figure 2.25 Single SiPM signals at the output of the amplifier produced by SensL [15]

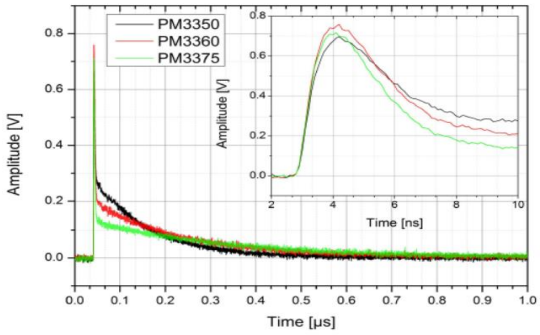

Figure 2.26 SiPM signals of KETEK devices [16]

2.2.3.b. *Gain (G)*

The gain *G* of the SiPM is defined as the number of carriers created during an avalanche discharge of one μcell. The *G* can be expressed as:

$$G = \frac{Q}{e^-} = \frac{(C_D + C_Q)\times(V_{Bias} - V_{BD})}{e^-} = \frac{(C_D + C_Q)\times \Delta V}{e^-} = \frac{C_{\mu cell}\times \Delta V}{e^-} \qquad 2.24$$

where e^- – is the electron charge, Q – is the charge created in one μcell during one avalanche. V_{BD} – is the breakdown voltage, C_D – is the capacitance of the reverse-biased diode, C_Q – is the stray capacitance, associated to R_q, $C_{\mu cell}$ – is the μcell capacitance, V_{Bias} – is the applied voltage, $\Delta V = V_{Bias} - V_{BD}$ – is the overvoltage.

Experimentally, the SiPM *G* can be calculated from the time integration of the device signals:

$$G = \frac{Q}{e^-} = \frac{\int I(t)dt}{e^-} = \frac{\int V_{Out}(t)dt}{R_{load}\cdot G_{Amplifier}\cdot e^-} \qquad 2.25$$

where $I(t)$ – is the current flowing from the detector to the read-out circuit, $\int V_{Out}(t)dt$ – is the area of the signal, $G_{Amplifier}$ – is the gain of the amplifier, R_{load} – is the input amplifier load resistance. A typical spectrum of the signal area is presented in Figure 2.27. We can distinguish the electronic pedestal (no signals from the SiPM) and peaks corresponding to the situations where one, two, three and more μcells were fired. The mean value of the 1 p.e. peak represents the most probable charge generated during one primary pulse and it allows determining the SiPM *G* as this charge divided by e^-.

The *G* as a function of V_{bias} for different SiPM`s produced by Hamamatsu HPK, SensL, FBK and KETEK is presented in Figure 2.28 [15], Figure 2.29 [23] and Figure 2.30 (Nagai, not published). Independent of the device, the *G* increases linearly with V_{bias}, as was expected from Eq. 2.24 but with different slopes determined by different $C_{\mu cell}$ (see Eq. 2.24). The *G* ranges from 1×10^5 to 4.5×10^6, while the $C_{\mu cell}$ shows values ranging from 25 to 500 fF. The different values of $C_{\mu cell}$ can be related to different active areas and depths of depleted regions from classical formula for the capacitance:

$$C = \varepsilon_0\varepsilon_{Si}\times\frac{A}{d} \qquad 2.26$$

where A – is the μcell active area, d – is the thickness of depleted region, ε_0 and ε_{Si} – are the vacuum and silicon permittivity respectively.

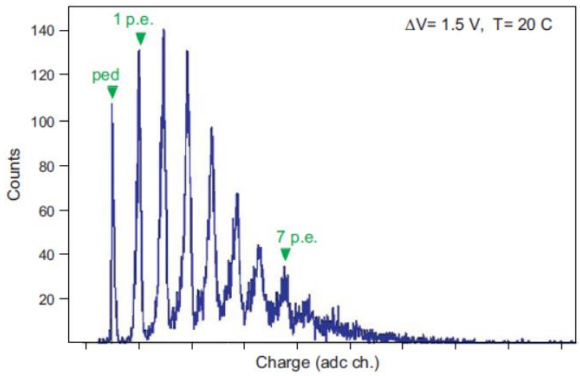

Figure 2.27 Spectra of the SiPM signal area. Each peak corresponds to a certain number of photoelectrons (p.e.) [2]

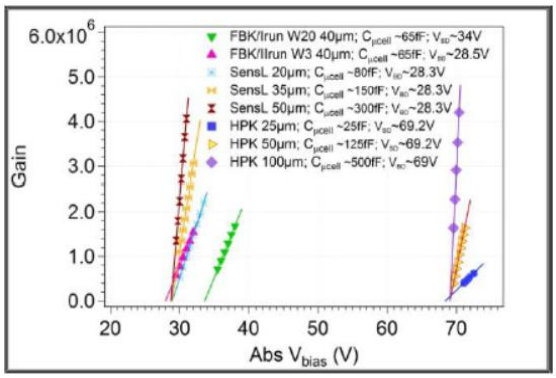

Figure 2.28 Gain vs. V_{bias} for different SiPM devices produced by Hamamatsu HPK, FBK and SensL [14]

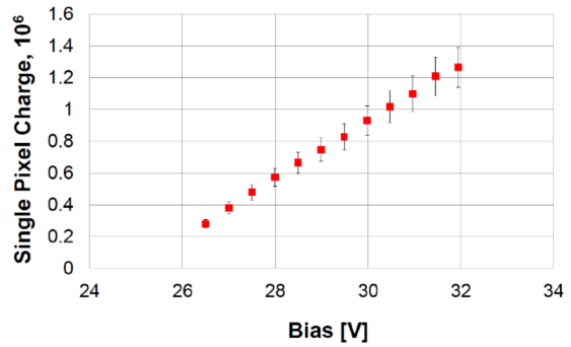

Figure 2.29 Gain vs. V_{bias} of SiPM with 20µm µcell size, produced by KETEK [23]

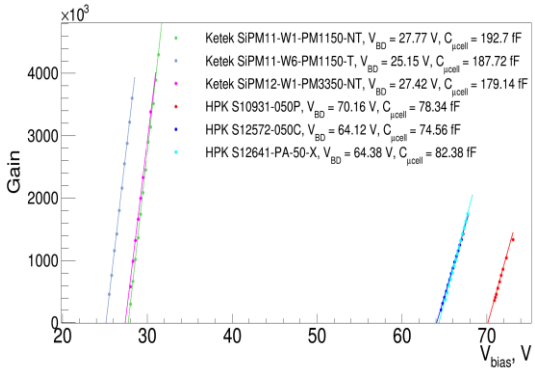

Figure 2.30 Gain vs. V_{bias} of SiPM`s produced by KETEK and Hamamatsu HPK (Nagai, not published)

2.2.3.c. *Breakdown voltage (V_{BD})*

The SiPM V_{BD} represents the voltage above which the electrical field inside the depleted region of µcells is high enough that free carriers (created by an absorbed photon or by a thermally generated carrier) can trigger an avalanche. Therefore, the V_{BD} determines the left range of device working region. Moreover, as was shown in [6], the precise value of V_{BD} should be known if an array of SiPMs is used, allowing therefore a uniformity of the final detection parameters.

The physical interpretation of the breakdown voltage is given by Sze [24]. The avalanche multiplication process can be triggered in Silicon by electrons or holes due to electrons and holes ionization rates. Following Sze [24], when the avalanche process is initiated by holes, the breakdown condition is given by the ionization integral:

$$\int_0^W \alpha_p \exp\left[-\int_0^x (\alpha_p - \alpha_n)dx'\right]dx = 1 \qquad 2.27$$

where α_p, α_n – are the holes and electrons ionization rates respectively, W – is the depletion region width. Whereas, when the avalanche process is initiated by electrons instead of holes, the breakdown condition is given by:

$$\int_0^W \alpha_n \exp\left[-\int_x^W (\alpha_n - \alpha_p)dx'\right]dx = 1 \qquad 2.28$$

Equations 2.27 and 2.28 are equivalent. Therefore the breakdown conditions doesn`t depend on the carriers type and it is determined only by multiplication process in the depletion region.

From the breakdown conditions described above and the field dependence of the ionization rates [25] [26], the breakdown voltage V_{BD}, the maximum electric field E_m and the depletion layer thickness d can be calculated (in approximation of one-sided abrupt junction, which it is supposed to represent the SiPM μcell structure in a first approximation):

$$V_{BD} = \frac{\mathrm{E}_m \cdot d}{2} = \frac{\varepsilon_s \cdot \mathrm{E}_m^2}{2e^-}\frac{1}{N_B} \qquad 2.29$$

where N_B – is the ionized background impurity concentration of the lightly doped side, ε_s – is the semiconductor impurity.

The V_{BD} can be determined experimentally from the plots of G vs. V_{bias} (see previous Section 2.2.3.b "*Gain (G)*") by extrapolating the linear fit to zero. The V_{BD} for different SiPM devices produced by Hamamatsu HPK, SensL, FBK and KETEK is indicated in Table 2.2 [14], [16]. We can observe that the values of the V_{BD} are very different for different producers: V_{BD} ~ 22 V for KETEK, V_{BD} 28 ÷ 32 V for SensL and FBK devices and V_{BD} ~69 V for Hamamatsu FBK, this difference reflecting variation of technology and design, different background impurity concentration and maximum values of the electrical field (See Eq. 2.29).

Moreover, the devices coming from the same producer and the same production type can have quite different V_{BD}. For example, Figure 2.31 shows the histogram of the V_{BD} for 16 monolithic arrays S11828-3344M produced by Hamamatsu HPK (16 SiPM`s per array, 256 SiPM`s in total) [6]. We can see that a variation of the V_{BD} of ~800 mV was observed for 16 arrays S11828-3344 produced by Hamamatsu HPK (each array has 16 SiPM`s, 256 SiPM`s in total). However, the SiPM technology evolved and today, monolithic arrays are not any more of actuality. To build large detection area of SiPM's, single devices are today tested one by one and only those with very close V_{BD} (e.g. within a given range required by the application) are mounted together in high area arrays.

Producer:	SiPM:	V_{BD} (V)
Hamamatsu HPK	S10362-11-25	69.2
	S10362-11-50	69.2
	S10362-11-100	69
	S10931-050P	70.16
	S12575-050C	64.02
	S12641-PA-50-(X)	64.05
SensL	SPM-20	28.3
	SPM-35	28.3
	SPM-50	28.3
FBK	W20-B10-T3V2PD/ I run	34
	W3-B3-T6V1PD/ II run	28.5
KETEK	PM3350	22.3*
	PM3360	22.24*
	PM3375	22.05*
	PM11-50NT	27.76
	PM11-50T	25.2
	PM33-50NT	27.62

Table 2.2 V_{BD} for SiPM devices produced by Hamamatsu, SensL FBK [15] and KETEK [16]. Measurements were done at +25 ^{0}C and (*) at -18 ^{0}C

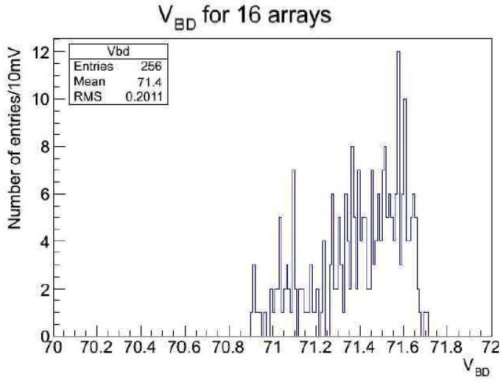

Figure 2.31 Histogram of the V_{BD} for 16 arrays S11828-3344M produced by Hamamatsu HPK (16 SiPM`s per array, 256 SiPM`s in total) [6]

2.2.3.d. Dark count rate (DCR)

The *DCR* of a SiPM represents the number of output pulses per second when the device is in the dark. Since the SiPM signals generated by an absorbed photon or by a dark generated carrier are identical, the *DCR* sets up the noise limit of the device when it has to be used for low (from one to few photons) light level detection.

The *DCR* is determined by few physical phenomena's:

- The dominating one is the thermal generated carriers, the theory of which was first derived by Shockley and Read [27] and then by Hall [28]. The Shockley-Read-Hall recombination rate can be expressed as:

$$R_{RSH} = \frac{pn - n_{ie}^2}{\tau_{p0}\left[n + n_{ie} \times \exp\left(\frac{E_{trap}}{kT_L}\right)\right] + \tau_{n0}\left[p + n_{ie} \times \exp\left(-\frac{E_{trap}}{kT_L}\right)\right]} \qquad 2.30$$

  where n, p – are the holes and electrons concentrations, τ_{p0}, τ_{n0} – are the hole and electron lifetimes respectively, E_{trap} – is a difference between trap energy level and intrinsic Fermi level, T_L – is the lattice temperature;
- If the electric field is enough strong (SiPM is operated at high ΔV), the electrons can tunnel through the bandgap via trap levels. Therefore the thermal generated carriers are amplified by trap-assisted tunneling TAT mechanism and Eq. 2.30 transforms to:

$$R_{RSH} = \frac{pn - n_{ie}^2}{\frac{\tau_{p0}}{1+\Gamma_p^{Dirac}}\left[n + n_{ie} \times \exp\left(\frac{E_{trap}}{kT_L}\right)\right] + \frac{\tau_{n0}}{1+\Gamma_n^{Dirac}}\left[p + n_{ie} \times \exp\left(-\frac{E_{trap}}{kT_L}\right)\right]} \quad 2.31$$

where Γ_p^{Dirac}, Γ_n^{Dirac} – are the hole and electron field-effect enhancement term for Dirac wells.

- Additional to trap-assisted tunneling, the generation rate can be enhanced by the Poole-Frankel effect [29], emission from Coulombic wells. Due to this effect the Eq. 2.30 transforms to:

$$R_{n,RSH} = \frac{pn - n_{ie}^2}{\frac{\tau_{p0}}{1+\Gamma_p^{Dirac}}\left[n + n_{ie} \times \exp\left(\frac{E_{trap}}{kT_L}\right)\right] + \frac{\tau_{n0}}{\chi_F + \Gamma_n^{Coul}}\left[p + n_{ie} \times \exp\left(-\frac{E_{trap}}{kT_L}\right)\right]} \quad 2.32$$

for electrons, and for holes:

$$R_{p,RSH} = \frac{pn - n_{ie}^2}{\frac{\tau_{p0}}{\chi_F + \Gamma_n^{Coul}}\left[n + n_{ie} \times \exp\left(\frac{E_{trap}}{kT_L}\right)\right] + \frac{\tau_{n0}}{1+\Gamma_p^{Dirac}}\left[p + n_{ie} \times \exp\left(-\frac{E_{trap}}{kT_L}\right)\right]} \quad 2.33$$

where χ_F – is the Poole-Frenkel thermal emission factor, Γ_n^{Coul} and Γ_p^{Coul} – are the Coulombic field-enhancement terms for electrons and holes respectively.

- With the increases of electrical field inside of the junction, the second physical phenomena known as band-to-band tunneling takes place. This mechanism describes transitions of electrons which tunnel directly from the valence band into the conduction band. Following the Hurkx [30] the band-to-band tunneling term can be taken into account as a Dirac δ-function generation term at the location of the maximum electric field:

$$R_{bbt}(x) = \frac{c_{bbt} V_j \left(F_m / F_0\right)^{3/2} e^{-F_0/F_m}}{e^-} \delta(x) \quad 2.34$$

where F_m – is the maximum electric field, F_0 – is the temperature dependent constant, c_{bbt} – is the temperature independent prefactor, V_j – is the reverse bias junction voltage (taken to be negative).

The schematic interpretations of a carrier generations due to SHR, TAT and Poole-Frenkel effect is presented in Figure 2.32 [31].

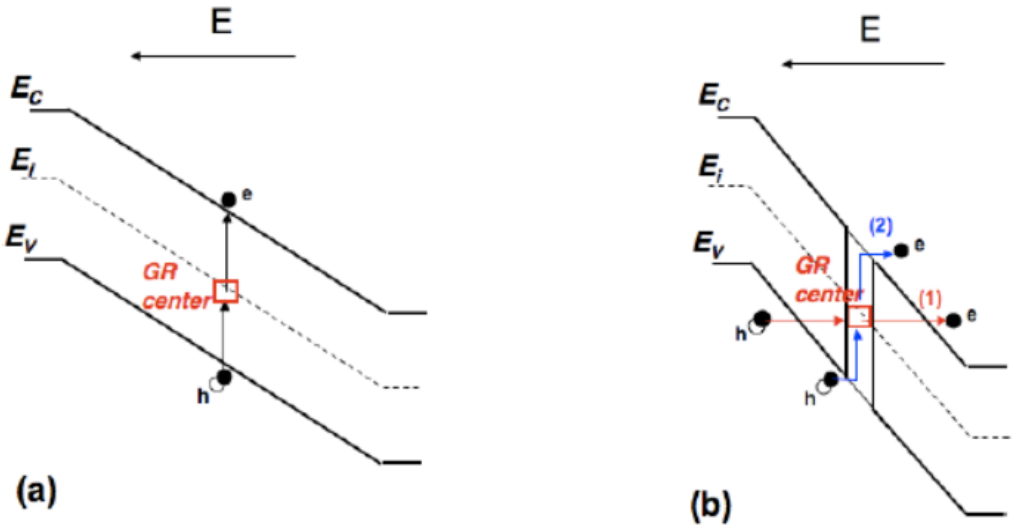

Figure 2.32 Thermally SHR generation of electron-hole pairs a). Field assisted generation b): TAT (1) and Poole-Frenkel effect [31]

An example of oscilloscope waveform recorded from a SiPM operated in the dark is presented in Figure 2.33. We can observe one signal coming from a single µcell which can be determined by one the physical effects described above. Such kind of signal is also called 1 p.e. primary uncorrelated pulse. However, two more types of signals, correlated to the primary one, can be observed:

- a primary signal followed short time after by a second signal called afterpulse (i.e. afterpulses are determined by carriers captured by trap levels in the junction depletion layer and subsequently released, determining new pulses correlated to the primary ones);
- a primary signal simultaneously followed by a signal coming from a neighboring µcell, determining a double signal called optical cross-talk (i.e. optical crosstalk is a photon emitted in a primary avalanche can start a second avalanche in a neighboring µcell).

More details about afterpulses and optical crosstalk will be given later in this section.

Experimental studies of DCR as a function of ΔV for SiPM`s from different producers have been published in various works: [32], [15], [2], [16] and [33]. As an example, the *DCR* corresponding to SiPM devices produced by Hamamatsu HPK, SensL and FBK measured at 0.5 p.e amplitude threshold is presented in Figure 2.34 [15]. The *DCR* as a function of ΔV for three SiPM`s produced by KETEK with different µcell sizes (50 × 50, 60 × 60 and 75 × 75 µm^2) is presented in Figure 2.35 [16]. From these plots we can observe the *DCR* increases with increasing the µcell size, from ~300 KHz/mm^2 to *DCR* ~400 KHz/mm^2 for the devices with 50 × 50 µm^2 and 75 × 75 µm^2 µcell sizes respectively at ΔV = 3 V. Such behavior shows that

DCR scales with the device area, therefore to correctly compare the *DCR* from different SiPM`s, the *DCR* should be normalized to the SiPM active area.

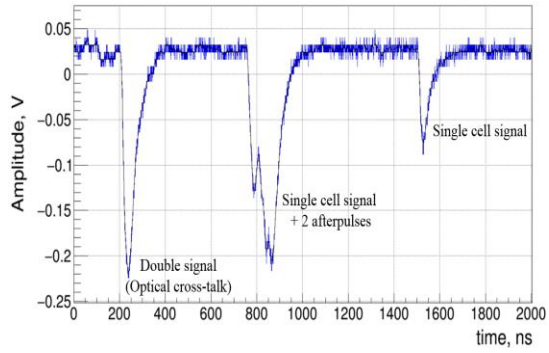

Figure 2.33 Oscilloscope waveform of different types of SiPM (Hamamatsu S10931-050P) dark signals (A. Nagai, not published)

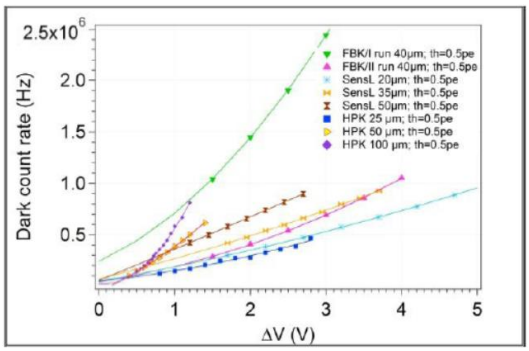

Figure 2.34 DCR vs. ΔV for SiPM`s with different μcell sizes produced by Hamamatsu HPK [15]

The comparison between *DCR* of Hamamatsu (old and new devices), KETEK, FBK (AdvanSiD) and SensL devices are presented in Figure 2.36 [33]. We can observe that for new Hamamatsu the *DCR* has been reduced from ~0.4 MHz/mm^2 to 0.05 MHz/mm^2 (~30%) at $\Delta V = 2.5$ V.

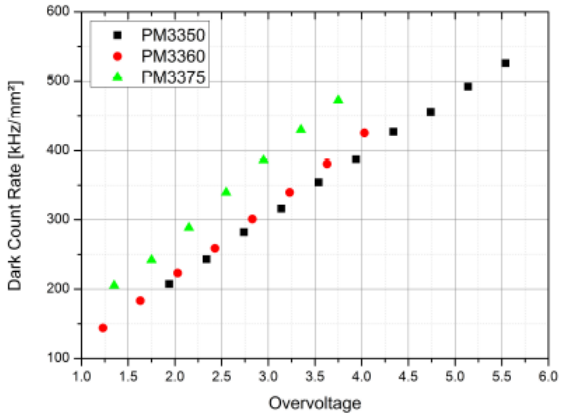

Figure 2.35 DCR vs. ΔV for SiPM`s with different μcell sizes produced by KETEK [16]

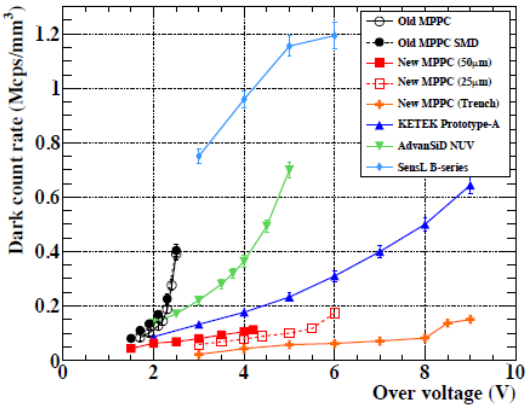

Figure 2.36 DCR vs. ΔV for SiPM produced by Hamamatsu, KETEK, FBK (AdvanSiD) and SensL [33]

2.2.3.e. Optical cross-talk

Optical crosstalk occurs when during the primary avalanche multiplication process (triggered by external photon or thermally generated carriers) external photons are emitted and starts secondary avalanches in one or more neighbor μcells. The secondary avalanche may be mostly simultaneous with the primary one (i.e. direct crosstalk) or delayed by several 10`s of ns (i.e. delayed crosstalk). A schematic drawing of optical cross-talk is presented in Figure 2.37 [34]. The situation when the primary avalanche in the middle μcell creates three external photons is shown. One of the photons directly reaches the neighbor μcell and initiates the direct cross-talk (P-CT). The second photon creates a carrier outside of avalanche multiplication region of the left neighbor μcell. This carrier drifts to the avalanche region, triggering a delayed secondary avalanche (characterized by a drift time with respect to the primary avalanche). This process is called delayed cross-talk (D-CT). The third photon leaves the SiPM without initiating any secondary avalanche, no cross-talk occurs (No-CT).

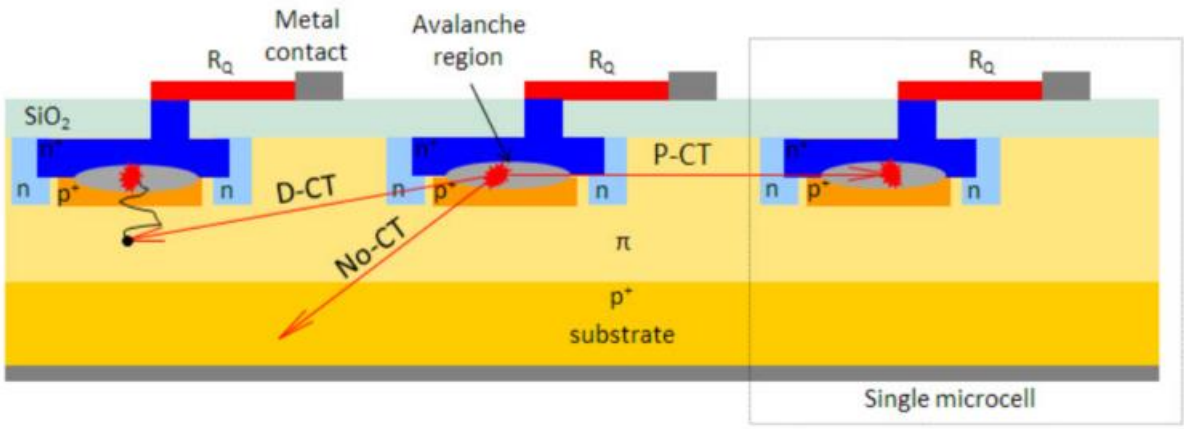

Figure 2.37 Schematic drawing of optical cross-talk between three neighbor μcells. The situations which create the direct (P-CT), delayed (D-CT) and no (No-CT) cross-talk are shown [34].

Following Lacaita [35] the 2.9×10^{-5} photons can be emitted with energy higher than 1.14 eV by one carrier crossing the junction. The typical number of carriers created in one avalanche is of order of 10^6 what results to ~30 emitted photons which can trigger optical cross-talk in the neighbor μcells. Since the number of charges in one avalanche increases with ΔV (See the Eq. 2.24), the number of emitted photons (optical cross-talk) increases with the ΔV too.

It was shown by Prochazka [36] that the optical cross-talk probability increases with reducing the distance between μcells, hence this phenomena sets a limits to the μcell density. To overcome this limitation some of these works [36] [37] proposed the injection of the metal trenches between the μcells in order to cover μcells from the emitted photons (see Figure 2.38). This idea was used by SiPM producers (i.e. Hamamatsu, KETEK, SensL etc.) and allowed to decreases the optical cross-talk probability by few times, as shown in Figure 2.39 [7] and Figure 2.40. Unfortunately trenches technology has also a drawback: it reduces the geometrical fill factor which leads to *PDE* decrease (see more details in the Section 2.2.4 “Photon detection efficiency (PDE)”).

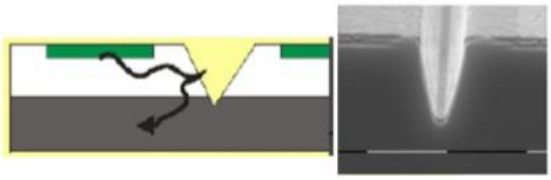

Figure 2.38 Example of the metal trench between to μcell [14]

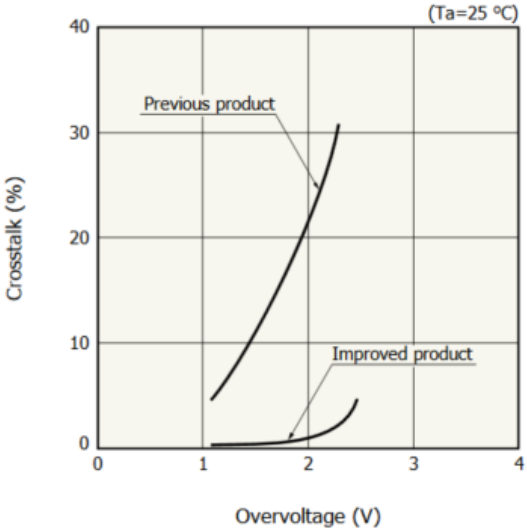

Figure 2.39 Typical example of a cross-talk probability vs. overvoltage for Hamamatsu devices without trenches (previous product) and with tranches (improved product) [7]

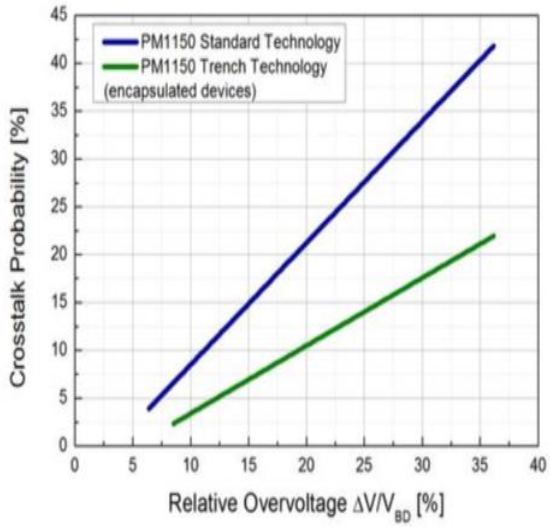

Figure 2.40 Optical cross-talk probability vs. relative overvoltage for a PM1150 with and without trenches

It can be observed (See Figure 2.39 and Figure 2.40) that trench technology doesn't reject completely the optical cross-talk. Following Rech [38] this behavior can be explained by the fact that no negligible contributions to cross-talk comes from the photons with indirect optical path which are reflecting off the bottom of the chip (See Figure 2.41 [38]).

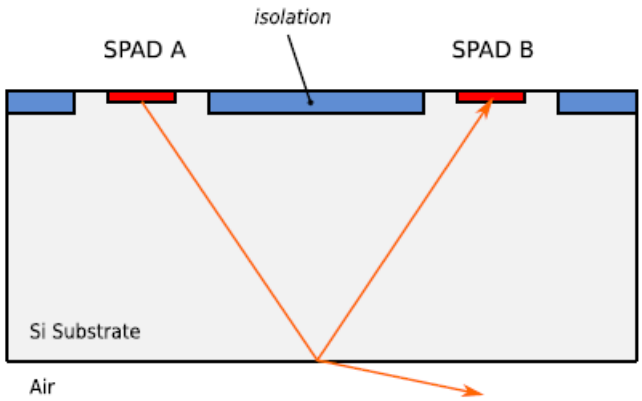

Figure 2.41 Schematic representation of the indirect emitted photon optical path contributing to optical cross-talk [38]

Experimentally, the optical cross-talk probability can be calculated from measurements of *DCR* as a function of threshold (See Figure 2.42, [32]). The probability of two or more simultaneous thermal pulses is negligible such that, without cross-talk, only signals with an amplitude of 1 p.e. should be observed. However, from Figure 2.42, additional to 1 p.e. pulses, we can observe pulses with amplitudes of 2 p.e, 3 p.e. and higher, these pulses appearing due to optical cross-talk. The cross-talk probability can be estimated as the ratio between dark rates measured at 1.5 p.e. and 0.5 p.e. thresholds.

The cross-talk probability as a function of ΔV for Hamamatsu and KETEK devices is presented in Figure 2.43 and Figure 2.44. As mentioned above, the cross-talk probability increases with increasing ΔV due to increasing of the device gain (See Eq. 2.24), this leading to increasing of the number of emitted photons. From Figure 2.43 and Figure 2.44 we can observe that independent of the producer the cross-talk probability increases with increasing µcell size, because the $C_{\mu cell}$ and G are increasing too (See Eq. 2.24).

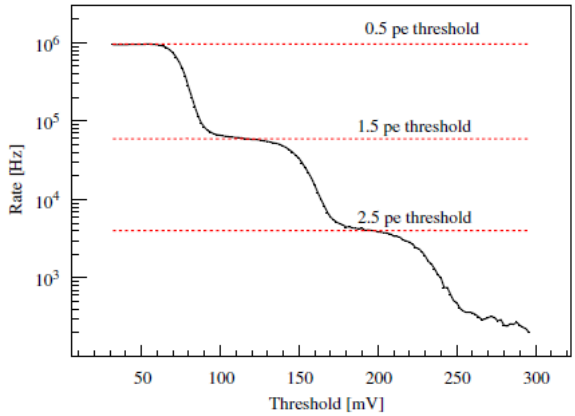

Figure 2.42 DCR vs. threshold of a Hamamatsu S10362-11-050C, operated at ΔV = 1.3V. The DCR at 0.5, 1.5 and 1.5 p.e. levels threshold are indicated by the rad dashed lines [32]

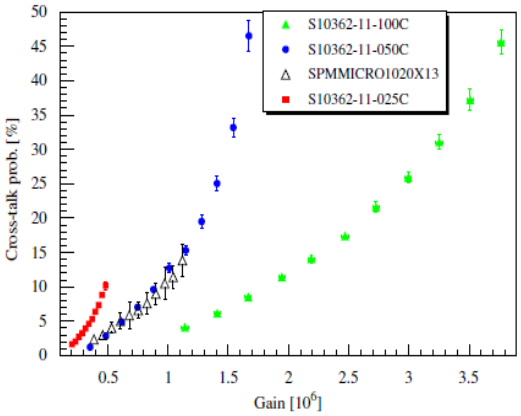

Figure 2.43 Cross-talk probability of the different SiPM`s as a function of their gain [32]

The cross-talk probability as a function of *ΔV* for SiPM devices produced by Hamamatsu, KETEK, SensL and FBK (AdvanSiD) is presented in Figure 2.45. As was expected, the latest devices with trench technology presented the lowest cross-talk probability.

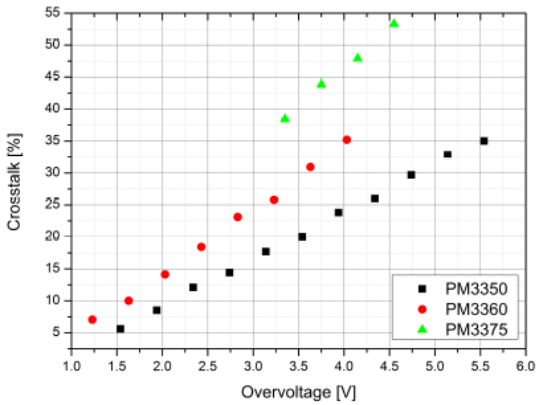

Figure 2.44 Cross-talk probability of KETEK devices with different µcell sizes [16]

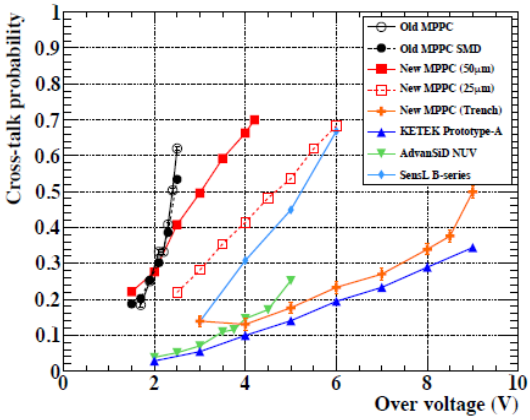

Figure 2.45 Cross-talk probability vs. ΔV for SiPM produced by Hamamatsu, KETEK, FBK (AdvanSiD) and SensL [33]

2.2.3.f. *Afterpulses*

Afterpulses are the second source of correlated noise. Afterpulses occur when during the primary avalanche multiplication process (triggered by external photon or thermally generated carriers) one or more carriers are captured by trap levels in the µcell junction depletion layer and released after some time, triggering a secondary avalanche discharge correlated to the primary one. The schematic interpretation of afterpulses mechanism is presented in Figure 2.46.

The amplitude of afterpulses strongly depends on the recovery state of the µcell, and can be expressed as:

$$A_{ap} = A_{1pe} \times \left[1 - \exp\left(- \frac{\Delta t}{\tau_{fall\ slaw}} \right) \right] \qquad 2.35$$

where A_{ap} and A_{1pe} – are the afterpulse and 1 p.e. pulse amplitudes respectively, $\tau_{fall\ slow}$ – is the SiPM signal falling edge slow time constant defined in Eq. 2.23, and Δt – is the time interval between primary pulse and afterpulse. A collection of primary pulses followed by afterpulses is presented in Figure 2.47 [39].

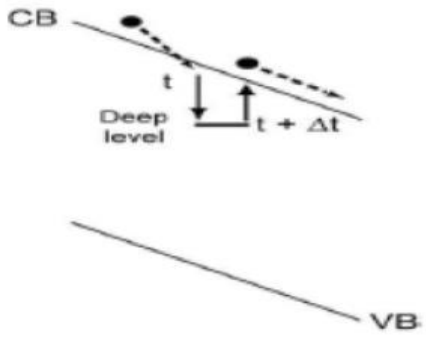

Figure 2.46 Schematic interpretation of the afterpulses mechanism. In the time moment t the carrier in the conductive band (CB) is captured by deep trap level and released again in time t+Δt [14]

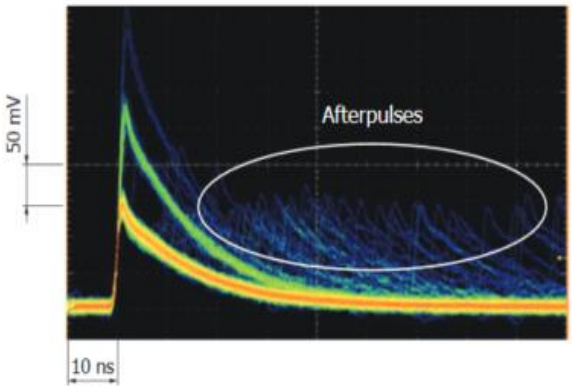

Figure 2.47 Collection of primary pulses followed by afterpulses [39]

Every afterpulse can produce at its side another avalanche, of which carriers may be trapped too and lead to a production of afterpulsing cascades. Following Para [40] afterpulsing with a constant afterpulse probability P_{AP} would lead to an increases of the number of total pulses by an additional contribution:

$$N_{aft} = P_{AP} + P_{AP}^2 + P_{AP}^3 + \ldots = \frac{P_{AP}}{1 - P_{AP}} \qquad 2.36$$

The measurements of afterpulses probability P_{AP} [32] as a function of the ΔV for three Hamamatsu and KETEK devices with different µcell sizes are presented in Figure 2.48 [32] and Figure 2.49 [16] respectively. For both measurements we can observe that P_{AP} increases with increasing the ΔV. Because the number of carriers in one avalanche increases with ΔV (see the Eq. 2.24), the probability that carriers may be trapped is increasing too.

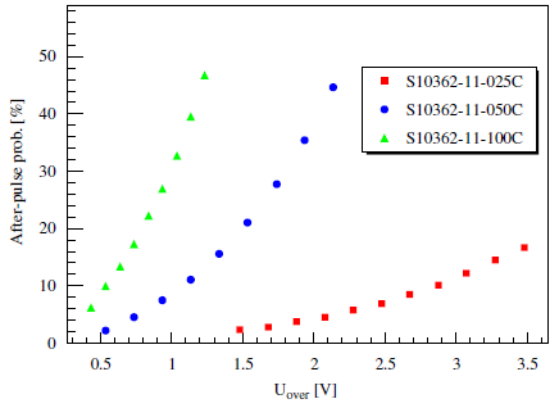

Figure 2.48 Afterpulses probability vs. ΔV for three Hamamatsu devices with different μcell size [32]

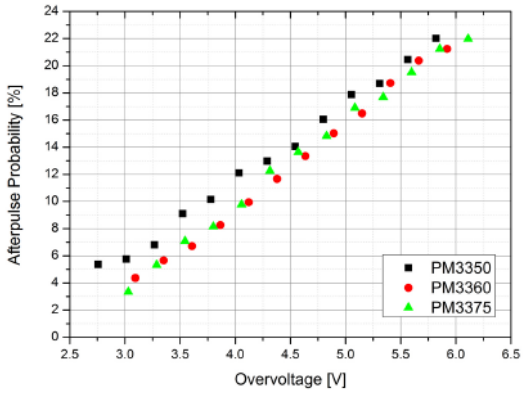

Figure 2.49 Afterpulses probability vs. ΔV for three KETEK devices with different μcell size measured at -20^{0}C [16]

2.2.4. **Photon detection efficiency (PDE)**

The *PDE* of a SiPM is defined as the ratio between the number of output signals of the device exceeding the *DCR* and number of photons falling on the detector surface. To be detected, a photon should reach the active area of the device, it should generate an electron-hole pair which should pass to high field region and trigger an avalanche. Therefore, the *PDE* of a SiPM is the product of three parameters: the quantum efficiency *QE*, the geometrical fill factor ε and the triggering probability P_{Geiger}:

$$PDE = QE \cdot \varepsilon \cdot P_{Geiger} \qquad 2.37$$

2.2.4.a. Quantum efficiency (QE)

The *QE* represents the probability that a photon will create an electron-hole pair that reach the high field region. Since the Silicon behaves as a mirror, reflecting more than 50% of incident light, the *QE* is a combination of two factors: the transmittance of the dielectric layer on the top of the μcell and the internal *QE*.

Following Tyagi [41], the optical light transmittance on the top of the SiPM μcell can be maximized, by implementing an anti-reflection coating ARC. The transmittance of the ARC depends on the wavelength and should be optimized for a given light color. The simulation of the ARC layer transmittance as a function of wavelength for different SiO_2 and Si_3N_4 thicknesses is presented in Figure 2.50 (C. Piemonte, not published) and shows that an optimal ARC for 420 nm wavelength can be obtained with ~20 nm of SiO_2 and ~30 nm of Si_3N_4.

The internal *QE* represents the probability that a photon which has already passed the ARC layer will create an electron-hole pair in the active thickness. According to the Beer-Lambert law, an incident photon flux I_{photon} will attenuate in silicon by creating electron-hole pairs:

$$I(\lambda, x) = I_{photon}(\lambda) \cdot \exp[-\alpha(\lambda) \cdot z] \qquad 2.38$$

where I_{photon} – is the photon flux of a given wavelength λ, α – is the absorption coefficient, z – is the depth in detector. The absorption coefficient for silicon as a function of wavelength is

presented in Figure 2.51 [14]. The penetration depth (depth at which the light intensity inside the material falls to *1/e*) for silicon is presented on the alternative y-axis.

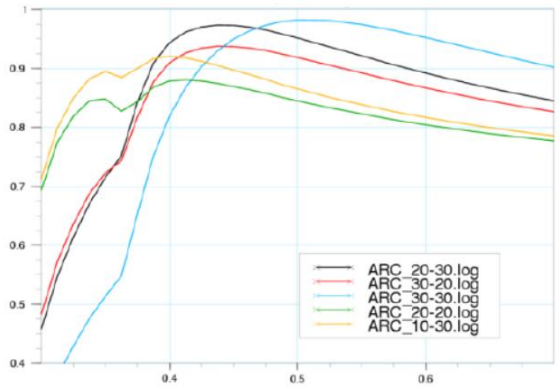

Figure 2.50 Simulation of ARC layer transmittance as a function of wavelength for different SiO_2 and Si_3N_4 thicknesses (C. Piemonte, not published)

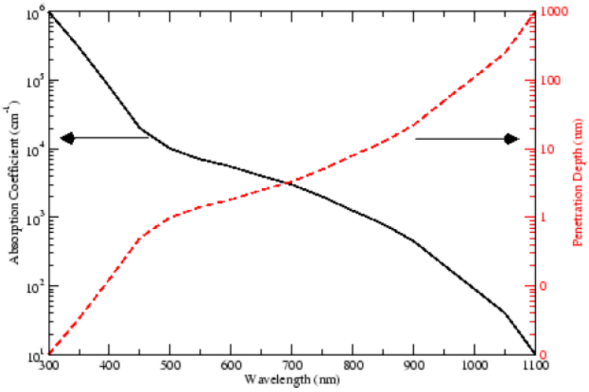

Figure 2.51 Absorption coefficient and penetration depth for silicon as a function of light wavelength

2.2.4.b. Geometrical fill factor (ε)

The ε represents the ratio between the sensitive area to the total detector surface. Typically the dead area is due to quenching resistance, connection between µcells (metal grid connection) and technological improvements (trenches). Since this dead area multiplies with the number of µcell, the best ε can be achieved with a small number of big µcells. The decrease of active area with decreasing µcell size is clearly seen in the relative sensitivity scan for Hamamatsu devices in Figure 2.52, Figure 2.53 and Figure 2.54 [32].

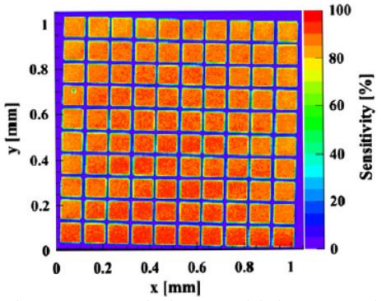

Figure 2.52 Relative sensitivity scan of the Hamamatsu S10362-11-100C, with 100 × 100 µm² µcell size and 100 µcells [32]

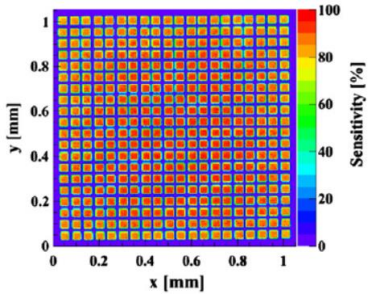

Figure 2.53 Relative sensitivity scan of the Hamamatsu S10362-11-50C, with 50 × 50 µm² µcell size and 400 µcells [32]

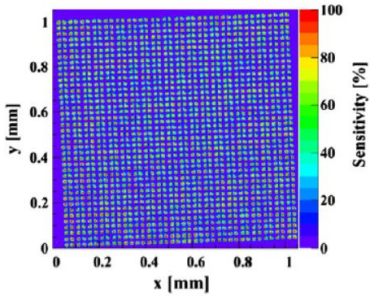

Figure 2.54 Relative sensitivity scan of the Hamamatsu S10362-11-25C, with 25 × 25 µm² µcell size and 1600 µcells [32]

2.2.4.c. Triggering probability (P_{Geiger})

The triggering probability P_{Geiger}, also well known as Geiger probability, represents the probability that a carrier reaching the high field region will trigger an avalanche. The pioneering studding of P_{Geiger} in avalanche diodes was done by Oldham [42]. In this work Oldham consider an avalanche n^+-p abrupt junction diode with depletion width W (with $x = 0$ taken at the n+ edge and $x = W$ taken at the p edge of the space-charge region). The $P_e(x)$ was defined as the probability that an electron starting at position x in the depletion layer will trigger an avalanche. The function $P_h(x)$ for holes was analogously defined. The triggering probability can be calculated from:

$$\frac{dP_e}{dx} = (1 - P_e) \cdot \alpha_e \left[P_e + P_h - P_e P_h \right] \quad 2.39$$

$$\frac{dP_h}{dx} = -(1 - P_h) \cdot \alpha_h \left[P_e + P_h - P_e P_h \right] \quad 2.40$$

where α_e and α_h – are the electrons and holes ionization rates respectively. By integrating these equations with two boundary conditions $P_e(0) = 0$ and $P_h(W) = 0$ and few simplifications (α_e, α_h – are function of the electrical field only, assuming one-dimensional geometry) the triggering probability was calculated by Oldham and the results for three overvoltages (ΔV = 0.1 V, 1 V and 10 V) are presented in Figure 2.55 [42]. We can see that an appreciable fraction of the carriers generated within the depletion region will not trigger an avalanche even at ΔV = 10 V. The probability that an electron or a hole, starting as a minority carrier from the neutral bulk and triggering an avalanche, is given by $P_e(W)$ or $P_h(x)$, respectively. This theoretical probability compared with the experimental measurements is presented in Figure 2.56 [42]. We can observe that $P_e(W)$ triggering probability increases with ΔV and reaches a plateau (saturation) at quite high $\Delta V \approx$ 8V. Also, completely different shapes of $P_e(W)$ and $P_h(x)$ can be observed.

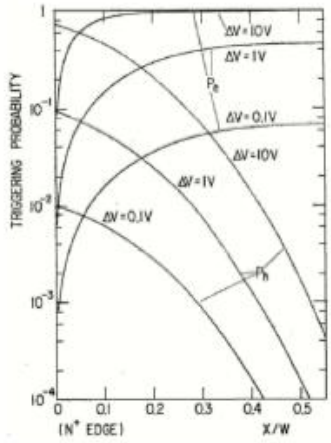

Figure 2.55 The triggering probabilities P_e and P_h an n^+-p diode at several voltages above the breakdown [42]

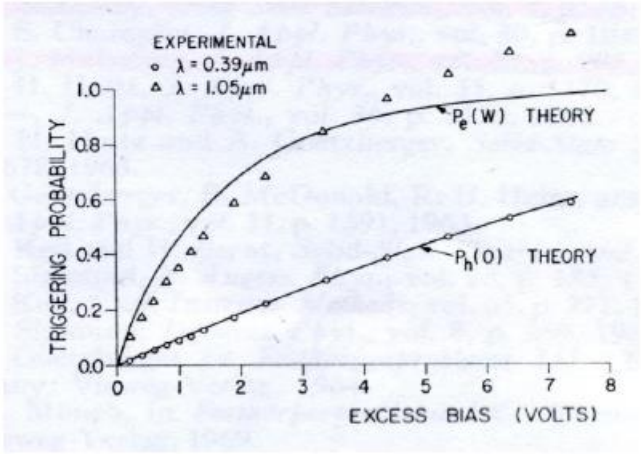

Figure 2.56 The theoretical calculation of P_e and P_h for carriers starting as minority carriers at the edge of the depletion region (lines) and experimental measurements of average number of detected photons (normalized at 3.4 V excess bias) [42]

Important work on this subject was done by McIntyre [43]. He showed that in approximation:

$$\alpha_h = k \cdot \alpha_e \quad 2.41$$

where k – is a constant independent of electrical field, the $P_h(0)$ and $P_e(W)$ can be calculated as a function of two parameters k and δ, from:

$$-\log\left[1-P_h(0)\right]=\frac{k}{1-k}\log\left[P_h(0)f(W)+1-P_h(0)\right] \qquad 2.42$$

$$1-P_h(0)=\left[1-P_e(W)\right]^k \qquad 2.43$$

$$f(W)=\exp\left[(1-k)\cdot\delta\right] \qquad 2.44$$

$$\delta=\int_0^W \alpha_e dx \qquad 2.45$$

The results of a numerical calculation of $P_h(0)$ and $P_e(W)$ as a function of k and δ are presented in Figure 2.57 [43]. We can observe that the shapes of $P_h(0)$ and $P_e(W)$ are strongly dependent of the ratio between α_h and α_e (i.e. parameter k).

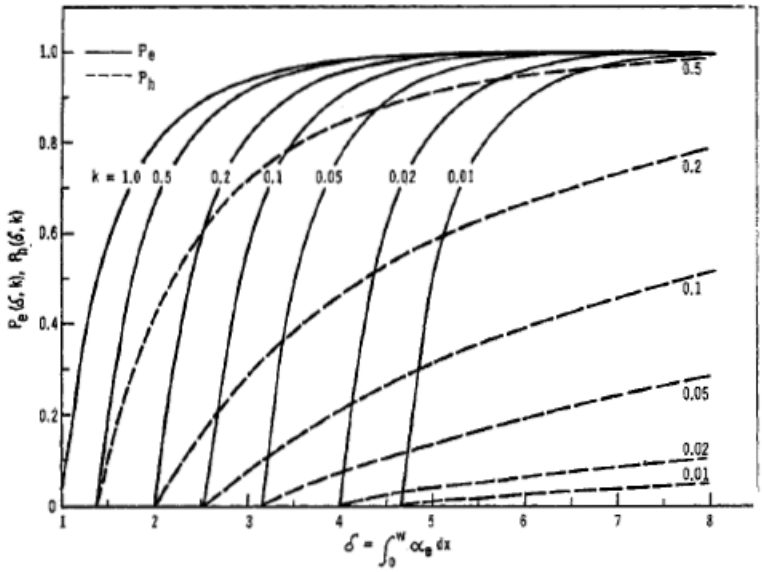

Figure 2.57 Numerical calculation of $P_e(W)$ and $P_h(0)$ as a function of two parameters k and δ [43]

2.2.4.d. Measurements of Photon Detection Efficiency (PDE)

The *PDE* of SiPM devices were investigated experimentally by few authors [15], [32], [2], [44], [33], [16]. The *PDE* as a function of overvoltage ΔV, for different light wavelengths and various SiPM Hamamatsu devices of different μcell sizes (25 μm, 50 μm and 100 μm) is presented in Figure 2.58 [32]. We can observe that the *PDE* increases with ΔV due to increasing of P_{Geiger} as expected from Oldham`s calculations and doesn't reach the plateau because of limited working range of the devices.

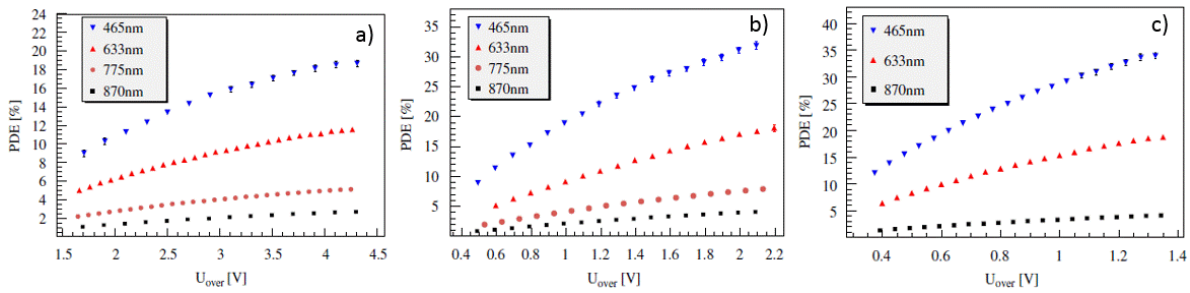

Figure 2.58 PDE as a function of ΔV for different light wavelengths for Hamamatsu devices: S10362-11-25 a) S10362-11-50 b) and S10362-11-100 c) [32]

The *PDE* as a function of *ΔV* for green light for three KETEK devices with different µcell sizes (50 µm, 60 µm and 75 µm) is presented in Figure 2.59. We can observe that PDE increases with increasing of device µcell size due to increasing the geometrical fill factor *ε*.

The relative *PDE* as a function of *ΔV* for Hamamatsu, KETEK, SensL and FBK (AdvanSiD) devices is presented in Figure 2.60. We can observe that the new Hamamatsu device without trenches has the highest *PDE*. Moreover, the devices with trenches show smaller *PDE* with respect to devices without trenches, since the trench technology involves a reduction of the geometrical fill factor.

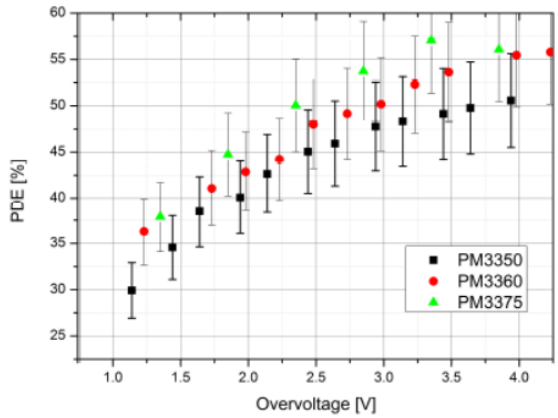

Figure 2.59 PDE vs. ΔV for KETEK devices with different µcell sizes [16]

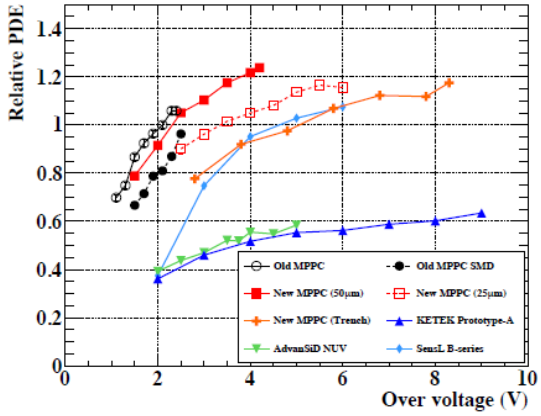

Figure 2.60 Relative PDE vs. ΔV for SiPM devices produced by Hamamatsu, KETEK, FBK (AdvanSiD) and SensL [33]

The *PDE* as a function of the wavelength *λ* for SiPM devices with different µcell size produced by Hamamatsu HPK is presented in Figure 2.61 [44]. We can observe that the *PDE* has a peak in the blue region (420 nm), and it increases from 20% to 40% with increasing the µcell size from 25 µm to 100 µm due to increasing the geometrical fill factor *ε*.

The *PDE* as a function of the wavelength *λ* for SiPM devices produced by SensL and FBK is presented in Figure 2.62 [15]. We can observe that for these devices the *PDE* has a peak in the green region (500 ÷ 600 nm) with the maximum value of the 6 ÷ 12%. The difference of the *PDE* values between these SiPM devices and those produced by Hamamatsu HPK can be related to different geometrical fill-factor *ε* and higher P_{Geiger} of the Hamamatsu HPK devices for blue light with respect to the FBK and SensL devices: for the HPK devices (i.e. p^+n junction on n-type substrate), the avalanches are triggered by the electrons which are traversing the high field region from the p^+ region to the n-substrate contact, instead for the FBK and SensL devices (i.e. n^+p junction on p-type substrate), the avalanches are triggered by holes, since they are traversing the high field region by traveling from the n+ region to the p^- substrate contact. Since

the electrons have higher P_{Geiger} than holes (see Figure 2.56), the P_{Geiger} for blue light is higher for Hamamatsu HPK devices with respect of FBK and SensL devices.

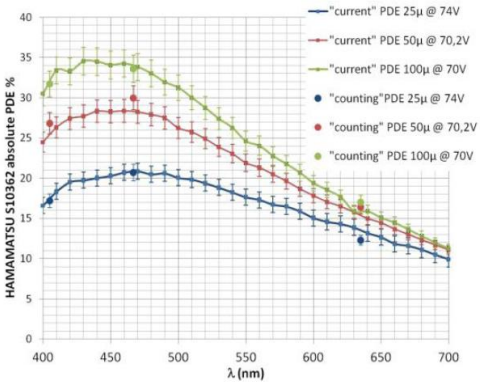

Figure 2.61 PDE as a function of wavelength for Hamamatsu devices with different µcell size: 25 µm (S10362-11-25), 50 µm (S10362-11-50) and 100 µm (S10362-11-100) [44]

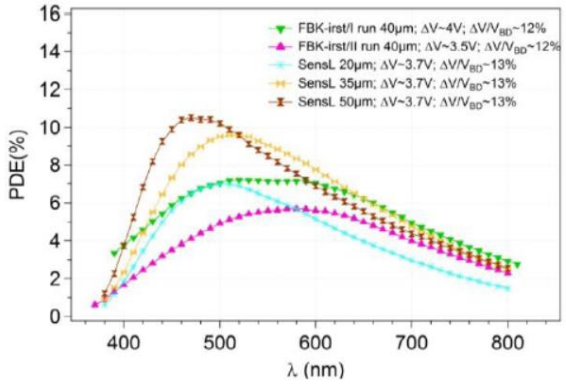

Figure 2.62 PDE as a function of wavelength for SiPM devices produced by FBK and SensL [15]

2.2.5. **Temperature dependence**

The temperature T represents an important parameter affecting the most part of SiPM parameters (i.e. IV characteristics, R_q, signal shape, V_{BD}, *DCR*, *PDE* etc.) and consequently leading to final variation of detection characteristics. The behavior of SiPM devices as a function of temperature near room T (from -25 ^{0}C to +65 ^{0}C) was studied by Pagano [45], Roncali [46] and Vacheret [2]. However, a study of SiPM parameters in a much wider temperature range down to cryogenic temperatures allows to have a closer look to the physical phenomena staying behind this temperature dependence and eventually finds equivalent operating conditions independent of temperature. Such studies were done by Cardini [47], Collazuol [48], Dinu [49] and Lightfoot [50] and selected results will be presented in the following.

In this Section, the temperature variation of the SiPM electrical parameters such as forward and reverse IV characteristics, quenching resistance, signal shape, gain, breakdown voltage, dark count rate, optical crosstalk and photon detection efficiency will be shown.

2.2.5.a. Forward IV characteristic vs. T

As was shown in the Section 2.2.2.a "*Forward IV characteristic*", the forward IV can be used for quenching resistor R_q calculation. Therefore the forward IV measured at different T can be used to study the variation of R_q with T.

The forward IV curves measured at different T [48] for an FBK device are presented in Figure 2.63. We can distinguish two regions: the first one with low current ($I < 10^3$ nA) and exponential current increase and the second one with high current ($I > 10^3$ nA) and linear current increase. Using the high current region and Eq. 2.18, the value of R_q was extracted and presented in Figure 2.64 [51]. The R_q decreases with increasing the T from ~90 MΩ at T = 50 K up to 0.48 MΩ at room T. The R_q was empirically parameterized as:

$$R(T) \approx 0.13 \cdot \left[1 + \frac{300\,\mathrm{K}}{T} \exp\left(\frac{300\,\mathrm{K}}{T}\right)\right] \mathrm{M\Omega} \qquad 2.46$$

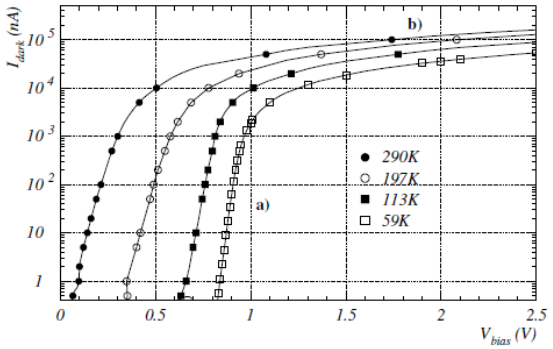

Figure 2.63 Forward IV characteristics at different temperatures for an FBK SiPM device. Low current region a): the voltage drop is linearly proportional to T. High current region b): the current limited by series and quenching resistances [48]

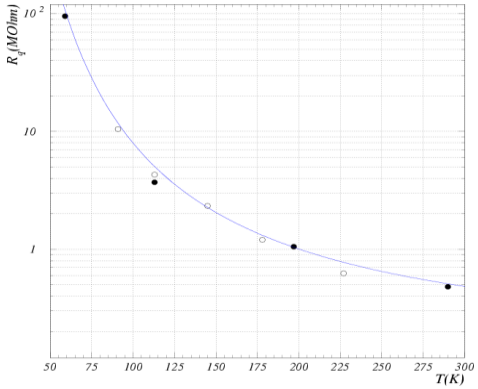

Figure 2.64 R_q calculated from forward IV characteristics vs. temperature [51]

Also, following Collazuol [48] the junction temperature can be measured precisely from the low current region. In this region the voltage at a given current is described by Eq. 2.17. Since the current is small (I < 10^3 nA) the $I\frac{R_S}{N_{\mu cell}} + I\frac{R_q}{N_{\mu cell}}$ term is negligible and the Eq. 2.17 transforms to:

$$V_{Bias} = \frac{\eta k T}{q}\left[\ln\left(\frac{I}{I_0} + 1\right)\right] \qquad 2.47$$

Therefore, the junction temperature can be calculated from the linear dependence of voltage drop at a given low current $\Delta V_{fwd}(I_{fix},T)$ with the temperature:

$$\Delta V_{fwd}(I_{fix},T) = V_{bias}^{fix}(I_{fix},T_{fix}) - \frac{\eta k T}{q}\left[\ln\left(\frac{I_{fix}}{I_0} + 1\right)\right] \qquad 2.48$$

where $V^{fix}_{bias}(I_{fix},T_{fix})$ – is the applied voltage at a fixed low current I_{fix}.

2.2.5.b. *Reverse IV characteristic vs. T*

As was shown in the Section 2.2.2.b "*Reverse IV characteristic*", the reverse IV can be used for breakdown voltage V_{BD} calculation. Therefore the reverse IV measured at different T can be used to study the variation of V_{BD} with T.

The reverse IV curves measured at different T for an FBK device are presented in Figure 2.65 [51]. The V_{BD} values have been extracted from these measurements the using the parabolic fit procedure (more details were given in the Section 2.2.2.b "*Reverse IV characteristic*") and are presented in Figure 2.66. We can observe that V_{BD} decreases linearly with T up to ~200 K, while below this T, the detector V_{BD} presents slower and nonlinear temperature dependence. More details about this T behavior of V_{BD} can be found later in the section (see 2.2.5.e "*VBD vs. T*").

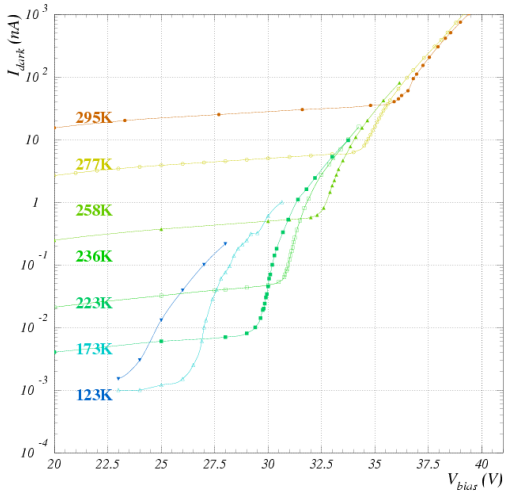

Figure 2.65 Reverse IV characteristics for different temperatures [51]

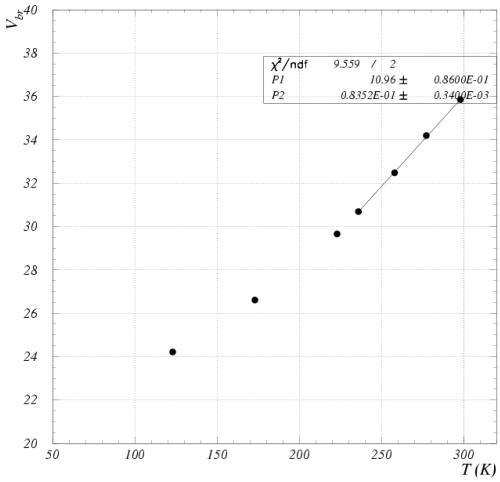

Figure 2.66 V_{BD} extracted from the reverse IV curves according the parabolic fit procedure as a function of T [51]

2.2.5.c. *Signal shape vs. T*

The variation of the R_q with T (See Figure 2.64) leads to variation of the SiPM signal shape. The SiPM signal shapes measured at different T are presented in Figure 2.67 [52], Figure 2.68 [49] and Figure 2.69 [47]. We can observe that the recovery time constant τ (signal length = $5 \times \tau$) decreases with increasing T. In Figure 2.69 c) the τ is so long that it is practically superimposed to the signal baseline. In Figure 2.67 b) and c) [52] we can clearly separate $\tau_{fall\ fast}$ and $\tau_{fall\ slow}$, while in Figure 2.67 a) [52] and Figure 2.69 a) – c) [47] the $\tau_{fall\ fast}$ can be seen only at low T.

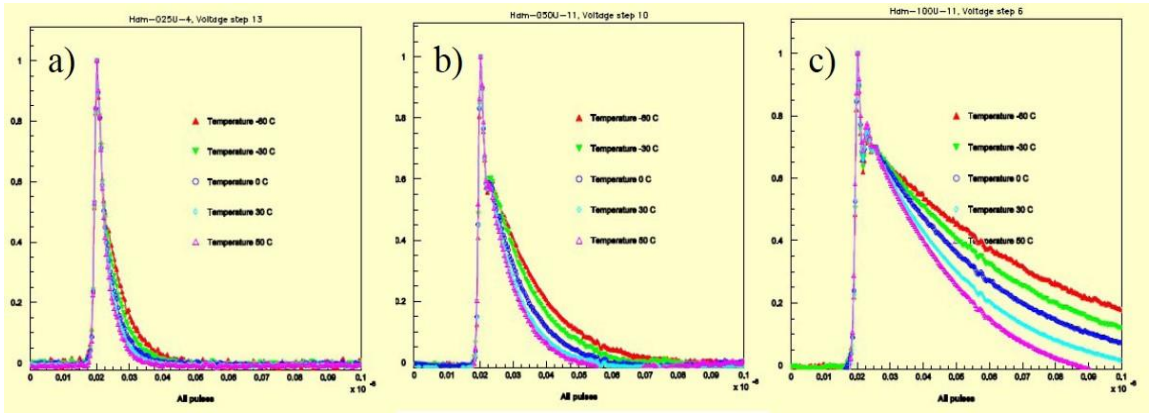

Figure 2.67 Normalized signal shape at different temperatures for the Hamamatsu SiPM`s with 25 × 25 μm^2 a), 50 × 50 μm^2 b) and 100 × 100 μm^2 c) μcell sizes [52]

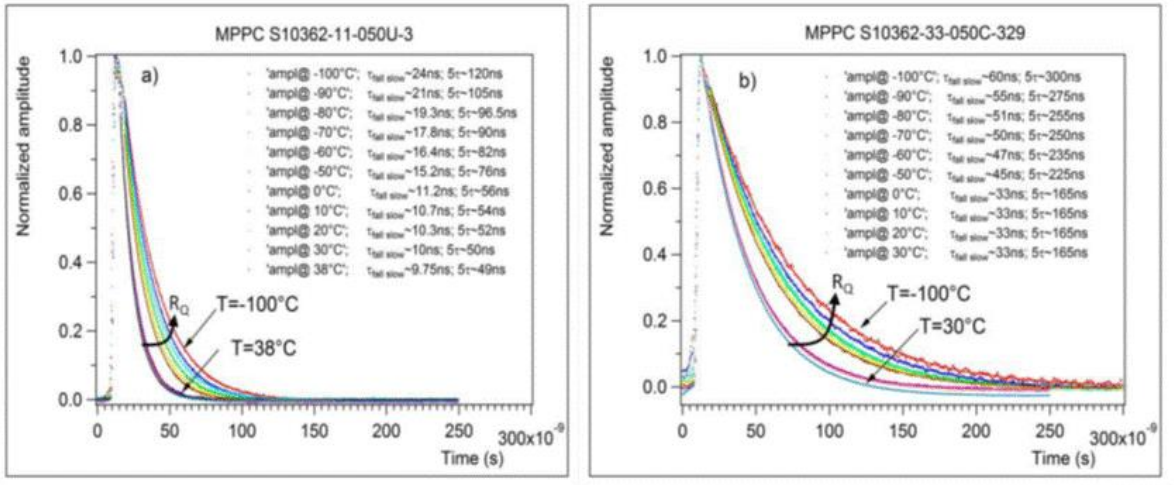

Figure 2.68 Normalized signal shape at different temperatures for the SiPM of a) 1×1 mm^2 and b) 3×3 mm^2 [49]

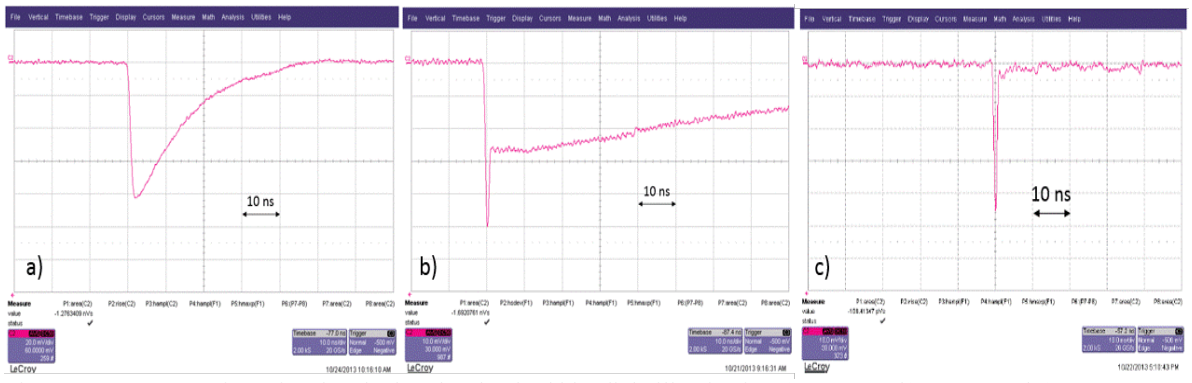

Figure 2.69 Average SiPM signal under low-level pulsed blue light illumination a) at 300 K, b) 77.4 K and c) 4.7 K [47]

2.2.5.d. G vs. T

The gain G of various SiPM Hamamatsu devices (e.g. 1 × 1 mm^2 and 3 × 3 mm^2 size) was experimentally determined from the time integration of device pulse (See Eq. 2.25) and

presented in Figure 2.70 [49]. We can observe that at a given T, the G increases linearly with V_{bias} as was expected from Eq. 2.24. At a given V_{bias}, the G increases by 2.7% with decreasing the T of 1 ^{0}C, if the device was initially biased to ΔV = 2 V. Following Dinu [14] the almost constant G (less than ~8% variation with T was observed) was observed if the ΔV is maintained constant independent of T.

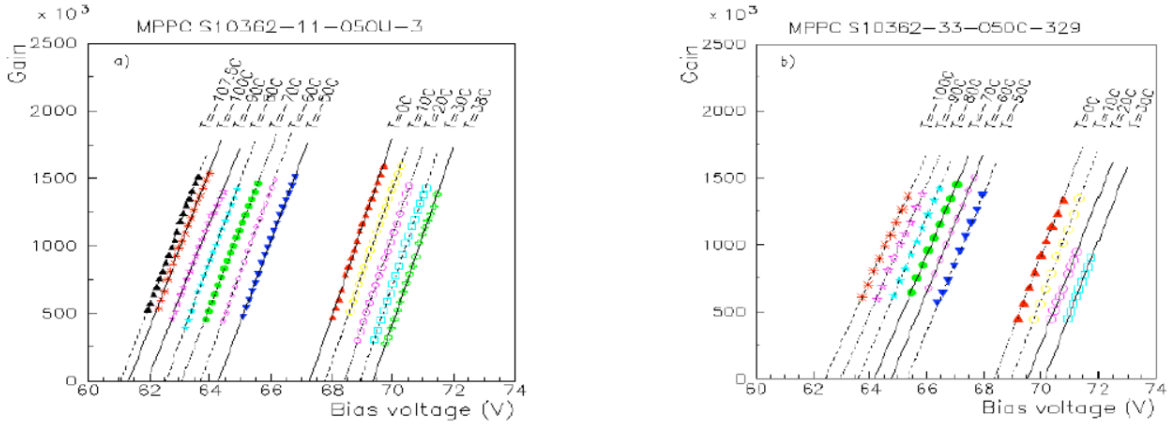

Figure 2.70 Gain G as a function of V_{bias} for the Hamamatsu devices: S10362-11-050 a) and S10362-33-050C b) [49]

The gain G measured in the T range from +25 ^{0}C down to -196 ^{0}C for SensL device is presented in Figure 2.71 [50]. Also the G measured for a given ΔV is independent of T and presented in Figure 2.72 [50].

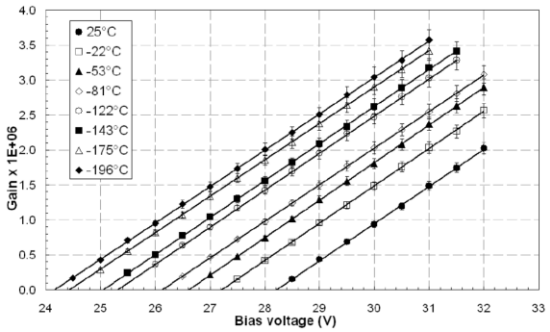

Figure 2.71 Gain G as a function of V_{bias} for SensL device [50]

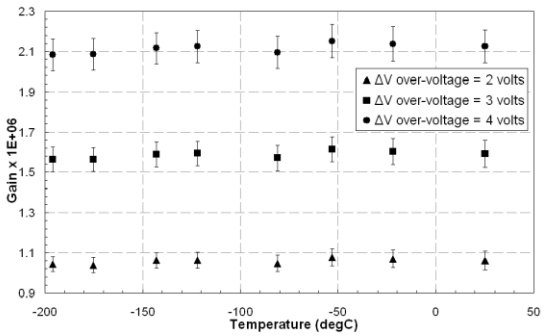

Figure 2.72 Gain G as a function of T for a constant ΔV for SenseL device [50]

2.2.5.e. V_{BD} *vs. T*

The V_{BD} as a function of T for the Hamamatsu and FBK devices is presented in Figure 2.73 [49] and Figure 2.74 [48]. We can observe that for all devices the V_{BD} decreases linearly with T up to ~180 K, with a temperature coefficient dV_{BD}/dT of ~58 mV/^{0}C and ~80 mV/^{0}C for Hamamatsu and FBK devices respectively. Below this 180 K, the detectors show slower and nonlinear temperature dependence.

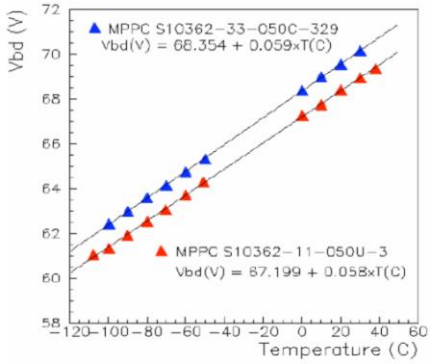

Figure 2.73 The V_{BD} as a function of T for Hamamatsu devices [49]

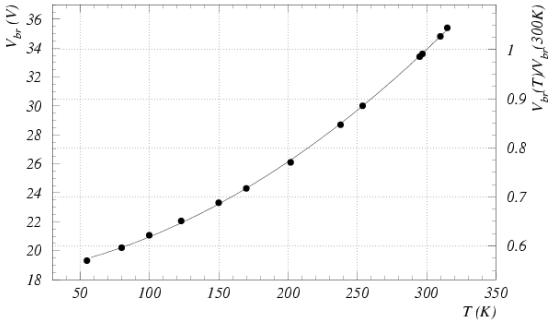

Figure 2.74 The V_{BD} as a function of T for FBK device [48]

The V_{BD} as a function of T for SensL device has been measured by Lightfoot [50] and presented in Figure 2.75 [50]. We can observe that V_{BD} decreases linearly with decreasing T, with a coefficient of 18.5 mV/^{0}C. From this data we cannot see any nonlinear behavior due to high experimental discrepancies.

Nonlinear increases of V_{BD} with increasing the T has been predicted by Crowell and Sze [53]. The predicted value of V_{BD} normalized to the room temperature value for devices with different background doping concentrations are presented in Figure 2.76 [53]. The experimental measurements of V_{BD} as a function of T for a p^+n abrupt junction with different impurity concentrations have been done by Chang [54] and presented in Figure 2.77.

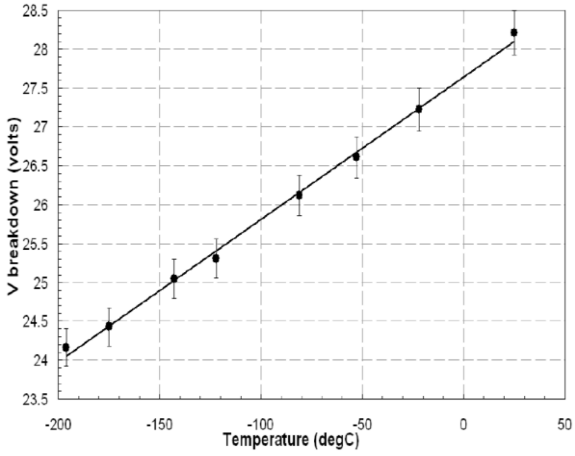

Figure 2.75 The V_{BD} as a function of T for SensL device [50]

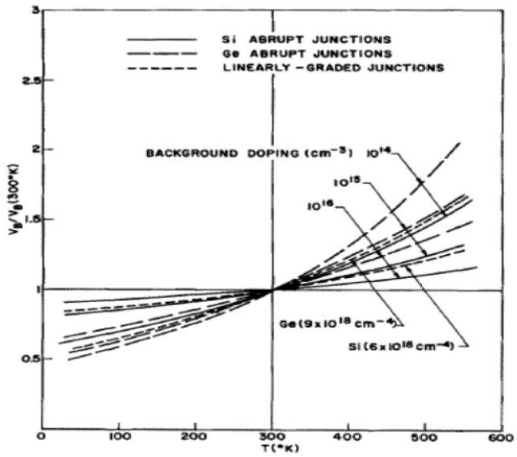

Figure 2.76 Normalized V_{BD} vs. T for Si and Ge p-n junctions. V_{BD} (300 K) is 2000, 330 and 60 V for Si abrupt junctions with background doping's of 10^{14}, 10^{15} and 10^{16} cm^{-3} respectively [53]

The V_{BD} temperature dependence of SiPM was investigated by Serra [18] using one-dimensional numerical TCAD simulation of GM-APD. Following these studies, the V_{BD} and its temperature coefficient increases with increasing the epitaxial layer thickness as presented in Figure 2.78 [18].

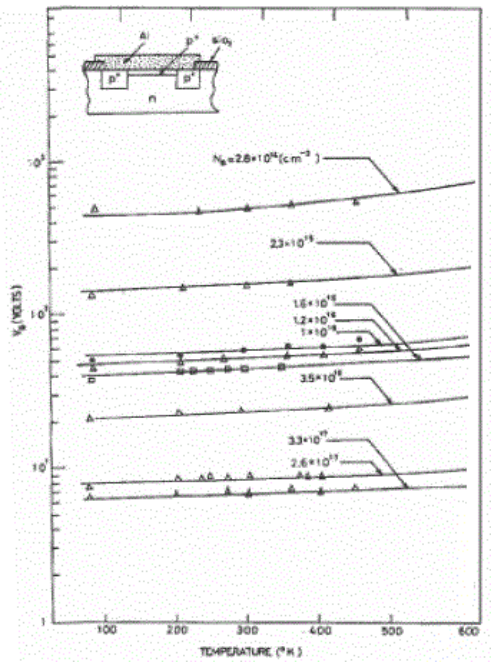

Figure 2.77 Experimental V_{BD} vs. T with impurity concentration as parameter [54]

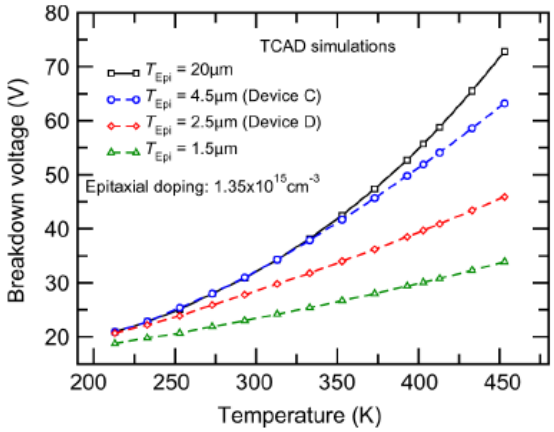

Figure 2.78 TCAD simulated V_{BD} as a function of T for four GM-APD devices with different epitaxial layer thickness [18]

2.2.5.f. *DCR vs. T*

The *DCR* of various SiPM Hamamatsu devices (e.g. 1 × 1 mm^2 and 3 × 3 mm^2) as a function of *ΔV* and different *T* is presented in Figure 2.79 [49]. We can observe that, at a given *T*, the *DCR* increases exponentially with *ΔV*, while at a given *ΔV* the *DCR* increases with *T* over many orders of magnitudes.

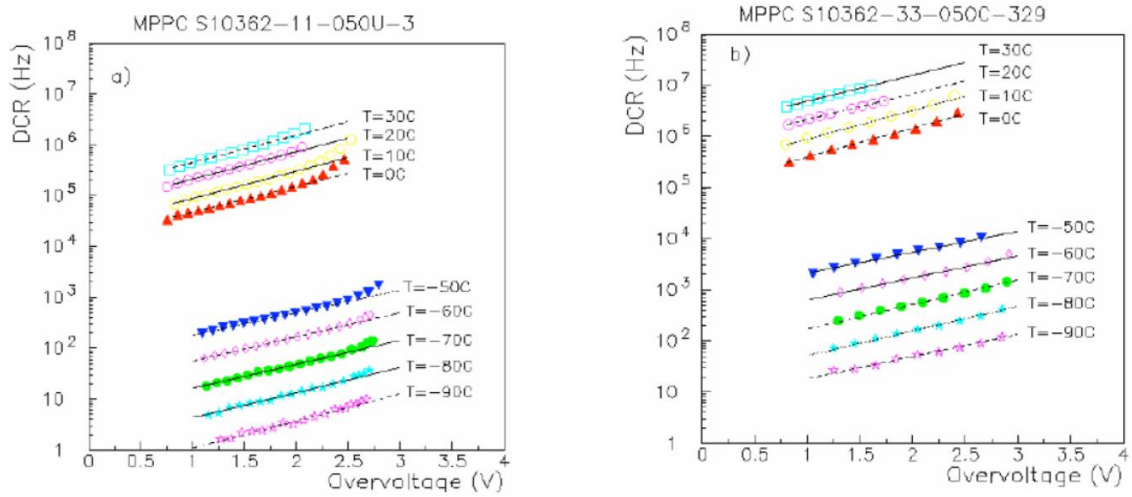

Figure 2.79 The DCR as a function of ΔV for different T for the Hamamatsu devices S10362-11-050 a) and S10362-33-050 b) [49]

The *DCR* at a given *ΔV* is proportional to the free carrier density which is related to the generation current $I_{generation}$. Following Tyagi [41] the $I_{generation}$ can be expressed as:

$$I_{generation} \cong A \cdot T^{3/2} \cdot \exp\left(-\frac{E_{act}}{k_B T}\right) \qquad 2.49$$

where E_{act} – is the thermal activation energy and A – is the constant of proportionality. Differentiating the Eq. 2.49 with respect to T, the temperature coefficient $(1/I)(dI/dT)$ of the reverse current can be obtained:

$$\frac{1}{I_{generation}}\left(\frac{dI_{generation}}{dT}\right) = \frac{1}{2T}\left[3 + \frac{E_{act}}{kT}\right] \qquad 2.50$$

For E_{act} = 1.16 eV, we obtain a change of about 8 %/K in the reverse current at 300 K. Fitting the *DCR* vs. $1/T$ with the Eq. 2.49 the estimation of E_{act} can be calculated. The E_{act} gives useful insight on the physical mechanisms (e.g. Shockley-Read-Hall generation, trap-assisted tunneling, band-to-band tunneling and etc.) leading to the *DCR*. Following Pancheri [55] the *DCR* is dominated by:

- injection from neutral region, when the E_{act} is close to the Si bandgap energy E_G = 1.12 eV;
- Shockley-Read-Hall generation when the E_{act} is close to the half the Si bandgap energy $E_G/2$ = 0.56 eV;
- Trap-assisted tunneling when the E_{act} is less than the half the Si bandgap energy $E_G/2$ = 0.56 eV
- Band-to-band tunneling when the E_{act} is close to zero.

The *DCR* at ΔV = 1 V and ΔV = 2 V as a function of $1/T$ is presented in Figure 2.80 [49] and the E_{act} of about 0.54 eV was obtained. This evidences that the DCR for these devices is dominated by Shockley-Read-Hall generation.

The *DCR* as a function of $1/T$ at ΔV = 1.5 V for the FBK device is presented in Figure 2.81 [48]. Following Collazuol, the main source of *DCR* in the range 200 K < T < 300 K is the Shockley-Read-Hall (SRH) generation enhanced to some extent by trap-assisted tunneling (in the high electric field region), while in the range 150 K < T < 200 K the band-to-band tunneling is dominating. Below the 150 K the suppression of the *DCR* is not well understood.

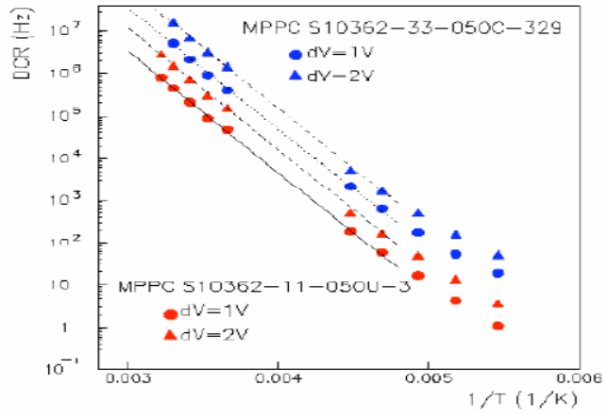

Figure 2.80 The DCR as a function of 1/T at constant ΔV for the Hamamatsu devices: S10362-11-050 and S10362-33-50 [49]

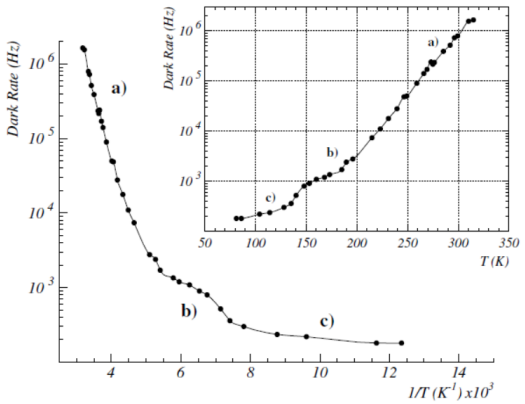

Figure 2.81 The DCR as a function of 1/T at ΔV = 1.5V for the FBK device T6-V1-PD run 2 [48]

2.2.5.g. *Optical cross-talk vs. T*

The optical cross-talk as a function of T was measured by Bouvier [56] down to -5 ^{0}C and by Lightfoot [50] down to -53 ^{0}C. For both measurements the cross-talk probability remained independent of T as presented in Figure 2.82 and Figure 2.83. This is not fully understood since the cross-talk is proportional to P_{Geiger} which might vary with T, as will be shown below.

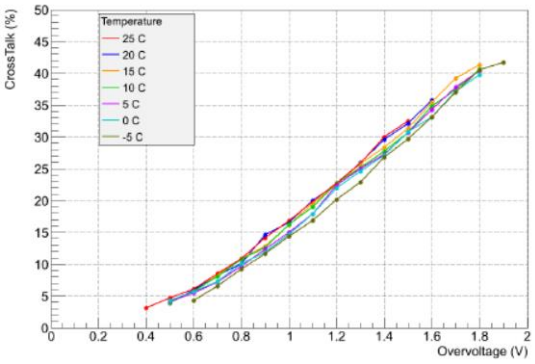

Figure 2.82 Cross-talk probability as a function of ΔV in T range from -5^0 C to +25 ^{0}C for Hamamatsu S10943-1071 device [56]

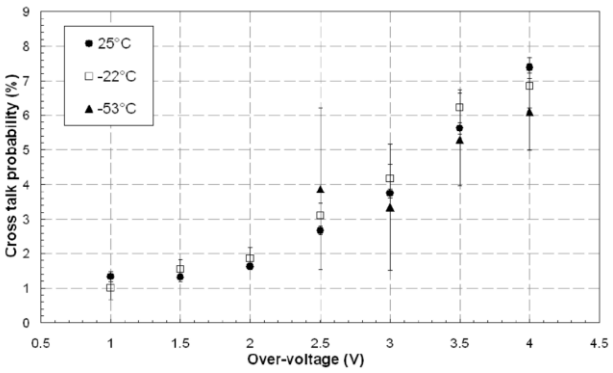

Figure 2.83 Cross-talk probability as a function of ΔV in T range from -53 ^{0}C to +25 ^{0}C for SensL device [50]

2.2.5.h. *Afterpulses vs. T*

The afterpulses probability P_{ap} as a function of T was measured by Collazuol [48] in the T range from 320 K down to 50 K for FBK device. The P_{AP} as a function of T at ΔV = 2 V is presented in Figure 2.84. We can observe that P_{AP} is almost constant down to ~110 K where is starts rising swiftly as T is further decreased. Following Collazuol [48] the possible explanation for the behavior below ~110 K is that new traps become active, which are related to carrier freeze-out.

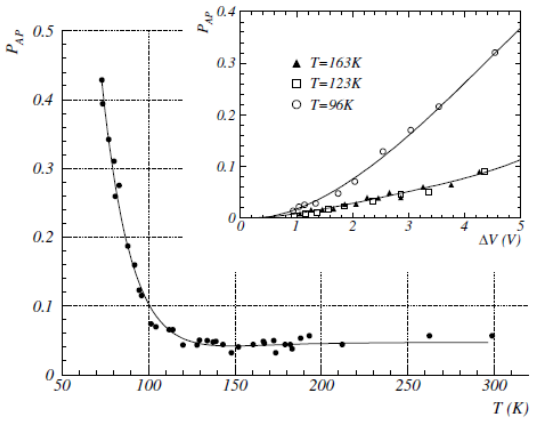

Figure 2.84 Afterpulsing probability P_{AP} as a function of T at $\Delta V = 2$ V for FBK device. The inset depicts P_{AP} as a function of ΔV [48]

2.2.5.i. *PDE vs. T*

The PDE for green light of a customized Hamamatsu SiPM for the T2K experiment in a *T* range from 15 ^{0}C to 25 ^{0}C has been measured by Vacheret [2] and the results are presented in Figure 2.85. The *PDE* as a function of *T* has been also measured by Lightfoot [50] in a *T* range from -196 ^{0}C to +25 ^{0}C for blue and red light, and presented in Figure 2.86. As it was already discussed in the Section 2.2.4 "Photon detection efficiency (PDE)" the *PDE* increases with increasing the *ΔV*. From both studies, there is no observable dependence of the *PDE* on the *T* for a fixed *ΔV*.

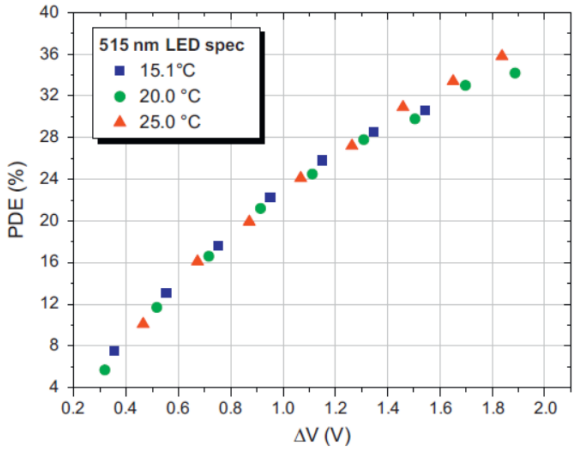

Figure 2.85 PDE for green light of a customized SiPM (1.3×1.3 mm^2, with 667 µcells of 50 × 50 µm^2, the device is based on the Hamamatsu commercial device S10362-11-050) as a function of overvoltage at three temperatures [2]

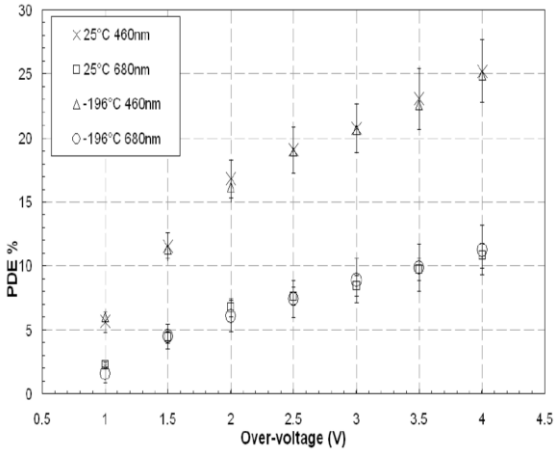

Figure 2.86 PDE for blue (λ=460nm) and red (λ=680nm) light of a SensL device as a function of overvoltage at T = +25 ^{0}C and T = -196 ^{0}C [50]

However, the measurements of *PDE* for blue, green and red light for the FBK device in the *T* range from 50 K to 300 K performed by Collazuol [48] show that *PDE* changes with *T*. The normalized *PDE* to the value at $T = 297$ K as a function of *T* at $\Delta V = 2$ V is presented in Figure 2.87 [48].

We can remark that *T* dependence of *PDE* is not clearly understood and more studies are required.

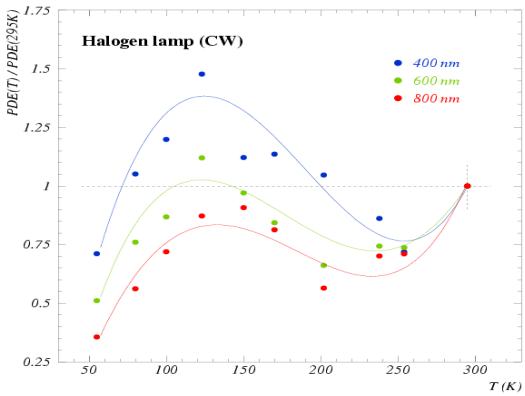

Figure 2.87 PDE (normalized to the value at T = 297 K) as a function of T at ΔV = 2 V, for blue, green and red lights, measured for an FBK device [48]

3. Investigation of SiPM parameters down to cryogenic temperatures

In previous Section 2.2.5 "Temperature dependence" we have seen that different characteristics of SiPM devices are changing with the temperature *T*. Moreover, it was shown that not all parameters (i.e. P_{Geger}, *DCR*) of SiPM devices produced by Hamamatsu have been studied in a wide *T* range. Therefore, to complete these studies and to have a closer look to the physical phenomena staying behind this *T* dependence the studies of SiPM parameters down to cryogenic *T* have been performed.

3.1. Experimental setup

During my thesis I participated to the design, installation and calibration of an experimental set-up dedicated for electrical, optical and *T* characterizations of SiPM devices. The measurements can be performed in dark or light conditions (LED or pulsed laser diode) at different *T* from 350 K down to 14 K.

A general view of the experimental setup is presented in Figure 3.1. The setup is equipped with a closed-cycle He cryocooler from Advanced Research System working on Gifford McMahon thermodynamic principle [57]. The setup is composed of a compressor, gas lines and a cold end located inside of the climatic chamber. To reduce the heat exchange with the external ambient, the climatic chamber has been carried out under vacuum conditions at $P < 10^{-4}$ mbar ensured by primary and turbo molecular pumps.

Figure 3.1 Experimental setup developed at LAL for the characterization of SiPM devices in a T range from 14 K to 350 K

A copper disk, in the tight contact with the cold end, was used to attach simultaneously four SiPM samples and temperature sensors *T* (will be called in the following *T* sensors). One *T* sensor, close to the SiPM under test, was used as a reference, while the others were used to control the uniformity of *T* over a full surface of the Cu disk. The reference *T* sensor together with a 50 Ω heater allowed us to control and stabilizes the *T* to the desired value using the PID system of a LakeShore 335 temperature controller. A close look inside the climatic chamber is presented in Figure 3.2.

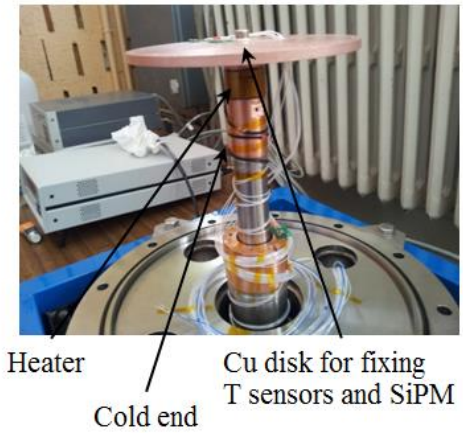

Figure 3.2 Zoom inside the climatic chamber. We can observe the cold end, where the lowest T is obtained, the 50 Ω heater to heat the system from 14 K to desired T and the Cu disk to mechanically fix the SiPMs and T sensors

3.1.1. **Climatic chamber**

The dedicated climatic chamber was designed and built by the LAL mechanical service (See drawing in Figure 3.3). This climatic chamber has been designed to provide:

- an easy access inside the chamber. To fulfill this requirement the chamber is composed by three separate parts: top and bottom covers, and main middle cylinder. Any of them can be removed to provide an easy access inside the chamber;
- optical and electrical feedthroughs to operate the SiPM under tests at a given condition and to provide an electrical connection between a LakeShore 335 temperature controller and temperature sensors with 50 Ω heater. To fulfill this requirement the chamber has seven vacuum feedthrough (four on the bottom cover, two in the middle cylinder and one on the top cover) and any of them can be composed by a flange with a necessary feedthrough (i.e. optical or electrical).

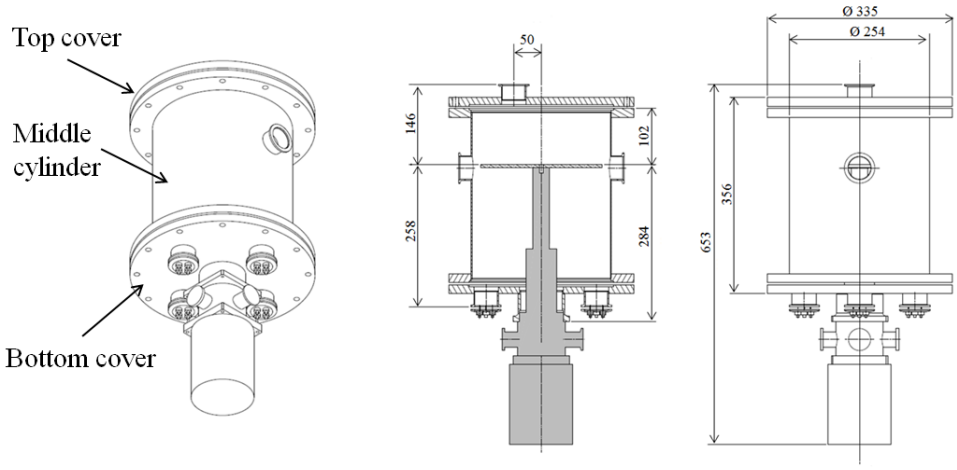

Figure 3.3 Drawing of the dedicated climatic chamber fit the cold end (design and construction done by LAL mechanical service). We can distinguish three part: top and bottom covers and middle cylinder

3.1.2. **Electrical connections**

Electrical connections between the internal and external sides of a climatic chamber were realized through two flanges with an electrical feedthrough. The first flange (presented in Figure 3.4) is used to provide a connection between LakeShore 335 temperature controller and four *T*

sensors and 50 Ω heater. This flange has 19 pins (See Figure 3.4 a)), 16 of them is used by *T* sensors (more details will be given in the next Section "*Light injection*") and 2 pins by a heater. The second flange with 4 floating ground SMB connectors (See Figure 3.4 b)) is used to provide a connection between SiPM devices under tests and the read-out chain (more information about read-out chain will be given later in the Section "*Read-out chain for DC / AC measurements*"). One floating ground SMB connector is used for one SiPM, central wire is used for a voltage supply and external wire for readout (e.g. SiPM output signals in AC mode or current in DC mode).

3.1.3. **Light injection**

To illuminate the SiPM detectors by low intensity light pulses Pilas diode lasers of different wavelengths (e.g. 467 nm, 523 nm and 635 nm) were used. Light was injected into the climatic chamber (where the SiPM devices were located) from the Pilas diode laser located outside, through a flange with an optical feedthrough (See Figure 3.4 c)). In the air part, 100 meters of optical fiber was used between the Pilas diode and the flange with an optical feedthrough to delay the light pulses by ~300 ns. This delay allows to separate in time the SiPM response with respect to the moment of the laser light signal and high frequency electronics noise generated by the laser driver.

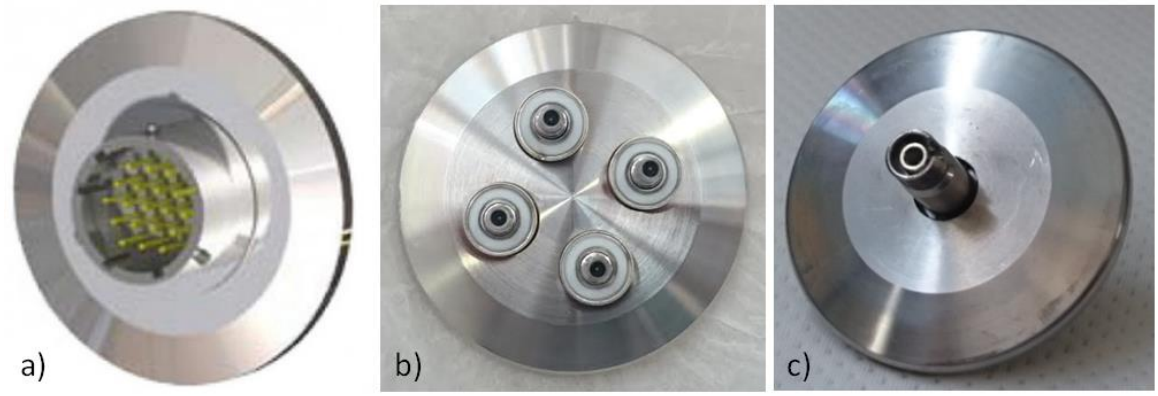

Figure 3.4 Photos of three flanges with electrical (a and b) and optical (c) feedthroughs: a) flange with 19 pins, is used to provide a connection between LakeShore 335 temperature controller and four T sensors and 50 Ω heater, b) flange with 4 floating ground SMB connectors is used to provide a connection between SiPM devices under tests and the read-out chain and c) flange with optical feedthrough is used to illuminate the SiPM detectors

3.1.4. **Temperature Sensors (T sensors)**

The LakeShore Silicon Diode Temperature Sensors DT-670 (will be called in the following *T* sensor) were used for *T* measurements. The general view of *T* sensor and its drawing are presented in Figure 3.5 a) and b). The *T* sensors were measured with a four-lead technique by a LakeShore 335 temperature controller. The electrical scheme of four-lead connection of *T* sensor is presented in Figure 3.5 c).

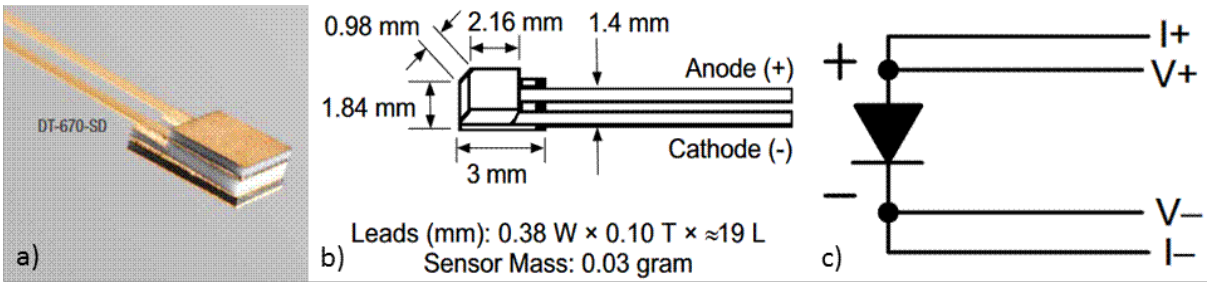

Figure 3.5 LakeShore Silicon Diode Temperature Sensor DT-670: a) general view, b) drawing and c) four-lead measurement scheme [58]

The purpose of four-lead measurements is to eliminate the effect of lead resistance on the measurements. Otherwise, lead resistance is a direct error when measuring a sensor. Following the LakeShore 335 temperature controller user`s manual [59] in a four-lead measurement, current leads and voltage leads are run separately up to the sensor. With separate leads there is little current in the voltage leads, so their resistance does not enter into the measurement. Resistance in the current leads will not change the measurements as long as the voltage compliance of the current source is not reached. When two-lead sensors are used in four-lead measurements, the short leads on the sensor have an insignificant resistance.

3.1.5. **Mechanical fixations**

As it was shown above, to transfer the heat (or cold) from the cold end to the SiPM devices and *T* sensors, a Cu disk was used in tight contact with a cold end. A Cu disk was screw directly on a cold end (the screw-bolt with a silver treatment was used) to achieve good heat (cold) exchange between them. The *T* sensors and SiPMs should be fixed properly on a Cu disk to ensure stable heat exchanges without heat losses. However, the geometrical dimensions of *T* sensors and SiPM packages are quite different. Moreover, SiPM packages are changing with device area (e.g. 1 × 1 mm^2, 1.2 × 1.2 mm^2, 2 × 2 mm^2 or 3 × 3 mm^2 total area) and vary from one producer to another, as shown in Figure 3.6. Therefore, the individual fixation mechanisms have been developed for each package:

- the *T* sensors have been fixed by clamping them between an additional PCB and Cu disk as presented in Figure 3.7;
- the SiPM devices mounted on a standard ceramic package (e.g. 1 × 1 mm^2, 1.2 × 1.2 mm^2, 2 × 2 mm^2 or 3 × 3 mm^2 total area) have been fixed by using dedicated cupper clams (given clamp for a given package size) designed and fabricated by mechanical engineers at LAL. An example of a Cu clamp developed for SiPM device produced by KETEK with a total area of 3 × 3 mm^2 is presented in Figure 3.8 (a, b and, c). Only two clamps with SiPM devices can be fixed simultaneously on a Cu disk as presented in Figure 3.7;
- the SiPMs devices mounted on dedicated PCB package have been fixed by a screw directly on a Cu disk as presented in Figure 3.7.

The reference *T* sensor was fixed as close as possible to the SiPM. In the case of Cu clamps, the reference *T* sensor was fixed between the Cu clamp and SiPM, while in the case of SiPM mounted on PCB the reference *T* sensor was fixed between the SiPM mounted on PCB and additional PCB. The mounting of two SiPM`s and four *T* sensors on the Cu disk is presented in Figure 3.7.

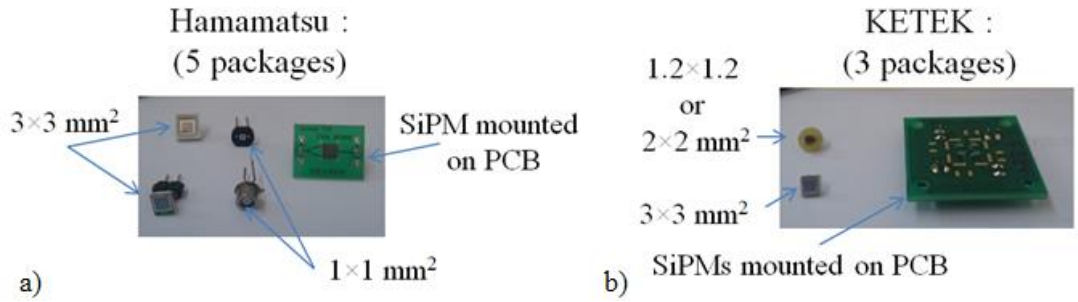

Figure 3.6 Example of different SiPM`s packages produced by a) Hamamatsu and b) KETEK

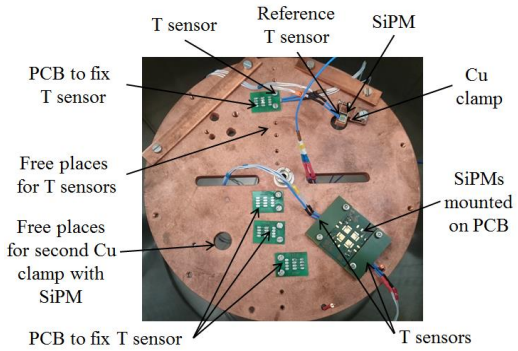

Figure 3.7 Cu disk with two SiPM and four T sensors. One SiPM in standard package is fixed by a Cu clamp while the another one mounted in a PCB screw on a Cu disk

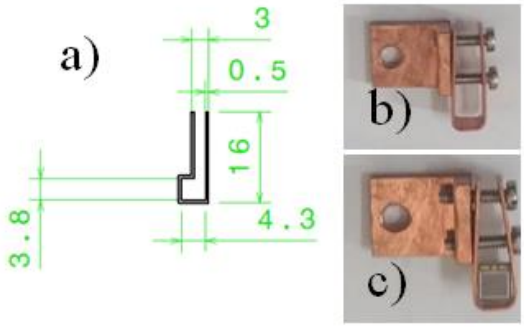

Figure 3.8 Cu clamp for KETEK 3×3 mm² device: a) drawing, b) empty Cu clamp and c) Cu clam with SiPM device (design and fabrication by mechanical engineers at LAL)

The thermal grease was used to achieve the best heat (cold) transfer between the cold end to Cu disk, Cu clamps, SiPM`s and *T* sensors.

3.1.6. **Temperature calibration**

To be confident that described above *T* sensors fixation ensures good heat exchange and as a result provides correct and reproducible *T* measurements, I have carried out three independent measurements. During each measurement, *T* sensors were fixed in different places:

- all *T* sensors were fixed in the center of Cu disk as presented in Figure 3.9 a);
- all *T* sensors were fixed on the left part of Cu disk as presented in Figure 3.9 b);
- all *T* sensors were fixed on the right part of Cu disk as presented in Figure 3.9 c);

The goal of each measurement was to record the *T* when the set-up is chilled to the lowest *T* ensuring good thermal equilibrium (*T* variation in time less than 0.01 K). The results are presented in the Table 3.1. We can observe that over three independent measurements the *T* varied from 13.49 K to 14.47 K, with a mean value of ΔT = 13.99 K. In average, the difference of 0.26 K was calculated between a given *T* sensor and ΔT. Moreover, any dependence of the measured *T* with respect to a distance between *T* sensor and the center of the Cu disk wasn't observed. From those measurements we can conclude that the developed setup is operating in a stable conditions and *T* is distributed uniformly over the full Cu disk surface.

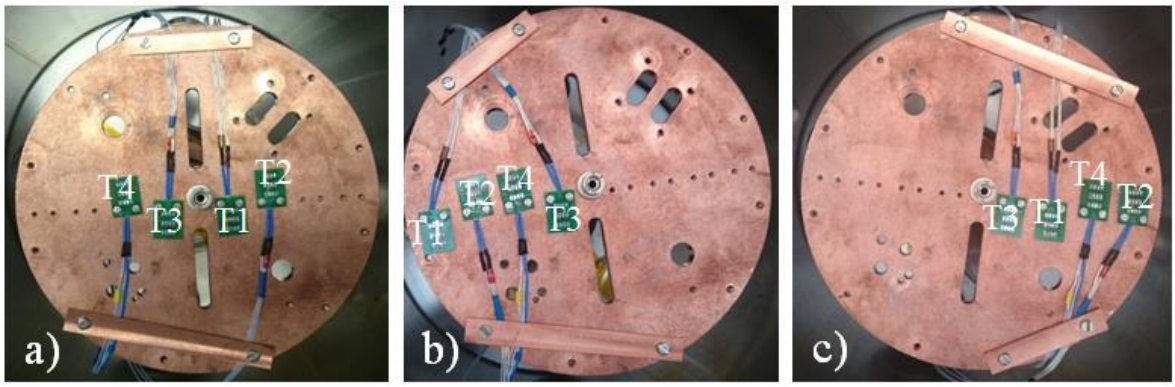

Figure 3.9 Independent T measurements: a) all T sensors in the center, b) all T sensors on the left side and c) all T sensors on the right side

Position of T sensors	T sensor	T (K)	<T> (K)	ΔT = |T - <T>| (K)	ΔT_{Max} (K)	<ΔT> (K)
Center	1	14.16	13.99	0.17	0.50	0.26
	2	14.25		0.26		
	3	13.56		0.43		
	4	13.89		0.10		
Left	1	13.61		0.38		
	2	14.16		0.17		
	3	13.49		0.50		
	4	13.89		0.10		
Right	1	14.01		0.02		
	2	14.46		0.47		
	3	14.47		0.48		
	4	13.95		0.04		

Table 3.1 The results over three independent T measurements

3.1.7. **Read-out chain for DC / AC measurements**

The developed setup allows both DC and AC tests on our SiPM detectors. The electrical schematics for DC and AC measurements are presented in Figure 3.10 and Figure 3.11 respectively. In both types of measurements (i.e. DC or AC) we can highlight two independent parts:

- one part located inside the climatic chamber and operated under vacuum $P < 10^{-4}$ mbar and various temperatures (from 14 K to 350 K), so-called *vacuum part*;
- a second part located outside the climatic chamber and operated under atmospheric pressure and room *T*, so-called *air part*.

Comparing Figure 3.10 and Figure 3.11 we can observe that the vacuum parts for both types of measurements (i.e. DC and AC) are identical and presented by SiPM connected to SMB connector, while the air parts are quite different. The air part for the DC measurements is presented by a Keithley 2611 source-meter, for bias voltage supply and current measurements, while the air part for the AC measurements is consisted of a Miteq AU-1332 amplifier (gain = 55 dB, bandwidth = 500 MHz) followed by a Tektronix TDS5054 oscilloscope for waveform acquisition (a bandwidth of 20 MHz was used for noise suppression) and a Keithley 2611 source-meter for SiPM bias voltage supply. Moreover, for AC measurement the 1 kΩ

resistance and 0.1 μF capacitance serve as a low-pass filter that eliminates the high frequency noise of the power supply.

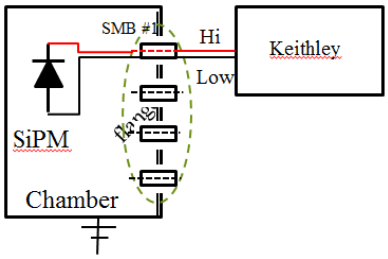

Figure 3.10 Electrical schematic to provide DC measurements of SiPM devices. The SiPM is connected to a Keithley source-meter through vacuum flange with a SMB connector

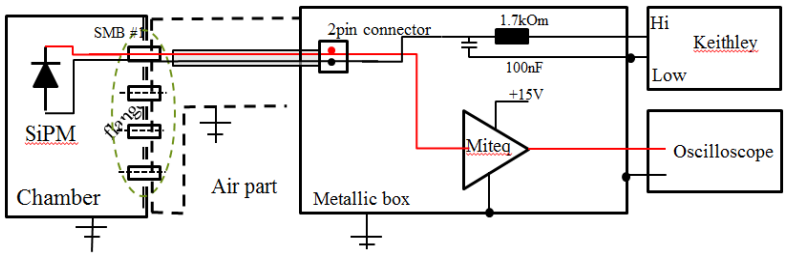

Figure 3.11 Electrical schematic used to provide the AC measurements of SiPM devices. Composed by a Miteq AU-1332 amplifier, Tektronix TDS5054 oscilloscope and Keithley 2611 source-meter.

Identical vacuum parts significantly simplify the operation of the developed setup. In this case, only the air part should be modified to switch from one type of measurements to another (e.g. from DC to AC or return back to DC). This minimizes the number of climatic chamber openings. It should be painted out that for both measurements types (i.e. DC or AC) the readout electronics is located outside the climatic chamber, at room *T*. This ensures the same experimental conditions (amplifier gain, electronic noise level) independent of the T inside the chamber.

3.1.8. Remote operation: LabView automatic data acquisition program

Two LabView programs have been developed for automatic data acquisition: one for DC and another one for AC measurements. Both programs have similar structure presented in block diagram in Figure 3.12. We can distinguish four main steps:

- read the desire *T* and V_{bias} ranges from the *Measurement conditions* procedure;
- each *T* should be stabilized by *Temperature stabilization* procedure;
- when the desired *T* is stabilized the measurements (DC or AC) should be done by *Data acquisition* procedure;
- during all the time when the developed LabView program is running the *Security stage* is running to be sure that vacuum inside the climatic chamber is enough low.

The *Measurement conditions* procedure was developed to set a full range of experimental conditions for data acquisition: *T* range, V_{bias} range, light intensity. These conditions will be transformed to *Temperature stabilization* and *Data acquisition* procedures.

The *Temperature stabilization* procedure was developed to set and stabilize the *T* inside a climatic chamber. This procedure sets the desirable temperature $T_{desirable}$ to a LakeShore 335 temperature controller and reads the temperature inside a climatic chamber $T_{chamber}$ from the reference *T* sensor every 4 second. The *Temperature stabilization* procedure considers that the *T* is stabilized if $T_{chamber}$ is within 0.1 K with respect to the $T_{desirable}$ and stable in time ($|dT_{chamber}/dt| < 0.01$).

The *Data acquisition* procedure has been developed to ensure automatic DC or AC measurements. In case of DC measurements, the *Data acquisition* procedure controls the

Keithley 2611 source-meter for IV measurements and the Tektronix AFG3102 pulse generator to set the light intensity (if necessary) by triggering the laser driver with given frequencies, while in case of AC measurements, the procedure controls the Keithley 2611 source-meter to bias a SiPM and the Tektronix TDS5054 oscilloscope for waveform acquisition. Independent of measurements type, the procedure has an access to a LakeShore 335 temperature controller to read a T from the reference T sensor and save it a file with experimental data. Moreover, if the T from the reference T sensor is far from the desire T the *Data acquisition* procedure has the right to pause the acquisition and reinitiate the *Temperature stabilization* procedure to repeatedly stabilize the T.

The *Security stage* is developed for the safety reasons, in particular, to not destroy the cold end by overheating if the vacuum inside a climatic chamber is not low enough. This procedure reads the pressure $P_{chamber}$ inside a climatic chamber and compares this value with the reference pressure P_{ref} (P_{ref} is set manually, by default $P_{ref} = 10^{-3}$ mBar) and doesn't allow to the LakeShore 335 temperature controller to use the heater if $P_{chamber} > P_{ref}$.

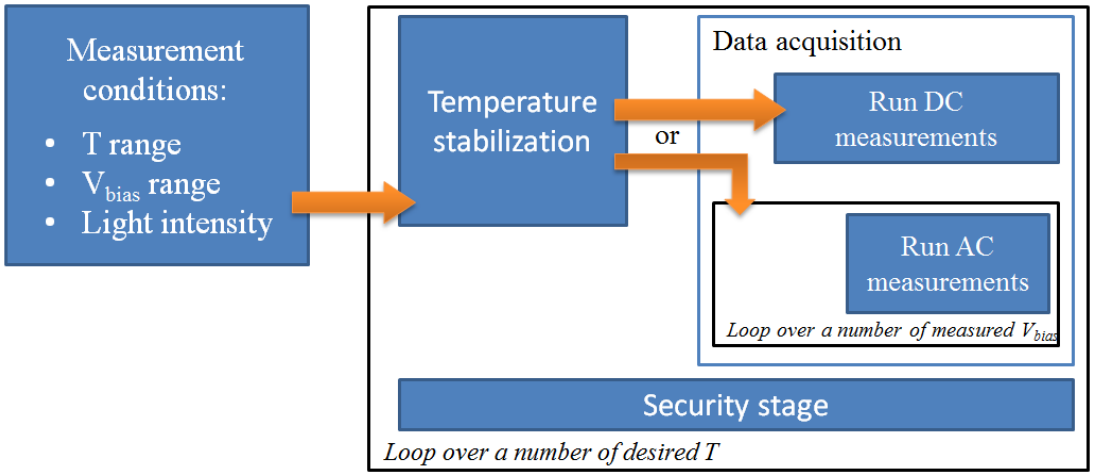

Figure 3.12 Block diagram of a developed LabView program for automatic data acquisition

3.2. Measured devices & measurements conditions

Using the developed setup, two sets of AC and DC measurements were done:

- *First set of measurements* has been performed in the *T* range from 238.15 K to 308.15 K, in a step of 10 K. During DC measurements (forward and reverse) the SiPM devices were operated in dark condition. While during the AC measurements the SiPM devices were illuminated by low intensity light laser pulses of different wavelength (e.g. 467 nm, 523 nm and 635 nm). In this set of measurements seven SiPM devices have been tested:
  - Three devices produced by Hamamatsu, with a total area of 3 × 3 mm^2 and a µcell size of 50 × 50 μm^2 ($N_{\mu cells}$ = 3600):
    - S10931-050P, this device has been already studied using the FermiLab setup [60] and it serve as reference for comparison calibration between LAL and FermiLab setups; we have to note that this device is coming from a production run of 2011;
    - S13082-050CS(X), this device is coming from a production run of 2015 and has low cross-talk probability as indicated in Hamamatsu datasheet;
    - S13360-3050CS, this device is also coming from a production run of 2015 and has low afterpulsing probability as indicated in Hamamatsu datasheet;
  - Four devices produced by KETEK, with a total area of 0.5 × 0.5 mm^2 and a µcell size of 50 × 50 μm^2 ($N_{\mu cells}$ = 100). All devices are coming from a production run of 2015.
    - Two devices with P-on-N structure:
      - SiPM19-W3-MP50-NT, no trenches;
      - SiPM19-W3-MP50-V1, with trenches;
    - Two devices without trenches and with N-on-P structure:
      - SiPM20-W4-50NT, with thinner p-epi layer, 2.0 µm depth of the epi-layer;
      - SiPM20-W5-50NT, with thicker p-epi layer, 2.4 µm depth of the epi-layer.
- *Second set of measurements* has been performed in the *T* range from 98.15 K to 318.15 K, in a step of 20 K. During forward DC measurements the SiPM devices were operated in dark condition, whereas the reverse DC measurements were done in few different conditions: dark and illuminated by three different intensities (low, medium and high) of light laser pulses of two different wavelengths (e.g. 467 nm, 635 nm). During AC measurements, the SiPM devices were illuminated by low intensity light laser pulses of two different wavelengths (e.g. 467 nm and 635 nm). In this set of measurements, three SiPM devices produced by Hamamatsu have been tested: S10931-050P, S13082-050CS(X) and S13360-3050CS (more details about these devices are given above).

For each studied device the DC measurements were done before AC, because they are much simpler, faster and the device working range can be determine. From these measurements the V_{BD} for each device at a given *T* has been determined (by using our IV model, more details will

be given in the Section 3.5 "Physical model of the reverse IV characteristic") and used in further AC measurements.

During the AC measurements, at each T 10000 waveforms of 2 µs length (*first set of measurements*) and 4 µs length (*second set of measurements*) were acquired at different V_{bias}. Data acquisition was triggered by the laser with the laser signal positioned at 1.55 µs after the beginning of the waveform. As it was already shown in the Section 2.2.5.e "V_{BD} *vs*. T", the V_{BD} of SiPM changes with T. Therefore, to measure the devices in comparable operating conditions independent of T, each V_{bias} has been selected to obtain the same ΔV with respect to V_{BD}. The Hamamatsu SiPM sample from 2011 was measured in a ΔV range of 0.4 V < ΔV < 2.7 V, while both Hamamatsu and KETEK SiPM samples from 2015 were measured in a ΔV range of 0.4 V < ΔV < 10 V. The upper limit of the bias voltage range is imposed by onset of strong afterpulsing leading to the amplifier saturation and baseline shifts. The Hamamatsu devices from 2011 have a working ΔV range of only 2.7 V while the latest generation of both vendors have a larger ΔV ~10 V, showing a considerable improvement of SiPM technology.

3.3. Static characterizations

3.3.1. Forward IV characteristic vs. T

Typical forward IV characteristics of SiPM devices produced by KETEK and Hamamatsu at different T are presented in Figure 3.13 and Figure 3.14 respectively (the forward IV characteristics of all others measured SiPM devices are given in the Annex 1 – Static measurements). From all measured devices, we found that at a given T and V_{bias}, the SiPM devices produced by Hamamatsu present more than one order of magnitude higher current with respect to the SiPM devices produced by KETEK. Therefore, by using the Ohm`s law ($U = I \times R$) we can conclude that SiPM devices produced by Hamamatsu have smaller total resistance R_{total} ($R_{total} = R_q/N_{\mu cell}$, where R_q – is the quenching resistor and $N_{\mu cell}$ – is the number of µcells). The smaller R_{total} for SiPM devices produced by Hamamatsu was expected due to higher $N_{\mu cell}$ ($N_{\mu cell}$ = 3600 for Hamamatsu and $N_{\mu cell}$ = 100 for KETEK devices, more details have been given in the Section 3.2 "Measured devices & measurements conditions").

As has been expected from the Section 2.2.5.a "*Forward IV characteristic vs. T*", in all measured forward IV characteristics, independent of measured detector and T, we can distinguish two regions:

- the first one with low current ($I < 10^{-4}$ A for Hamamatsu devices and $I < 10^{-6}$ A for KETEK devices) and exponential current increase;
- the second one with high current ($I > 10^{-4}$ A for Hamamatsu devices and $I > 10^{-6}$ A for KETEK devices) and linear current increase.

The region of an exponential increases can be used to cross-check the T with the one measured by reference T sensor, while the region of the linear increases can be used to calculate R_q.

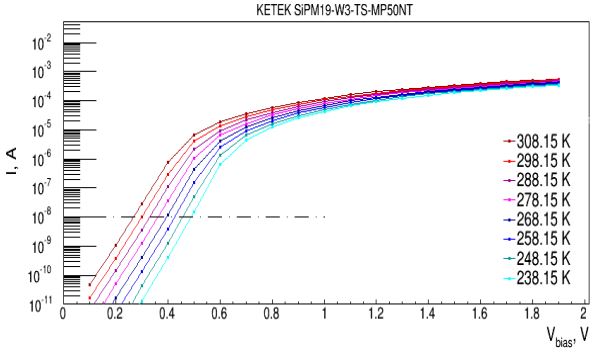

Figure 3.13 Forward IV characteristics of KETEK SiPM19-W3-MP50-NT detector measured in T range from 238.15 K to 308.15 K. The constant current used for cross-check of T is represented as horizontal dashed line

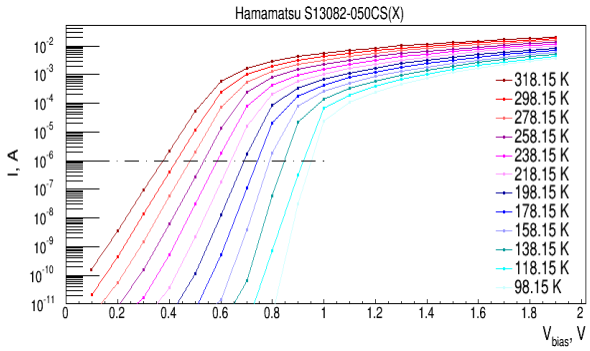

Figure 3.14 Forward IV characteristics of Hamamatsu S13082-050CS(X) detector measured in T range from 98.15 K to 318.15 K. The constant current used for cross-check of T is represented as horizontal dashed line

The voltage drop V_{drop} at a constant current (shown as a dashed horizontal line in Figure 3.13 and Figure 3.14 has been used to cross-check the T with the one measured by reference T sensor. A constant current of 1 µA and 10 nA has been chosen for devices produced by Hamamatsu and KETEK respectively (for more information see the Section 2.2.5.a) "*Forward IV characteristic vs. T*". The V_{drop} as a function of T measured by reference T sensor, for both sets of measurements is presented in Figure 3.15 and Figure 3.16. We can observe that V_{drop} increases linearly with decreasing T for all measured devices except one Hamamatsu S10932-050P device. This behavior indicates that T has been measured correctly for four KETEK

devices and two Hamamatsu devices, while *T* measurements errors should be taken into account for Hamamatsu S10932-050P device.

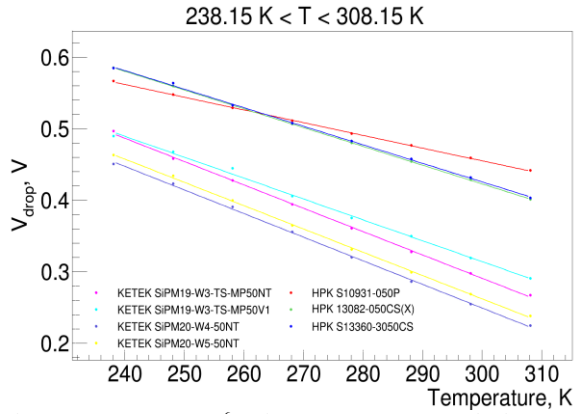

Figure 3.15 V_{drop} at 10^{-6} A for Hamamatsu HPK devices and at 10^{-8} A for KETEK devices as a function of T for cross-checking the T measurements

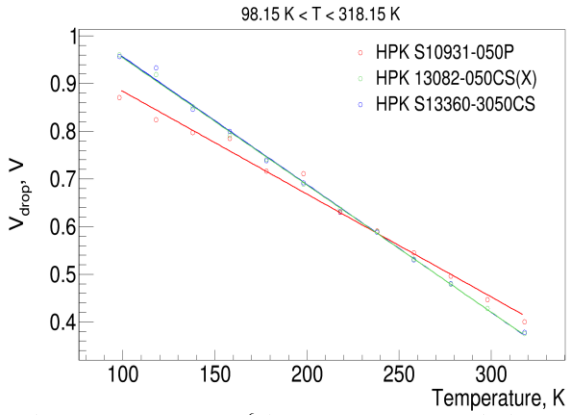

Figure 3.16 V_{drop} at 10^{-6} for Hamamatsu HPK devices as a function of T for cross-checking the T measurements

Using the high current region and the Eq. 2.18, the value of R_q was extracted for KETEK and Hamamatsu devices and presented in Figure 3.17 and Figure 3.18. It can be observed that at T = 298.15 K, the R_q is very different for different devices and is ranging from ~60 kΩ up to ~347 kΩ for KETEK SiPM20-W5-50NT and SiPM19-W3-MP50V1 devices respectively. Moreover, independent of measured detector, the R_q exhibits large variation with T, with decreasing values when T increases (i.e. negative T coefficient). The R_q ranges from ~757 kΩ at T = 98.15 K down to ~125 kΩ at T = 318.15 for Hamamatsu HPK S10932-050P device. This dependence is related to T variation of polysilicon resistance, as given by the expression [61]:

$$R_q = a + b\sqrt{T} \cdot \exp\left(\frac{c}{T}\right) \qquad 3.1$$

where a, b and c – are the coefficients related to processing parameters of polycrystalline silicon resistor (i.e. grain size, doping concentration and trap density). The a, b, and c were set as free coefficients and Eq. 3.1 was used to fit R_q as a function of T for all detectors and presented by dashed lines in Figure 3.17 and Figure 3.18. Following the Collazuol [48] the T variation of polysilicon resistance can be also described by empirical function:

$$R_q = a + \frac{b}{T} \times \exp\left(\frac{c}{T}\right) \qquad 3.2$$

where a, b and c – are the free coefficients. The Eq. 3.2 was also used to fit R_q as a function of T for all detectors and presented by solid lines in Figure 3.17 and Figure 3.18. For the measurements at T range from 238.15 K up to 308.15 (See Figure 3.17) we can see that both fit functions show the same results and good agreement between the experimental data and fit functions can be observed for all KETEK and Hamamatsu HPK devices. However for the measurements at T range from 98.15 K up to 318.15 (See Figure 3.18) we can observe that fit functions show very different shapes, and empirical function, presented by Eq. 3.2 shows much better agreement with experimental data. Therefore we can conclude that expression presented by Eq. 3.1 is not well adapted to describe correctly the experimental data down to cryogenic T. Also for all Hamamatsu devices we can see a good agreement between R_q calculated from *first* and *second sets of measurements* (opened and closed dots in Figure 3.18).

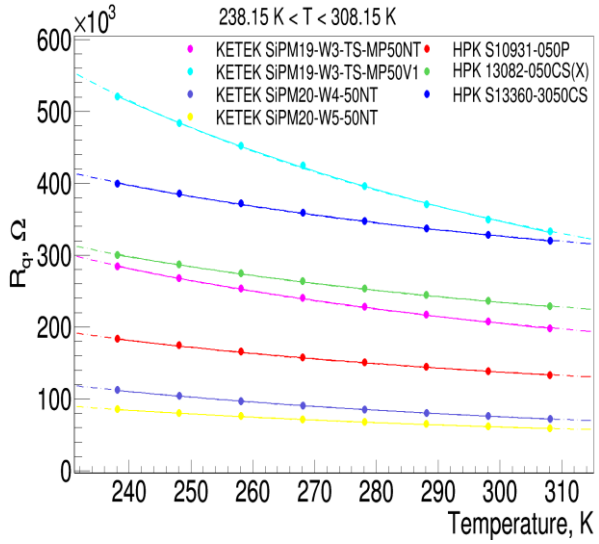

Figure 3.17 R_q calculated from forward IV characteristics vs. temperature for KETEK devices. The expressions presented by Eq. 3.1 (dashed lines) and Eq. 3.2 (solid lines) have been used for fit

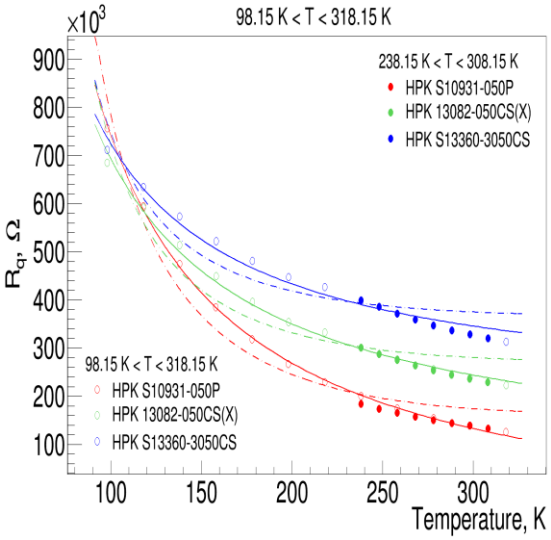

Figure 3.18 R_q calculated from forward IV characteristics vs. temperature for Hamamatsu HPK devices from the measurements in T range from 98.15 K to 318.15 K (open dots) and in T range from 238.15 K to 308.15 K (closed dots). The expressions presented by Eq. 3.1 (dashed lines) and Eq. 3.2 (solid lines) have been used for fit

3.3.2. **Reverse IV characteristic vs. T**

Typical reverse IV characteristics of SiPM devices produced by KETEK and Hamamatsu at different T are presented in Figure 3.19 and Figure 3.20 respectively (the forward IV characteristics of all other measured SiPM devices are given in the Annex 1 – Static measurements). Independent of measured detector, we can observe that at a given V_{bias} the current decreases with decreasing T. It should be pointed out, that below the T = 238.15 K shapes of IV characteristics reach the instrumentation measurements limit of 2 pA and the fast increase of the current just above the V_{BD} cannot be seen anymore. *Therefore, the V_{BD} cannot be determined precisely below this T by using the methods described in the Section 2.2.2.b "Reverse IV characteristic".*

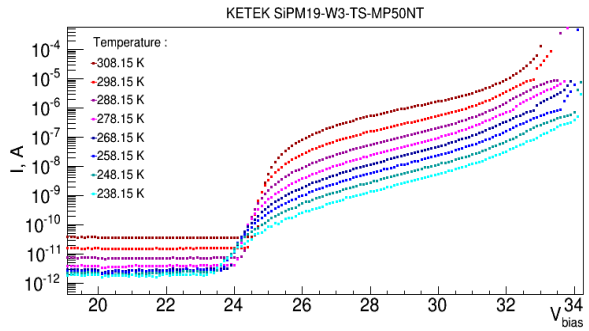

Figure 3.19 Reverse IV characteristics of KETEK SiPM19-W3-MP50-NT detector measured in T range from 238.15 K to 308.15 K

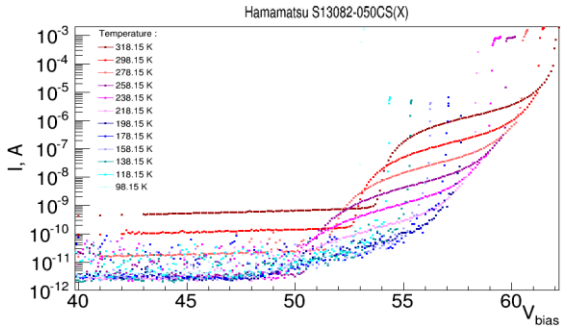

Figure 3.20 Reverse IV characteristics of Hamamatsu S13082-050CS(X) detector measured in T range from 98.15 K to 318.15 K

The breakdown voltage $V_{BD\text{-}DC\text{-}2d}$ values have been extracted from these measurements by using the inverse logarithmic derivative method (more details were given in the Section 2.2.2.b "*Reverse IV characteristic*") for a T range from 238.15 K to 318.15 K and the results are presented in Figure 3.21. It can be observed that at T = 298.15 K, the $V_{BD\text{-}DC\text{-}2d}$ ranges from ~24.25 V up to ~40.5 V for KETEK SiPM devices and from ~51.5 V up to ~70.3 V for Hamamatsu SiPM devices. In particular, the KETEK devices with P-on-N structure (SiPM19-

W3-MP50NT and SiPM19-W3-MP50V1) show similar values of $V_{BD\text{-}DC\text{-}2d} \cong 24.5$ V, while the devices with N-on-P structure show a $V_{BD\text{-}DC\text{-}2d} \cong 31.5$ V (SiPM20-W4-50NT, thinner p-epi layer) and $V_{BD\text{-}DC\text{-}2d} \cong 40.5$ V (SiPM20-W5-50NT, thicker p-epi layer). The Hamamatsu devices from 2015 year production run (S13082-050CS(X) and S13360-3050CS) show the value of $V_{BD\text{-}DC\text{-}2d} \cong 52$ V, while the device from 2011 year production run (S10931-050P) shows the value of $V_{BD\text{-}DC\text{-}2d} \cong 70.3$ V.

The difference of $V_{BD\text{-}DC\text{-}2d}$ corresponding to different devices at a given T reflects a variation of technology and design of the detectors. In particular, it can be related to the difference in the concentration of ionized background impurity (See Eq. 2.29) and to the difference between epitaxial layer thicknesses (See the Section 2.2.3.c "*Breakdown voltage (V_{BD})*"). It should be pointed out that KETEK SiPM20-W5-NT shows the lowest current and has already reached the instrumentation limit of 2 pA at T = 248.15 K. Therefore, for this device the values of the $V_{BD\text{-}DC\text{-}2d}$ should be ignored below 258.15 K.

A linear dependence of the $V_{BD\text{-}DC\text{-}2d}$ as a function of T has been found for all devices. The slope of the linear fit allows the calculation of the $V_{BD\text{-}DC\text{-}2d}$ temperature coefficient $\frac{dV_{BD-DC-2d}}{dT}$. We can certainly recognize the value of $\frac{dV_{BD-DC-2d}}{dT} \cong 21 \div 30 \frac{mV}{K}$ for KETEK devices and the $\frac{dV_{BD-DC-2d}}{dT} \cong 42 \div 55 \frac{mV}{K}$ for the Hamamatsu devices. Comparing the $\frac{dV_{BD-DC-2d}}{dT} = 21.8 \frac{mV}{K}$ for KETEK SiPM20-W4-50NT (thinner p-epi layer) and the $\frac{dV_{BD-DC-2d}}{dT} = 30.1 \frac{mV}{K}$ for KETEK SiPM20-W5-50NT (thicker p-epi layer) we can conclude that $\frac{dV_{BD-DC-2d}}{dT}$ increases with increasing the epitaxial layer thickness (as it was already discussed in the Section 2.2.3.c "*Breakdown voltage (V_{BD})*").

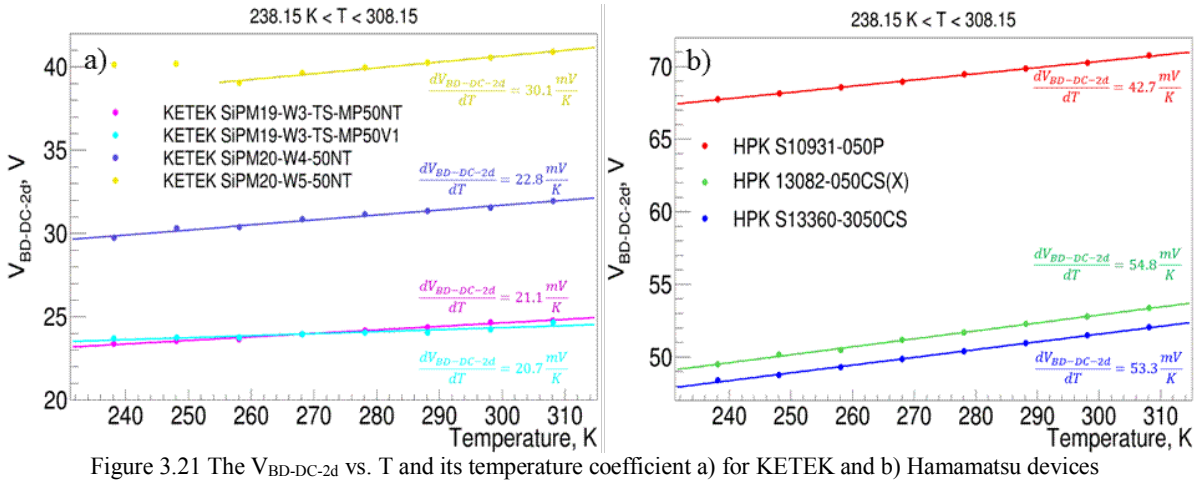

Figure 3.21 The $V_{BD\text{-}DC\text{-}2d}$ vs. T and its temperature coefficient a) for KETEK and b) Hamamatsu devices

To overcome the instrumental limit of 2 pA and to determine the $V_{BD\text{-}DC\text{-}2d}$ below 238.15 K, the SiPM devices current has been increased by illumination. The SiPM devices IV`s at different T have been measured under illumination with three light intensities (low, middle and high). Two separate measurements were done, one with blue λ = 467 nm and another one with red λ = 635 nm laser pulses. To simplify the further analysis, the light intensities of blue and

red lasers have been adapted to produce equal SiPM photocurrent at 98.15 K. Typical results for one Hamamatsu device are presented in Figure 3.22 a) low b) middle and c) high light intensities, the measurements done with blue and red laser light being presented by dots and solid lines respectively.

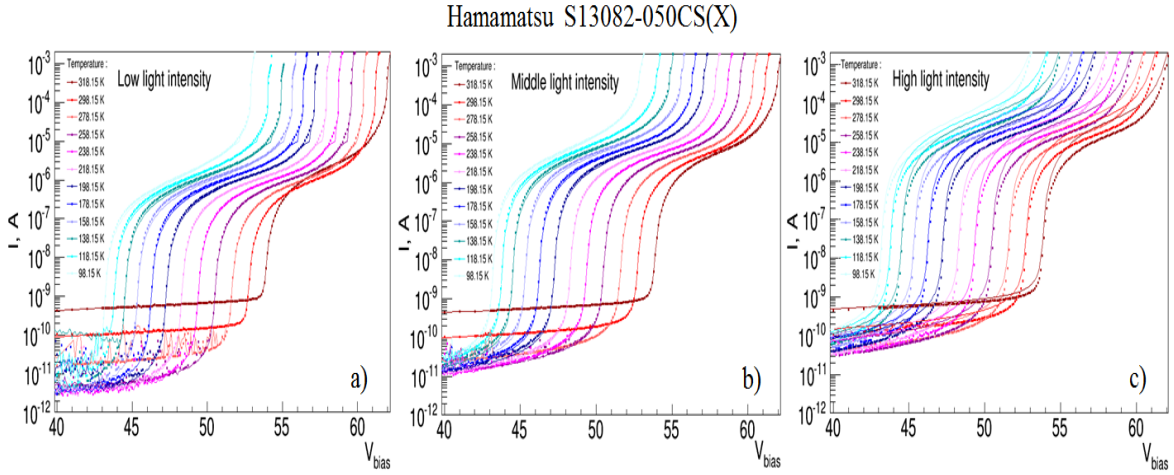

Figure 3.22 Reverse IV for Hamamatsu S103082-050CS(X) device as a function of T measured at: a) low b) middle and c) high light intensities. The separate measurements were done by using blue λ = 467 nm and red λ = 635 nm laser pulses and presented as dots and solid lines respectively. The light intensities of blue and red lasers have been adapted to produce equal SiPM photocurrent at 98.15 K

The IV curves of the SiPM devices measured under illumination have been also used for the $V_{BD\text{-}DC\text{-}2d}$ calculation. The $V_{BD\text{-}DC\text{-}2d}$ as a function of T for SiPM devices produced by Hamamatsu and calculated from dark and illuminated (with red light) measurements are presented in Figure 3.23. Independent of measured detector we can observe a good agreement between the $V_{BD\text{-}DC\text{-}2d}$ calculated from the measurements done with different light intensities (i.e. low, middle and high), while we can distinguish a shift of $V_{BD\text{-}DC\text{-}2d}$ calculated from measurements done in dark and illuminated conditions. This shift increases with decreasing T and ranges from ~200 mV at T = 298.15 K up to ~500 mV at T = 238.15 K for Hamamatsu S10931-050P device. This behavior is related to poor precision of IV measurements in dark conditions due to much smaller current with respect to the illuminated conditions. Also, we can observe that $V_{BD\text{-}DC\text{-}2d}$ decreases linearly with decreasing T up to 200 K for all measured Hamamatsu devices. Below this value, all detectors present slower and nonlinear T dependence. Therefore, the third order polynomial fit has been applied:

$$F(T) = p_0 + p_1 \cdot T + p_2 \cdot T^2 + p_3 \cdot T^3 \qquad 3.3$$

where p_0, p_1, p_2 and p_3 – are free parameters. The temperature coefficients for breakdown voltage and their relationships with structure of SiPM devices will be described in the Section 3.4.3.b "V_{BD} *vs*. T".

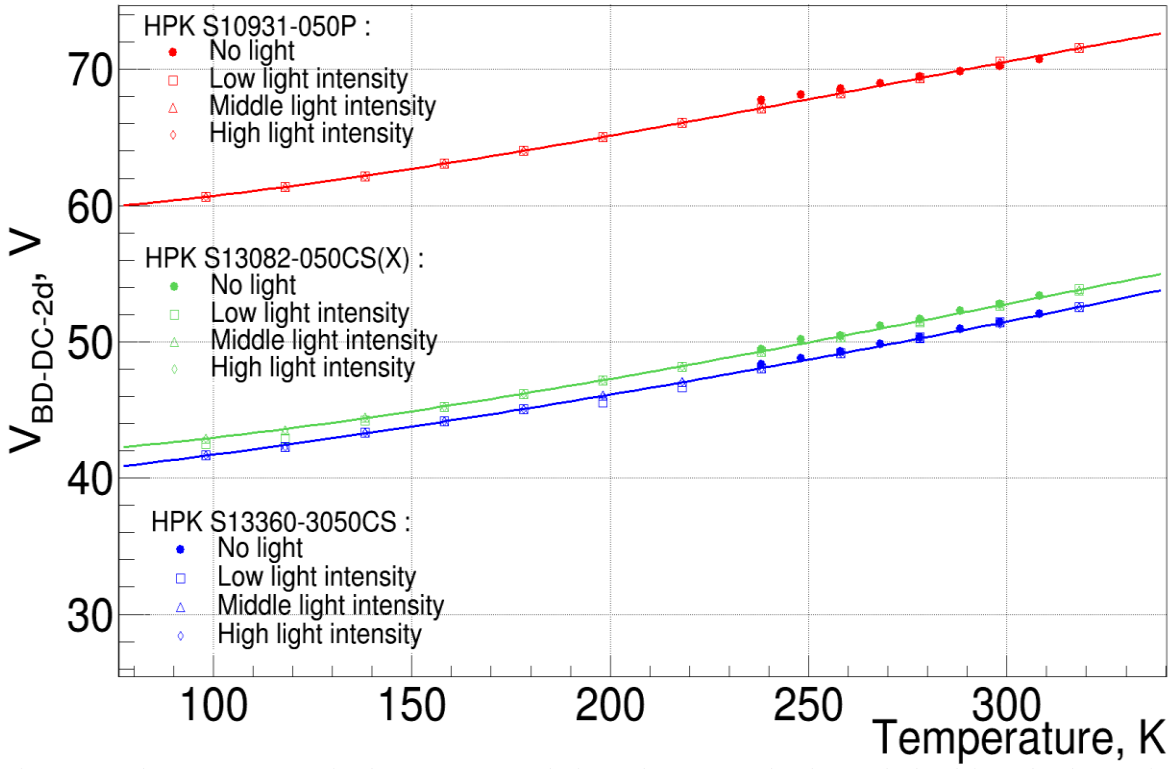

Figure 3.23 The $V_{BD\text{-}DC\text{-}2d}$ vs. T for three Hamamatsu devices. The $V_{BD\text{-}DC\text{-}2d}$ has been calculated from the shapes of IV curves measured at dark conditions and with light illuminations of three intensities: low, middle and high

For the moment we have used the reverse IV characterizations for the V_{BD} calculation, but as will be shown in the Section 3.5 “Physical model of the reverse IV characteristic”, these measurements contain much more information which can be used to characterize the SiPM devices.

3.4.Dynamic characterizations

3.4.1. Automatic analysis procedure

The dynamic characterizations lead to a huge amount of experimental data (tens of Gb/device). Therefore an automatic procedure for data analysis, based on ROOT data Analysis Framework [62], has been developed. This procedure uses experimental waveforms from oscilloscope as input files and creates output Ntuples files with SiPM pulses characteristics for each experimental condition (T and V_{bias}). The main steps of developed algorithm are:

- *Waveform analysis* to eliminate the differentiation of the waveform determined by the readout-electronics and to restore its zero baseline;
- *Pulse finding procedure* to determine time intervals containing SiPM pulses;
- *Analysis of SiPM pulse characteristics* to calculate the main SiPM parameters.

All these steps will be presented in details in the following Sections.

The development and the calibration of the automatic procedure were performed on experimental data of two Hamamatsu devices: S10362-11-050U and S10931-050P measured previously to my PhD thesis (work done by A. Para, N. Dinu and Fermilab technical team). These measurements were done in T range from 328.15 K down to 98.15 K and details on the experimental setup and the first results can be found in the reference [14]. A short description of the developed procedure and physics results have been published in the references [63] and [60]. This procedure worked successfully and consequently it was used for the analyses of most recent SiPM devices measured by myself using the LAL cryogenic setup described in the Section 3.1 "Experimental setup".

3.4.1.a. Waveform analysis

In this chapter typical waveforms acquired at different T and V_{bias} are shown. Their main characteristics as: baseline, threshold and baseline fluctuation are explained in details and presented as a function of T and V_{bias}.

3.4.1.a.1. Waveform parameters

As an example, two typical waveforms, acquired at T of 25 ^{0}C and low and high V_{bias} of 69.02 V and respectively of 70.62 V, are presented in Figure 3.24 a) & b). Depending on the applied V_{bias}, various types of signals can be observed. For, example, in waveforms acquired at low V_{bias} (Figure 3.24 a)), we can distinguish single SiPM pulse[1] (e.g. coming from one SiPM μcell) and high frequency electronics noise (e.g. noise amplitude comparable with 1p.e. signal amplitude), while the baseline of such waveforms is zero. In the waveforms acquired at high V_{bias}, the amplitude of SiPM pulses increases and consequently, the high frequency electronics noise phenomena become less important. However, two other phenomena become visible, like train of SiPM pulses[2] and a shift of the waveform baseline typically appearing after a train of pulses (Figure 3.24 b)).

[1] "single pulse" – is the SiPM signal coming from one SiPM μcell and separated by the neighboring pulses by a time interval higher than its recovery time

[2] "train of pulses" – is the two or more SiPM signals appearing with a time interval between them less than SiPM detector recovery time. The first pulse in a train of pulses is called in this thesis primary pulse and all others secondary pulses

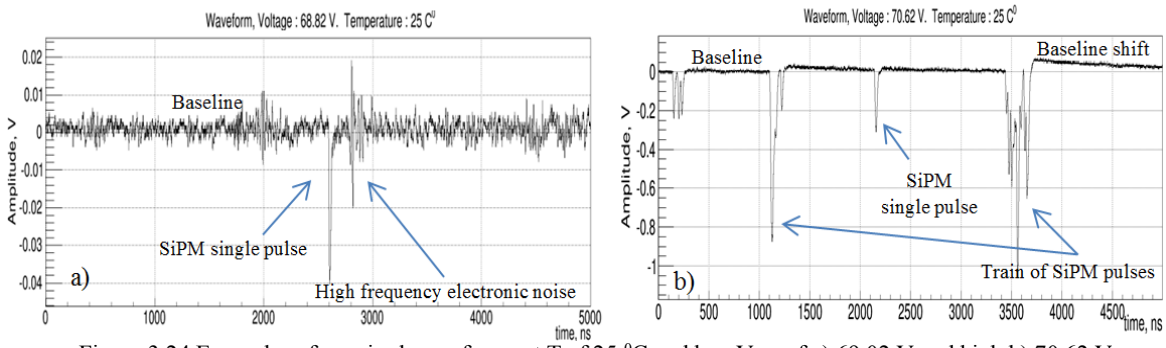

Figure 3.24 Examples of acquired waveforms at T of 25 ^{0}C and low V_{bias} of a) 69.02 V and high b) 70.62 V

The high frequency electronic noise and the baseline shift have a negative impact on further analysis of SiPM pulses (e.g. determine errors in the SiPM parameters calculation). Therefore, for their evaluation, the distribution of points amplitudes over all waveforms acquired at T of 25 ^{0}C and V_{bias} of 70.62 V has been calculated and the result is presented in Figure 3.25. We can mention here that this distribution is characteristic of all waveforms acquired at a given T and V_{bias} (e.g. constant characteristics of our read-out electronics and SiPM detectors), while it should be recalculated if T or V_{bias} are changing. However, independent of experimental conditions, such distribution presents three main regions, as following:

- The majority of events are concentrated in the central region; this region showing a Gaussian shape of which mean and standard deviation are related to the waveform baseline and respectively its fluctuation σ;
- The negative amplitudes observed in the left region, are related to SiPM pulses and high frequency electronics noise. In this region, we can even see few peaks related to 1 p.e., 2 p.e and 3 p.e SiPM signals respectively;
- The right region, with positive amplitudes, is created by the baseline shift. This baseline shift also affects the positive part of the central region making it wider on the right side (nonsymmetrical).

We can remark that one of the most important waveform parameters we are looking for, in particular the baseline fluctuation, can be evaluated from the standard deviation of the Gaussian central part. Therefore, the waveform`s amplitude distributions have been calculated for all experimental conditions (various T and V_{bias}) and the resulting standard deviation of the Gaussian central part as a function of T and V_{bias} is presented in Figure 3.26.

We can observe that σ shows a linear increase with V_{bias}, at a given T and becomes more significant at higher T. Three effects can contribute to σ: high frequency noise, SiPM pulses and baseline shift. The contribution from the high frequency noise can be neglected because it is fully related to the readout chain which was all the time in the same conditions (under room T) and should not show any variation with T. From Figure 3.25 we can observe that 1 p.e. position is quite far from the central region what means that contributions from SiPM pulses to σ is small. Moreover, this contribution should decrease with V_{bias} due to increase of SiPM pulses amplitude and as a result distances between the central region and 1 p.e. position. We can conclude that increase of σ with T is mostly related to the baseline shift.

The phenomena of baseline shift as well as the method used for its removal and zero baseline restoration are explained in detail in the following section.

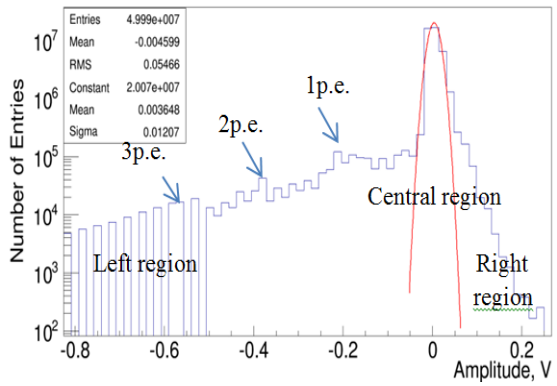

Figure 3.25 Histogram with all amplitudes acquired at V_{bias} = 70.62 V and T = 25 ^{0}C

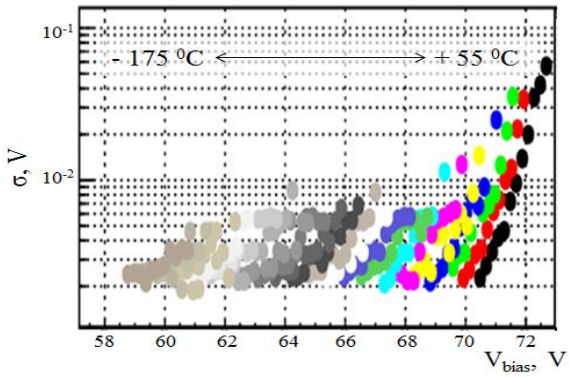

Figure 3.26 Mean baseline fluctuation σ as a function of T and V_{bias}

3.4.1.a.2. Baseline restoration

We expected that the baseline shift is related to a differentiation determined by various passive components used in our read-out chain. Therefore, to explain the baseline shift phenomenon, the working principle of a simple differentiation RC chain should be understood. The RC differentiating chain (see Figure 3.27) produces output signals V_{out} proportional to derivative dV_{in}/dt of an input V_{in} signal. The working principle of such RC chain was simulated by using SPICE models in LTspice software [64]. A square pulse of 50 ns width (t_w = 50 ns) has been injected to the simulated circuit. As a function of the ratio between injected pulse width t_w and circuit time constant $\tau = R \times C$, two typical types of output signals can be found: for short τ ($t_w = 5\tau$) of the RC chain is presented in Figure 3.28 a) and for long τ ($5\tau >> t_w$) in Figure 3.28 b). Therefore this simulation demonstrates that the baseline shift observed in our experimental data is clearly related to the differentiation of the read-out chain. To eliminate this effect from acquired waveforms the baselines should be restored. To restore the baseline shift correctly, more deeply understanding of differentiation RC chain should be done. In particular, the analytical solution for the RC filter should be found and it is presented in the following.

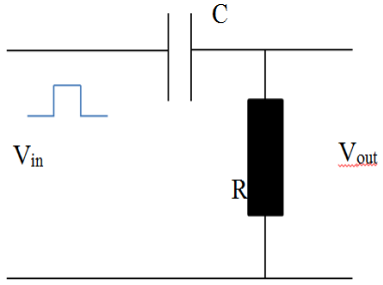

Figure 3.27 Typical differentiation RC chain

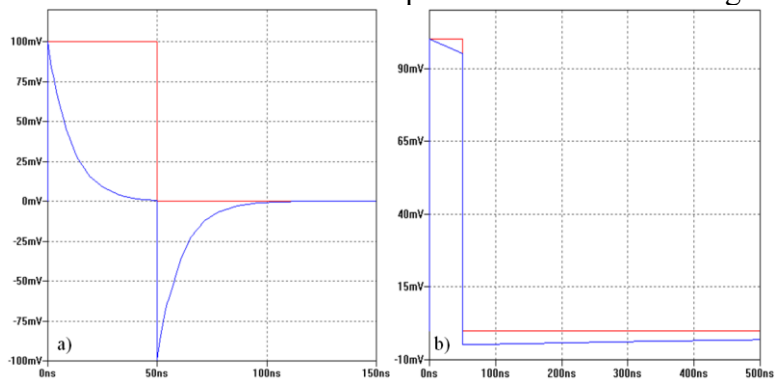

Figure 3.28 Typical differentiation RC chain output signal (blue) after injected square signal (red), when a) 5τ=t_w and b) 5τ>>t_w

The output signals shapes can be also obtained analytically from solving the system of equations which appears from Kirchhoff's Laws:

$$V_{In} = V_C + V_R \qquad 3.4$$

where V_{In} – is the input voltage, V_C and V_R – are the voltage across the capacitor and resistor respectively. The relationship between voltage and current in a resistor and capacitor:

$$I_C = C\frac{dV_C}{dt} \tag{3.5}$$

$$I_R = \frac{V_R}{R} \tag{3.6}$$

Capacitor and resistor are connected in series. Therefore:

$$I_C = I_R \Rightarrow C\frac{dV_C}{dt} = \frac{V_R}{R} \tag{3.7}$$

Putting V_R from the Eq. 3.4 to the Eq. 3.7:

$$\frac{1}{RC}\left(V_{In} - V_C\right) = \frac{dV_C}{dt} \Rightarrow \frac{dt}{RC} = \frac{dV_C}{\left(V_{In} - V_C\right)} \tag{3.8}$$

Integrating the Eq. 3.8:

$$\frac{t}{RC} = -\ln\left(V_{In} - V_C\right) + K \tag{3.9}$$

where K – is the integration constant, which can be determined from boundary conditions. We assume that before initial time $t < 0$, the V_{In} was stable in time and equal to initial voltage V_0 ($V_{In} = V_0$). Therefore, the capacitor will be charged to V_{In} and K can be calculated from the Eq. 3.9 at $t = 0$, as:

$$0 = -\ln\left(V_{In} - V_0\right) + K \Rightarrow K = \ln\left(V_{In} - V_0\right) \tag{3.10}$$

Putting K from the Eq. 3.10 to the Eq. 3.9:

$$\frac{t}{RC} = -\ln\left(V_{In} - V_C\right) + \ln\left(V_{In} - V_0\right) \Rightarrow \exp\left(-\frac{t}{RC}\right) = \frac{V_{In} - V_C}{V_{In} - V_0} \tag{3.11}$$

Therefore, the responses of the RC filter to the input step function of height V_{In} across the capacitor and resistor:

$$V_C = V_{In} \times \left(1 - \exp\left(-\frac{t}{RC}\right)\right) \tag{3.12}$$

$$V_R = V_{In}\exp\left(-\frac{t}{RC}\right) \tag{3.13}$$

Finally the response to the input Dirac delta function $\delta(t_0)$ across the resistor:

$$V_R(t) = \delta(t_0) - \frac{1}{RC} \times \exp\left(-\frac{t - t_0}{RC}\right) \times u(t) \tag{3.14}$$

where $u(t)$ – is the Heaviside step function ($u(t \leq t_0) = 0$, whereas $u(t > t_0) = 1$).

A similar behavior is presented in our read-out chain due to the presence of passive components. For example, if a square pulse of 50 ns width and of 5 ns leading and falling edges is injected into our read-out chain, the output pulse shows a shape similar to the one described in Figure 3.28 b) (see Figure 3.29 and Figure 3.30). We can observe that the injected pulse is

characterized by zero baseline, while the output pulse is followed by a baseline shift with a given time constant $\tau_{read\text{-}out}$, which appears due to reasons described above. Similar situation affects all acquired waveforms. As a result, each SiPM pulse presents a distorted shape (changed values of pulse amplitude and length) and it sits on a shifted baseline created by previous pulses. As it was already shown above, this baseline shift decay in time with a time constant:

$$\tau_{read-out} = R_{load} \times C_{effective} \qquad 3.15$$

where R_{load} – is the load resistance (50 Ω), $C_{effective}$ – is the effective read-out chain capacitance.

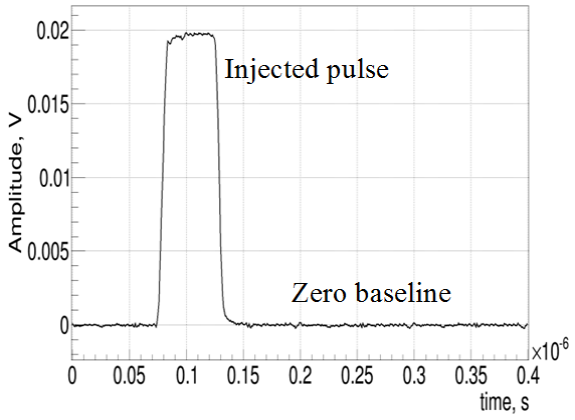

Figure 3.29 Injected square pulse to our read-out chain

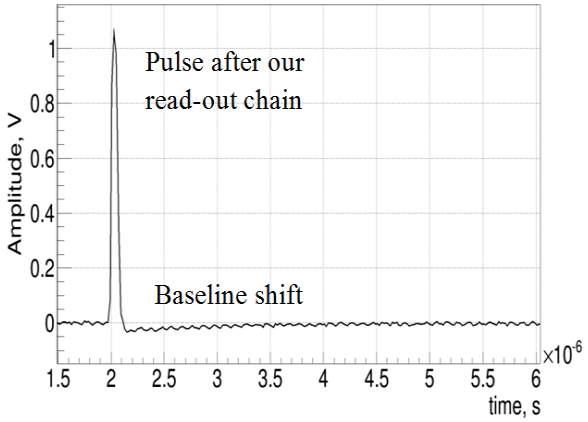

Figure 3.30 Square pulse after our read-out chain

To restore the original waveforms shapes, a baseline restoration procedure has been developed and used. In the first step, the average baseline shift was obtained from averaging the normalized SiPM pulses (see Figure 3.31). After, the $\tau_{read\text{-}out}$ was calculated from the exponential fit of the average baseline shift:

$$F(t) = a \cdot \exp^{-t/\tau} \qquad 3.16$$

where t – is the time position, a and τ are free parameters. The $\tau_{read\text{-}out}$ as a function of V_{bias} and T is presented in Figure 3.32. For our read-out chain a $\tau_{read\text{-}out}$ of~1.2 μs was found, independent of T and V_{bias}.

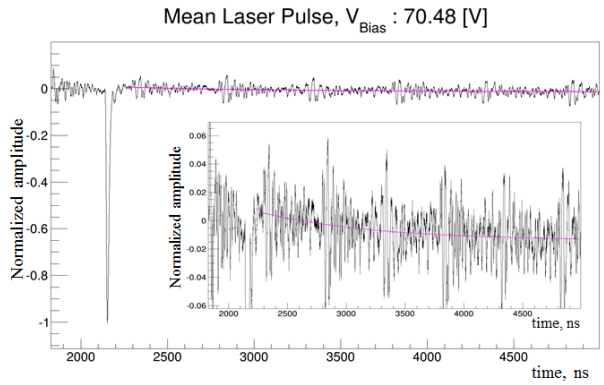

Figure 3.31 Average normalized SiPM pulse and average baselines shift with the exponential fit (magenta line) for $\tau_{red\text{-}out}$ calculation. The insert shows a zoom to the average baseline shift

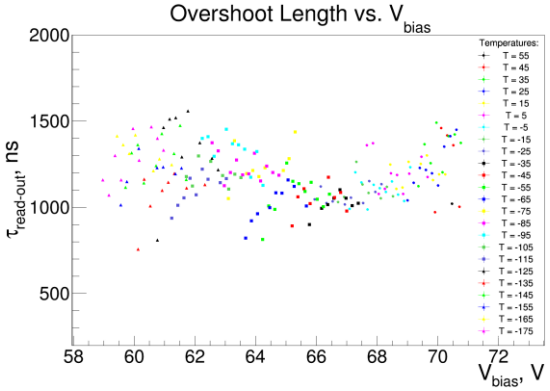

Figure 3.32 $\tau_{read\text{-}out}$ as a function of T and V_{bias}

Knowing $\tau_{read\text{-}out}$, the corrected input amplitude to our read-out chain can be calculated for each waveform point as:

$$V_{Inp}(n) = V_{Exp}(n) - V_{Shift}(n-1) \qquad 3.17$$

where n – is the point number in a waveform, $V_{Inp}(n)$ and $V_{Exp}(n)$ – are the corrected and original amplitudes at a given point number n, $V_{Shift}(n - 1)$ – is the baseline shift at a given point number n, created by all amplitude points V_{Inp} in a number range from 0 to n - 1.

Waveforms consist of discreet points with given amplitudes $V_{Inp}(n_0)$. Therefore, each point can be presented as Dirac delta function multiplied to a point amplitude: $\delta(n_0) \times V_{Inp}(n_0)$. Therefore, the Eq. 3.12 can be applied to acquired waveforms as:

$$V_{Exp}(n) = V_{Inp}(n_0) \times \delta(n_0) - \frac{\Delta t}{\tau_{read-out}} \times V_{Inp}(n_0) \times \exp\left(-\frac{(n-n_0)\cdot\Delta t}{\tau_{read-out}}\right) \times u(n) \qquad 3.18$$

where $u(n)$ – is the Heaviside step function ($u(n \leq n_0) = 0$ and $u(n > n_0) = 1$), Δt – is the time increment. The schematic interpretation of the Eq. 3.16 is presented in the Figure 3.33 (a and b). We can observe that injected amplitude V_{Inp} at a given point number n_0 into the read-out chain creates the output signal with positive amplitude V_{Exp} at the same point n_0 and additional negative baseline shift. Moreover, we can observe that baseline shift starts from a point number $n_0 + 1$ with an amplitude $V_{Exp}/\tau_{read\text{-}out}$. Therefore, all waveforms amplitudes which appear after $n_0 + 1$ will be biased by this baseline. Using the Eq. 3.18 the shape of baseline shift created by $V_{Inp}(n_0)$ can be described as:

$$V_{Shift}(n-1) = \frac{\Delta t}{\tau_{read-out}} \times V_{Inp}(n_0) \times \exp\left(-\frac{(n-n_0)\cdot\Delta t}{\tau_{read-out}}\right) \times u(n) \qquad 3.19$$

where $V_{Shift}(n)$ – is the amplitude of a baseline shift at a given point position n. It should be pointed out that Eq. 3.19 describes baseline shift created only by one point amplitude $V_{Inp}(n_0)$. The contributions to a baseline shift at a point number n, created by all n - 1 points in a given waveform can be calculated as:

$$V_{Shift}(n-1)=\sum_{i=1}^{i=n-1}\frac{V_{Inp}(i)}{\tau_{read-out}}\times\exp\left[-\frac{(n-n_i)\cdot\Delta t}{\tau_{read-out}}\right]=\sum_{i=1}^{i=n-1}\frac{V_{Inp}(i)}{\tau_{read-out}}\times\exp\left[-\frac{\Delta t}{\tau_{read-out}}\right]^{n-i} \quad 3.20$$

Or, in simpler recursive form:

$$V_{Shift}(n)=V_{Shift}(n-1)\times\exp\left[-\frac{\Delta t}{\tau_{read-out}}\right]-V_{Inp}(n)\times\frac{\Delta t}{\tau_{read-out}} \quad 3.21$$

Combining the Eq. 3.17 and Eq. 3.21, the $V_{Inp}(n)$ can be calculated as:

$$V_{Inp}(n)=V_{Exp}(n)-V_{Shift}(n-1)\times\exp\left[-\frac{\Delta t}{\tau_{read-out}}\right] \quad 3.22$$

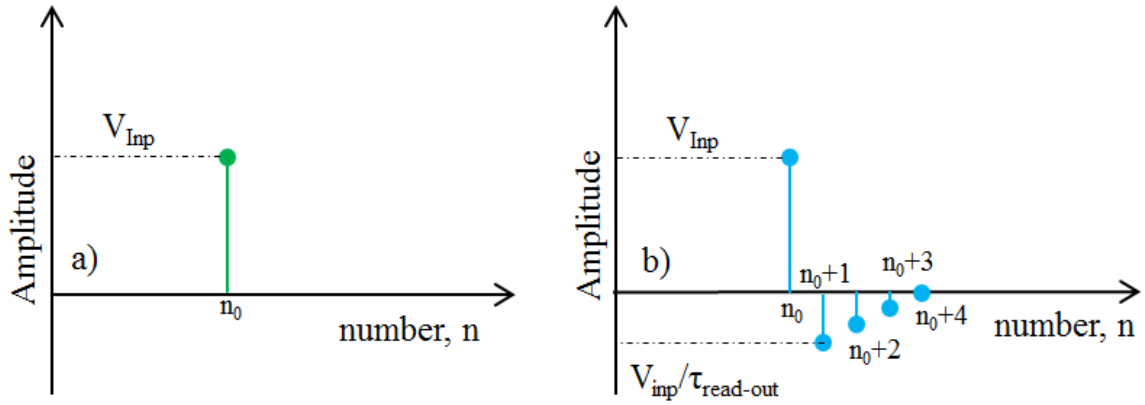

Figure 3.33 The schematic interpretation of the Eq. 3.18: a) injected amplitude V_{inp} into our read-out chain, at a given point number n_0 and b) output amplitude from our read-out chain, equal to V_{Inp} at a same point number n_0 and additional negative baseline

Using recursive Eq. 3.21 and Eq. 3.22 with initial conditions:

$$V_{Inp}(0)=0 \quad 3.23$$

$$V_{Shift}(0)=V_{Exp}(0) \quad 3.24$$

the restored waveform was obtained and it is presented in Figure 3.34 (blue line) in comparison with the original waveform (black line). We can observe that restored waveform has not any baseline shift which is clearly seen in the original waveform (e.g. at time ~1400 ns and ~3800 ns).

However, we can also note that restored waveform has a strange slope. This slope is related to initial condition which was not included properly in our calculation. In the presented calculation we assumed that $V_{Shift}(0) = V_{Exp}(0)$ (See the Eq. 3.24), what is not always true, because the first waveform point can be affected by previous events. Therefore, the system of equations for waveform restoration can be presented as:

$$V_{Inp}(0) = 0 \tag{3.25}$$

$$V_{Shift}(0) = V_{Exp}(0) - DC_{offset} \tag{3.26}$$

$$V_{Inp}(n) = V_{Exp}(n) - V_{Shift}(n-1) \times \exp\left[-\frac{\Delta t}{\tau_{read-out}}\right] - DC_{offset} \tag{3.27}$$

$$V_{Shift}(n) = V_{Shift}(n-1) \times \exp\left[-\frac{\Delta t}{\tau_{read-out}}\right] - V_{Inp}(n) \times \frac{\Delta t}{\tau_{read-out}} \tag{3.28}$$

where DC_{offset} – is the offset of the first experimental point in the waveform, related to the baseline shift due to previous events.

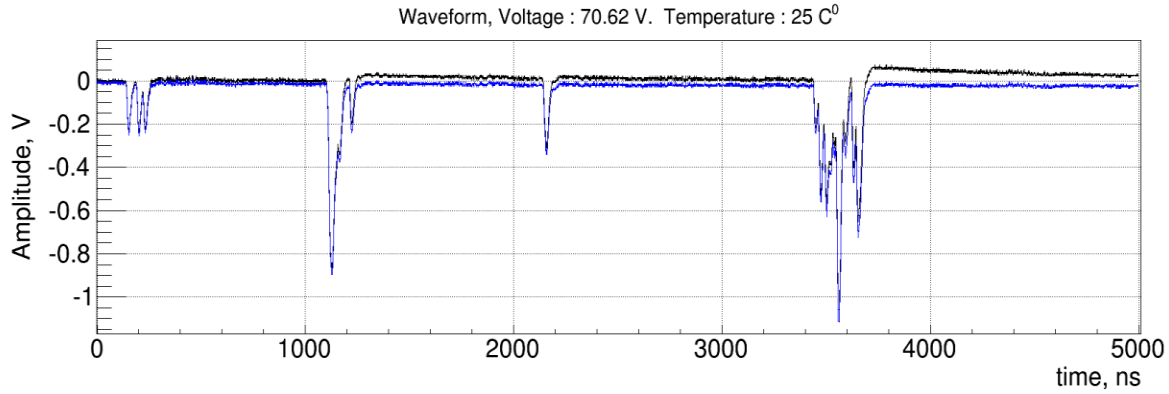

Figure 3.34 Initial waveform (black), and after baseline restoration

It should be pointed out that, in principle, different waveforms can be characterized by different DC_{offset}. However, we do not have any information about what was happening before the first waveform point, and we cannot calculate DC_{offset} directly from acquired experimental waveforms $V_{Exp}(n)$. Nevertheless, the reconstructed waveform slope has a direct link to DC_{offset}, and can be used for DC_{offset} calculation.

The relationship between DC_{offset} and waveform slope has been studied by applying the Eq. 3.25 ÷ Eq. 3.28 with a known $DC_{offset} = DC_{offset}^{known}$ to a known waveform. The known waveform can be a waveform at which all amplitudes are equal to zero (zero waveform). We have used a zero waveform because, independent of DC_{offset}, the reconstructed waveform amplitudes should be zero too. Therefore, by applying the Eq. 3.25 ÷ Eq. 3.28 with a given $DC_{offset}^{known} = 1\,V$, the amplitude shift $\Delta(DC_{offset}^{known})$ of the last point of a restored waveform (which creates the waveform slope) was calculated as:

$$\Delta\left(DC_{offset}^{known}\right) = V_{Inp}\left(N_{points}\right) \tag{3.29}$$

where N_{points} – is the number of points in a waveform and $V_{Inp}(N_{points})$ – is the last point amplitude in the restored waveform. The $\Delta(DC_{offset}^{known})$ determines a restored waveform slope:

$$slope(DC_{offset}) = arctg\left(\frac{\Delta(DC_{offset})}{N_{points}}\right) \cong \frac{\Delta(DC_{offset})}{N_{points}} \qquad 3.30$$

The direct link k between DC_{offset}^{known} and waveform slope can by calculated by dividing the Eq. 3.30 by DC_{offset}^{known}:

$$k = \frac{slope(DC_{offset})}{DC_{offset}^{known}} = \frac{1}{N_{points}} \times \frac{\Delta(DC_{offset}^{known})}{DC_{offset}^{known}} \qquad 3.31$$

The Eq. 3.31 is extremely important, because it gives the relationship between DC_{offset} and waveform slope. Therefore for any reconstructed waveform with a given *slope*, the DC_{offset} can be calculated as:

$$DC_{offset} = \frac{slope}{k} \qquad 3.32$$

The Hough transform [65] has been used to calculate restored waveform slope (DC_{offset}). The main idea of this algorithm is that a straight line $y = constant + slope \times x$ can be represented as a point *(constant, slope)* in the parameter space. By variation of the first parameter *constant* in a given range $[c_{min}; c_{max}]$ with a given step of Δc the second parameter *slope* can be calculated as:

$$\text{slope} = (V^n - \text{constant})/t^n \qquad 3.33$$

where V^n, t^n – is the waveform amplitude and time for a given point number n. 2D histogram of obtained parameter space for the waveform from Figure 3.34 is presented in Figure 3.35. From this figure the *slope* of a -1.74×10^{-6} radian has been obtained as a mean of slice through the bin with maximum entries, and the result is presented in Figure 3.36.

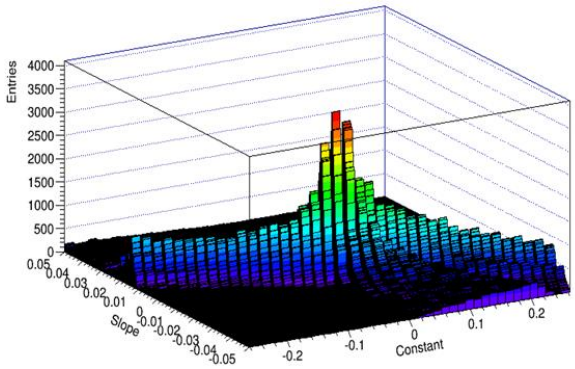

Figure 3.35 Calculated parameter space for selected waveform (T = 25 ^{0}C, V_{bias} = 70.62 V) using Hough transform

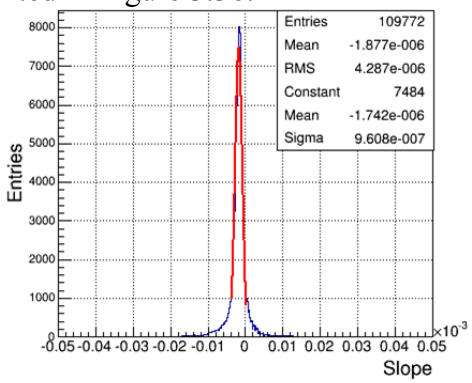

Figure 3.36 Slice through the bin with maximum entries

Summarizing all observations above, the baseline reconstructed procedure can be presented in four main steps:

- apply the Eq. 3.21 ÷ Eq. 3.24 to the experimental waveform, to obtain a reconstructed waveform with a given slope;
- calculate the slope for a given reconstructed waveform;
- use the slope to calculate the DC_{offset} for a given waveform;

- recalculate the reconstructed waveform, without baseline shift and slope, by applying the Eq. 3.25 ÷ Eq. 3.28 with a DC_{offset} (calculated in the previous step) to the experimental waveform.

The example of a waveform at V_{bias} = 70.62 and T = 25 ^{0}C before (black line) and after (red line) baseline restoration procedure (presented by the Eq. 3.25 ÷ Eq. 3.28) is presented in Figure 3.37. It can be seen that the zero baseline was restored, and a correct further analysis of SiPM pulses can be performed, in this step of our analysis procedure, as will be presented in the following section.

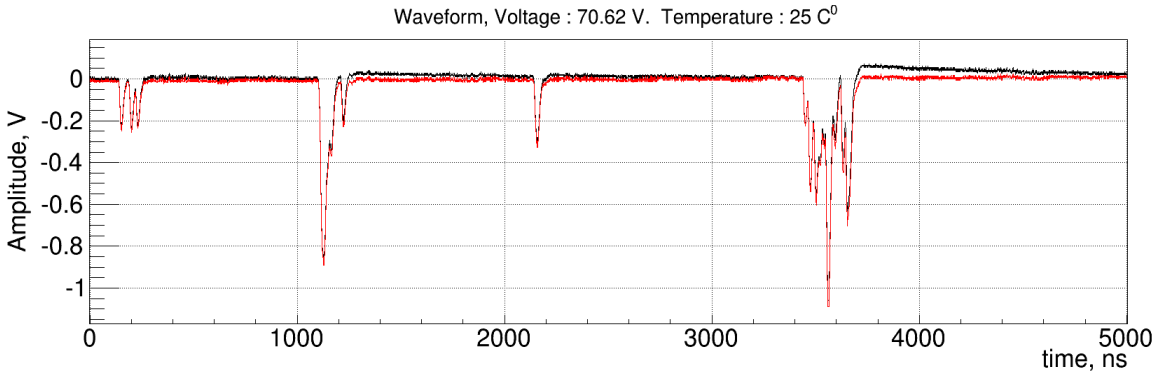

Figure 3.37 Example of a waveform before (black) and after (red) baseline restoration

3.4.1.b. Pulse analysis

Once the waveforms baselines are restored, the SiPM pulse finding procedure can be used to find SiPM pulses. In this chapter we are giving a close look to developed pulse finding algorithm. It is based on the usage of a given threshold to identify the pieces of the waveforms containing potential candidates of SiPM pulses. Most of possible situations that can appear when a waveform crosses a given threshold are shown. The developed algorithm to separate real SiPM pulses from high frequency electronics noise and train of pulses will be described in detail. To understand the structure of a train of pulses and to decompose a train of pulses into separate pulses, a simple simulation procedure has been developed and used.

3.4.1.b.1. Pulse finding procedure

The pulse finding procedure has been developed to determine all time intervals (what will be called in the following "waveforms pieces") which can contain the SiPM pulses. For this task, the threshold is calculated as:

$$\text{threshold} = 5 \times \sigma \qquad 3.34$$

where σ – is the baseline fluctuation calculated in the Section 3.4.1 "Automatic analysis procedure". Nevertheless the threshold can be crossed by waveforms pieces with different kind of experimental data: real SiPM pulses (single or train) or high frequency electrical noise. In this Section, all possible situations will be shown and analyzed.

The simplest situation appears when a waveform piece with a real single SiPM pulse crosses the threshold (see Figure 3.38). However, it can happen that high frequency electric noise has enough high amplitude to cross a threshold too; such situation is presented in Figure 3.39. And the last but not the least (may be one of the most interesting situations) is the situation when a train of pulses crosses the threshold (See Figure 3.40). As it was already mentioned above

(Section 3.4.1 "Automatic analysis procedure"), some situations like a high frequency noise are more probable at low ΔV (small 1 p.e. amplitude) another like a train of pulses at high ΔV (high probability of afterpulses, thermal generated pulses and optical crosstalk).

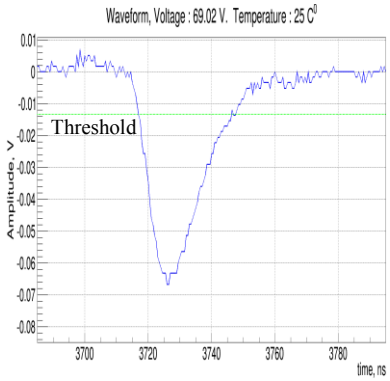

Figure 3.38 Single SiPM pulse crosses a threshold

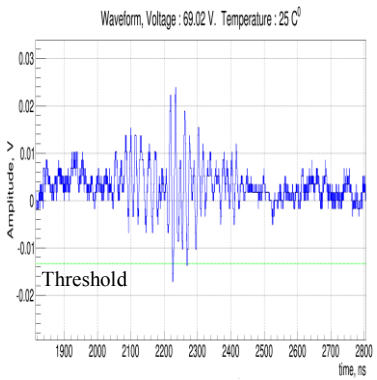

Figure 3.39 High frequency electronic noise crosses a threshold

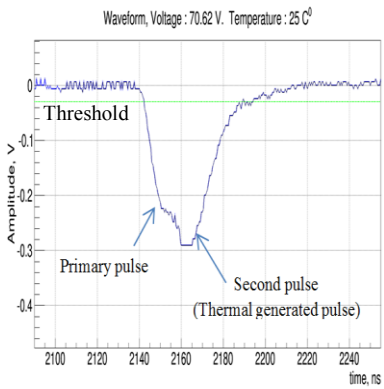

Figure 3.40 Train of pulses crosses a threshold

Independent of the number of pulses in a train of pulses, in the following, the first pulse will be always called the primary pulse. Typically, the primary pulse is followed by one or more afterpulses, as was shown in Figure 3.40, but if the detector is operated at high enough overvoltage (ΔV = 2.5 ÷ 5V.) a train of pulses can be created by different scenarios: thermal generated pulses (See Figure 3.41), afterpulses and/or optical crosstalk (See Figure 3.42). In a given train of pulses, all pulses after the primary pulse (independent if they are afterpulses or thermal generated carriers or cross-talk) will be called secondary pulses.

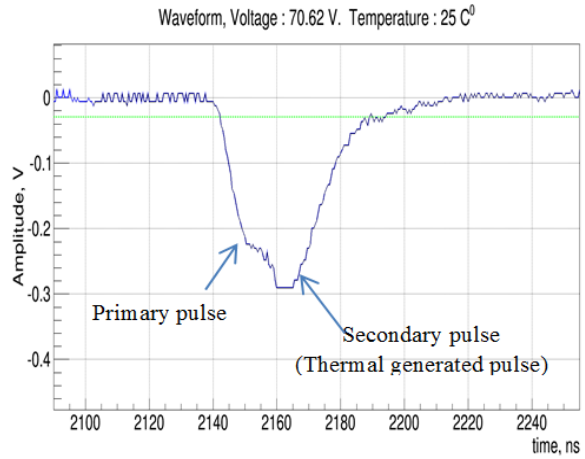

Figure 3.41 Train of pulses created by a primary pulse and secondary pulse, presented by a thermaly generated pulse

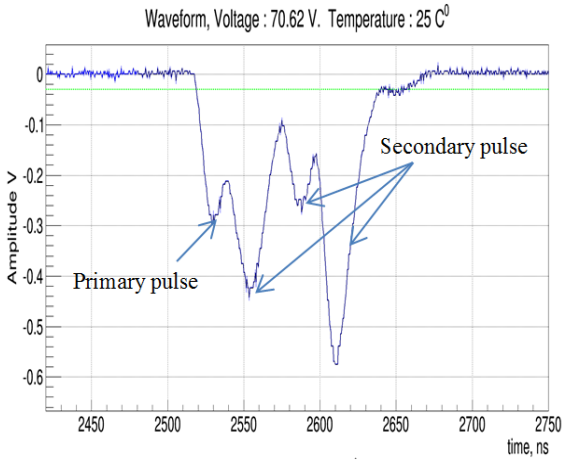

Figure 3.42 Train of pulses created by a primary pulse and secondary pulses, presented by afterpulses, optical cross-talk and thermally generated pulses

In this step of analysis, any piece of a waveform which crosses the threshold (various examples shown in Figure 3.38 ÷ Figure 3.42) will be considered as a possible SiPM pulse. Further analysis based on a typical SiPM pulse shapes (called in the following "template") is used to separate pieces with real SiPM pulses from all others.

3.4.1.b.2. Templates

At a given T, the normalized SiPM pulse shape is independent of the applied V_{bias}. However, because of T dependence of quenching resistance R_q (as it was already shown in the Sections 2.2.5.a) and 3.3.1 "Forward IV characteristic vs. T") we expect that the pulse shape changes with T. Therefore, for each T the typical normalized pulse of SiPM (what will be called in the

following template) has been determined by selecting ten "single SiPM pulses". To remove electronic pedestal, the baselines of each pulse have been calculated as mean amplitude values over an interval of 40 ns length before SiPM pulse leading edge. After baseline subtraction, all selected pulses have been normalized and the template was created as an average over them. The collection of templates at different T calculated for Hamamatsu device is presented in Figure 3.43.

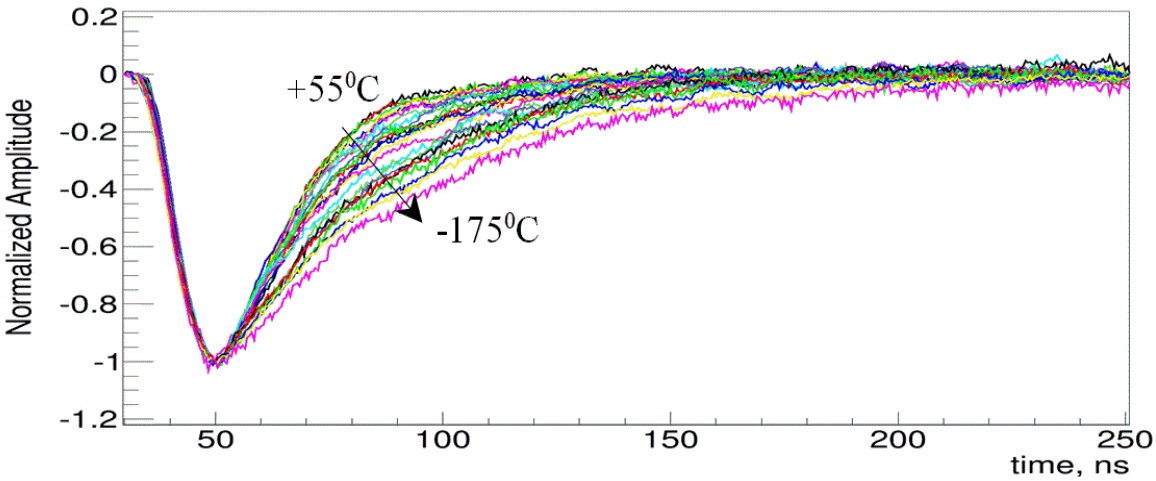

Figure 3.43 Collection of templates at different T, calculated for Hamamatsu S10932-050P device

For each template, the main parameters were calculated:

- the $t^{template}_{rise}$ defined as the time during which template amplitude increases from 10% to 90% of a maximum value (in absolute value);
- the $t^{template}_{recovery}$ defined as $5 \times \tau^{template}$, where $\tau^{template}$ is a time constant calculated from template falling edge exponential fit:

$$f\left(t, a, \tau^{template}\right) = a \times \exp\left(-\frac{t}{\tau^{template}}\right) \qquad 3.35$$

where a – is a free parameter;

- the $Q^{template}$ for each template has been calculated as:

$$Q^{template} = \int I(t)dt = \frac{1}{R \times G_{amplifier}} \int V^{template}(t)dt \qquad 3.36$$

where $I(t)$ – is the current at time t, $G_{amplifier}$ – is the amplifier gain ($G_{amplifier}$ = 55 dB), R – is the input amplifier load resistance (R = 50 Ω), $V^{template}(t)$ – is the template amplifier value at time t.

3.4.1.b.3. Pulse characteristics

In this step of analysis, each piece of waveform which crosses the threshold will be considered as a possible SiPM pulse and will be called in the following possible SiPM pulse. For each possible SiPM pulse, the main parameters such as: *time position* t_{pulse}, t_{before}[3], t_{after}[4],

[3] t_{before} – is the time distance between analyzed piece of waveform and the previous one
[4] t_{after} – is the time distance between analyzed piece of waveform and the next one

baseline BL_{pulse}, *amplitude* A_{pulse}, *rise time* t_{rise}, *recovery time* $t_{recovery}$, *chi-square* χ^2, *charge* Q and *expected charge* $Q_{expected}$ have been calculated. A typical possible SiPM pulse (with single SiPM pulse) and its main parameters are presented in Figure 3.44.

The various parameters presented in Figure 3.44 are defined as:

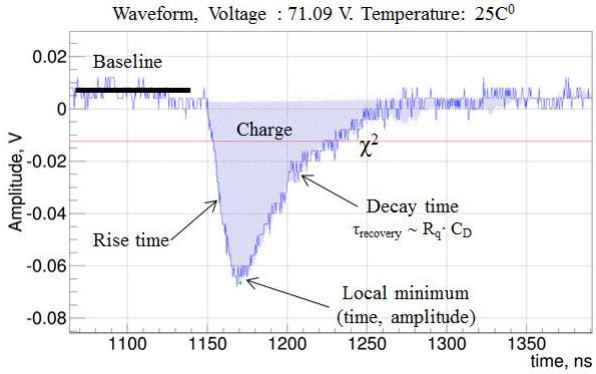

Figure 3.44 Piece of waveform at T = +25 ^{0}C, V_{bias} = 71.09 V which crosses the threshold with calculated characteristic

- the t_{pulse} is given by the time of the point with maximum amplitude (in absolute value);
- the t_{before} and t_{after} have been calculated as a time interval between analyzed possible SiPM pulse and neighboring possible SiPM pulses;
- the BL_{pulse} has been calculated as an average amplitude over a time interval of 40 ns length before starting the possible SiPM pulse leading edge (40 ns is an input parameter to analysis procedure and can be easily changed);
- the A_{pulse} has been calculated as a difference between maximum amplitude value (in absolute value) and calculated BL_{pulse};
- the t_{rise} has been calculated as a time during which possible SiPM pulse amplitude increases from 10% to 90% of a maximum value (in absolute value). The $t_{recovery}$ has been calculated as $5 \times \tau$, where τ is a time constant calculated from possible SiPM pulse falling edge exponential fit:

$$f(t,a,\tau) = a \times \exp\left(-\frac{t}{\tau}\right) \qquad 3.37$$

where a – is a free parameter;

- the *chi-square* χ^2, has been calculated for a comparison between normalized possible SiPM pulse and template at a given T as:

$$\chi^2 = \frac{\sum_{t=0}^{N_{points}} \left(y^{template}(t) - \frac{y_{pulse}(t)}{|A_{pulse}|} \right)}{N_{points}} \qquad 3.38$$

where $y^{template}(t)$ – is the template amplitude value at time t, $y_{pulse}(t)$ – is the possible SiPM pulse amplitude value at time t, A_{pulse} – is the possible SiPM pulse amplitude and N_{points} – is the number of experimental points used in χ^2 calculation;

- the *charge* Q for each possible SiPM pulse has been calculated as:

$$Q = \int I(t)dt = \frac{1}{R \times G_{amplifier}} \int V(t)dt \qquad 3.39$$

where $I(t)$ – is the current at time t, $G_{amplifier}$ – is the amplifier gain ($G_{amplifier}$ = 55 dB), R – is the input amplifier load resistance (R = 50 Ω), $V(t)$ – is the pulse amplifier value at time t. The integral has been calculated in a time range equal to pulse rise time plus pulse recovery time by using the numerical trapezoidal rule [66];

- the *expected charge* $Q_{expected}$ characterizes typical SiPM pulse charge at a given T with an amplitude equal to studied possible SiPM pulse A_{pulse}, and has been calculated as:

$$Q_{expected} = A_{pulse} \times Q^{template} \qquad 3.40$$

where $Q^{template}$ – is the template charge at a given T.

All calculated parameters have been used further to separate single SiPM pulses from high frequency electronics noise and train of pulses.

3.4.1.b.4. Pulse identification

As it was already discussed above, each piece of waveform selected previously by the program and considered as possible SiPM pulse contains either high frequency electronics noise, either single SiPM pulse or train of SiPM pulses. Therefore, to provide correctly further analysis each possible SiPM pulse should be treated differently according to contained situation (e.g. high frequency electronics noise, single SiPM pulse or train of SiPM pulses). The developed procedure takes a decision on how to treat a given possible SiPM pulse by comparing the shape of a piece of waveform with a shape of template at a given T. In particular, two main parameters characterizing these shapes are compared:

- the template rise time $t^{template}{}_{rise}$ with the corresponding rise time t_{rise} of the possible SiPM pulse;
- the template charge $Q_{expected}$ with the corresponding charge Q_{pulse} of the possible SiPM pulse.

Therefore, few cuts to these parameters have been imposed based on the following considerations and all possible SiPM pulses with:

- $t_{rise} < Cut^{Min}_{RiseTime}$ or $Q_{pulse} < 0.7 \times Q_{expected}$ will be considered as a high frequency noise and removed from further analysis, because the high frequency electronics noise has much sharper leading edge and smaller charge with respect to real SiPM pulses;
- $Q_{pulse} > 1.3 \times Q_{expected}$ will be considered as a train of pulses, because the train of pulses has much bigger charge with respect to single SiPM pulses due to secondary pulses contribution;
- $0.7 \times Q_{expected} < Q_{pulse} < 1.3 \times Q_{expected}$ will be considered as a single SiPM pulses, because the real SiPM pulses charge can varying from μcell to another due to calculation or measurements uncertainties with a mean value of $Q_{expected}$. In our analysis we considered that this uncertainty is less than 30% (it is an input parameter which can be easily changed).

All waveform pieces with single SiPM pulses are saved for further SiPM parameters analyses (e.g. G, V_{BD}, $C_{\mu cell}$ etc.) while the pieces with train of pulses are sent to template subtraction procedure for decomposition (See the Section 3.4.1.b "Template subtraction procedure") for further SiPM afterpulses studies. However, to perform a correct decomposition, the structure of various types of train of pulses (e.g. signal shape, presented as leading and falling edges) should be studied.

3.4.1.b.5. Structure of a train of pulses and waveform simulation program

A program has been developed to simulate waveforms with a known number of SiPM pulses (e.g. single, cross-talk and train of pulses presented by single pulse plus one afterpulse) with predefined parameters (e.g. t_{pulse} and A_{pulse}). These waveforms have been used to study:

- the contribution of secondary pulse (presented by an afterpulse) to the shape of a train of pulses which will be shown in the present Section;
- the efficiency of the template subtraction and pulse finding procedures, that will be described in the next Section 3.4.1.c "*Efficiency of automatic analysis* procedure".

As a function of our interest of studies and the input parameters, each simulated waveform can contain:

- Single SiPM pulses, simulated as a template shape at a given T multiplied to a given amplitude (input parameter) A_{sim};
- Train of pulses, simulated as a sum of primary and delayed secondary pulses. Both pulses shapes were calculated as a template shape at a given T multiplied to primary and secondary pulses amplitudes respectively. The primary pulse amplitude A_{sim} was set as an input parameter, while the secondary pulse amplitude $A_{secondary}$ was calculated as:

$$A_{\mathrm{sec}ondary} = A_{sim} \times \left(1 - \exp\left(-\frac{\Delta t}{\tau^{template}}\right)\right) \qquad 3.41$$

  where Δt – is the time delay between primary and secondary pulses, $\tau^{template}$ – is the time constant calculated from template falling edge as shown in the Section 3.4.1.b "Templates";
- Optical cross-talk, simulated as a probability (input parameter) that any simulated pulse can initiate a simultaneous additional pulse.

The real experimental waveforms are affected by electronics noise. Therefore, measured amplitudes values of the experimental waveforms are spread near their real meaning. To add this effect to a simulated waveforms their amplitudes values have been randomly spread by Gaussian distribution with a standard deviation σ_{noise} near their "real" values. The σ_{noise} describes the electronics noise magnitude. As it was already discussed in the Section 3.1 "Read-out chain for DC / AC measurements" our read-out chain is operated in the stable conditions independent of T and V_{bias}. Therefore, for our experimental conditions σ_{noise} is constant and a value of σ_{noise} = 2.7 mV has been measured.

Three typical simulated situations will be used to describe the structure of the train of pulses. Obtained information will be used in the next chapter for the decomposition of a train of pulses.

As it was already mentioned in the Section 3.4.1.b "Pulse finding procedure" only when the secondary pulse arrives in a time interval less than $t^{template}_{recovery}$, the shape of primary pulse will be disturbed and train of pulses will be created (See Figure 3.45 a)). Otherwise separate pulses will be obtained, as shown in Figure 3.45 b).

If the time interval between primary and second pulses is comparable with $t^{template}_{rise}$ (or less) the primary pulse rising edge will be also affected. As a result the shape of a train of pulses will look like a single SiPM pulse with bigger amplitude and width in comparison with a typical 1 p.e. pulse (e.g. template). The simulation of such train of pulses is presented in Figure 3.45 c). We can see that local minimums (red dot) are shifted in time with respect to primary pulse position. In the same time, if the distance between pulses is equal or bigger than $t^{template}_{rise}$, pulses inside a train of pulses can be reconstructed with their main parameters as if they arrive separately by implementing template subtraction procedure.

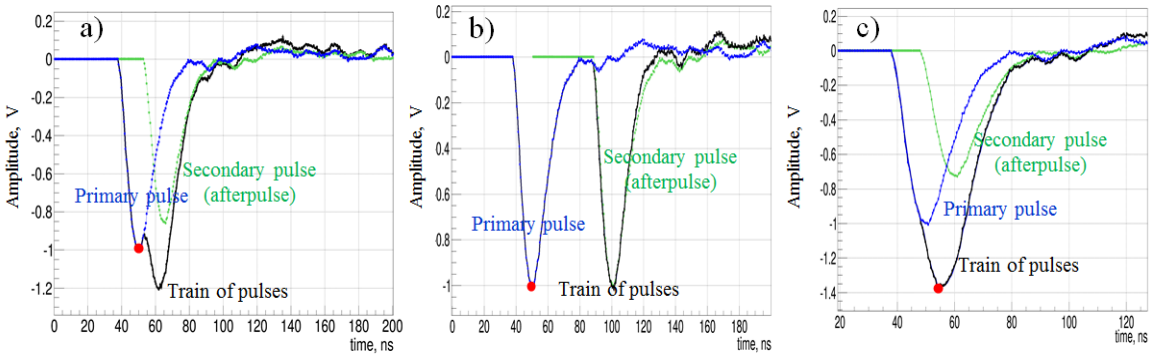

Figure 3.45 Simulation of a train of pulses (black) which consist of a primary pulse (blue) and afterpulse (green) with a time delay Δt of a) 15 ns, b) 50 ns and c) and 10ns

It should be pointed out that, in all these simulations, the primary pulses were located at time position of 50 ns with the amplitudes of 1 V. The secondary pulses were located with a time delay Δt of 15 ns, 50 ns and 10 ns respectively and their amplitudes were calculated from Eq. 3.41.

3.4.1.b.6. Template subtraction procedure

To obtain correct information (time position, amplitude and charge) of pulses which are combined in a train of pulses, a template subtraction procedure has been developed. The main steps of developed algorithm are:

1. find the position and amplitude of a primary pulse;
2. multiplied the template to the primary pulse amplitude;
3. locate the template in the position of the primary pulse;
4. save the template shape, amplitude, position and charge as parameters of the reconstructed primary pulse;
5. subtract the template, to obtain a new shape of a train of pulses without primary pulse;
6. consider the obtained shape as a new train of pulses;
7. repeat the algorithm, until the amplitude of the new train of pulses is bigger than the waveform amplitude or a given cut value.

It should be pointed out that the quality of presented algorithm is fully depending on point #1, which is not trivial. Therefore, the work of developed algorithm will be shown in details on the simulated examples which were presented in Figure 3.45 (a, b and c). From those figures we can observe three important points:

- since the secondary pulses appear mostly due to afterpulses (the probability that thermal carrier trigger the second avalanche during $t_{recovery}$ is much smaller and around 1%, for *DCR* of 200 kHz and $t_{recovery}$ of 50 ns), the primary pulse rising edge can be affected by secondary pulses only if the $\Delta t < t_{rise}$, where Δt – is the time interval between primary and secondary pulses;
- if the $\Delta t >> t_{rise}$ the rising edge of primary pulse will not be effected by secondary pulse (see Figure 3.45 a and b). Therefore the rising edges of primary pulse and train of pulses will be equal;
- if the $\Delta t \approx t_{rise}$ the rising edge of primary pulse will be effected by secondary pulse. As a result the rising edge of a train of pulses will be a superposition of the rising edges of primary and secondary pulses (see Figure 3.45 c).

Taking into account the observations above, we can conclude that a rising edge of a train of pulses equal to a rising edge of primary pulse (see Figure 3.45 a and b), or at least contain it (see Figure 3.45 c).Therefore, a rising edge of a train of pulses has been used to find the position of a primary pulse. Moreover, the chi-square χ^2_{rise} calculated for a comparison between the rising edges of a train of pulses and template will be minimal only if the template is located in the position of the primary pulse. Therefore, at each point of the rising edge of a train of pulses the template has been located, and the χ^2_{rise} has been calculated as:

$$\chi^2_{rise}(t) = \sum_{j=(t-t_{rise})}^{t} \omega(t) \cdot \left(y^{pulse}(j) - \left| y^{pulse}(t) \right| \times y^{template}\left(t^{template}_{\min} + j - t \right) \right)^2 \qquad 3.42$$

where t – is the template location, $t_{min}{}^{template}$ – is the position of the template minimum, $y^{template}(t)$ and $y^{pulse}(t)$ – are the template and pulse amplitudes at time t respectively and $\omega(t)$ – is the weighting factor which is used to decrease the weight of the beginning of rising edge which is much more effected by electrical noise. Applying the Eq. 3.42 to the simulated trains of pulses, presented in the Figure 3.45, the χ^2_{rise} as a function of t was calculated and presented in Figure 3.46. We can observe that, following these calculations, the primary pulse time position is 50 ns for the first and the second situations and 51.5 ns for the third situation.

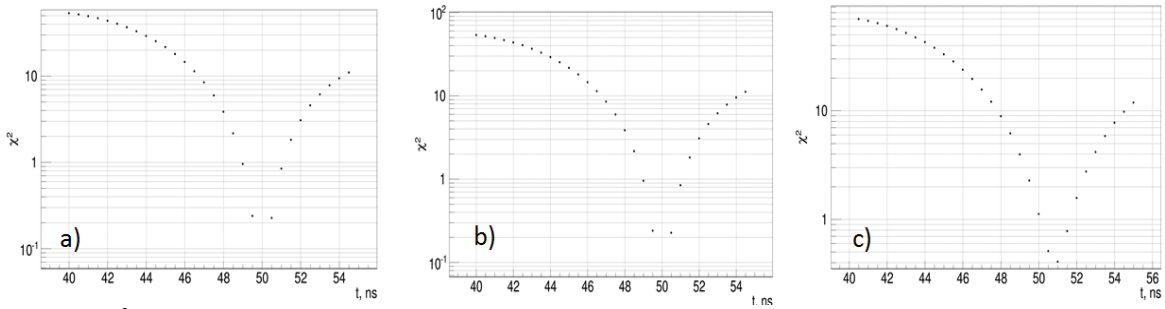

Figure 3.46 χ^2 as a function of template position calculated from Eq. 3.42 for simulated SiPM pulses presented in the Figure 3.45

Applying the described above template subtraction procedure to the simulated trains of pulses, presented in the Figure 3.45, the shapes of the primary and secondary pulses have been found and presented in Figure 3.47.

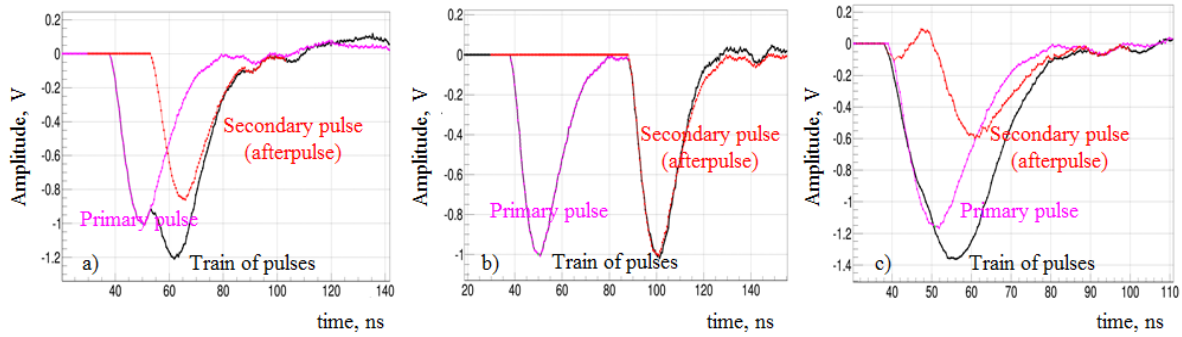

Figure 3.47 Simulated train of pulses (black) and reconstructed primary (magenta) and secondary (red) pulses

Comparing the shapes, positions and amplitudes of the simulated (See Figure 3.45) and reconstructed (See Figure 3.47) primary and secondary pulses we can conclude that proposed procedure has reconstructed correctly the pulses for first and second situations (See Figure 3.47 a) and b)). While for the third situation (See Figure 3.47 c)) the position of the primary pulse has been found with 1.5 ns shift with respect to simulated position. This 1.5 ns shift leads to 20% and 14% of difference between simulated and reconstructed pulses amplitudes for primary and secondary pulses respectively. Also it can be observed that for the third situation (See Figure 3.47 c)) a fake baseline fluctuation before secondary pulse was created. Therefore, we can conclude that proposed procedure can reconstruct the shapes of primary and secondary pulses correctly only if the $\Delta t > 15$ ns. This limitation is related to the phenomena that, if the $\Delta t < 15$ ns the train of pulses rising edge will be effected by the secondary pulse, as has been shown in the Figure 3.47 c). To overcome this limitation, the pulse amplitude $y^{pulse}(t)$ in the Eq. 3.42 should be varied too. As a result the χ^2_{rise} should be calculated as a function of template position t, and pulse amplitude y_{Max}. Therefore the Eq. 3.42 was transformed to:

$$\chi^2_{rise}(t; y_{Max}) = \sum_{j=(t-t_{RT})}^{t} \omega(t) \cdot \left(y^{pulse}(j) - |y_{Max}| \times y^{template}\left(t^{template}_{\min} + j - t\right)\right)^2 \qquad 3.43$$

Applying the Eq. 3.43 to the simulated trains of pulses presented in the Figure 3.45, the χ^2_{rise} as a function of a t and y_{Max} was calculated and presented in Figure 3.48. We can observe that, following these calculations, a primary pulse time position of 50 ns was found for all three situations.

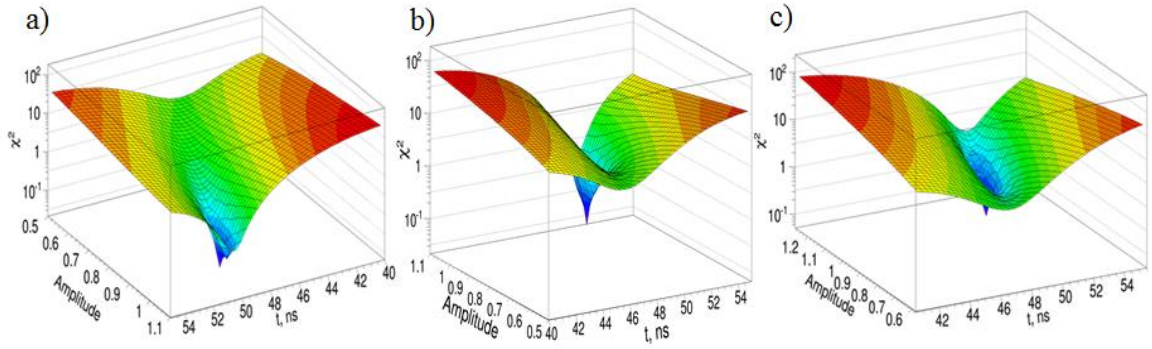

Figure 3.48 χ^2 as a function of template position and amplitude calculated from Eq. 3.43 for simulated SiPM pulses presented in the Figure 3.45

Applying the described above template subtraction procedure (with χ^2_{rise} calculated from Eq. 3.43) to the simulated trains of pulses, presented in the Figure 3.45, the correct shapes of the primary and secondary pulses have been found and presented in Figure 3.49.

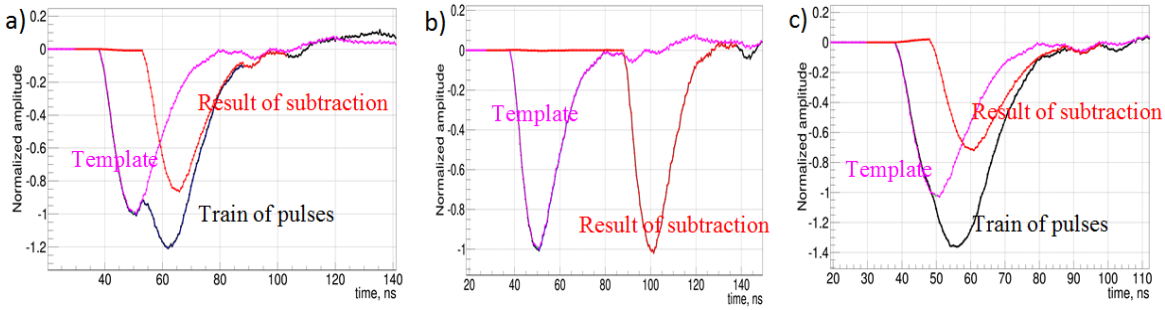

Figure 3.49 Simulated train of pulses (black) and template (magenta) is located in a time position where χ^2 has a minimum

We can conclude that proposed template subtraction procedure can reconstruct the shapes of primary and secondary pulses correctly, if the Δt > 10 ns. This time limitation of Δt is fully related to the t_{rise} (and implicitly to the read-out chain) which is used for χ^2_{rise} calculation. Therefore, for a faster read-out chain (t_{rise} will be smaller) the limitation for the Δt will be smaller. For example, for a read-out chain with 500 MHz bandwidth, a limitation of Δt ~2 ns has been found.

In this Section the template subtraction procedure has been applied to "ideal" simulated data. However, the "real" shapes of experimental waveform are disturbed by electronics noise which can affect the efficiency of developed procedure. Therefore, the efficiency of template subtraction procedure will be studied as a function of electronics noise and described in the next Section.

3.4.1.c. Efficiency of automatic analysis procedure

Before passing to SiPM parameters calculation, we should know the efficiencies of pulse finding procedure. It has been calculated from the simulated waveforms with a known number of SiPM pulses.

As it was already mentioned in the Section 3.4.1.b "Structure of a train of pulses and waveform simulation ", for our experimental conditions the σ_{noise} is a constant. However, the signal to noise ratio depends on T and V_{bias} because, as will be shown in the Section 3.4.3.e "*Signal amplitude vs. V_{bias} vs. T*", the A_{pulse} is changing with T and V_{bias}. Therefore, the efficiency of the developed algorithm has been studied as a function of the simulated signal to noise ratio A_{sim}/σ_{noise}. However to simplify the analysis, the A_{pulse} had been set to a constant value of 100 mV and σ_{noise} was being varying from 50 mV down to 1 mV.

To calculate the efficiency of the pulses finding procedure $E_{P.F.P.}$, the waveforms with a known number $N_{sim}(1\ p.e.)$ of 1 p.e. SiPM pulses and optical cross-talk pulses N_{ct} have been simulated as a function of the ratio A_{sim}/σ_{noise}. For all simulated waveforms, the pulse finding procedure described previously has been applied. The $E_{P.F.P.}$ for a given $A_{1p.e}/\sigma_{noise}$ was calculated at present, as a ratio between the number of founded 1 p.e. SiPM pulses $N_{found}(1\ p.e.)$ to the $N_{sim}(1\ p.e.)$:

$$E_{P.F.P.}\left(A_{1p.e.}/\sigma_{noise}\right)=\frac{N_{found}(1p.e.)}{N_{simulated}(1p.e.)}\times 100\% \qquad 3.44$$

The $E_{P.F.P.}$ as a function of $A_{1p.e}/\sigma_{noise}$ is presented in Figure 3.50. We can observe that $E_{P.F.P.}$ decreases with decreasing the $A_{1p.e}/\sigma_{noise}$. The most significant drop of $E_{P.F.P.}$ can be observed when $A_{1p.e}/\sigma_{noise}$ < 10. However, even for extremely noisy waveform ($A_{1p.e}/\sigma_{noise}$ = 2) we can

note that 75% of pulses will be founded, while, if the ratio $A_{1p.e}/\sigma_{noise} > 10$ the developed pulse finding procedure shows constantly high efficiency > 95%. For our experimental conditions, the $A_{1p.e}/\sigma_{noise}$ is changing in a range from 5 (T = -175 ^{0}C and ΔV = 0.5 V) to 30 (T = 45 ^{0}C and ΔV = 2.5 V), as a function of T and ΔV, therefore the $E_{P.F.P.}$ is ranging from 92% to 98%.

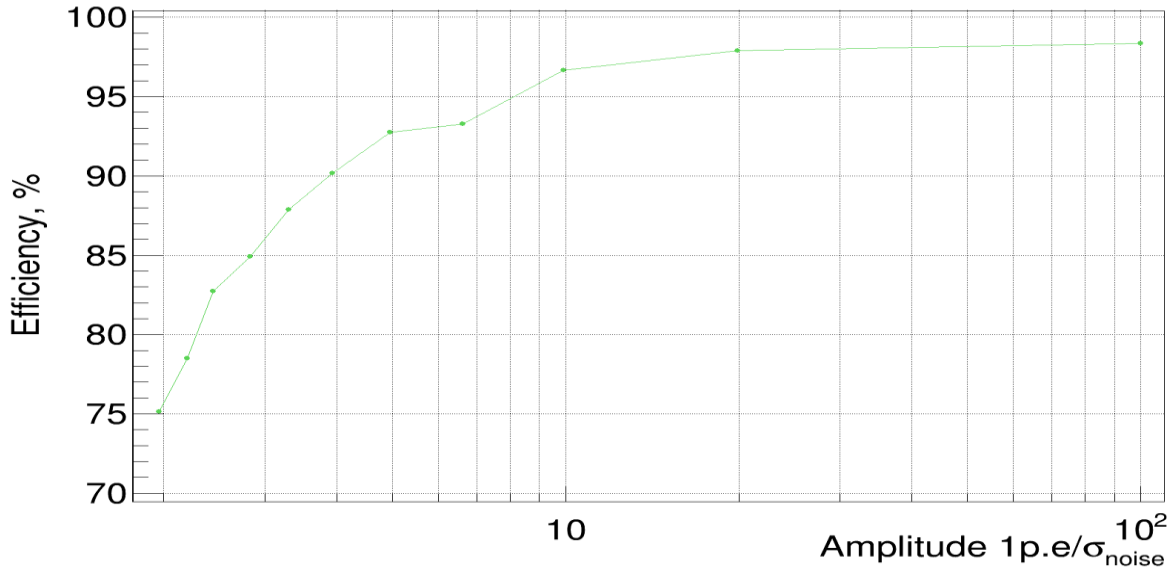

Figure 3.50 Pulse finding procedure efficiency ($E_{P.F.P.}$) as a function of electrical noise standard deviation ($A_{1p.e.}/\sigma_{noise}$)

3.4.2. **Properties of Poisson statistics for DCR & P_{Geiger} calculation**

In this Section it will be shown how the properties of Poisson statistics are used for *DCR* and P_{Geiger} calculation. As it was already mentioned in the Section 3.2 " Measured devices & measurements conditions", the data acquisition was triggered by the laser trigger signal positioned at 1.55 μs later with respect to the waveform beginning. For every waveform, the local minimum A_{min} of the waveform amplitude (we are working with negative pulses) has been calculated within 20 ns "laser" gate[5]. A typical distribution of A_{min} for waveforms acquired at T = 298.15 K and V_{bias} = 71.09 V is presented in Figure 3.51 a). We can observe various peaks, each of them corresponding to a given number of fired μcells (e.g. detected 1 p.e., 2 p.e. and 3 p.e.).

The number of photons in the laser light pulses is expected to follow the Poisson distribution. However, the observed distribution of p.e. is distorted due to optical cross-talk and afterpulses. In particular, the number of events with an amplitude exceeding 1 p.e. amplitude (e.g. 2 p.e., 3 p.e. and 4 p.e. peaks) is enhanced, while the number of events with and amplitude equal to 1 p.e. amplitude (e.g. 1 p.e. peak) is artificially low due to cross-talk and afterpulses phenomena. Nevertheless, these phenomena do not affect the 0 p.e. peak. Therefore, 0 p.e. peak indicates the number of recorded waveforms $N_{laser}(0)$ with no SiPM signal and consequently it can be used to determine the average number of detected photons k_{laser} without any influence from these two effects (e.g. cross-talk and afterpulses). Using the Poisson distribution, the probability to detect a given number of photoelectrons $n_{p.e}$ can be determined:

[5] "laser" gate - is the time gate centered on the expected arrival time of the laser signal

$$P\left(n_{p.e.}\right)=\frac{\left(k\right)^{n_{p.e.}}}{n_{p.e.}!}\times e^{-k} \tag{3.45}$$

where k – is the average number of detected photons. Therefore, the probability to detect 0 p.e. is:

$$P\left(0\right)=e^{-k} \tag{3.46}$$

From the other hand, at a given T and V_{bias} the $P(0)$ can be calculated as the ratio between the number $N(0)$ of waveforms with no SiPM signal within a given time gate and the total number $N(total)$ of acquired waveforms:

$$P\left(0\right)=\frac{N\left(0\right)}{N\left(total\right)} \tag{3.47}$$

From the Eq. 3.46 and Eq. 3.47 the value of average number of detected photons within 20 ns "laser" gate k_{laser} can be determined as:

$$k_{laser}=-\ln\left(P_{laser}\left(0\right)\right)=-\ln\left(\frac{N_{laser}\left(0\right)}{N_{laser}\left(total\right)}\right) \tag{3.48}$$

where $N_{laser}(0)$ and $N_{laser}(total)$ – are the number of waveform with no SiPM signal within the "laser" gate and respectively the total number of recorded waveforms.

However, thermal SiPM pulses can appear within "laser" gate used for A_{min} calculation. Therefore the value of k_{laser} was corrected for dark SiPM pulses using an auxiliary "dark" gate[6]:

$$k_{laser}^{corrected}=-\ln\left(P_{laser}\left(0\right)\right)+\ln\left(P_{dark}\left(0\right)\right)=-\ln\left(\frac{N_{laser}\left(0\right)}{N_{laser}\left(total\right)}\right)+\ln\left(\frac{N_{dark}\left(0\right)}{N_{dark}\left(total\right)}\right) \tag{3.49}$$

where $k_{laser}{}^{corrected}$ – is the corrected average number of detected photons, $N_{dark}(0)$ and $N_{dark}(total)$ – are the number of waveforms with no SiPM signal within "dark" gate and the total number of recorded waveforms. The typical distribution of A_{min} calculated within 20 ns "dark" gate is presented in Figure 3.51 b).

[6] "dark" gate - is the time gate which has similar length as a "laser" gate, but located before it to avoid the light influence .

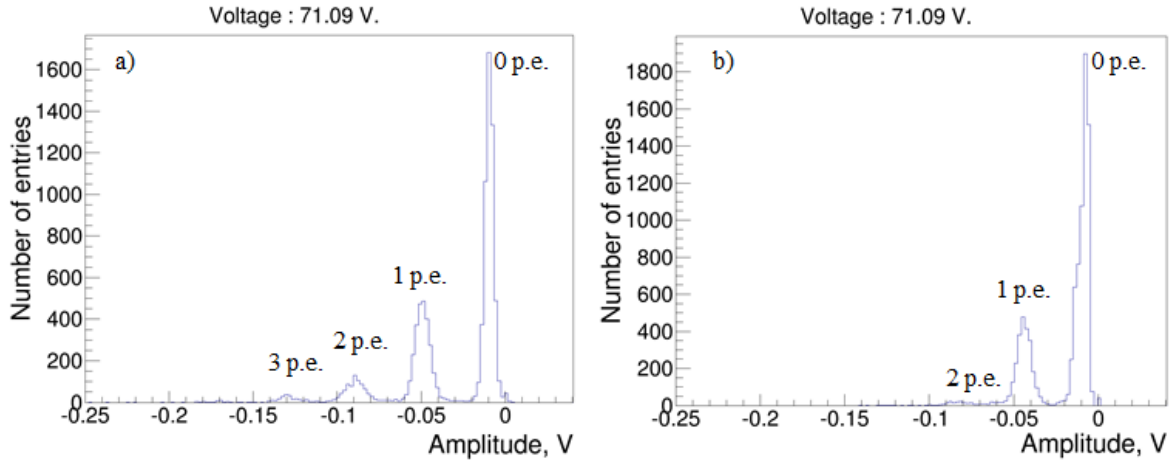

Figure 3.51 Local minimum of a waveform amplitude calculated within 20 ns gate a) where the pulses from laser are expected and b) in the beginning of the waveform where the SiPM was in dark conditions. Results are presented for Hamamatsu S10932-050P device

The $k_{laser}^{corrected}$ is related to the P_{Geiger} as:

$$k_{laser}^{corrected} = \langle n_{laser} \rangle \times P_{Geiger} \tag{3.50}$$

where $<n_{laser}>$ – is the average number of photons illuminating the SiPM. Even if the absolute value of $<n_{laser}>$ is not known, the relative P_{Geiger} can be studied.

The value of average number of detected photons within 20 ns "dark" gate k_{dark} can be used to determine the rate of thermal pulses as:

$$F_{Thermal} = \frac{k_{dark}}{20ns} = -\frac{\ln(P_{dark}(0))}{20ns} = -\frac{\ln\left(\frac{N_{dark}(0)}{N_{dark}(total)}\right)}{20ns} \tag{3.51}$$

The P_{Geiger} and thermal rate calculated from the Eq. 3.49 and the Eq. 3.51 respectively will be presented as a function of V_{bias} and T in the next Section.

3.4.3. **Calculation of SiPM parameters**

3.4.3.a. G vs. V_{bias} vs. T

The G at a given V_{bias} and T has been calculated from Eq. 2.25. The gain G as a function of V_{bias} for four KETEK devices in T range from 238.15 K to 308.15 K is presented Figure 3.52 a), b), c) and d), while the results from *first and second sets of measurements* for Hamamatsu SiPM devices are presented in Figure 3.53 a), b) and c). We can observe that for a given T, the G increases linearly with V_{bias} as was discussed in the Section 2.2.5 "Temperature dependence". We can distinguish good agreement between G for all three Hamamatsu devices calculated from *first and second sets of measurements* presented by open and closed dots in Figure 3.53.

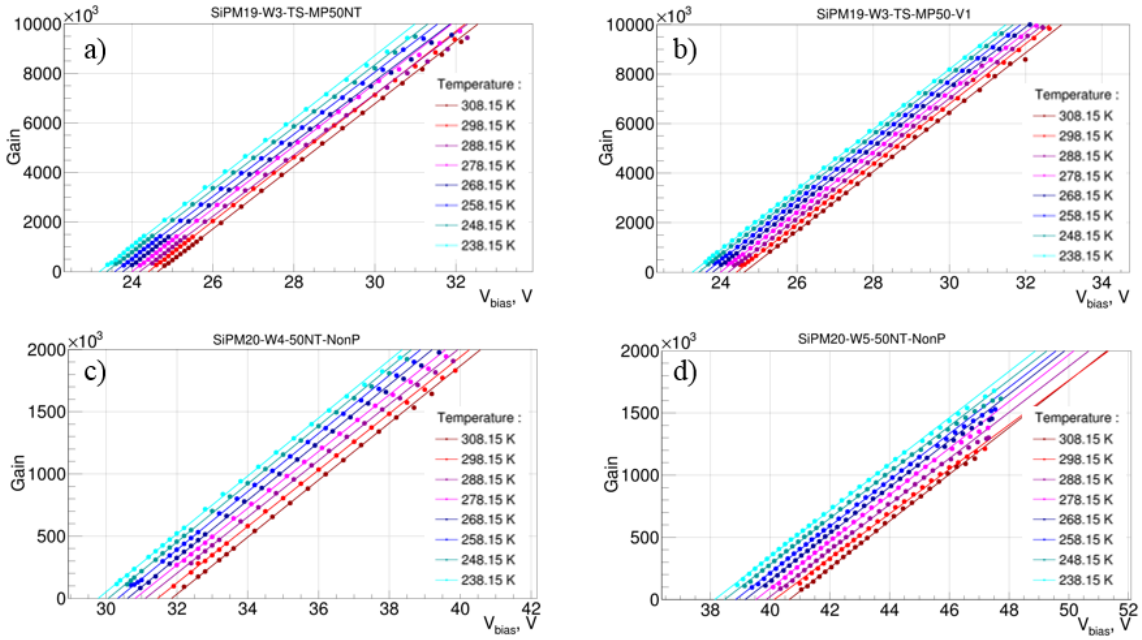

Figure 3.52 G vs. V_{bias} in the T range from 238.15 K to 308.15 K for KETEK SiPM devices: a) SiPM19-W3-TS-MP50NT, b) SiPM19-W3-TS-MP50-V1, c) SiPM19-W4-50NT-NonP and d) SiPM19-W5-50NT-NonP

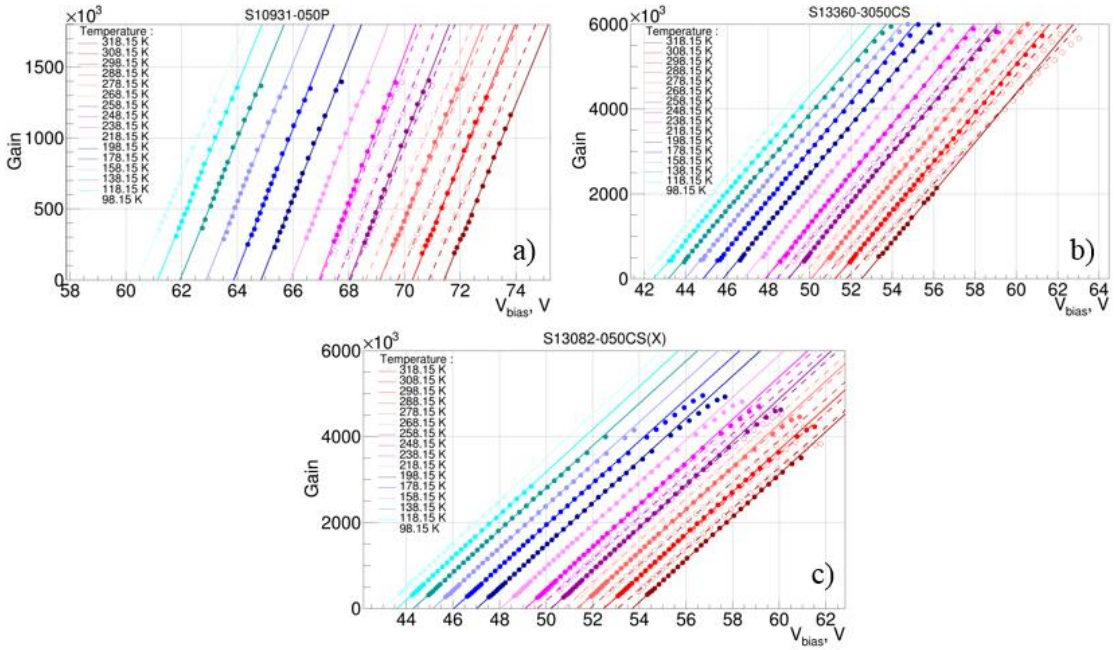

Figure 3.53 G vs. V_{bias} in the T range from 98.15 K to 318.15 K for Hamamatsu SiPM devices: a) S10931-050P, b) S13082-050CS(X) and c) S13360-3050CS. The results from *first set of measurements* are presented by open dots and dashed lines, while the results from *second set of measurements* are presented by closed dots and solid lines

Also, we can conclude that the working range (defined in Section 3.2 "Measured devices & measurements conditions") of Hamamatsu SiPM devices has been significantly increased during last three years, from ~3 V for the device of 2011 year production run up to ~8 V for the devices from 2015 year production run. This improvement allows the increasing of the *G* up to ~5 × 10^6. Moreover, we can observe that KETEK SiPM devices of P-on-N structure, with and without trenches (SiPM19-W3-TS-MP50NT and SiPM19-W3-TS-MP50-V1) can reach even two times higher *G* in the same working range of ~8 V, while KETEK SiPM devices of N-on-P

structure (SiPM20-W4-50NT-NonP and SiPM20-W5-50NT-NonP) show similar G like 2011 Hamamatsu device (S10931-050P). These different behaviors of the G as a function of V_{bias} at a given T can be related to different values of $C_{\mu cell}$ (see Eq. 2.24) (more details will be discussed further in this section, see "$C_{\mu cell}$ *vs.* T".

3.4.3.b. V_{BD} *vs.* T

The V_{BD} at a given T has been calculated from the plots of G vs. V_{bias} (see previous Section 3.4.3.a "G *vs.* V_{bias} *vs.* T") by extrapolating the linear fit to zero. The V_{BD} as a function of T for four KETEK devices is presented in Figure 3.54 a) and b), while the results from *first and second sets of measurements* for Hamamatsu SiPM devices are presented in Figure 3.55 a) and b). The V_{BD} temperature variation (238.15 K < T < 308.15 K) of KETEK devices has been approximated by linear function ($f(T) = a + b \times T$, where a and b – are free parameters), while the V_{BD} temperature variation (98.15 K < T < 318.15 K) of Hamamatsu devices has been approximated by the third order polynomial function presented by Eq. 3.3.

Independent of the measured device, we can observe that V_{BD} increases with increasing T. The simple explanation of this behavior is that the carriers passing through the depletion layer under high electrical field have sufficient energy to generate an electron hole pair and consequently to contribute to an avalanche creation. However, they lose part of their energy due to optical phonon generation after traveling a mean free path λ. The λ decreases with increasing the T. Therefore at high T, for a given distance at a given electrical field, the carriers lose more energy due to shorter λ which leads to higher frequency of phonon generation $\sim 1/\lambda$. Therefore, with increasing T, the carriers must pass to a higher potential difference or voltage to reach the sufficient energy to generate an electron hole pair, phenomena directly related to the increase of V_{BD} with increasing T.

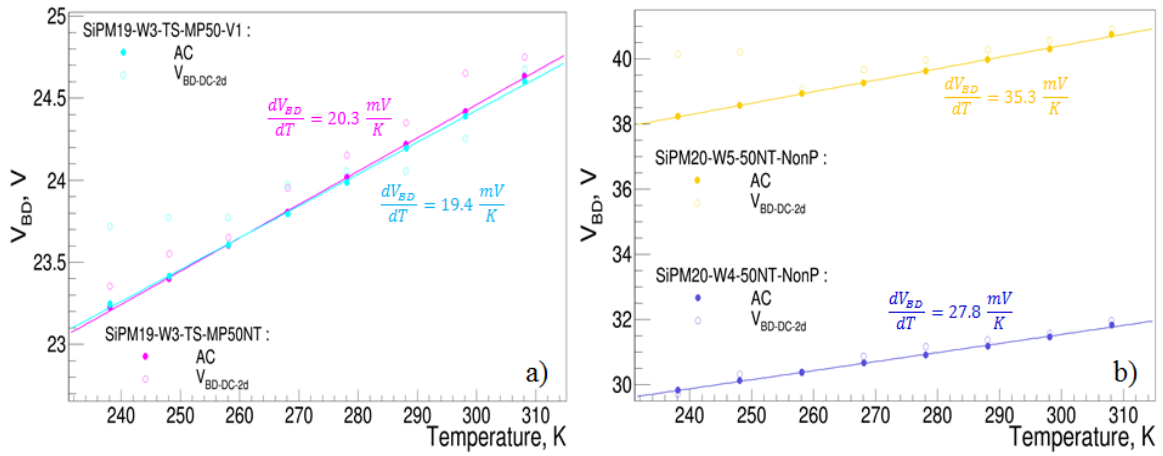

Figure 3.54 The V_{BD} (calculated from AC measurements) and $V_{BD\text{-}DC\text{-}2d}$ (calculated from DC measurements) vs. T for KETEK SiPM devices with a) P-on-N structure and b) N-on-P structure. Also the T coefficients for V_{BD} are presented

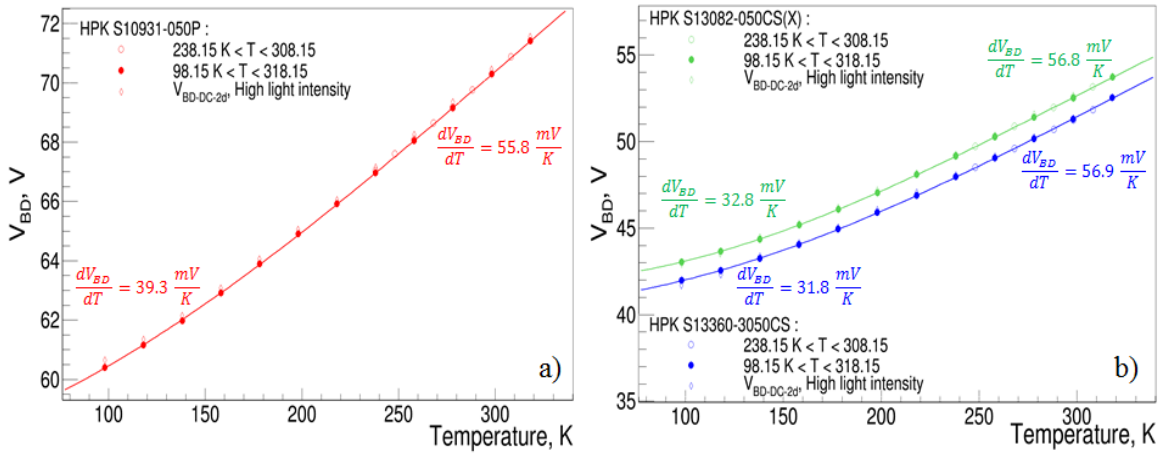

Figure 3.55 The V_{BD} (calculated from AC measurements) and $V_{BD\text{-}DC\text{-}2d}$ (calculated from DC measurements) vs. T for Hamamatsu SiPM devices from a) 2011 year production run and b) 2015 year production run. Also the T coefficients for V_{BD} are presented

It can be observed that both KETEK SiPM devices of P-on-N structure with and without trenches (SiPM19-W3-TS-MP50NT and SiPM19-W3-TS-MP50-V1) show very close values of V_{BD} independent of T. In the same time, by comparing the another's two KETEK SiPM devices of N-on-P structure (SiPM20-W4-50NT-NonP and SiPM20-W5-50NT-NonP) we can observe that SiPM20-W4-50NT-NonP shows a V_{BD} ~8 V smaller with respect to V_{BD} of SiPM20-W5-50NT-NonP. Following the numerical TCAD simulations performed by Serra [18] and presented already in the Section 2.2.5.e "V_{BD} *vs.* T", the V_{BD} increases with increasing the thickness of the epitaxial layer. Therefore, based on the V_{BD} calculations, we can confirm that SiPM19-W3-TS-MP50NT and SiPM19-W3-TS-MP50-V1 have the same thickness of epitaxial layer. This result is as expected since these devices are coming from the same Si wafer. Moreover, the SiPM20-W4-50NT-NonP device should have a thinner epitaxial layer with respect to SiPM20-W5-50NT-NonP, this result being in good agreement with the information given by producer: the epitaxial layer thicknesses of SiPM20-W4-50NT-NonP is 2 µm while of SiPM20-W5-50NT-NonP is 2.4 µm.

For the Hamamatsu SiPM devices we can observe that the device (S10931-050P) from 2011 year production run shows a V_{BD} of 18 ÷ 20 V higher than V_{BD} calculated for the devices (S13082-050CS(X) and S13360-3050CS) from 2015 year production run, over full T range. In the same time, the S13082-050CS(X) shows only a V_{BD} ~1 V higher with respect to S13360-3050CS device. Even without any information from the producer about the structural parameters but using the reasons already described in the previous paragraph, we can conclude that the difference between of the epitaxial layer thickness of various 2015 Hamamatsu devices is very small, while this difference is bigger between 2015 and 2011 devices (e.g. the SiPM device from 2011 (S10931-050P) year production run has thicker epitaxial layer with respect to SiPM devices from 2015 year production run).

The variation between V_{BD} calculated for different devices can be also related to another technological parameters like: impurity concentration [54] or/and background doping's concentration [53]. However, we have related this V_{BD} variation to different thicknesses of epitaxial layers because these differences will be confirmed by $C_{\mu cell}$ calculation reported in the Section 3.4.3 "$C_{\mu cell}$ *vs.* T".

The variation of V_{BD} with T presented in the Figure 3.54 and Figure 3.55 allow the calculation of $\frac{dV_{BD}}{dT}$ temperature coefficients, values that are reported directly in the plots. Similar to the FBK devices reported in the Section 2.2.5.e "V_{BD} *vs.* T", the V_{BD} shows a linear behavior with T down to 200 K, whereas a non-linear behavior is visible below 200 K. Therefore, for each Hamamatsu SiPM device measured below 200 K, two $\frac{dV_{BD}}{dT}$ have been reported in the plots, one for $T > 200$ K and another for $T < 200$ K.

The $\frac{dV_{BD}}{dT}$ temperature coefficients allow the calculation of SiPM G variation with T when V_{bias} is kept constant as following:

$$\frac{G(T+\Delta T)}{G(T)} = \frac{C_{\mu cell} \times \Delta V(T+\Delta T)}{e^-} \times \frac{e^-}{C_{\mu cell} \times \Delta V(T)} = \frac{V_{bias} - V_{BD}(T+\Delta T)}{\Delta V(T)} = \frac{V_{bias} - V_{BD}(T) + \frac{dV_{BD}}{dT}\Delta T}{\Delta V(T)} = 1 + \frac{dV_{BD}}{dT} \times \frac{\Delta T}{\Delta V(T)} \quad 3.52$$

where $G(T)$ and $G(T+\Delta T)$ – are the SiPM gain at the temperature T and $T + \Delta T$, $\Delta V(T)$ – is the initial operating overvoltage and $\Delta V(T+ \Delta T)$ – is the overvoltage after temperature increase from T to $T + \Delta T$. From the Eq. 3.52 we can observe that the variation of the SiPM G with T at a given V_{bias} depends on initial operating overvoltage. Therefore, the variation of studied SiPM devices G with T at different initial overvoltages (i.e. ΔV = 1V, 2 V, 4 V, 6 V and 8 V) is presented in Table 3.2. Since the variation of V_{BD} with T is linear only down to ~200 K, the results for Hamamatsu SiPM devices are presented by two numbers: the first one for T range below 200 K and the second one for the T range above 200 K. We can observe that the variation of G with at a given V_{bias} is much more significant at low ΔV.

Devices		$\frac{100\%}{\Delta T} \times \frac{G(T+\Delta T)}{G(T)}\Big\|_{\Delta T=1K}$				
		ΔV = 1V	ΔV = 2V	ΔV = 4V	ΔV = 6V	ΔV = 8V
KETEK	SiPM19-W3-TS-MP50NT	2	1	0.5	0.3	0.3
	SiPM19-W3-TS-MP50-V1	1.9	1	0.5	0.3	0.2
	SiPM20-W4-50NT	2.8	1.4	0.7	0.5	0.4
	SiPM20-W5-50NT	3.5	1.8	0.9	0.6	0.4
HPK	S10931-050P	3.9 ÷ 5.5	2 ÷ 2.8	-	-	-
	S13082-050CS(X)	3.3 ÷ 5.7	1.7 ÷ 2.9	0.8 ÷ 1.4	0.55 ÷ 1	0.4 ÷ 0.7
	S13360-3050CS	3.3 ÷ 5.7	1.7 ÷ 2.9	0.8 ÷ 1.4	0.55 ÷ 1	0.4 ÷ 0.7

Table 3.2 The variation of SiPM gain with T if the V_{bias} is kept constant

The breakdown voltage calculated from DC measurements $V_{BD\text{-}DC\text{-}2d}$ (for more details see the Section 2.2.2.b "Reverse IV characteristic") are also presented in Figure 3.54 a) and b) for KETEK devices and in Figure 3.55 for Hamamatsu SiPM devices. We can observe a difference between V_{BD} and $V_{BD\text{-}DC\text{-}2d}$ which ranges from ~10 mV up to 600 mV. Therefore, the fast and simple inverse logarithmic derivative method should be used with precaution, since the $V_{BD\text{-}DC\text{-}2d}$ can contain systematic errors with respect to the absolute value of V_{BD}. Moreover, the *IV physical model* describing the shape of the IV curves over full working range of various SiPM`s devices has been developed to take an advantages of IV measurements (e.g. fast and simple) to determine the breakdown voltage precisely.

3.4.3.c. G vs. ΔV vs. T

The G as a function of ΔV for KETEK and Hamamatsu SiPM devices is presented in Figure 3.56 and Figure 3.57 respectively. At a given T, the G increases linearly with ΔV, as already described by Eq. 2.24. At a given ΔV, it can be observed that G is almost constant independent of T, presenting a variation from ~1% to ~6%. These small variations over the wide range of T used in our measurements (i.e. 70 K and 220 K for KETEK and Hamamatsu devices respectively) probably reflect the systematic errors of the analysis procedure and are related to the variation of the pulse shapes and the external noise with T. This is attested also by the fact that $C_{\mu cell}$ (i.e. slope of G vs. ΔV) shows no particular dependence with T, as will be shown in the following section.

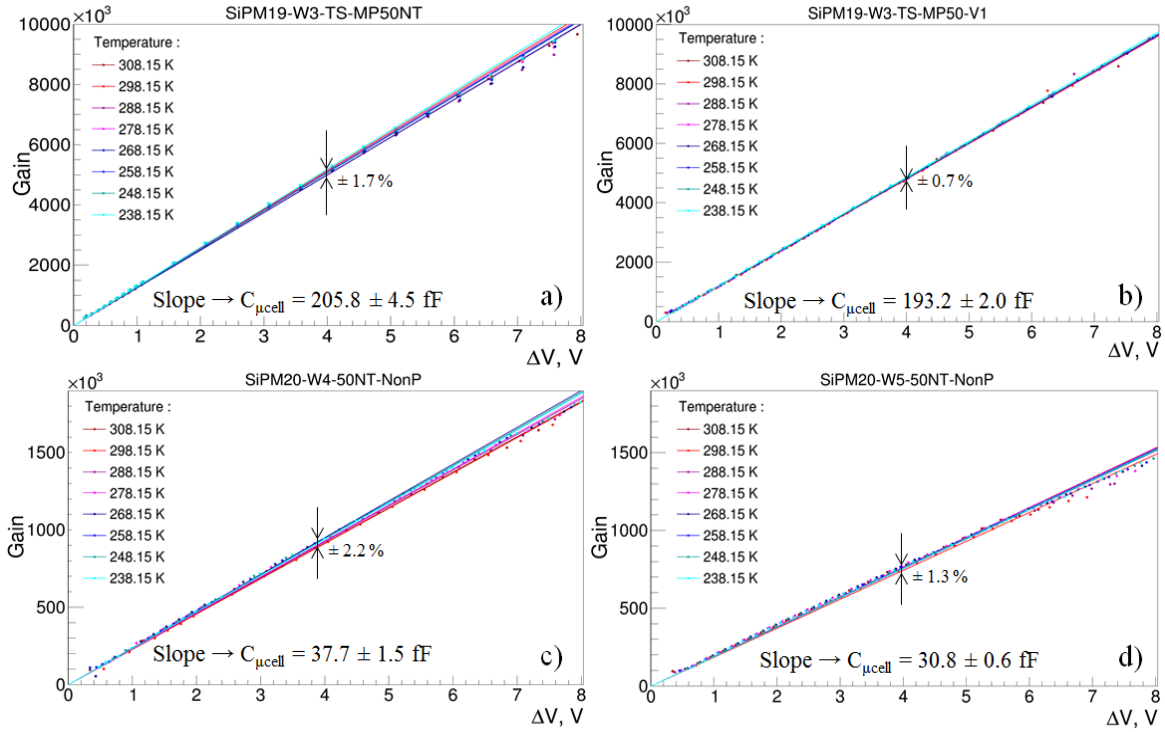

Figure 3.56 G vs. ΔV in the T range from 238.15 K to 308.15 K for KETEK SiPM devices: a) SiPM19-W3-TS-MP50NT, b) SiPM19-W3-TS-MP50-V1, c) SiPM19-W4-50NT-NonP and d) SiPM19-W5-50NT-NonP

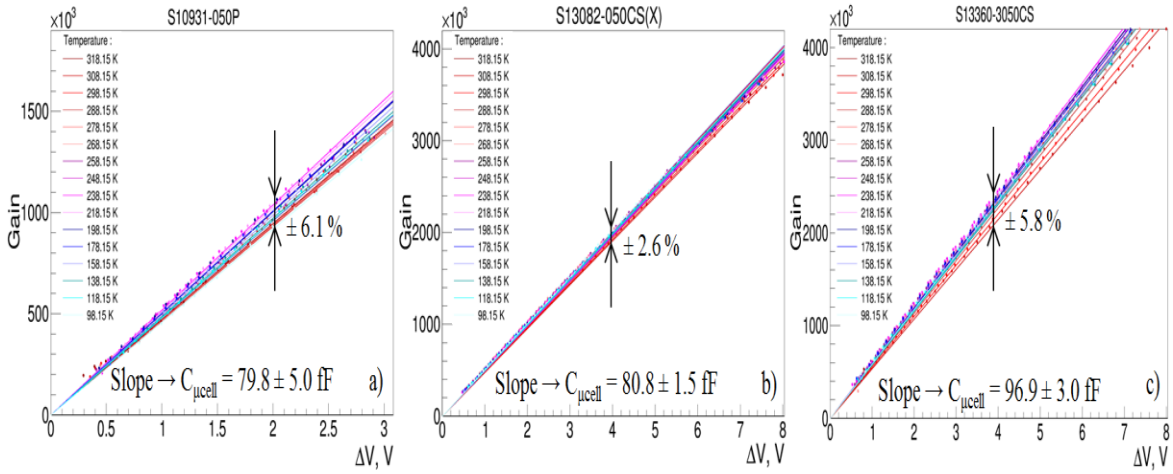

Figure 3.57 G vs. ΔV in the T range from 238.15 K to 308.15 K for Hamamatsu SiPM devices a) S10931-050P, b) S13082-050CS(X) and c) S13360-3050CS

3.4.3.d. $C_{\mu cell}$ vs. T

The $C_{\mu cell}$ of various KETEK and Hamamatsu SiPM devices was calculated from the slope of the linear fits presented in Figure 3.56 and Figure 3.57 and its T dependence is presented in the Figure 3.58 (a and b) and Figure 3.59. We can observe that $C_{\mu cell}$ does not depend on T and has a value of 30.8 fF for KETEK SiPM20-W5-50NT-NonP and 205.8 fF for KETEK SiPM19-W3-TS-MP50NT. The $C_{\mu cell}$ is related to µcell geometry, through the plan parallel capacitance equation:

$$C = \varepsilon_0 \cdot \varepsilon_{Si} \times \frac{A}{d} \qquad 3.53$$

where $\varepsilon_0 = 8.854 \times 10^{-14}$ F/cm – is the permittivity of the free space, $\varepsilon_{Si} = 11.9$ – is the silicon dielectric constant, A – is the active area and d – is the depletion thickness of µcell. The overall µcell area (i.e. pitch) of all measured devices is 50 × 50 µm^2 (for more details see the Section 3.2 "Measured devices & measurements conditions"). In first approximation we can assume that all measured devices have the same A. Even if there is some difference between the A of measured SiPM devices, this difference should be in order of only few %. Therefore, the difference between $C_{\mu cell}$ of measured devices can be related to µcell depletion thickness d.

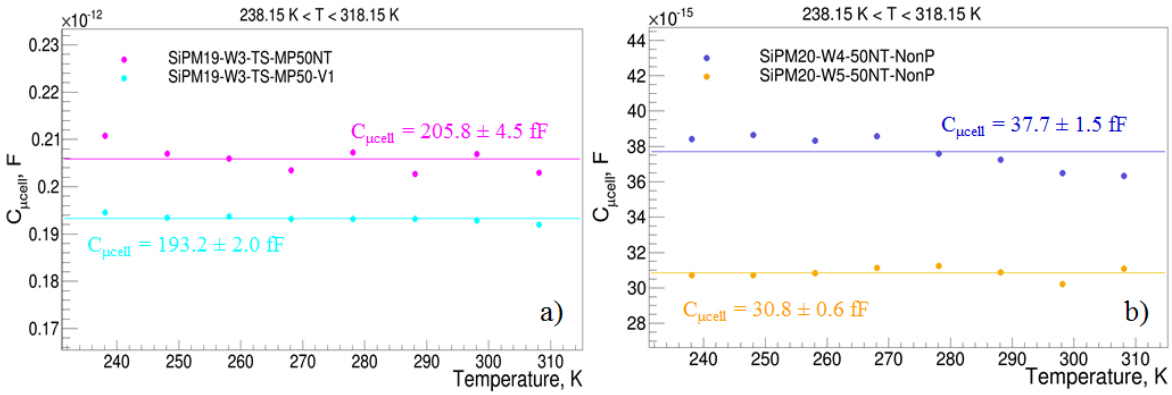

Figure 3.58 The $C_{\mu cell}$ vs. T for KETEK SiPM devices with a) P-on-N structure and b) N-on-P structure

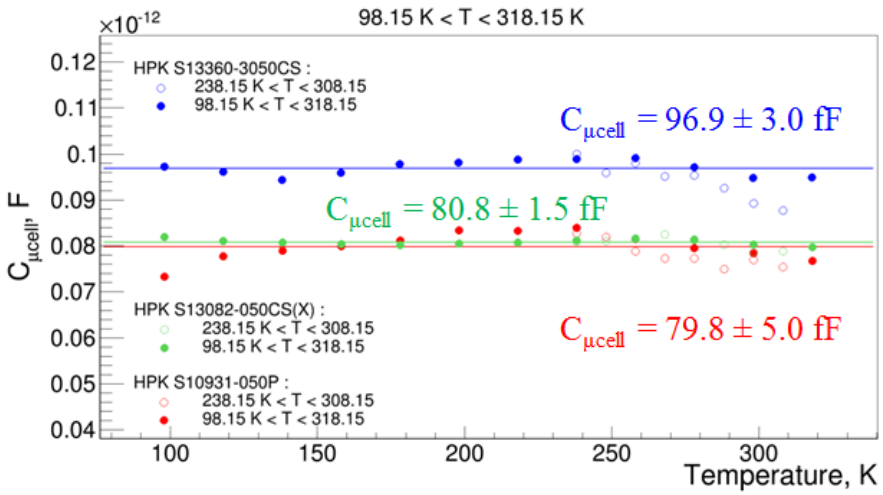

Figure 3.59 The $C_{\mu cell}$ vs. T for Hamamatsu SiPM devices

Assuming that KETEK devices with N-on-P structure (SiPM20-W4-50NT-NonP and SiPM20-W5-50NT-NonP) have equal *A*, we can obtain the relationship between their *d* from the Eq. 3.53 as:

$$d_5 = \frac{C_4}{C_5} \times d_4 = 1.22 \times d_4 \qquad 3.54$$

where d_5 and C_5 – are the depletion thickness and $C_{\mu cell}$ of SiPM20-W5-50NT-NonP and d_4 and C_4 – are the depletion thickness and $C_{\mu cell}$ of SiPM20-W4-50NT-NonP. From the Eq. 3.54 we can conclude that SiPM20-W5-50NT-NonP device has 22% wider depletion thickness. This observation is in good agreement with the information given by producer, the SiPM20-W4-50NT-NonP device having an epi-layer of 2.0 µm thickness, while the SiPM20-W5-50NT-NonP device has an epi-layer of 2.4 µm thickness (20% higher).

Knowing the $C_{\mu cell}$ and epi-layer thickness for SiPM20-W4-50NT-NonP and SiPM20-W5-50NT-NonP devices we can check if the classical Eq. 3.53 describes the values of $C_{\mu cell}$ by assuming that:

- active area *A* is equal to overall µcell area (i.e. pitch). Therefore $A = 50 \times 50\ \mu m^2$;
- thickness of depletion region *d* is equal to epi-layer thickness.

Therefore, for SiPM20-W4-50NT-NonP device:

$$C_{\mu cell} = \varepsilon_0 \cdot \varepsilon_{Si} \times \frac{A}{d} = 8.854 \times 10^{-14}\ F/cm \times 11.9 \times \frac{50 \times 50 \mu m^2}{2 \mu m} = 131.7\ fF \qquad 3.55$$

And for SiPM20-W5-50NT-NonP device:

$$C_{\mu cell} = \varepsilon_0 \cdot \varepsilon_{Si} \times \frac{A}{d} = .854 \times 10^{-14}\ F/cm \times 11.9 \times \frac{50 \times 50 \mu m^2}{2.4 \mu m} = 109.8\ fF \qquad 3.56$$

We can observe that the values of $C_{\mu cell}$ calculated from the Eq. 3.55 and Eq. 3.56 are overestimated with respect the values calculated from the experimental results (from the slope of the linear fits of *G* vs. ΔV). To find the reason of such disagreement, the active area of SiPM20-W4-50NT-NonP and SiPM20-W5-50NT-NonP has been checked with the

microscope. The photos of these two devices done with the microscope are presented in Figure 3.60 (a and b). We can observe that the both devices have 20 × 20 = 400 µcells on a total area of 0.5 × 0.5 mm^2. Therefore, we can conclude that the producer did a typo on device labels and that both SiPM20-W4-50NT-NonP and SiPM20-W5-50NT-NonP devices have 25 × 25 µm^2 µcell size. As a result, the Eq. 3.55 and Eq. 3.56 will be transformed into:

$$C_{\mu cell} = \varepsilon_0 \cdot \varepsilon_{Si} \times \frac{A}{d} = 8.854 \times 10^{-14} \, F/cm \times 11.9 \times \frac{25 \times 25 \mu m^2}{2 \mu m} = 32.9 \, fF \qquad 3.57$$

for SiPM20-W4-50NT-NonP device and for SiPM20-W5-50NT-NonP device:

$$C_{\mu cell} = \varepsilon_0 \cdot \varepsilon_{Si} \times \frac{A}{d} = 8.854 \times 10^{-14} \, F/cm \times 11.9 \times \frac{25 \times 25 \mu m^2}{2 \mu m} = 27.4 \, fF \qquad 3.58$$

We can observe that the values of $C_{\mu cell}$ calculated from the Eq. 3.57 and Eq. 3.58 is smaller by ~12% than the one obtained from experimental measurements. This difference can be related to our assumptions which were done previously. In particular, for real SiPM devices:

- the active area A is smaller than µcell size, due to dead area (for more details see the Chapter 2, Section 2.2.4.b "Geometrical fill factor (ε)");
- in the case of $n^+/p/\pi/p^+$ structure (See Figure 2.16), the depletion region is generated by electrical field between n^+ and p^+ layers. Therefore, the thickness of depletion region d is around few hundreds of nm thinner than epi-layer due to thickness of n^+ region (more details will be given in Annex 3 – Numerical TCAD C-V simulation).

Therefore, we can conclude that the Eq. 3.53 *describes precisely the values of* $C_{\mu cell}$*, especially if the geometrical fill factor* ε *is known.*

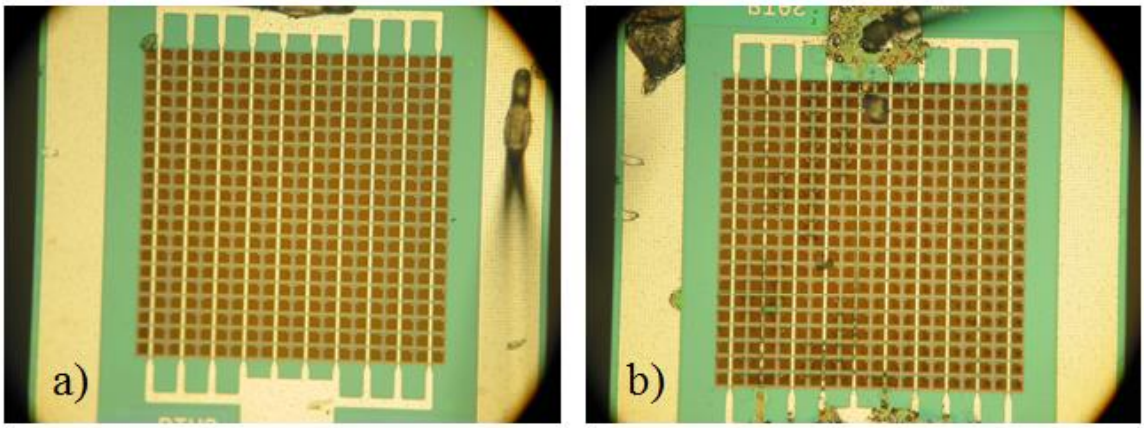

Figure 3.60 Microscope photos of KETEK SiPM devices a) SiPM20-W4-50NT-NonP and b) SiPM20-W5-50NT-NonP

The small difference of ~6 % between the $C_{\mu cell}$ calculated for the KETEK devices with P-on-N structure with and without trenches (SiPM19-W3-TS-MP50NT and SiPM19-W3-TS-MP50-V1) can be related to a difference between their A, because the SiPM19-W3-TS-MP50-V1 has a trench technology which decreases the A (as it was already discussed in the Section 2.2.3.e "*Optical cross-talk*"). However, one can argue that trench technology introduces an additional capacitance due to their metalized trenches between µcells, therefore SiPM19-W3-TS-MP50-V1 should have bigger $C_{\mu cell}$ with respect to SiPM19-W3-TS-MP50NT device, what was not observed in our measurements. This contradiction is related to the fact that trench

technology adds a parasitic grid capacitance C_g (see the equivalent circuit of the SiPM in Figure 2.23). The C_g does not take part to avalanche multiplication; therefore it cannot be measured from the slope of G vs. ΔV. However C_g can be seen on CV measurements.

From $C_{\mu cell}$ calculated for the KETEK devices with P-on-N structure with and without trenches (SiPM19-W3-TS-MP50NT and SiPM19-W3-TS-MP50-V1) we can calculate the width of depleted region d which from the Eq. 3.53 as:

$$d = \varepsilon_0 \cdot \varepsilon_{Si} \times \frac{A}{C_{\mu cell}} = 8.854 \times 10^{-14} \, F/cm \times 11.9 \times \frac{50 \times 50 \mu m^2}{205.8 fF} = 1.3 \mu m \qquad 3.59$$

As it was already mentioned above, the d is slightly smaller than epi-layer thickness. Therefore, we can expect that KETEK devices with P-on-N structure with and without trenches (SiPM19-W3-TS-MP50NT and SiPM19-W3-TS-MP50-V1) have a *thickness of epi-layer of ~1.4 µm.*

Even if we do not have enough information from the producer about the Hamamatsu devices (e.g. true active area, trenches, depth of the epi-layer, etc.) we can calculate the d from these devices from the values of their $C_{\mu cell}$.

The A of 38 × 38 µm^2 for the Hamamatsu S10931-050P has been measured by Dinu [60]. Therefore the d can be calculated as:

$$d = \varepsilon_0 \cdot \varepsilon_{Si} \times \frac{A}{C_{\mu cell}} = 8.854 \times 10^{-14} \, F/cm \times 11.9 \times \frac{38 \times 38 \mu m^2}{79.8 fF} = 1.9 \mu m \qquad 3.60$$

We can expect that Hamamatsu S10931-050P has a *thickness of epi-layer of ~2 µm.*

The Hamamatsu S13082-050CS(X) and S13360-3050CS devices have a geometrical fill factors ε of 61% and 74% respectively, as indicated in Hamamatsu datasheets. Therefore, the S13082-050CS(X) device has A = 0.61 × 50 × 50 µm^2, and the d of:

$$d = \varepsilon_0 \cdot \varepsilon_{Si} \times \frac{A}{C_{\mu cell}} = 8.854 \times 10^{-14} \, F/cm \times 11.9 \times \frac{0.61 \times 50 \times 50 \mu m^2}{80.8 fF} = 2 \mu m \qquad 3.61$$

We can expect that Hamamatsu S13082-050CS(X) has a *thickness of epi-layer of ~2.1 µm.*

And the S13360-3050CS device has A = 0.74 × 50 × 50 µm^2, and the d of:

$$d = \varepsilon_0 \cdot \varepsilon_{Si} \times \frac{A}{C_{\mu cell}} = 8.854 \times 10^{-14} \, F/cm \times 11.9 \times \frac{0.74 \times 50 \times 50 \mu m^2}{96.9 fF} = 2 \mu m \qquad 3.62$$

We can expect that Hamamatsu S13360-3050CS has also a *thickness of epi-layer of ~2.1 µm.*

The cumulative results are presented in Table 3.3.

Devices		thickness of epi-layer (µm)
KETEK	SiPM19-W3-TS-MP50NT	1.4
	SiPM19-W3-TS-MP50-V1	1.4
	SiPM20-W4-50NT	2.0

	SiPM20-W5-50NT	2.4
Hamamatsu	S10931-050P	2.0
	S13082-050CS(X)	2.1
	S13360-3050CS	2.1

Table 3.3 Thickness of epi-layers of KETEK and Hamamatsu SiPM devices

3.4.3.e. Signal amplitude vs. V_{bias} vs. T

The 1 p.e. amplitude as a function of V_{bias} for four KETEK devices in a T range from 238.15 K to 308.15 K is presented Figure 3.61 a), b), c) and d), while the results from *first and second sets of measurements* for Hamamatsu SiPM devices are presented in Figure 3.62 a), b) and c). We can observe that for a given T, the 1 p.e. amplitude increases linearly with V_{bias}. However, the slope of increase is changing with T, so 1 p.e. amplitude increases faster with increasing V_{bias} at high T.

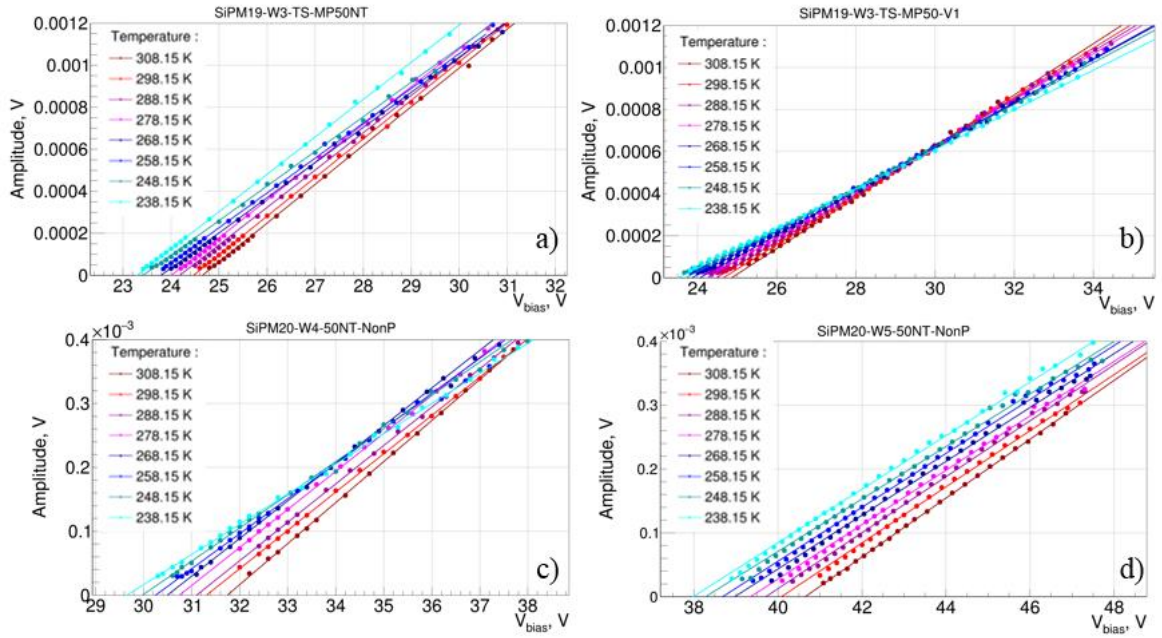

Figure 3.61 1 p.e. amplitude vs. V_{bias} in the T range from 238.15 K to 308.15 K for KETEK SiPM devices: a) SiPM19-W3-TS-MP50NT, b) SiPM19-W3-TS-MP50-V1, c) SiPM19-W4-50NT-NonP and d) SiPM19-W5-50NT-NonP

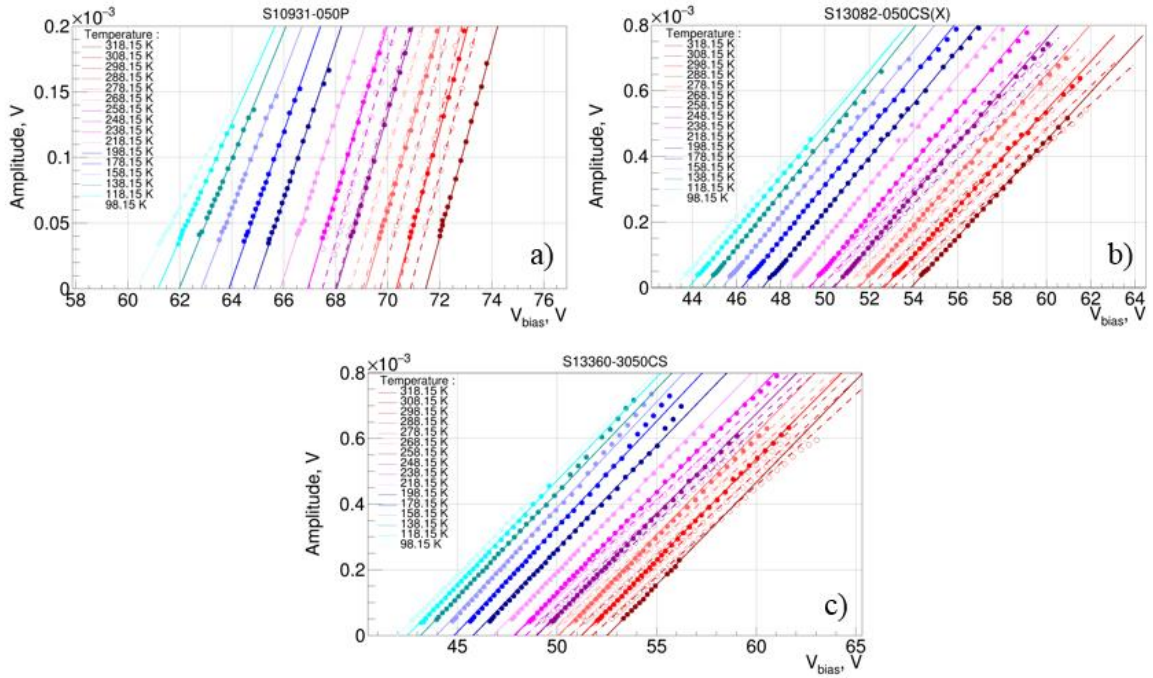

Figure 3.62 1 p.e. amplitude vs. V_{bias} in the T range from 98.15 K to 318.15 K for Hamamatsu SiPM devices: a) S10931-050P, b) S13082-050CS(X) and c) S13360-3050CS. The results from *first set of measurements* are presented by open dots and dashed lines, while the results from *second set of measurements* are presented by closed dots and solid lines

3.4.3.f. DCR vs. ΔV vs. T

As it was already mentioned in the Section 3.2 " Measured devices & measurements conditions", the data acquisition was triggered by the laser trigger signal positioned at 1.55 µs later with respect to the waveform beginning. Therefore, during this 1.55 µs, each device has been operated in dark conditions and this time interval has been used to calculate the dark count rate *DCR*. It has been calculated for all devices in *T* range from 308.15 K down to 248.15 K by using the Eq. 3.51. The *DCR* calculated for KETEK and Hamamatsu SiPM devices is presented in Figure 3.63 (a, b, c and d) and Figure 3.64 (a, b and c) respectively. We can observe poor precision of *DCR* calculation below ~10 kHz due to low statistics.

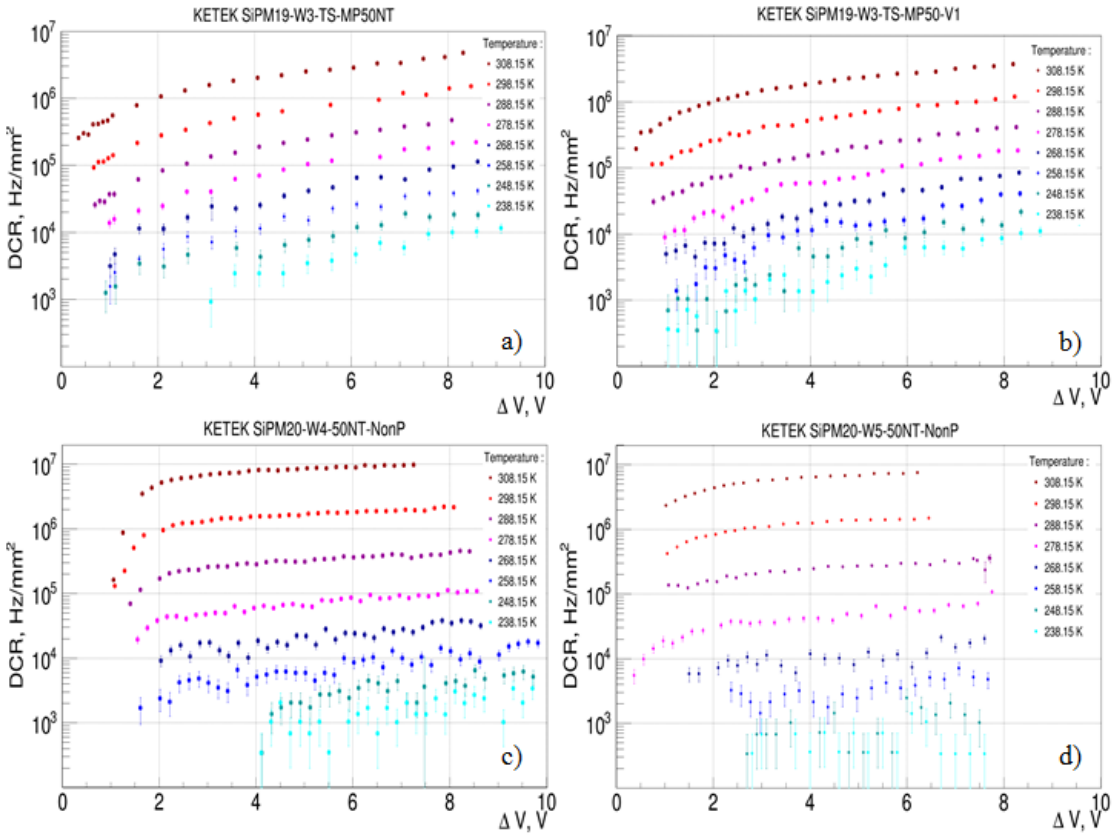

Figure 3.63 DCR vs. ΔV in the T range from 238.15 K to 308.15 K for KETEK SiPM devices: a) SiPM19-W3-TS-MP50NT, b) SiPM19-W3-TS-MP50-V1, c) SiPM19-W4-50NT-NonP and d) SiPM19-W5-50NT-NonP

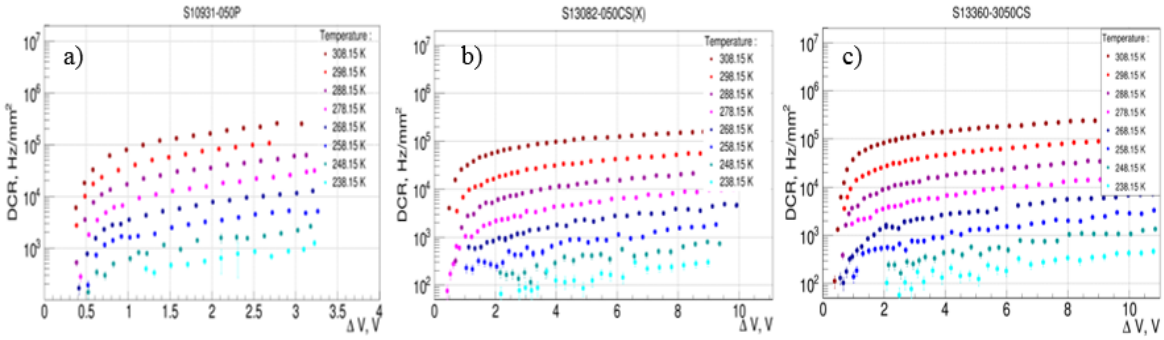

Figure 3.64 DCR vs. ΔV in the T range from 238.15 K to 308.15 K for Hamamatsu SiPM devices: a) S10931-050P, b) S13082-050CS(X) and c) S13360-3050CS

To calculate the *DCR* below ~10 kHz an additional type of measurements was performed. During these measurements the SiPM devices were operated in dark conditions. The data acquisition was triggered by the Tektronix TDS5054 oscilloscope if the SiPM signal amplitude is exceeding a given threshold value. This threshold value has been set to 0.5 p.e. SiPM pulse amplitude. The *DCR* has been calculated as:

$$DCR = \frac{1}{< t >} \qquad 3.63$$

where <*t*> – is the average time interval between two neighboring triggered events. To ensure a fast acquisition rate and measure high values of *DCR*, the oscilloscope has been operated in

fast acquisition mode (see Tektronix operating manual [67]). This mode should allow acquisition of up to 10^5 waveforms per second, therefore to measure *DCR* up to 100 KHz. Hoverer, it has been found that the dead time of data taking acquisition starts to be significant if $<t>$ is less than 0.1 ms (i.e. *DCR* = 10 KHz). Therefore, such method can be used to determine the *DCR* only up to 10 KHz.

The comparison between *DCR* calculated from the Eq. 3.51 (from Poisson statistics) and from the Eq. 3.63 (additional measurements with Tektronix TDS5054 oscilloscope) corresponding to Hamamatsu S13360-3050CS device is presented in Figure 3.65. A good agreement is observed between the two methods below 2 KHz, while above this value the *DCR* calculated from Eq. 3.63 (rectangles) starts to saturate for the reasons described above. Therefore, the *DCR* of Hamamatsu SiPM devices has been calculated from both methods: from the Eq. 3.63 to *DCR* below 2 KHz and from the Eq. 3.51 to *DCR* above 2 KHz. The results are presented in Figure 3.66, Figure 3.67 and Figure 3.68.

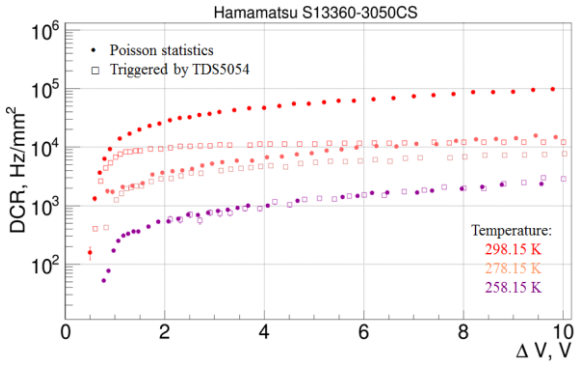

Figure 3.65 Comparison between DCR calculated from Poisson statistics (dots) and from additional measurements with Tektronix TDS5054 oscilloscope (rectangles). The calculations were done for Hamamatsu S13360-3050CS device at three T: 258.15 K, 278.15 K and 298.15 K

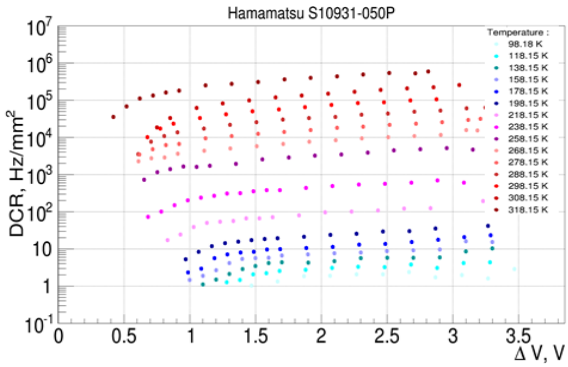

Figure 3.66 DCR vs. ΔV in the T range from 98.15 K to 318.15 K for Hamamatsu S10931-050P SiPM device

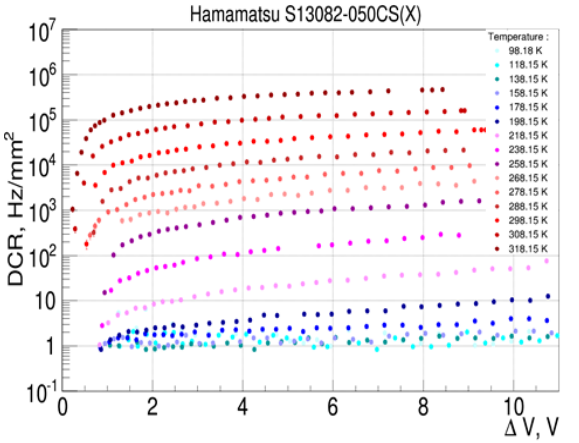

Figure 3.67 DCR vs. ΔV in the T range from 98.15 K to 318.15 K for Hamamatsu: S13082-050CS(X) SiPM device

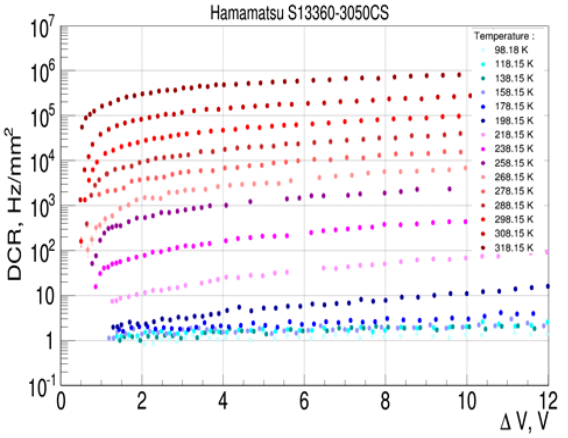

Figure 3.68 DCR vs. ΔV in the T range from 98.15 K to 318.15 K for Hamamatsu S13360-3050CS SiPM device

For all KETEK and Hamamatsu SiPM devices we can observe that at a given ΔV, the *DCR* increases with *T* over many orders of magnitude.

The *DCR* at ΔV = 2 V, 4 V, 6 V and 8 V as a function of *T* are presented in Figure 3.69 a), b), c) and d) respectively. Because of shorter working range, the results for Hamamatsu S10931-050P device are presented only at ΔV = 2 V, for the same reason the results for KETEK SiPM20-

W5-50NT are not presented at ΔV = 8 V. We can observe that at a given T, the Hamamatsu SiPM devices show lower *DCR* per unit of area than devices produced by KETEK.

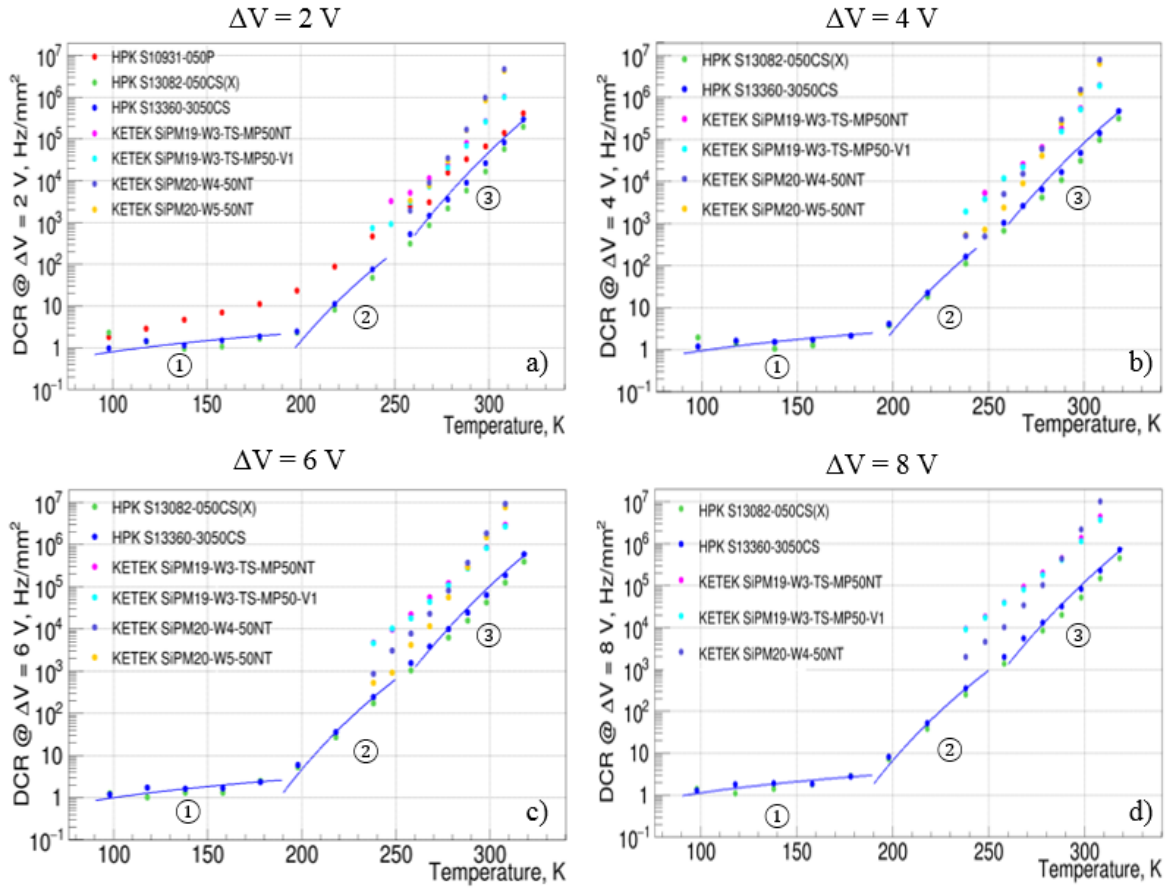

Figure 3.69 DCR at ΔV = 2 V, 4 V, 6 V and 8 V as a function of temperature for the Hamamatsu HPK and KETEK SiPM devices . The DCR vs. has been fitted by Eq. 3.64 in different T regions: (1) 98.15 K < T < 178.15 K; (2) 198.15 K < T < 248.15 K and (3) 258.15 K < T < 318.15 K. As an example, the fit functions are presented for Hamamatsu S13360-30CS

As it was already discussed in the Chapter 2, Section 2.2.5.f "*DCR vs. T*", the temperature variation of the *DCR* at a given ΔV is related to the temperature variation of the generation current $I_{generation}$ given by Eq. 2.49. Therefore, the *DCR* at a given $\Delta V = Const.$ as a function of T has been fitted with a form:

$$DCR(T, \Delta V = Const.) = A \cdot T^{3/2} \cdot \exp\left(-\frac{E_{act}}{k_B T}\right) \qquad 3.64$$

where A and E_{act} – have been set as fit free parameters. The fit has been performed in three different regions:

- *low T range* from 98.15 K up to 178.15 K;
- *middle T range* from 198.15 K up to 248.15 K;
- *high T range* from 258.15 K up to 318.15 K.

The E_{act} corresponding to each region has been determined from fit at ΔV = 2 V, 4 V, 6 V and 8 V and the average $\langle E_{act} \rangle$ is presented in the Table 3.4.

Devices		<E_{act}> (eV)		
		low T range (98.15K<T<178.15K)	middle T range (198.15K<T<248.15K)	high T range (258.15K<T<318.15K)
KETEK	SiPM19-W3-TS-MP50NT	Not measured	0.446 ± 0.028	0.707 ± 0.006
	SiPM19-W3-TS-MP50-V1		0.434 ± 0.044	0.697 ± 0.009
	SiPM20-W4-50NT		0.641 ± 0.175	1.047 ± 0.007
	SiPM20-W5-50NT		0.644 ± 0.047	1.049 ± 0.006
HPK	S10931-050P	0.023	0.332	0.663
	S13082-050CS(X)	$(0.25 \pm 0.28)\cdot 10^{-3}$	0.377 ± 0.011	0.739 ± 0.01
	S13360-3050CS	8.6×10^{-5}	0.398 ± 0.004	0.733 ± 0.011

Table 3.4 Average activation energy <E_{act}> calculated for the KETEK and Hamamatsu HPK SiPM devices

From the results presented in Table 3.4 we can mention that:

- *high T range (T > 258.15 K)*, the dominated source of DCR for KETEK N-on-P devices (SiPM20-W4-50NT and SiPM20-W5-50NT) is expected to be carrier injection from neutral region, while for all other devices (both KETEK and Hamamatsu P-on-N) the main source of *DCR* is expected to be a combination between the Shockley-Read-Hall carrier generation and injection from neutral region;
- *middle T range (198.15 K <T < 258.15 K)*, the main source of *DCR* for the SiPM20-W4-50NT and SiPM20-W5-50NT devices is expected to be a combination between the Shockley-Read-Hall generation and injection from neutral region, while for another two KETEK devices (SiPM19-W3-TS-MP50NT and SiPM19-W3-TS-MP50-V1) the main source of *DCR* is expected to be the Shockley-Read-Hall generation enhanced to some extent by trap-assisted tunneling. For the SiPM devices produced by Hamamatsu the main source of *DCR* in this *T* region is expected to be the trap-assisted tunneling;
- *low T range (T < 178.15 K)*, the main source of *DCR* for the SiPM devices produced by Hamamatsu is expected to be the Band-to-band tunneling, which has a weak dependence on *T*.

3.4.3.g. Optical cross-talk vs. ΔV vs. T

The optical cross-talk probability P_{XT} has been calculated from the measurements done for *DCR* calculation (has been described in the previous section). At a given *T* and V_{bias} the P_{XT} has been calculated as:

$$P_{XT} = 100\% \times \frac{N_{1.5\,p.e}}{N_{0.5\,pe}} \qquad 3.65$$

where $N_{0.5p.e.}$ and $N_{1.5.p.e.}$ – are the number of SiPM signals with amplitude exceeding 0.5 p.e. and 1.5 p.e. amplitudes respectively. The P_{XT} as a function of ΔV calculated in the *T* range from 298.15 K down to 98.15 K for SiPM devices produced by Hamamatsu is presented in Figure 3.70 (a, b and c). We can observe that in range of our systematic errors the P_{XT} is remained independent of *T* for all three measured SiPM devices in *T* range from 298.15 K down to

98.15 K. Also, we can conclude that P_{XT} has been significantly reduced in SiPM devices from 2015 production run with respect to the device from 2011 year production run. In particular, from P_{XT} = ~20% at ΔV = 2 V for the S10931-050P device down to ~2.5% and ~1.4% for the S3360-3050CS and S13082-050CS(X) devices respectively at the same ΔV.

The obtained results are in good agreement with information given in Hamamatsu datasheets. In particular, in Hamamatsu datasheets we can find the P_{XT} = 3% at ΔV = 3 V for S13082-050CS(X) and S13360-3050CS devices, and in our measurements we found P_{XT} of 2.9% and 4% respectively for those devices.

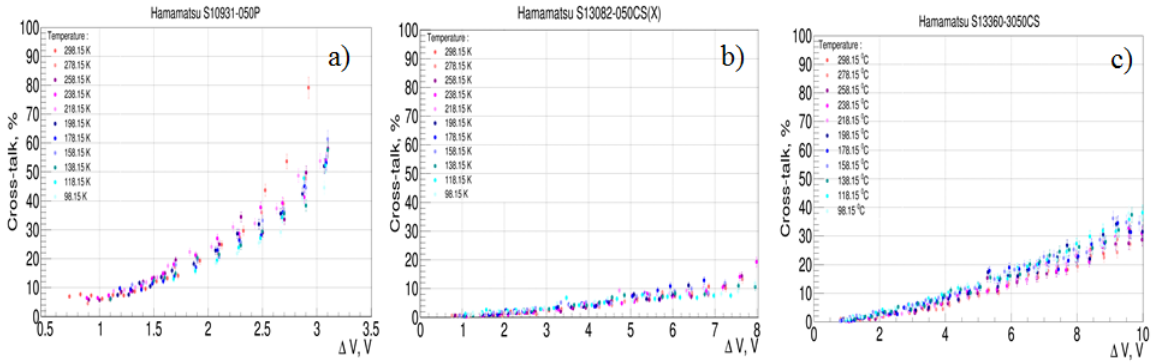

Figure 3.70 Optical cross-talk probability vs. V_{bias} in the T range from 98.15 K to 298.15 K for SiPM devices produced by Hamamatsu: a) S10931-050P, b) S13082-050CS(X) and c) S13360-3050CS

3.4.3.h. P_{Geiger} vs. ΔV vs. T

The Geiger probability $P_{Geiger\text{-}AC}$ can be calculated by using the Eq. 3.50. However, the absolute scale of the $P_{Geiger\text{-}AC}$ is not known since we do not know the average number of photons $<n_{laser}>$ illuminating the SiPM. As it was already shown in the Section 2.2.4 "Triggering probability (P_{Geiger})", we can expect that, at a given V_{bias}, the $P_{Geiger\text{-}AC}$ reaches the plateau at its maximum value $P_{plateau}$. Therefore, we have normalized the $P_{Geiger\text{-}AC}$ to be 1 at the highest bias voltage at T = 298.15 K (independently of each device). The normalization was done by dividing P_{Geiger} values at all measured T and V_{bias} by $P_{plateau}$ at T = 308.15 K. The $P_{plateau}$ at T = 298.15 K has been determined from the parameterization of the $P_{Geiger\text{-}AC}$ as following:

$$P_{Geiger}(\Delta V) = P_{plateau} \times \left[1 - \exp(p \cdot \Delta V)\right] \qquad 3.66$$

where $P_{plateau}$ – is the value of $P_{Geiger\text{-}AC}$ at a plateau (maximum value), p – is the parameter depending on the SiPM design and composition of free carriers. After normalization, the $P_{Geiger\text{-}AC}$ was parameterized as:

$$P_{Geiger}(\Delta V) = 1 - \exp(p \cdot \Delta V) \qquad 3.67$$

The Figure 3.71 (a and b) shows the Geiger probability $P_{Geiger\text{-}AC}$ calculated from AC measurements (dots) as a function of ΔV measured at T = 298.15 K, with blue and red laser light. Moreover, the parameterization done using Eq. 3.67 is also shown (continuous lines), providing a good description of experimental data.

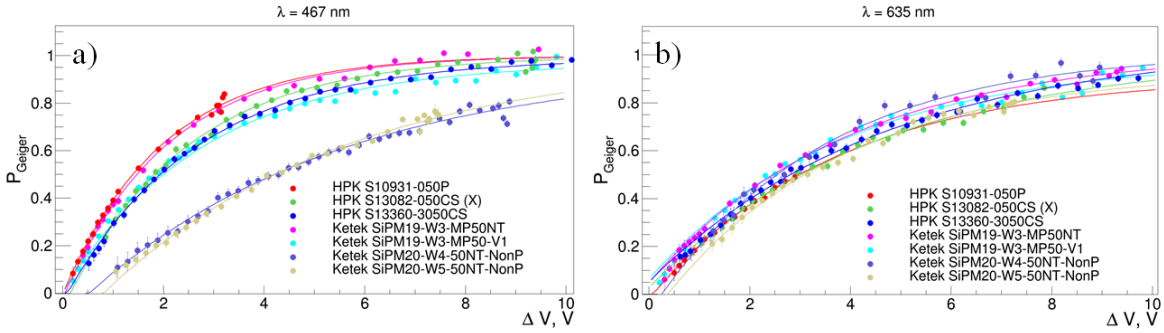

Figure 3.71 $P_{Geiger\text{-}AC}$ vs. ΔV at T = 298.15 K for various SiPM devices measured with a) blue λ = 467 nm and b) red λ = 635 nm laser light

The Figure 3.71 a) demonstrates that the KETEK devices with N-on-P structure (SiPM20-W4-50NT-NonP and SiPM20-W5-50NT-NonP) show smaller $P_{Geiger\text{-}AC}$ for blue light with respect to all other devices with P-on-N structure as has been expected from the Section 2.2.4 "Measurements of Photon Detection Efficiency". Also from the Figure 3.71 we can observe that the working range of the HPK S10931-050P device from 2011 year production run was too small to allow reaching the maximum of $P_{Geiger\text{-}AC}$, while the technology of 2015 devices, independent of the vendor, is greatly improved, allowing operation near the plateau of $P_{Geiger\text{-}AC}$.

Typical $P_{Geiger\text{-}AC}$ vs. ΔV of SiPM devices produced by KETEK at different T and measured with different wavelengths are presented in Figure 3.72 (the $P_{Geiger\text{-}AC}$ vs. ΔV of all other measured SiPM devices are given in the Annex 2 - PGeiger measurements). Independent of measured detector, we can observe that $P_{Geiger\text{-}AC}$ varies with T and this variation is different for different wavelengths. The $P_{Geiger\text{-}AC}$ at a given ΔV (ΔV = 2 V for S10931-050P device and ΔV = 4 V for all others devices) as a function of T is presented in Figure 3.73 (a ÷ d) and Figure 3.74 (a ÷ c) for the SiPM devices produced by KETEK and Hamamatsu respectively. By comparing the results for Hamamatsu devices from *two sets of measurements* (see Figure 3.74 open and close dots) we can observe that the laser intensity was not stable in time and was varying around ± 30%. Therefore, it is hard to conclude if the variation of $P_{Geiger\text{-}AC}$ with T is related to physics of SiPM or variation of laser intensity.

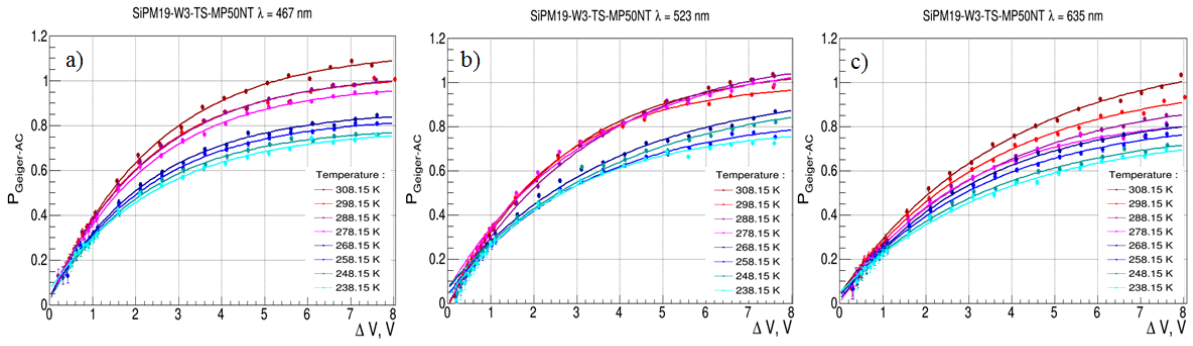

Figure 3.72 $P_{Geiger\text{-}AC}$ vs. ΔV at T range from 308.15 K down to 238.15 K for SiPM device produced by KETEK and measured with a) blue λ = 467 nm, b) green λ = 523 nm and c) red λ = 635 nm laser light

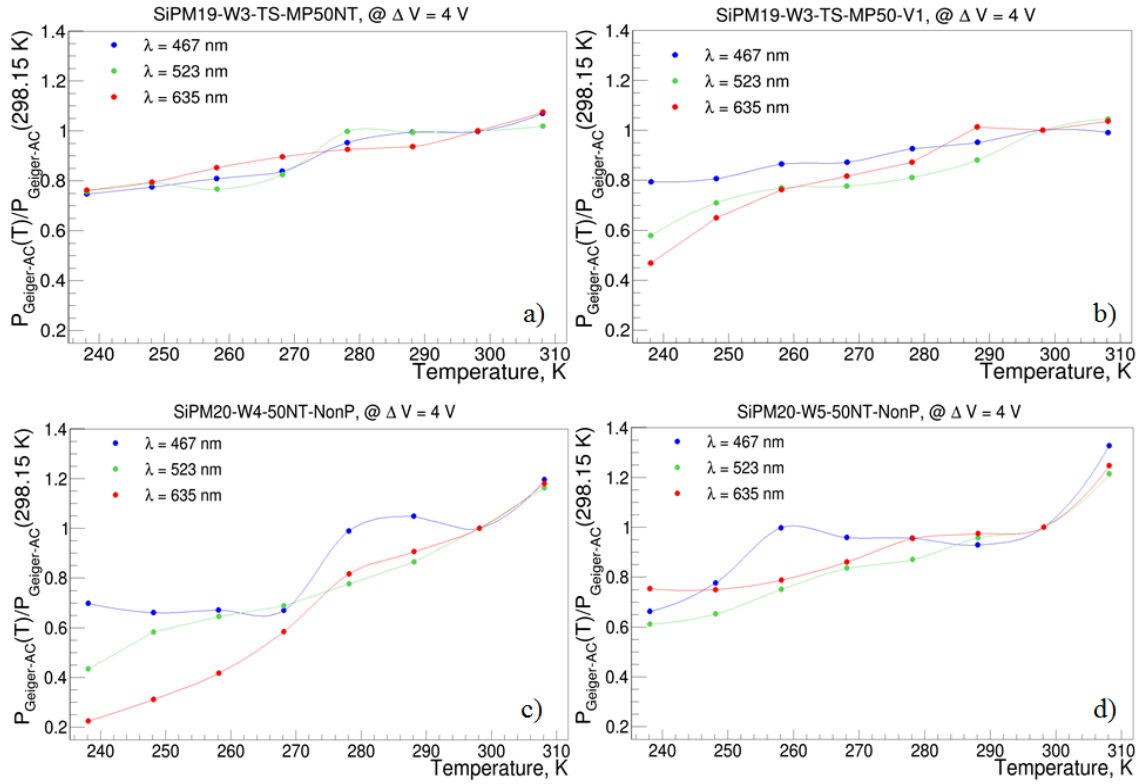

Figure 3.73 $P_{Geiger\text{-}AC}$ vs. T at ΔV = 4 V measured with blue λ = 467 nm, green λ = 523 nm and red λ = 635 nm laser light for SiPM devices produced by KETEK: a) SiPM19-W3-TS-MP50NT, b) SiPM19-W3-TS-MP50-V1, c) SiPM20-W4-50NT-NonP and c) SiPM20-W5-50NT-NonP. Each data set at fixed λ is normalized to the value at T = 298.15 K

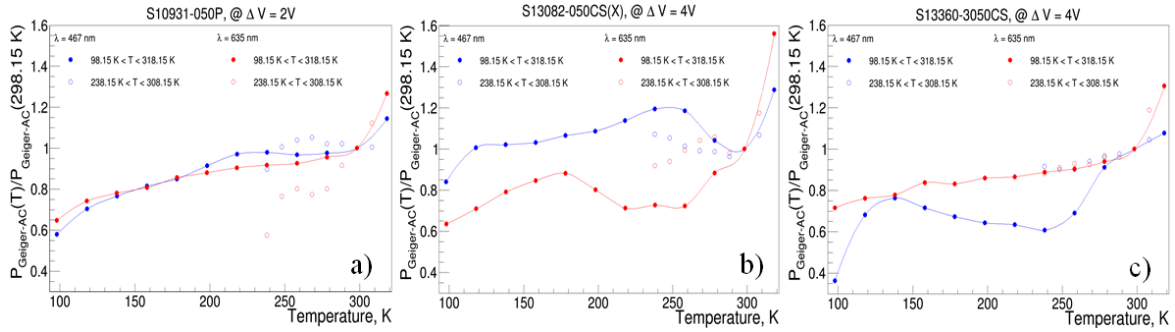

Figure 3.74 $P_{Geiger\text{-}AC}$ vs. T at a given ΔV (ΔV = 2 V for S10931-050P and ΔV = 4 V for S13082-050CS(X) and S13360-3050CS) measured with blue λ = 467 nm and red λ = 635 nm laser light for SiPM devices produced by Hamamatsu: a) S10931-050P, b) S13082-050CS(X) and c) S13360-3050CS. Each data set at fixed λ is normalized to the value at T = 298.15 K

3.5. Physical model of the reverse IV characteristic

As it was already shown in the Section 2.2.2.b "*Reverse IV characteristic*", the reverse IV characteristics has been already used in various works for fast V_{BD} calculation based on the inverse logarithmic derivative method. However, such calculation method should be used with precaution, since the corresponding result of $V_{BD\text{-}DC\text{-}2d}$ can contain systematic errors with respect to the absolute value of V_{BD}. To overcome this limitation, but also to determine other SiPM parameters such as working range and the shape of P_{Geiger}, an IV model based on various physical mechanisms contributing to the shape of the IV characteristic has been developed. In this Section, this model will be described in details.

For all temperatures and devices, the experimental IV curves have similar shapes as shown in the Figure 3.75, indicating several regimes of the bias voltage: (1) the "pre-breakdown" region below V_{BD} and (2) the "post-breakdown" region above V_{BD}, characterized itself by "just-above", "transition", "far-above" and "post-second breakdown" zones. Each region reflects different physical mechanisms, as explained in the following:

- The *"pre-breakdown"* region below breakdown voltage V_{BD}, where the current $I_{pre\text{-}BD}$ shows a relatively slow increase with the bias voltage; in this region, the current $I_{pre\text{-}BD}$ is given by the surface dark current (i.e. ionic impurities deposited on the surface during device fabrication) and the bulk dark current (i.e. Shockley-Read-Hall (SRH) thermal generated carrier`s enhanced by carriers from trap-assisted or band-to-band tunneling). We parameterize this component as:

$$I_{pre-BD}(V_{bias}) = \exp(a \cdot V_{bias} + b) \qquad 3.68$$

  This parameterization ignores the increase of the carrier-induced current due to increase of the gain with the bias voltage;

- The *"post-breakdown"* region above breakdown voltage V_{BD}, where the current $I_{post\text{-}BD}$ shows a fast increase with the bias voltage; as a function of the main contributing physical mechanisms, this region can be divided in few more zones:
  - *"just-above"* the breakdown voltage, where the current $I_{post\text{-}BD}$ is given predominantly by the bulk thermal generated carriers $dN_{carriers}/dt$, increasing with the bias voltage due to the gain and the Geiger probability P_{Geiger} as following

$$I_{post-BD}(V_{bias}) = C_{\mu cell} \times (V_{bias} - V_{BD}) \times \frac{dN_{carriers}}{dt} \times P_{Geiger} \qquad 3.69$$

    where V_{BD} – is the breakdown voltage and $C_{\mu cell}$ – is the μcell capacitance. In this region P_{Geiger} is the primary factor determining the shape of the IV curve, while the afterpulsing is negligible and following McIntyre [68] it can be parameterized as:

$$P_{Geiger}(V_{bias}) = 1 - \exp(p \times (V_{bias} - V_{BD})) \qquad 3.70$$

    (more details will be given in the Annex 4 - P_{Geiger} parameterization")

- *"far-above"* the breakdown voltage, where the $I_{post\text{-}BD}$ is further amplified by afterpulsing and cross-talk effects. Due to their non-linear nature, the afterpulses are expected to be the dominant effect in this region leading to a multiplicative factor [40]:

$$G_{AP}(V_{bias}) = 1 + \frac{P_{ap}(V_{bias})}{1 - P_{ap}(V_{bias})} \qquad 3.71$$

where $P_{ap}(V_{bias})$ denotes the probability that an afterpulse will be produced by a single avalanche. $P_{ap}(V_{bias})$ should be linearly rising with overvoltage and the recursive nature of afterpulsing leads to a fast increase of the current up to reaching a "second breakdown region", at a critical voltage, V_{CR}, where $P_{ap}(V_{CR}) = 1$, thus:

$$P_{ap}(V_{bias}) = \frac{V_{bias} - V_{BD}}{V_{CR} - V_{BD}} \qquad 3.72$$

- *"transition"* zone located between *"just-above"* and *"far-above"* regions, where the $I_{post\text{-}BD}$ is a combination of the currents from these two regions and it is given by bulk thermal generated carriers enhanced by gain, P_{Geiger} and afterpulses;
- *"post-second breakdown"* zone, where run-away afterpulses and non-quenching effects lead to a very high current limited by the total series resistance of the device.

Taking into account all these contributions, the $I_{post\text{-}BD}$ can be expressed as:

$$\begin{aligned} I_{post-BD}(V_{bias}) &= I_{pre-BD}(V_{bias}) + \frac{dN_{carriers}}{dt} \times \frac{V_{CR} - V_{BD}}{V_{CR} - V_{bias}} \times [1 - \exp(p \times (V_{bias} - V_{BD}))] \times C_{\mu cell} \times (V_{bias} - V_{BD}) = \\ &= \exp(a \cdot V_{bias} + b) + \frac{dN_{carriers}}{dt} \times \frac{V_{CR} - V_{BD}}{V_{CR} - V_{bias}} \times [1 - \exp(p \times (V_{bias} - V_{BD}))] \times C_{\mu cell} \times (V_{bias} - V_{BD}) \end{aligned} \qquad 3.73$$

where a, b, $dN_{carriers}/dt$, V_{CR}, V_{BD}, $C_{\mu cell}$, and p – are the free parameters.

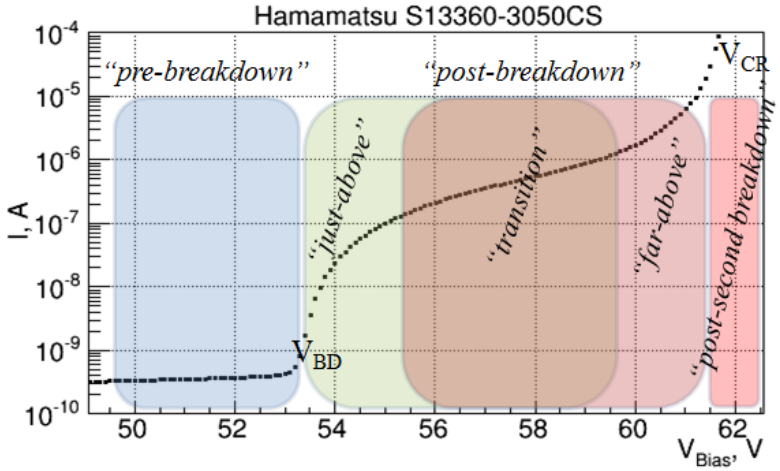

Figure 3.75 Typical reverse IV characteristics for Hamamatsu S13360-3060CS devise. The main regions (e.g. pre-breakdown, just-above, far-above and post-second breakdown) are pointed out

3.5.1. **Experimental data at room T fitted by the IV model**

As it was already discussed in the Section 3.2 "Measured devices & measurements conditions" the reverse IV measurements were done as a function of T in few different conditions: (1) dark and (2) illuminated by laser pulses of three intensities (low, medium and high) and two wavelengths (e.g. 467 nm, 635 nm). In this section these experimental data acquired at room T = 298.15 K will be used to test the proposed IV model.

3.5.1.a. Dark conditions

In this section the IV measurements performed in dark conditions at T = 298.15 K will be analyzed.

The Eq. 3.73 can be used to fit the IV curve at a given T by seven free parameters: a, b, $dN_{carriers}/dT$, $C_{\mu cell}$, V_{BD}, p and V_{CD}. However, for simplification, the fit procedure can be done in two steps:

- use the Eq. 3.68 to fit the pre-BD region and then extrapolate this fit to the post-BD region. From this step the "a" and "b" free parameters will be defined;
- fit the post-BD region by Eq. 3.73 using fixed "a" and "b" parameters defined in the previous step.

Also, to reduce the number of free parameters, the $dN_{carriers}/dT \times C_{\mu cell}$ can be replaced by only one p_{NC}. Taking into account this contribution, the $I_{post\text{-}BD}$ can be expressed as:

$$I_{post-BD}(V_{bias}) = I_{pre-BD}(V_{bias}) + p_{NC} \times \frac{V_{CR} - V_{BD}}{V_{CR} - V_{bias}} \times \left[1 - \exp\left(p \times (V_{bias} - V_{BD})\right)\right] \times (V_{bias} - V_{BD}) \qquad 3.74$$

The procedure described above was used to fit the experimental IV characteristics of various SiPM devices produced by Hamamatsu and KETEK at room T = 298.15 K and the fits are shown as lines in Figure 3.76 (a, b and c) and Figure 3.77 (a, b, c and d) respectively.

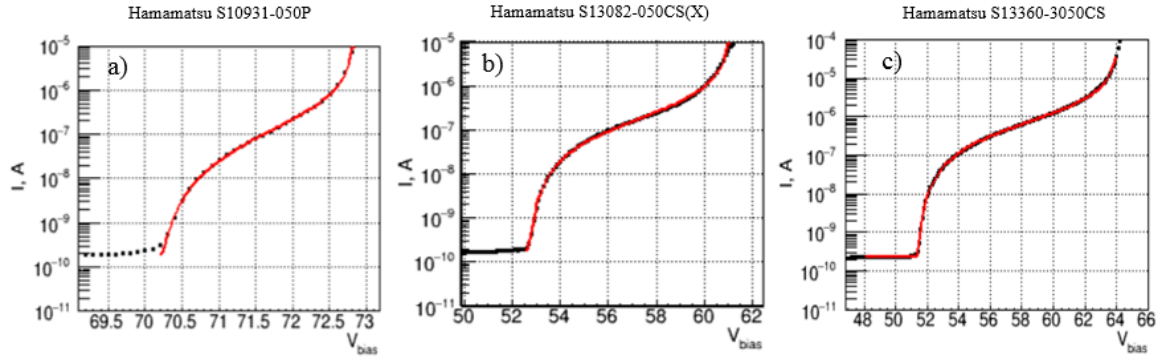

Figure 3.76 Reverse IV characteristics (dots) and fit (lines) for Hamamatsu SiPM devices: a) S10931-050P b) S13082-050CS(X) and c) S13360-30050CS at T = 298.15 K and dark conditions

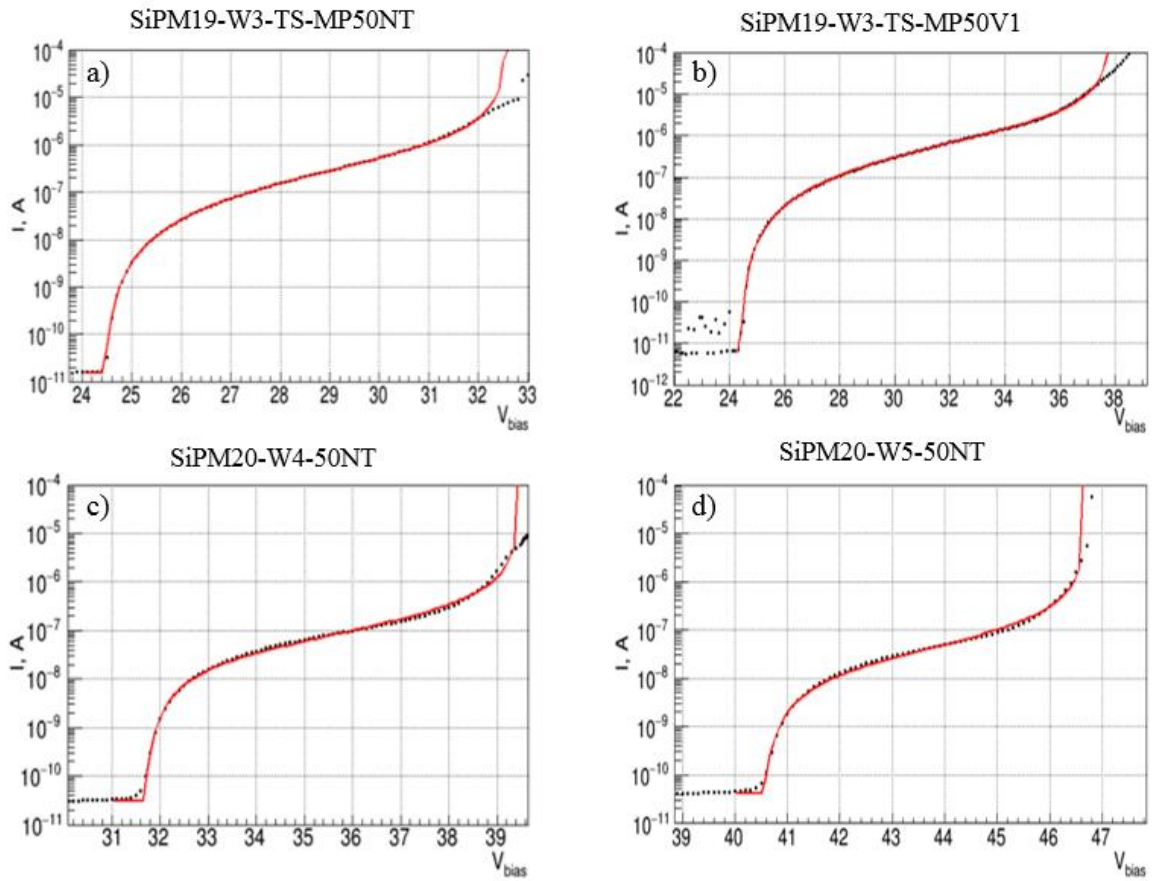

Figure 3.77 Reverse IV characteristics (dots) and fit (lines) for KETEK SiPM devices: a) SiPM19-W3-TS-MP50NT, b) SiPM19-W3-TS-MP50-V1, c) SiPM19-W4-50NT and d) SiPM19-W5-50NT at T = 298.15 K and dark conditions

A good agreement of our model with the experimental data for all Hamamatsu devices over a large range of currents 10^{-12} A < $I_{post\text{-}BD}$ < 10^{-5} A can be observed, while some discrepancies between experimental data and fit results can be observed in the "far above" region for KETEK devices (in particular for SiPM19-W3-TS-MP50NT and SiPM19-W3-TS-MP50-V1). The observed discrepancies are related to the absence of the fast current increases near second breakdown. The second breakdown is spread over ~1 V range around V_{CR} because of a voltage drop between the applied V_{bias} and the real voltage across the SiPM. The real voltage across the SiPM device V_{SiPM} is slightly smaller than applied V_{bias}:

$$V_{SiPM} = V_{bias} - I \times \frac{N_{fired}\left(R_q + R_s\right)}{N_{\mu cell}} \qquad 3.75$$

where I – is the current across the SiPM, N_{fired} and $N_{\mu cell}$ – are the number of simultaneously fired and total number of µcells and R_q and R_s – are the quenching and diode series resistance. The difference between V_{SiPM} and V_{bias} increases with increasing V_{bias} because of high I and N_{fired}. This effect is negligible for the Hamamatsu devices because of high $N_{\mu cell}$ = 3600. However, it is significant for KETEK devices SiPM19-W3-TS-MP50NT and SiPM19-W3-TS-MP50-V1 because of small $N_{\mu cell}$ = 100, and less significant for another two SiPM20-W4-50NT and SiPM20-W5-50NT devices because of higher $N_{\mu cell}$ = 400.

These fits can be also used to determine the breakdown voltage $V_{BD\text{-}IV\ Model}$, the working range V_{CR} - $V_{BD\text{-}IV\ Model}$ and the shape of Geiger triggering probability. The $V_{BD\text{-}IV\ Model}$ and the working range for all SiPM devices are presented in Table 5. The shape of Geiger triggering

probability $P_{Geiger\text{-}DC}$ calculated from IV model for Hamamatsu and KETEK SiPM devices is presented in Figure 3.78 and Figure 3.79 respectively.

Device		$V_{BD\text{-}IV\ Model}$	$V_{CR} - V_{BD\text{-}IV\ Model}$
Hamamatsu	S10931-050P	70.207 ± 0.011	2.64 ± 0.017
	S13082-050CS(X)	52.671 ± 0.013	8.46 ± 0.07
	S13360-3050CS	51.381 ± 0.01	12.81 ± 0.011
KETEK	SiPM19-W3-TS-MP50NT	24.463 ± 0.004	8.112 ± 0.561
	SiPM19-W3-TS-MP50-V1	24.437 ± 0.004	13.37 ± 0.031
	SiPM20-W4-50NT	31.697 ± 0.032	7.781 ± 0.034
	SiPM20-W5-50NT	40.533 ± 0.009	6.165 ± 0.039

Table 5 The breakdown voltage $V_{BD\text{-}IV\ Model}$ and working range $V_{CR} - V_{BD\text{-}IV\ Model}$ determined form IV model for various SiPM devices at T = 298.15 K and dark conditions

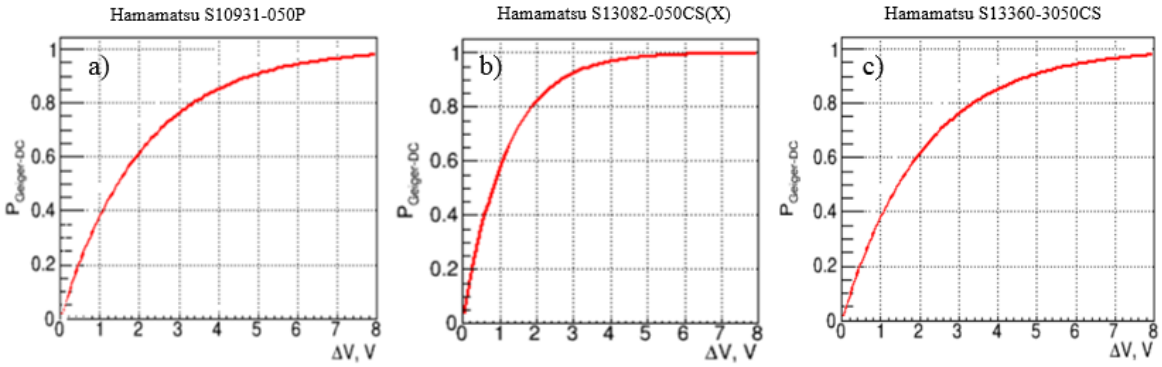

Figure 3.78 The shape of Geiger triggering probability $P_{Geiger\text{-}DC}$ from IV Model for Hamamatsu SiPM devices: a) S10931-050P b) S13082-050CS(X) and c) S13360-30050CS at T = 298.15 K and dark conditions

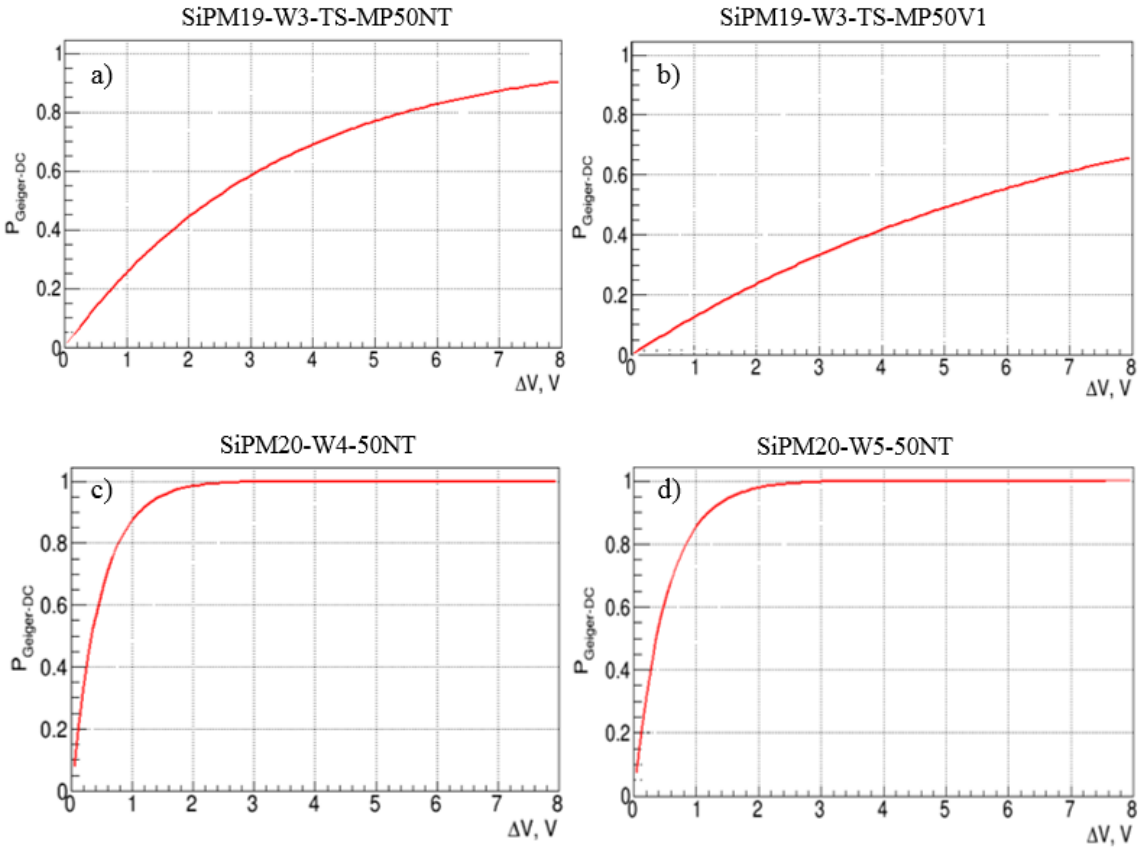

Figure 3.79 The shape of Geiger triggering probability $P_{Geiger\text{-}DC}$ from IV Model for KETEK SiPM devices: a) SiPM19-W3-TS-MP50NT, b) SiPM19-W3-TS-MP50-V1, c) SiPM19-W4-50NT and d) SiPM19-W5-50NT at T = 298.15 K and dark conditions

3.5.1.b. Light conditions

In this section the IV measurements performed at room $T = 298.15$ K with blue ($\lambda = 467$ nm) and red light ($\lambda = 635$ nm) will be analyzed.

To work with the IV curve generated only by the light of a given wavelength (i.e. in the same way as avalanches during AC acquisition) and to eliminate the contribution from bulk thermal generated carriers, the IV curves in dark conditions have been also measured and subtracted from the measurements with light.

It has been found that for the condition described above (e.g. subtracted dark current) the proposed model does not describe precisely the experimental data over full "post-breakdown" region. In particular, some discrepancies between experimental data and fit results can be observed either in the *"just-above"* or in the *"far-above"* regions. However, it was found that IV model can fit range in *"just-above"* region correctly as well as in *"far-above"* region if these regions are fitted separately. The IV curves measured with blue and red light after subtraction of the dark currents (dots) at $T = 298.15$ K and the fits (lines) are shown in Figure 3.80 (a and b) and Figure 3.81 (a and b).

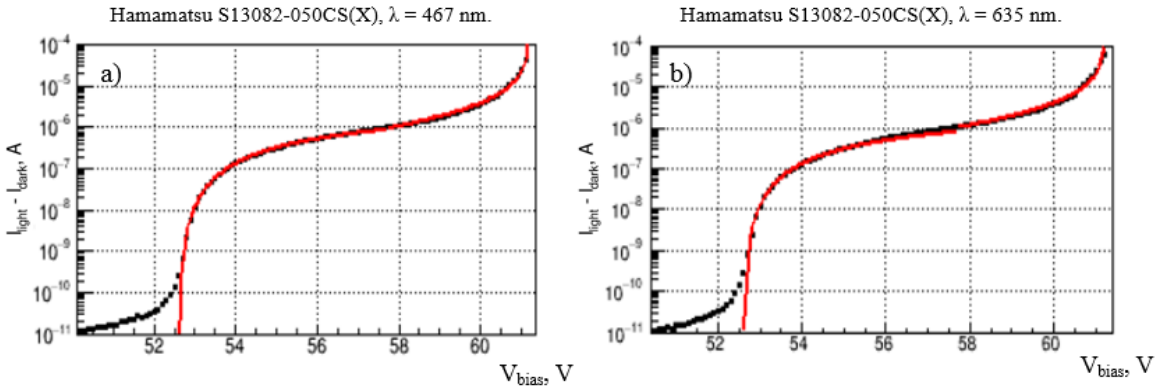

Figure 3.80 Reverse IV characteristics (dots) measured with a) blue and b) red light and fit (lines) for Hamamatsu SiPM S13082-050CS(X) device at T = 298.15 K. The dark current has been subtracted

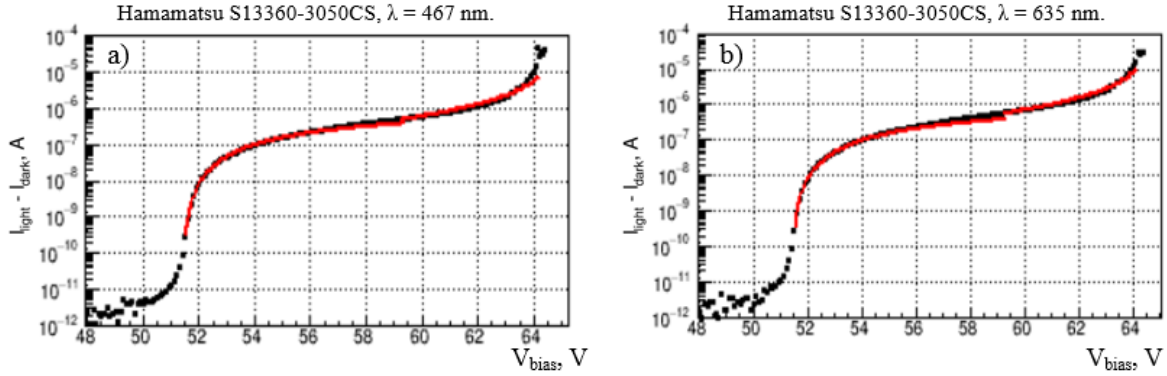

Figure 3.81 Reverse IV characteristics (dots) measured with a) blue and b) red light and fit (lines) for Hamamatsu SiPM S13360-3050CS device at T = 298.15 K. The dark current has been subtracted

These fits was also used to determine the breakdown voltage $V_{BD\text{-}IV\ Model}$, the working range V_{CR} - $V_{BD\text{-}IV\ Model}$ and the shape of Geiger triggering probability $P_{Geiger\text{-}DC}$. The $V_{BD\text{-}IV\ Model}$ and working range are presented in Table 6 (in our model, the second breakdown is described by V_{CR} (e.g. voltage at which $P_{ap} = 1$) and the working range was calculated as a difference between the V_{CR} and $V_{BD\text{-}IV\ Model}$). The $P_{Geiger\text{-}DC}$ for blue and red light, calculated from IV model for Hamamatsu S13082-050CS(X) and S13360-3050CS devices are presented in Figure 3.82.

Hamamatsu	λ = 467 nm		λ = 635 nm	
	$V_{BD\text{-}IV\ Model}$	V_{CR} - $V_{BD\text{-}IV\ Model}$	$V_{BD\text{-}IV\ Model}$	V_{CR} - $V_{BD\text{-}IV\ Model}$
S13082-050CS(X)	52.643 ± 0.002	8.582 ± 0.002	52.615 ± 0.002	8.647 ± 0.002
S13360-3050CS	51.405 ± 0.005	13.298 ± 0.041	51.405 ± 0.005	13.183 ± 0.030

Table 6 The breakdown voltage $V_{BD\text{-}IV\ Model}$ and working range V_{CR} - $V_{BD\text{-}IV\ Model}$ at T = 298.15 K, determined form DC measurements done with blue and red light for two Hamamatsu devices: S13082-050CS(X) and S13360-3050CS

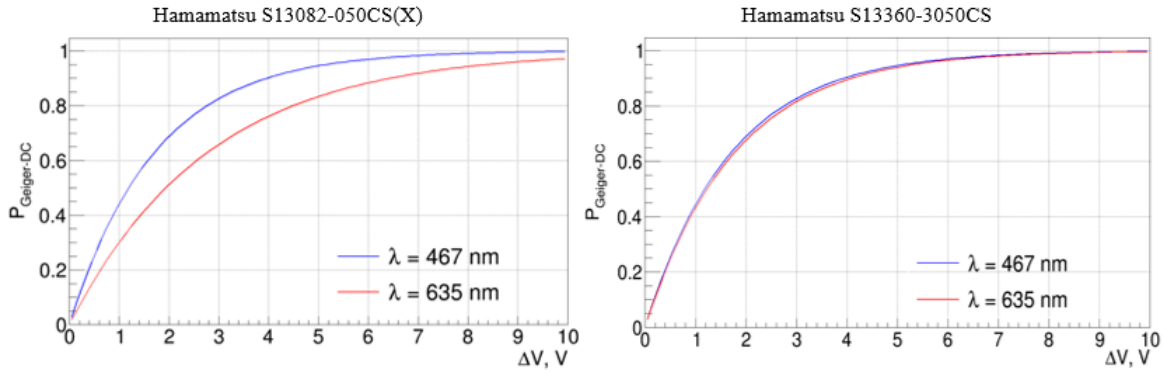

Figure 3.82 Shape of Geiger triggering probability $P_{Geiger\text{-}DC}$ for blue and red light obtained from IV Model for Hamamatsu SiPM devices: a) S13082-050CS(X) and b) S13360-30050CS at T = 298.15 K

3.5.2. **Experimental data at various T fitted by IV model**

In this section the experimental data acquired at different T will be used to test the proposed IV model.

3.5.2.a. Dark conditions

In this section the IV measurements performed in a *T* range from 308.15 K down to 238.15 K in dark conditions will be analyzed.

As it was already discussed the Eq. 3.74 can be used to fit IV curve at a given *T* by using six free parameters (e.g. *a*, *b*, p_{NC}, V_{CR}, V_{BD} and *p*). Also, due to dark conditions, we can expect that the $p_{NC} = C_{\mu cell} \times dN_{carriers}/dt$ is defined by the dependence on *T* of $I_{generation}$ given by (see also Eq. 2.49):

$$p_{NC} = C_{\mu cell} \times \frac{dN_{carriers}}{dt} = C_{\mu cell} \times A \cdot T^{3/2} \cdot \exp\left(-\frac{E_{act}}{k_B T}\right) \qquad 3.76$$

However, the Eq. 3.76 describes only the *T* dependence of thermal generated carriers. Since the $I_{post\text{-}BD}$ implies additional physical mechanisms (e.g. afterpulsing, P_{Geiger}) with eventually their own *T* dependence, the Eq. 3.76 cannot be used for a simultaneous fit of all IV curves at various *T*. Consequently, a more generic function with polynomial and exponential temperature dependence has been defined:

$$p_{NC} = C_{\mu cell} \times \frac{dN_{carriers}}{dt} = (1 + n_0 \times T + n_1 \times T^2) \times \exp(n_2 + n_3 \times T) \qquad 3.77$$

where *T* – is the temperature and n_0, n_1, n_2 and n_3 – are the free parameters.

The procedure described above was used to fit the experimental IV characteristics of various Hamamatsu and KETEK SiPM devices in *T* range from 308.15 K down to 238.15 K and the fits are shown as lines in Figure 3.83 (a, b and c) and Figure 3.84 (a, b, c and d) respectively. A good agreement of our model with the experimental data for all Hamamatsu devices over a large range of currents 10^{-12} A < $I_{post\text{-}BD}$ < 10^{-4} A can be observed, while some discrepancies between experimental data and fit results can be observed in the "far above" region for KETEK devices due to voltage drop (see the Section 3.5.1.a "Dark conditions"). We can observe that this difference increases with decreasing the *T* due to increases of R_q and consequently to the voltage drop as presented in the Eq. 3.75.

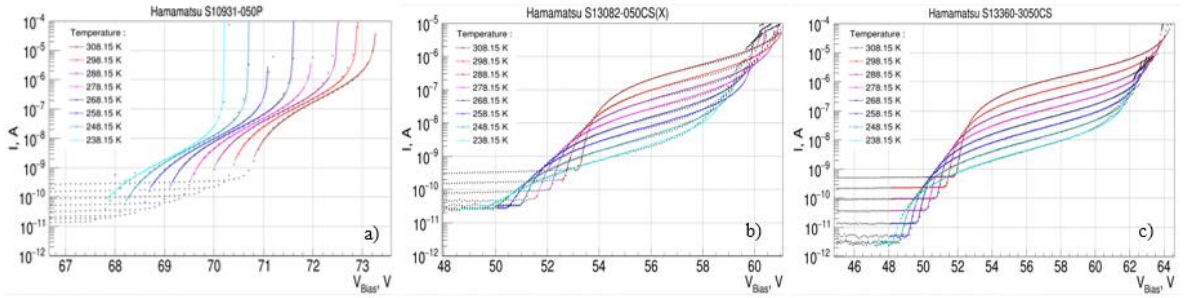

Figure 3.83 Reverse IV characteristics (dots) and fit (lines) for Hamamatsu SiPM devices: a) S10931-050P b) S13082-050CS(X) and c) S13360-30050CS in a T range from 308.15 K down to 238.15 K and dark conditions

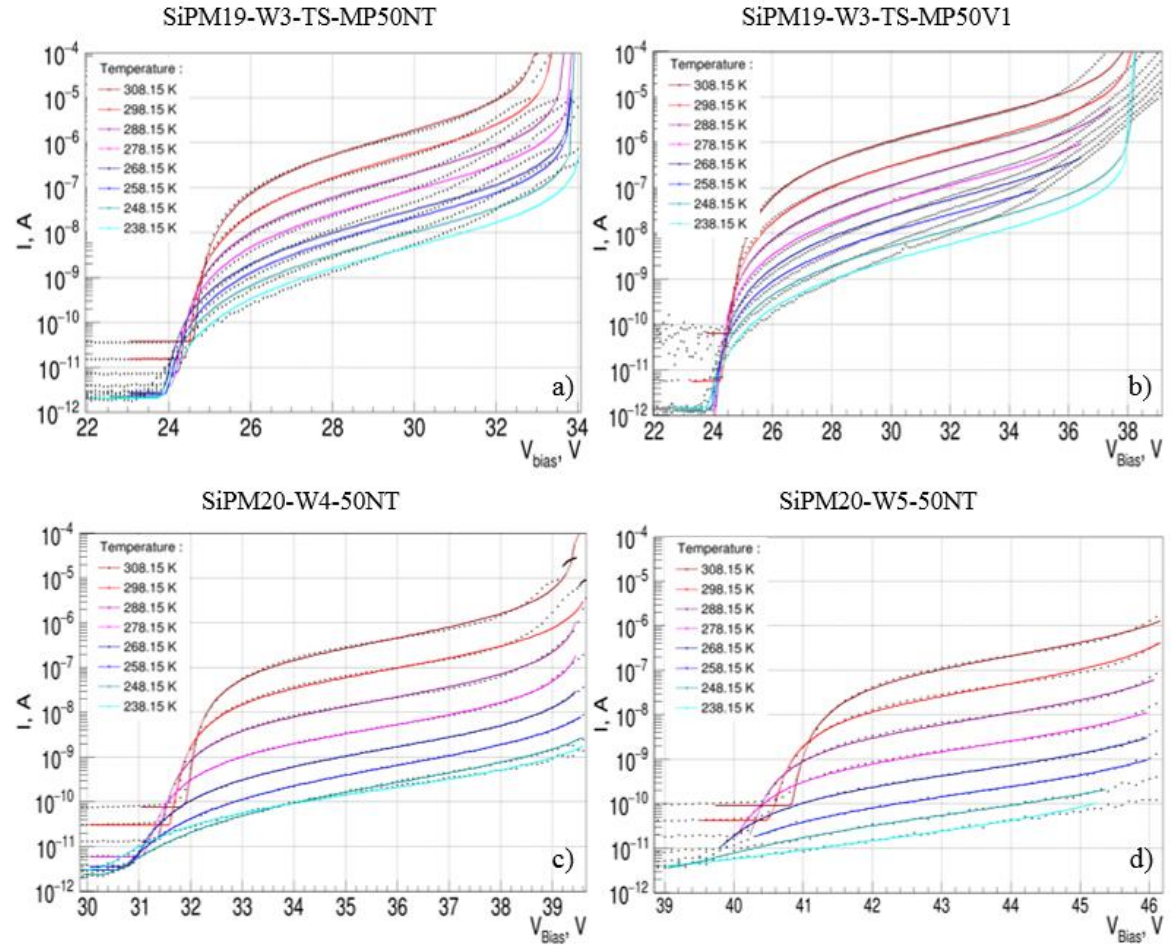

Figure 3.84 Reverse IV characteristics (dots) and fit (lines) for KETEK SiPM devices: a) SiPM19-W3-TS-MP50NT, b) SiPM19-W3-TS-MP50-V1, c) SiPM19-W4-50NT and d) SiPM19-W5-50NT in a T range from 308.15 K down to 238.15 K and dark conditions

These fits can be also used to determine the breakdown voltage $V_{BD\text{-}IV\ Model}$, the working range V_{CR} - $V_{BD\text{-}IV\ Model}$ and the shape of Geiger triggering probability $P_{Geiger\text{-}DC}$ as well as their variation with T and the obtained results will be presented in the following.

3.5.2.a.1. $\underline{V_{BD}\ vs.\ T}$

The $V_{BD\text{-}IV\ Model}$ values obtained from DC-acquisition/IV model in T range from 308.15 K down to 238.15 K for Hamamatsu and KETEK SiPM devices are presented in Figure 3.85 and Figure 3.86. Moreover, the V_{BD} calculated from AC acquisition/Gain linearity (for more details see the Section 3.4.3.b "V_{BD} *vs.* T") in the same T range are also given. We can observe a good agreement regarding the T variation of the breakdown voltages, with very similar temperature

coefficients. However, there is a significant and systematic difference: the values of the $V_{BD\text{-}IV\ Model}$ are few hundreds mV higher than the values of V_{BD} calculated from AC acquisition, for all measured devices and T. This discrepancy reflects the fundamental difference in the physical significance of the "breakdown" voltage determined by these two methods. The "IV-based" measurement is sensitive to the ones of avalanche phenomenon and it determines the "breakdown" as defined by fundamental papers of McIntyre [68], [69] and [43]. The AC/Gain linearity method determines the voltage to which the voltage across the diode is reduced to quench the avalanche. The latter is naturally lower than the former and our results are consistent with this expectation.

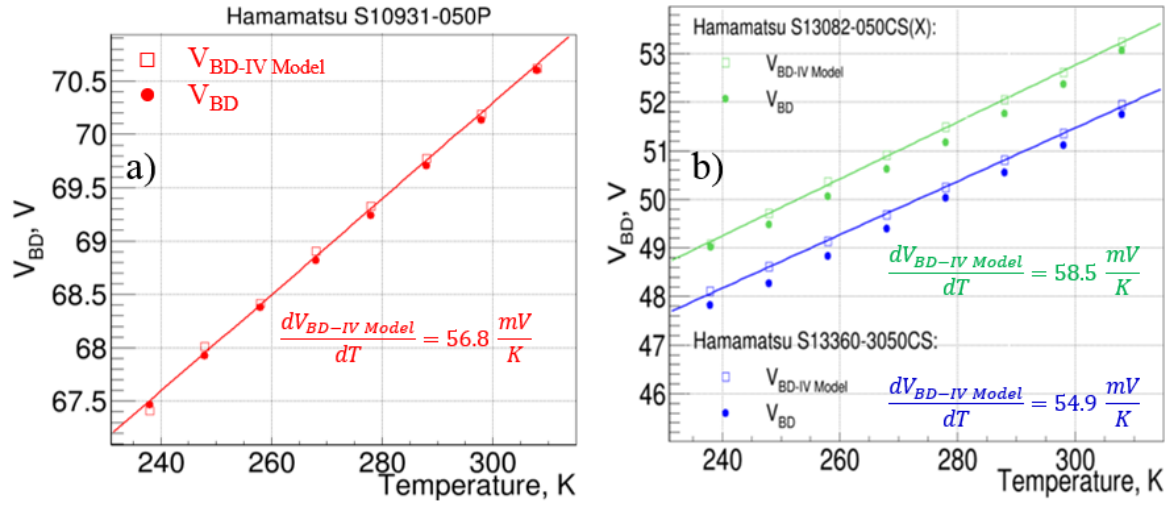

Figure 3.85 The $V_{BD\text{-}IV\text{-}Model}$ (calculated from IV model) and V_{BD} (calculated from AC measurements) vs. T for Hamamatsu SiPM devices a) S10931-050P and b) S13082-050CS(X) and S13360-3050CS and their temperature coefficients $\frac{dV_{BD-IV\ Model}}{dT}$

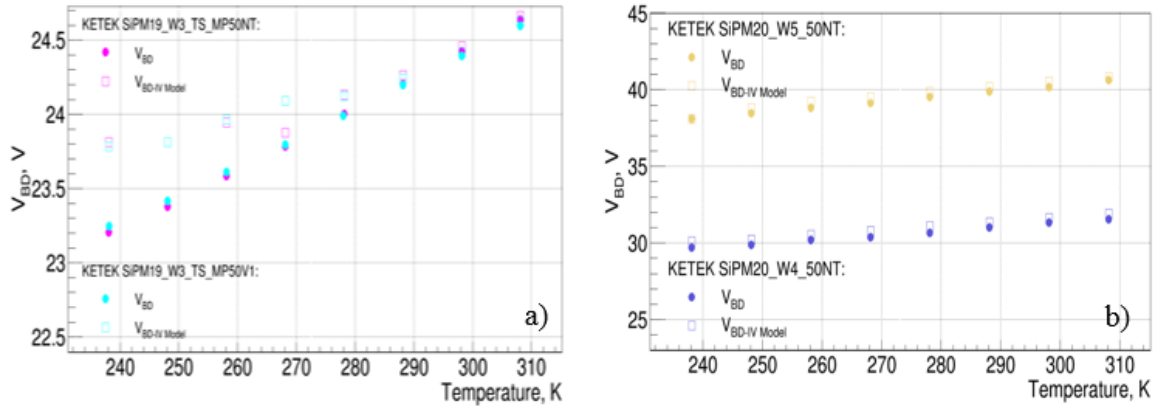

Figure 3.86 The $V_{BD\text{-}IV\text{-}Model}$ (calculated from IV model) and V_{BD} (calculated from AC measurements) vs. T for KETEK SiPM devices a) SiPM19-W3-TS-MP50NT and SiPM19-W3-TS-MP50V1 and b) SiPM-W4-50NT and SiPM-W5-50NT

3.5.2.a.2. Working range vs. T

The upper value of the V_{bias} is limited by high afterpulsing probability leading to the second breakdown. In our model, the second breakdown is described by V_{CR} (e.g. voltage at which P_{ap} = 1). Therefore, the working range of SiPM devices has been calculated as a difference between the V_{CR} and $V_{BD\text{-}IV\ Model}$. The results for Hamamatsu SiPM devices are presented in Figure 3.87. We are not presenting the results for KETEK devices due to absence of the fast current increases near second breakdown (for more details see the Section 3.5.1.a "Dark conditions"). We can observe that the Hamamatsu device from 2011 year production run (i.e.

S10931-050P) has a working range of only 2.7 V while the latest generation from 2015 year production run (i.e. S13082-050CS(X) and S13360-3050CS) have a larger working range of ~10 V, showing a considerable improvement of SiPM technology.

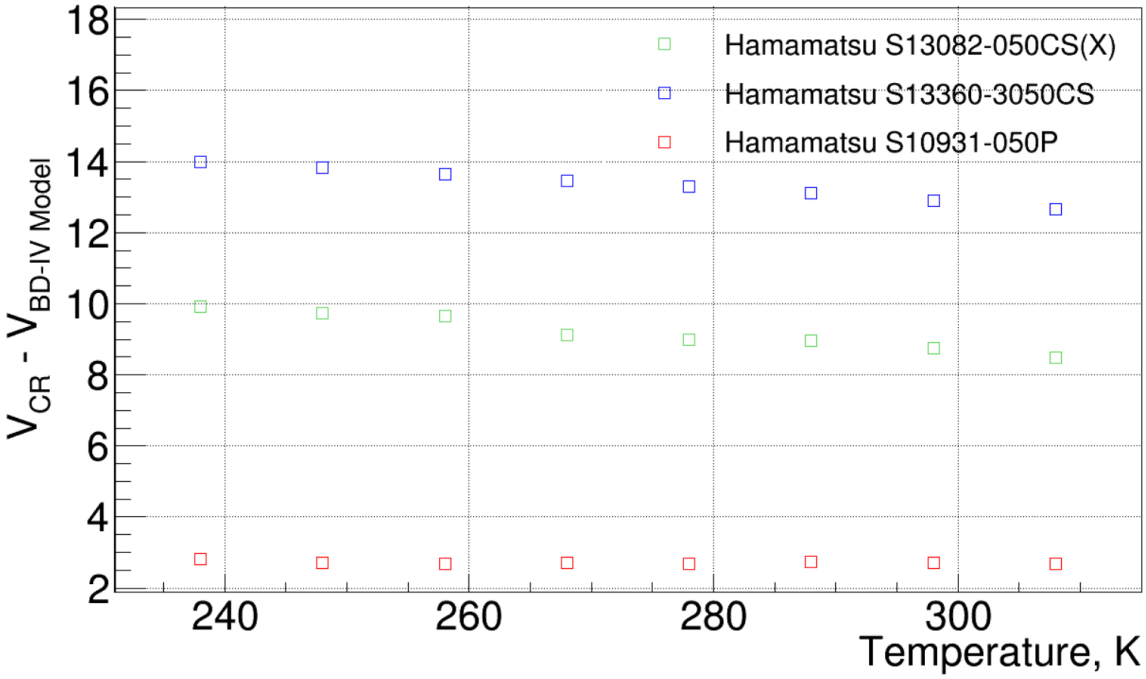

Figure 3.87 Working range ($V_{CR} - V_{BD\text{-}IV\ Model}$) vs. T for Hamamatsu SiPM device

3.5.2.a.3. $P_{Geiger\text{-}DC}$ vs. T

Figure 3.88 (a, b and c) and Figure 3.90 (a, b, c and d) show the shape of Geiger probability $P_{Geiger\text{-}DC}$ obtained from dark DC acquisition/IV model as a function of ΔV in a T range from 308.15 K down to 238.15 K for Hamamatsu and KETEK SiPM devices (for SiPM20-W4-50NT and SiPM20-W5-50NT devices the results are not presented at 238.15 K due to low current). Independent of measured device we can observe that, at a given ΔV, the $P_{Geiger\text{-}DC}$ decreases with decreasing T.

The $P_{Geiger\text{-}DC}$ at a given ΔV (ΔV = 2 V for S10931-050P device and ΔV = 4 V for all others devices) as a function of T is presented in Figure 3.89 (a, b and c) and Figure 3.91 (a, b, c and d) for Hamamatsu and KETEK devices respectively. We can observe that for all measured devices $P_{Geiger\text{-}DC}$ shows much stronger variation with T with respect to $P_{Geiger\text{-}AC}$ (see the Section 3.4.3.h "P_{Geiger} *vs.* ΔV *vs.* T"). This variation can be related to:

- *measurements reasons;* in our IV model, the shape of $P_{Geiger\text{-}DC}$ is mostly determined by the fast current increases in "*just-above*" region. Therefore, the precision of current measurements in this region is extremely important to obtain a correct shape of $P_{Geiger\text{-}DC}$. The instrumentation measurements limit is 2 pA and it does not depend of T. Since the current decreases with decreasing T, the relative precision of measurements and consequently determinations of $P_{Geiger\text{-}DC}$ decreases too. Therefore, the variation of $P_{Geiger\text{-}DC}$ with T could be the reflection of measurements precision;
- *physical reasons;* the IV curve is determined by avalanches produced by both types of free carriers (electrons and holes) presumably generated everywhere in the depleted region, whereas AC acquisition is performed by a given type of carriers (mostly

electrons for blue light and holes for red light since our devices are $p^+/n/n\text{-epi}/n^+$ structure) and mostly generated at a given depth due to penetration depth (see Figure 2.51).

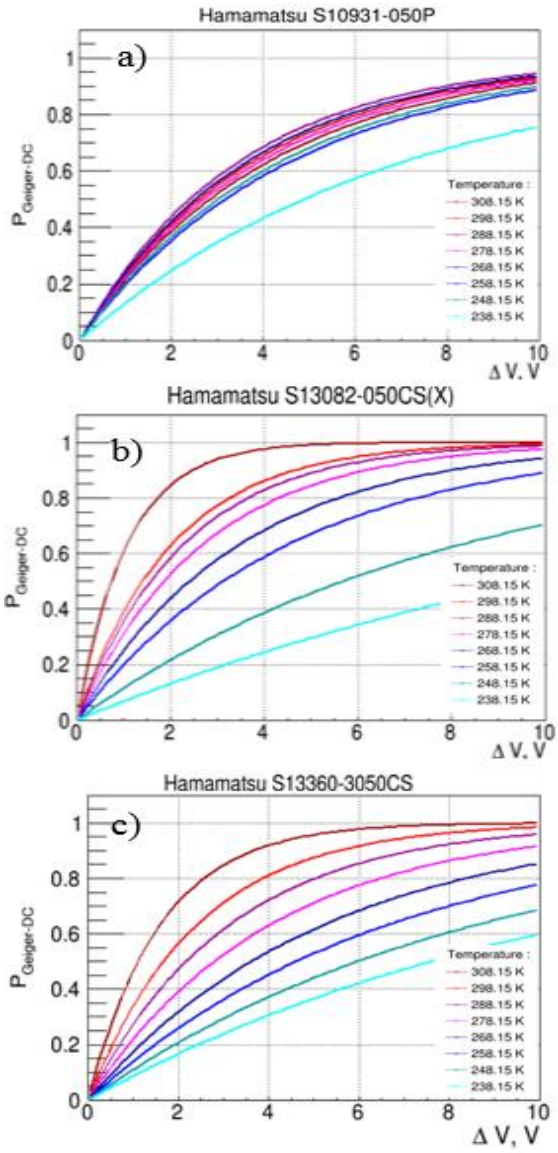

Figure 3.88 $P_{Geiger\text{-}DC}$ vs. ΔV at T range from 308.15 K down to 238.15 K for SiPM device produced by Hamamatsu: a) S10931-050P b) S13082-050CS(X) and c) S13360-3050CS

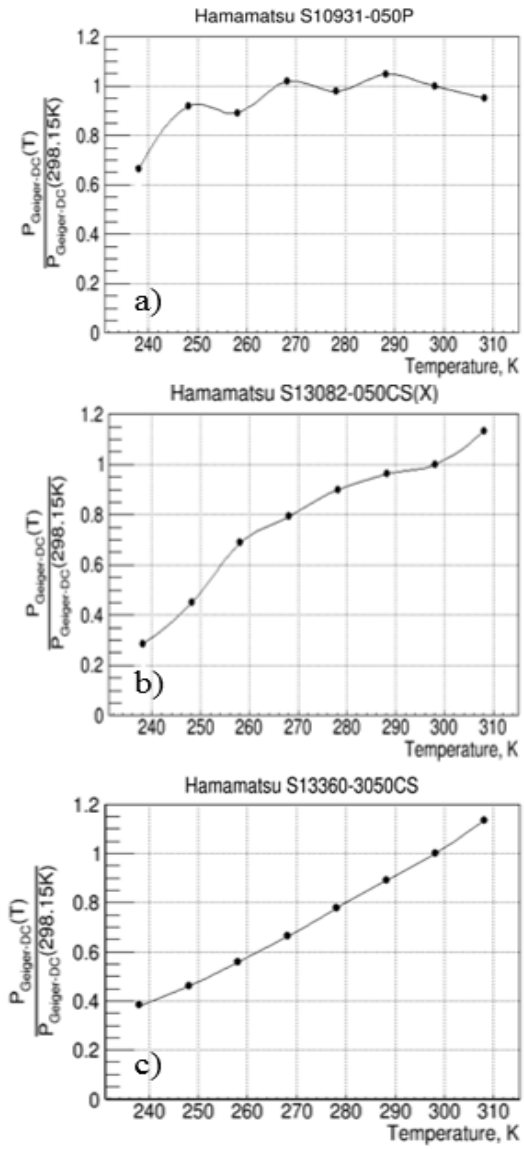

Figure 3.89 $P_{Geiger\text{-}DC}$ vs. T at a given ΔV for SiPM devices produced by Hamamatsu: a) S10931-050P, ΔV = 2 V b) S13082-050CS(X), ΔV = 4 V and c) S13360-3050CS, ΔV = 4 V. Each data set at fixed λ is normalized to the value at T = 298.15 K

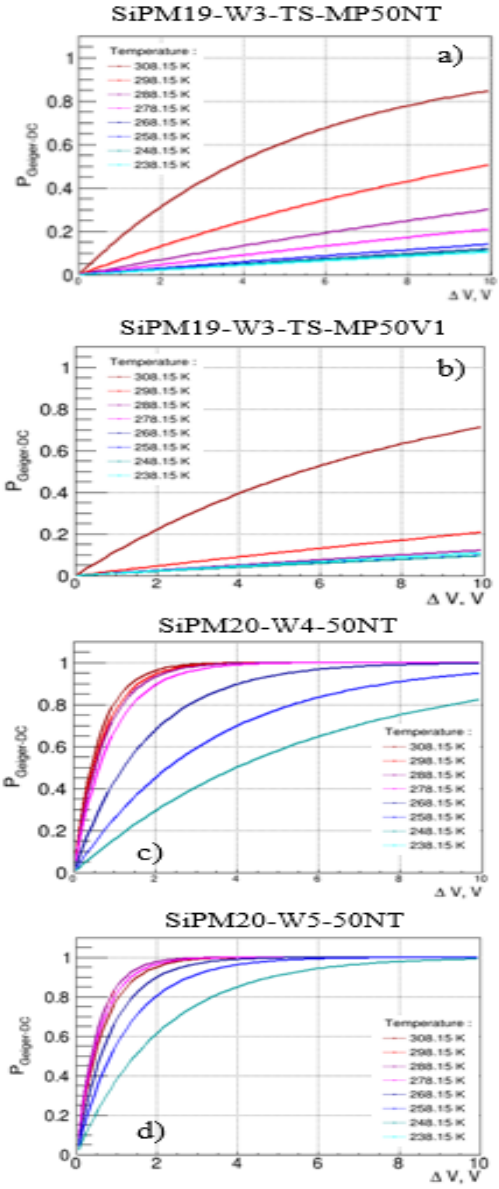

Figure 3.90 $P_{Geiger\text{-}DC}$ vs. ΔV at T range from 308.15 K down to 238.15 K for SiPM device produced by KETEK: a) SiPM19-W3-TS-MP50NT, b) SiPM19-W3-TS-MP50-V1, c) SiPM19-W4-50NT and d) SiPM19-W5-50NT at T range from 308.15 K down to 238.15 K

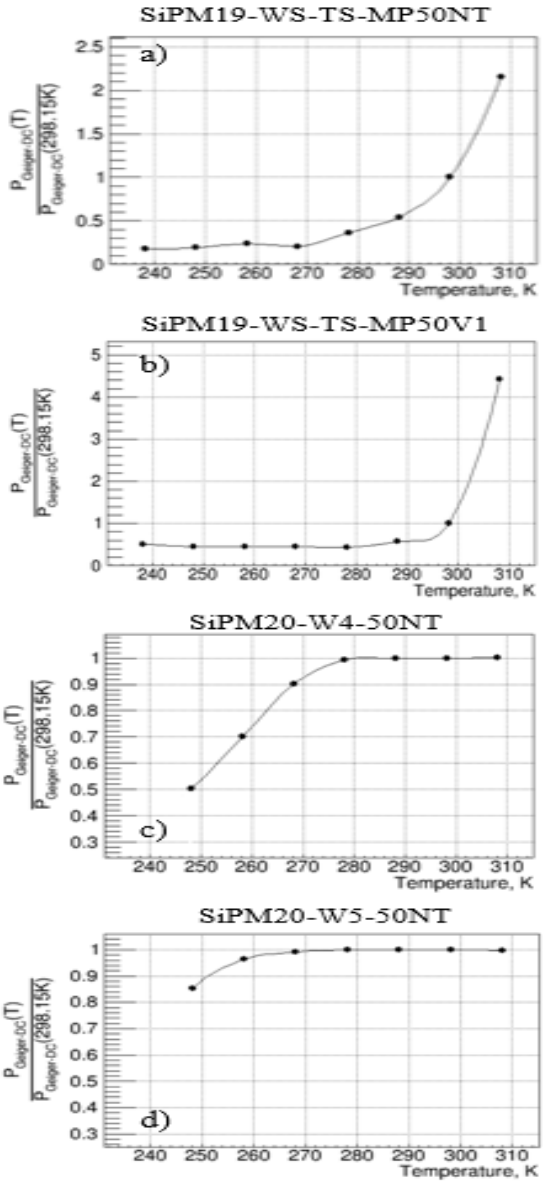

Figure 3.91$P_{Geiger\text{-}DC}$ vs. T at a given ΔV = 4 V for SiPM devices produced by KETEK: a) SiPM19-W3-TS-MP50NT, b) SiPM19-W3-TS-MP50-V1, c) SiPM19-W4-50NT and d) SiPM19-W5-50NT. Each data set at fixed λ is normalized to the value at T = 298.15 K

To obtain the final shape of $P_{Geiger\text{-}DC}$ independent of temperature, it is suitable to perform the IV measurements in light conditions. This will imply a high current exceeding the instrumental limit and minimizing the measurement error and in the same time, based on the light wavelength, it will give information on the carriers type triggering the avalanches. Therefore, the reverse IV measurements were also performed with light and will be analyzed in the next Section.

3.5.2.b. Light conditions

In this section the IV measurements performed in a *T* range from 318.15 K down to 98.15 K with blue (λ = 467 nm) and red light (λ = 635 nm) will be analyzed.

To work with the IV curve generated only by the light of a given wavelength (i.e. in the same way as avalanches during AC acquisition) and to eliminate the contribution from bulk thermal

generated carriers, the IV curves in dark conditions have been also measured and subtracted from the measurements with light. Also, since the dark current has been subtracted, we can expect that due to constant laser light intensity independent of T, the $p_{NC} = C_{\mu cell} \times dN_{carriers}/dt$ should not depend on T (i.e. $p_{NC} = C_{\mu cell} \times dN_{carriers}/dt = Const.$ for all T). Therefore, the IV curves measured at various T can be fitted simultaneously with an identical $dN_{carriers}/dt$ parameter.

To describe correctly the full working range of SiPM devices in these conditions (e.g. identical $dN_{carriers}/dt$ over all T and IV curves after dark current subtraction) two separate fits were performed: one in the *"just-above"* region and another one in *"far-above"* region. Both fits were extrapolated to the *"transition"* region to describe full working range of a given SiPM device at a given T. The IV curves measured with blue and red light after subtraction of the dark currents (dots) in T range from 318.15 K down to 98.15 K and the fits (lines) are shown in Figure 3.92 (a and b) and Figure 3.93 (a and b).

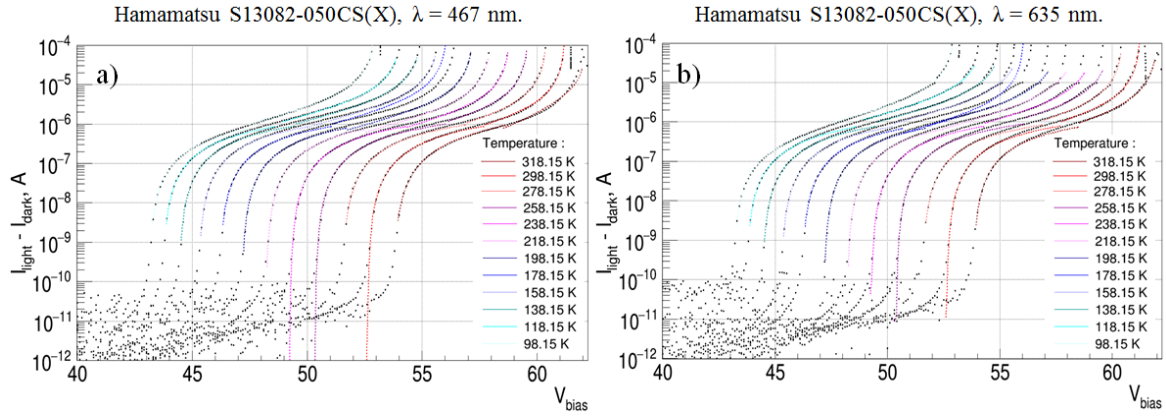

Figure 3.92 Reverse IV characteristics (dots) measured with a) blue and b) red light after dark current subtraction and fit (lines) for Hamamatsu SiPM S13082-050CS(X) device in T range from 318.15 K down to 98.15 K

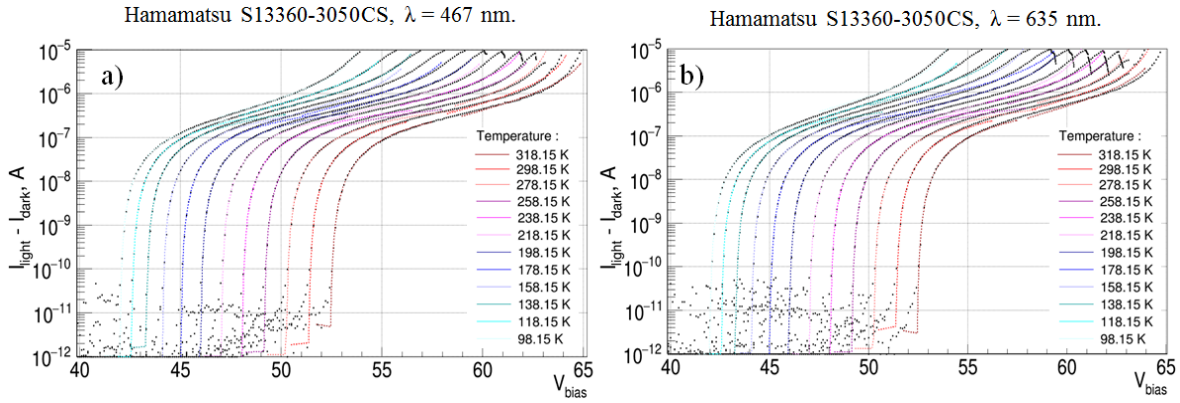

Figure 3.93 Reverse IV characteristics (dots) measured with a) blue and b) red light and fit (lines) after dark current subtraction for Hamamatsu SiPM S13360-3050CS device in T range from 318.15 K down to 98.15 K

3.5.2.b.1. V_{BD} *vs. T*

Figure 3.94 presents the comparison between $V_{BD\text{-}IV\ Model}$ values obtained from DC-acquisition/IV model from measurements with light (i.e. blue and red light) and the V_{BD} calculated from AC acquisition/Gain linearity (for more details see the Section 3.4.3.b "V_{BD} *vs. T*") in a T range from 318.15 K down to 98.15 K for two Hamamatsu SiPM devices: S13082-050CS(X) and S13360-3050CS. We can observe very similar values of $V_{BD\text{-}IV\ Model}$ calculated from IV curves measured with blue and red light. However, as it was already discussed above,

the $V_{BD\text{-}IV\text{-}Model}$ shows slightly higher values with respect to the V_{BD}. Also the temperature coefficients $\frac{dV_{BD-IV\ Model}}{dT}$ are reported directly in the plots and similar to the values calculated from AC measurements (See the Section 3.4.3.b "V_{BD} *vs. T*").

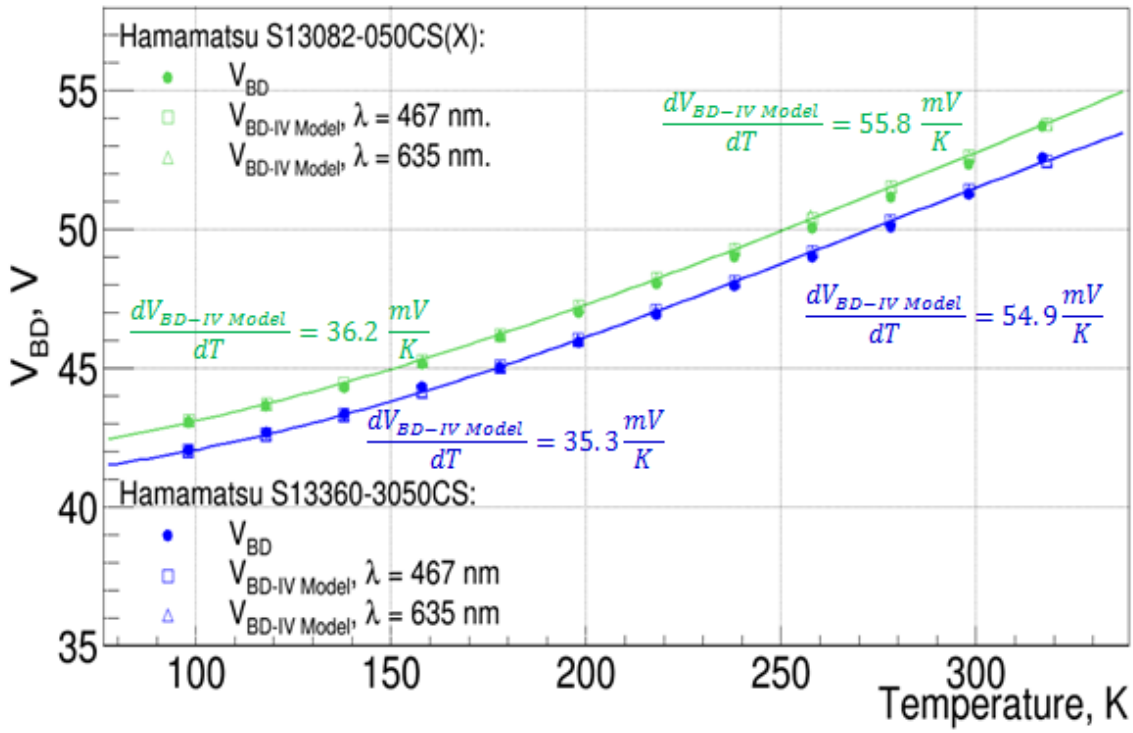

Figure 3.94 The $V_{BD\text{-}IV\ Model}$ (calculated from IV model) and V_{BD} (calculated from AC measurements) vs. T for Hamamatsu SiPM devices: S13082-050CS(X) and S13360-3050CS. Also the T coefficients for $V_{BD\text{-}IV\ Model}$ are presented

3.5.2.b.2. Working range vs. T

Figure 3.95 shows the working range of two Hamamatsu SiPM devices as a function of *T* calculated from IV measurements with blue and red light.

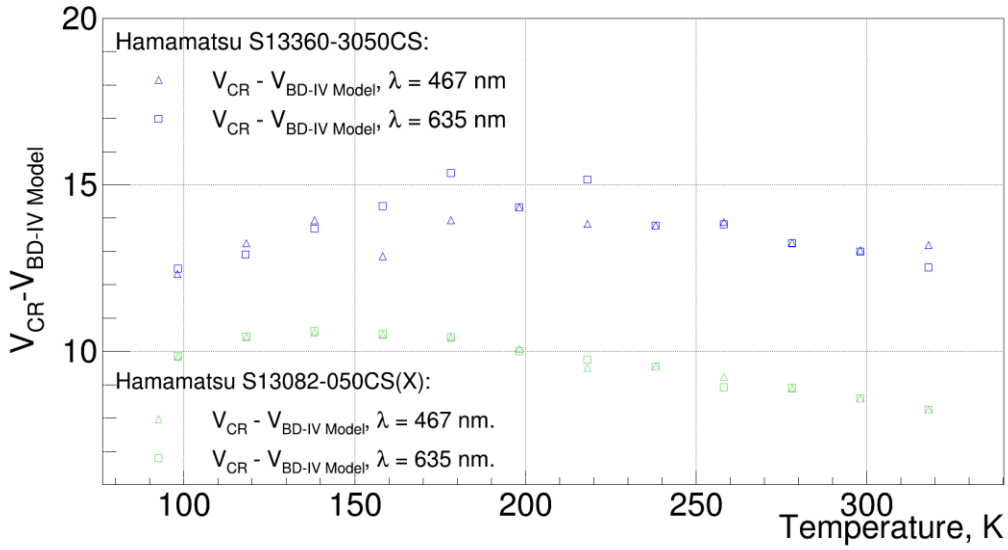

Figure 3.95 Working range ($V_{CR} - V_{BD\text{-}IV\ Model}$) vs. T for two Hamamatsu SiPM device: S13082-050CS(X) and S13360-3050CS calculated from revers IV measurements done with blue (λ=467 nm.) and red (λ=635 nm.) light

3.5.2.b.3. P_{Geiger} vs. T

The shapes of $P_{Geiger\text{-}DC}$ for blue light (λ = 467 nm) and red light (λ = 635 nm) have been obtained from DC acquisition/IV model as a function of ΔV in a T range from 318.15 K down to 98.15 K and presented in Figure 3.96 (a and b) and Figure 3.97 (a and b). We can observe that, at a given ΔV and T, the $P_{Geiger\text{-}DC}$ shows slightly higher value for blue light (λ = 467 nm) than for red light (λ = 635 nm) as it was already seen from the AC measurements (see the Section 3.4.3.h "P_{Geiger} *vs.* ΔV *vs.* T"). However, we can also observe that for both studied SiPM devices at λ = 467 nm and at a given ΔV the $P_{Geiger\text{-}DC}$ slightly increases with T decreasing. In particular for S13082-050CS(X) device we can see ~0.4% increases with the decreasing the T from 298.15 K down to 98.15 K. This behavior can be related to the T variation of QE which has not been included in our model.

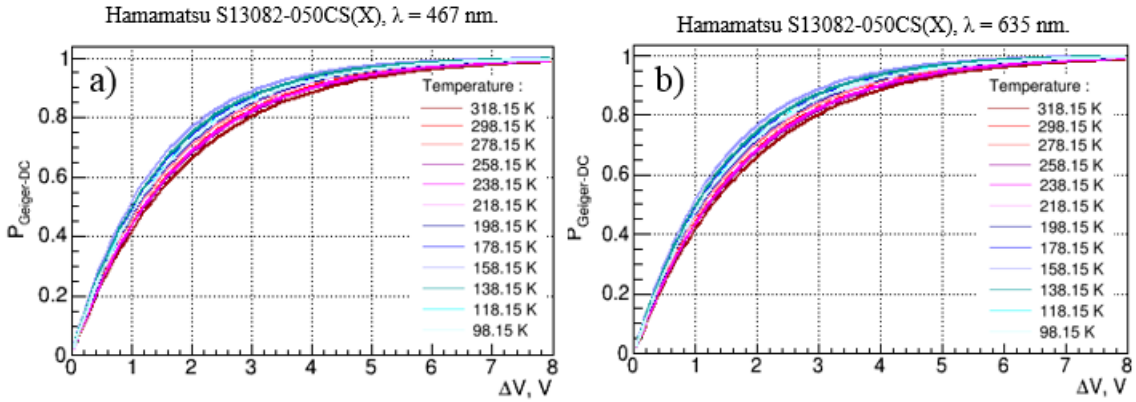

Figure 3.96 $P_{Geiger\text{-}DC}$ vs. ΔV at T range from 318.15 K down to 98.15 K for SiPM device produced by Hamamatsu S13082-050CS(X) and measured with a) blue λ = 467 nm and b) red λ = 635 nm laser light

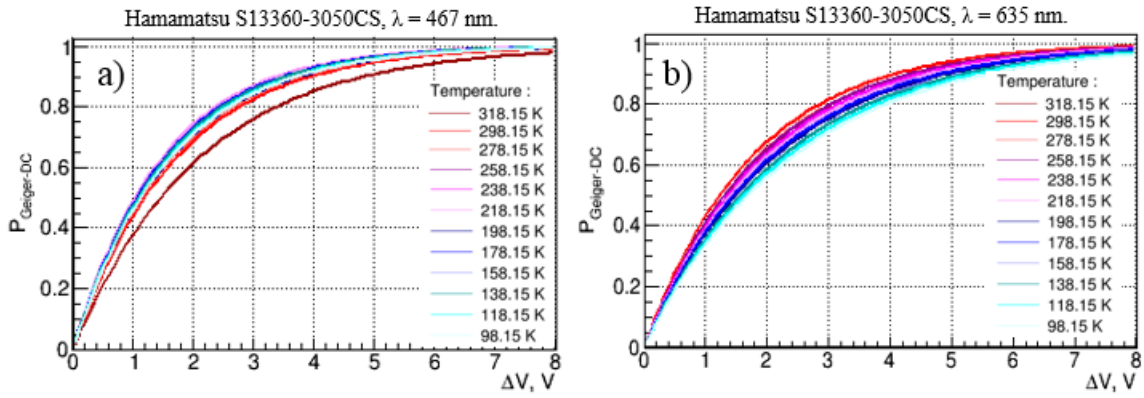

Figure 3.97 $P_{Geiger\text{-}DC}$ vs. ΔV at T range from 318.15 K down to 98.15 K for SiPM device produced by Hamamatsu S13360-3050CS and measured with a) blue λ = 467 nm and b) red λ = 635 nm laser light

Figure 3.98 shows the $P_{Geiger\text{-}DC}$ calculated from the IV curves acquired under illumination of blue (λ = 467 nm) and red (λ = 635 nm) laser light. Each data set at fixed λ has been normalized to the value at T = 298.15 K. We can observe that for both devices the $P_{Geiger\text{-}DC}$ (λ = 467 nm) is constant over full range of T from 318.15 K down to 98.15 K, while the $P_{Geiger\text{-}DC}$ (λ = 635 nm) decreases with decreasing the T. However, we can also observe that for both devices the $P_{Geiger\text{-}AC}$ (see the Section 3.4.3.h "P_{Geiger} *vs.* ΔV *vs.* T") shows much higher variation with T with respect to the $P_{Geiger\text{-}DC}$. Moreover, this T variation is fluctuating near a given value, therefore we can expect that during the experimental AC measurements the laser intensity was not fully stable and variated in a range ± 40%. During the DC measurements the same lasers

have been used but the variations of light intensities are not seen, because of much higher light intensity these variations are negligible.

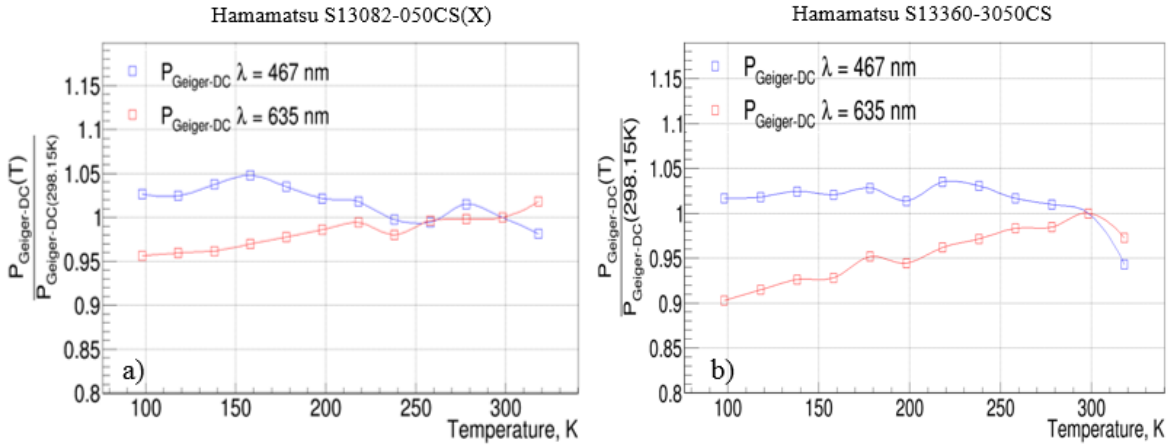

Figure 3.98 The $P_{Geiger\text{-}DC}$ for Hamamatsu SiPM devices: a) S13082-050CS(X) and b) S13360-3050CS measured at T range from 318.15 K down to 98.15 K for two light wavelength: λ = 467 nm. and λ = 635 nm. Each data set at fixed λ has been normalized to the value at T = 298.15 K

4. Investigation of SiPM parameters in a bio-medical context

In the previous chapter, the study of various SiPM devices was performed in the context of understanding their main electrical and optical parameters as a function of temperature and the related physical phenomena. In this chapter, the SiPM parameters will be studied from the point of view of their use in a bio-medical application, particularly for building a beta-sensitive intracerebral probe dedicated to measure the local concentration of radiolabeled molecules on awake and freely moving animal in order to study new animal models of human brain disorders.

4.1. Introduction

The understanding of human brain disorders (i.e. neurodegenerative diseases, tumor growth, neuropsychiatric disorders) as well as the development of new potential therapies against these diseases can benefit today from new animal models. However, the better understanding of functional processes in the brain with animal models require the development of technological tools adapted to small animal brain studies and able to combine quantitative molecular measurements with behavioral studies.

Several approaches dedicated to behavioral neuroimaging have been studied during past ten years [70]. In nuclear molecular imaging these developments are primarily focused on preclinical Positron Emission Tomography (PET) technologies (i.e. a β^+ emitter tracer is injected into the animal body and emitted positrons interact with electrons and produce two anti-parallel photons which are detected in coincidence by opposite arrays of detectors to reconstruct the image). In the first and the simplest approach, behavioral experiments are carried out after injection of the tracer, the animals being free to move for 30 minutes in an open field. However, in order to acquire brain images with a microPET, the rodent is subsequently anesthetized and scanned [71]. A second approach (Rat conscious animal PET or RatCAP) relies on a wearable PET device allowing imaging for the entire brain on awake animals [72]. However, due to its weight, this device cannot be applied to completely freely moving animals, restraining the conditions where it can be used. The third approach uses a head-motion tracking system within a PET scanner [73]. However, this system requires mechanisms to restrain the animal movements.

No one of these approaches allow a real-time recording of the local time-activity of a molecular radiotracer in freely moving animals [72]. In this context, the concept of a beta-sensitive intracerebral probe, allowing to measure the local concentration of radiolabeled molecules on awake and freely moving animal, was patented by Delpierre [74]. Based on this concept, few prototypes were developed up today and they will be briefly described in the following.

4.1.1. Principle of beta-sensitive intracerebral probes

The working principle of the beta-sensitive probe has been described by Pain [75]. It is based on a β^+ emitting tracer, which is injected into the body of the animal. In contrast with the PET detection method, the β^+ particles are subsequently directly detected by the beta-sensitive probe. The β^+ particles have a limited range of free path before interaction with the biological tissues and further annihilation. This limited range allows the definition of a detection volume centered on the sensitive part of the probe with its size depending on the energy spectrum of the positron. The higher the energy of the β^+ particle is emitted by the isotope decay (e.g. ^{18}F, ^{11}C and ^{15}O), the longer the distance it travels in the tissue before annihilation and therefore, the larger is the

detection volume (in average less than 1 mm in the brain tissue for positrons emitted by ^{18}F). Thus, it is possible to define a region of interest with a size of the order of the rodent brain loci to determine the local activity concentration of injected radiotracers. The probe, which is implanted into the region of interest of the brain by stereotaxic surgery, has thus to be small enough (typically of a 500 μm width) to prevent from invasiveness effects and has to be biocompatible. The detector has to be highly sensitive to low energy β particles in order to measure a signal typically of a few keV due to the small detection volume.

Two versions of the beta-sensitive intracerebral probes have been developed: "Sonde IntraCerebrale" (SIC) and pixelated intracerebral probe (PIXSIC). Both versions will be described in the following.

4.1.2. "Sonde IntraCerebrale" SIC

The first version of the beta-sensitive intracerebral probe, the so-called SIC, has been developed by Pain [76] and its general architecture is presented in Figure 4.1. We can distinguish three main parts, presented by:

- *The probe (1)*; its construction took into account several physical and biological constrains, in particular the need of a low-density material, minimization of optical loss, suitability for brain implantation, low weight and bio-compatibility; *The probe* consists of a 1 mm long and 1 mm in diameter plastic scintillating fiber (Bicron BCF-12) fused to a 1 mm in diameter clear fiber light guide (Bicron BCF-98). The length of clear fiber light guide is adjustable to ensure the position of the scintillating part near the region of interest. A 1 mm in diameter *EMA coated optical guide (2)* links the probe to *the external photodetector (3)*;
- *The photodetector (3);* its choice was guided by two major constraints: to be able to detect low amount of light and the need to create a low weight and a compact photodetector module compatible with a freely moving configuration of the detector. Therefore, one of the lightest photon detector available at that time on the market has been selected, particularly the photomultiplier tube with a 9 mm diameter active area photocathode from Hamamatsu (Hamamatsu R7400P, with 16 mm diameter and 12 mm seated length);
- *SIC Prototype and Photomultiplier Readout (4&5),* which has been developed and configured to support up to four implanted probes. It is composed of three major elements:
    - four photo-detection modules, each including a photomultiplier, its associated socket and a miniaturized programmable high-voltage converter;
    - an interface module containing four low-noise single channel boards, a low-voltage supply and a voltage control unit;
    - a portable PC including a multimodal PCI-bus-compatible acquisition board allowing up to 16 channels to be encoded.

  The acquisition was controlled by user-friendly software written under LabView software.

The SIC has to be a real-time beta-sensitive device to count local radioactivity of a tracer with a spatial resolution compatible with the dimensions of rat brain structure which is around few cubic millimeters. Therefore, the SIC has to ensure high sensitivity, low intrinsic noise,

time resolution compatible with physiological and pharmacological processes and supply a wide dynamic range.

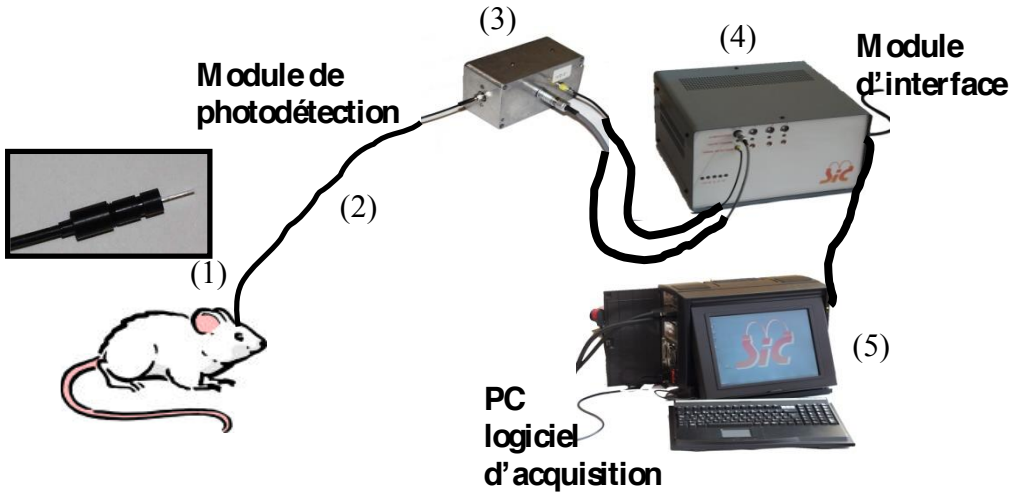

Figure 4.1 General architecture of SIC. The probe is first implanted using stereotaxic surgery and sealed with cement to the skull (1). During experiments, a clear flexible optical fiber guide (2) is connected to the probe so that the signal is transmitted to a photo-detection module (3). The resulting electric signal is amplified, threshold, and integrated in the interface module (4) and then transmitted to an acquisition board on a portable PC (5). The signal is finally processed and displayed using a LabView software interface providing online measurement of the radioactivity concentration evolution in the detection volumes surrounding each implanted probe. Note that the freely moving configuration of the system will include a rotating collector mounted on the top of the animal cage and connected to the photo-detection module so that the animal remains unrestrained. [76].

Measurements made *on tissue-equivalent phantoms filled with ^{18}F shown* a 2.7% detection efficiency corresponding to a 0.55 Hz/kBq/ml sensitivity for a 1 mm diameter probe with a 1 mm long scintillation tip. The expected signal levels ranges from 10 to 1000 Bq and allows the sampling time of 1 s, which is well suited to pharmacological studies. Also, the preliminary test showed a linear response of SIC device to ^{18}F decay up to ~1200 Bq. This value is consistent with biological kinetics measurements which will not exceed 1000 Bq count rate value (according to known cerebral doses and SIC efficiency).

The first SIC biological validation was realized by injecting various [^{18}F]-fluorodeoxyglucose FDG quantities in an anesthetized rat which had two probes implanted in the cerebellum and the striatum respectively. This preliminary study in an *anesthetized rat* confirmed the biocompatibility of the implanted probe with the cerebral tissues and showed that the dimensions and weight of the mechanical parts fixed on the rat skull were appropriate.

However, the single pixel scheme of SIC device does not provide any spatial information on the radiotracer distribution. Moreover, to make SIC compatible with experiments *in awake, freely moving animals*, the photo-detection modules should be integrated in the rat cage and use a slip ring set on the top of the cage. To overcome these limitations, the pixelated intracerebral probe PIXSIC has been developed by Maerk et. al. [77].

4.1.3. **Pixelated intracerebral probe PIXSIC**

A general view of a rat wearing the PIXSIC is presented in Figure 4.2 [77]. We can observe that the architecture of the device is based on two mechanically independent parts:

- a head socket which is fixed on the animal`s skull (see Figure 4.3). The head socket carriers the 200 μm thick, 690 μm wide and 17 mm long probe, whose pixelated sensitive part is implemented into the brain region. The sensitive part consisted of a reverse-biased, high-resistivity silicon detector divided into 10 pixels of 500 μm × 200 μm × 200 μm (see Figure 4.4). Each pixel consisted of a diode and it is read-out in parallel by a custom designed application-specific integrated circuit (ASIC) which is also integrated in the head socket;
- the backboard which includes the RF components and the power supply that enable the wireless operation of the system.

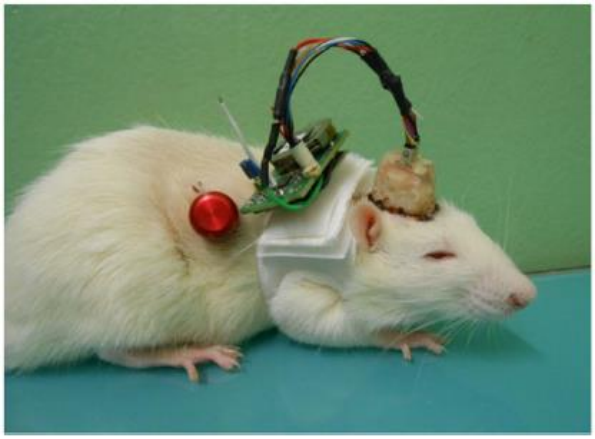

Figure 4.2 PIXSIC detector geometry: the head-socket fixed on the skull supporting the probe and the backpack on an awake rat [77]

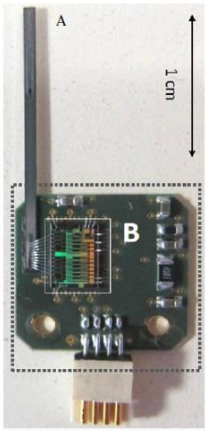

Figure 4.3 Prototype of the PIXSIC head socket: a) silicon probe and b) PCB with ASIC

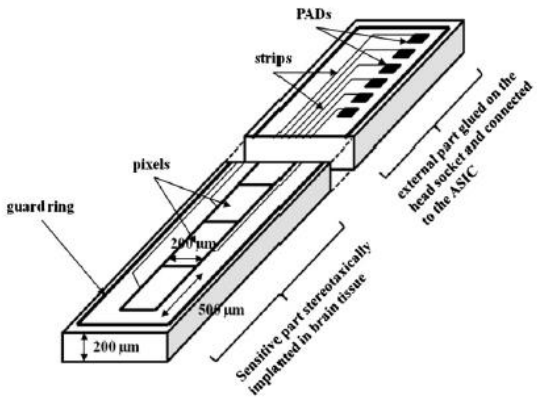

Figure 4.4 Schematic view of the 17 mm long and 200 μm thick Si probe, including the pixelated sensitive part implanted in brain tissue and an external part flued on the head socket and connected to the ASIC

The PIXSIC has provided some very promising results especially for behavioral neuroimaging. In particular, its compactness and autonomous design based on a radiofrequency data exchange link has offered the possibility to perform fully freely moving behavioral experiments with rats with minimal stress during acquisition. Its pixelated detection scheme adds “imaging” features by recording of the time-activity curves in different brain regions along the probe position. Nevertheless, although successfully validated in various physical and biological context [77] and [78], this probe design suffers from several issues that are strongly

limiting its utilization for longitudinal and freely moving studies. Notably, the thickness of the probe, reduced to 200 μm in order to drecrease the γ-rays background noise coming from the annihilation of positrons in tissue, makes the device very brittle and very difficult to manipulate. Moreover, despite its thinness, the probe has still a high sensitivity to γ-rays, which leads to substantial noise during experiments with radiotracers. The beta sensitivity of the probe also degrades due to the dead areas of the sensor used to stabilize the leakage current with guard rings. Last but not least, since each pixel is connected to the signal processing chip through electronic tracks routed along the sensor and wire-bonded to the PCB integrating the ASIC chip, the signal integrity suffered from noise added along this distance of about 2 cm.

4.2. New miniaturized probe for charged particles detection in molecular imaging based on SiPM (SONIM)

Taking into account the advantages (e.g. low cost, compact, autonomous, biocompatibility, sampling time) and drawbacks (mechanically-brittle, sensitivity to gamma rays) of SIC and PIXSIC projects and the impressive technological evolution of SiPM devices of the last years, the usage of last generation SiPM device as photodetector would offer the possibility to overcome the drawbacks of PIXSIC and SIC prototypes and to develop high sensitivity, ultra-miniaturized scintillator-based intracerebral probe that can be directly mounted on the rodent head. In particular, the high gain, high detection efficiency and low-operative voltage (i.e. $V_{bias} < 80$ V) of SiPM make this device very attractive to replace the PMT in the SIC device in order to develop a fully stand-alone detection probe. In fact, this replacement will significantly miniaturize the photo-detection module, and will allow its integration in a head socket smaller than the one done in PIXSIC project. The use of plastic fiber coupled to the SiPM will also decrease the sensitivity to gamma rays compared to silicon sensors and as the same time, will improve the beta sensitivity thanks to the continuous detection all along the fiber (no dead areas). From a practical point of view, the plastic fiber is less brittle that silicon sensors and the high gain of SiPM will allow to implement simplified readout electronics less sensitive to electromagnetic interference. The general architecture of new miniaturized probe for charged particles detection in molecular imaging based on SiPM (SONIM) is presented in Figure 4.5. We can distinguish three main parts, presented by:

- *The probe (1)*; its construction, similar to one used in SIC, took into account several physical and biological constrains, in particular the need of a low-density material, minimization of optical loss, suitability for brain implantation, low weight and bio-compatibility; *The probe* consists of a 5 mm long and 0.5 mm in diameter plastic scintillating fiber thermally fused to a 10 mm long and 0.5 mm in diameter clear fiber light guide;
- *SiPM (2)*; it coupled to *the probe* (from the clear fiber side) and read out by dedicated *miniaturized electronics*;
- *Miniaturized electronics (3)*; which includes shaping and amplification modules, the power supply for SiPM and the wireless operation module to transfer data to PC.

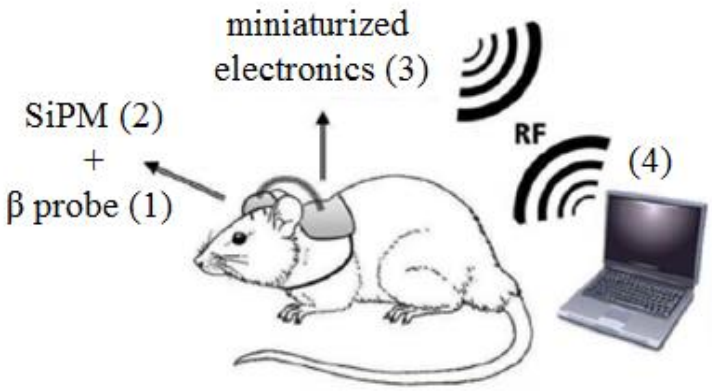

Figure 4.5 General architecture of SONIM. (1) β^+ sensitive probe implanted into rat brain in one side and coupled to a small low noise SiPM (2) device on another. The SiPM signals read out by dedicated low power consumption electronic (3) which also transmits the experimental data to PC (4)

However, the high dark count rate and correlated noise (optical crosstalk and afterpulses) of SiPM can hamper the detection of low-light events produced by low energy beta particles in plastic scintillators. Following our request, new SiPM prototypes have been developed by KETEK Company with particular characteristics like small size and low thermal and correlated noises. I report here the results of an experimental study aiming to compare the beta sensitivity of an intracerebral probe based on these new SiPMs specially developed to satisfy the requirements of our application, and a commercially available device from Hamamatsu Company.

4.2.1. **SiPM devices for SONIM project**

We have defined three most adapted devices for our application (i.e. small size, low noise, and high photo-detection efficiency):

- Two small KETEK devices of 0.5 × 0.5 mm^2 size with 50 × 50 μm^2 µcell size (100 µcells) specifically developed for our project (see Figure 4.6):
  - SiPM19-W3-TS-MP50-V1 with optical trenches (Figure 4.6, device type 1);
  - SiPM19-W3-TS-MP50NT without trenches (Figure 4.6, device type 2);
- Standard Hamamatsu device of 1.3 × 1.3 mm^2 size with 50 × 50 μm^2 µcell size (667 µcells):
  - S13360-1250PE (See Figure 4.7).

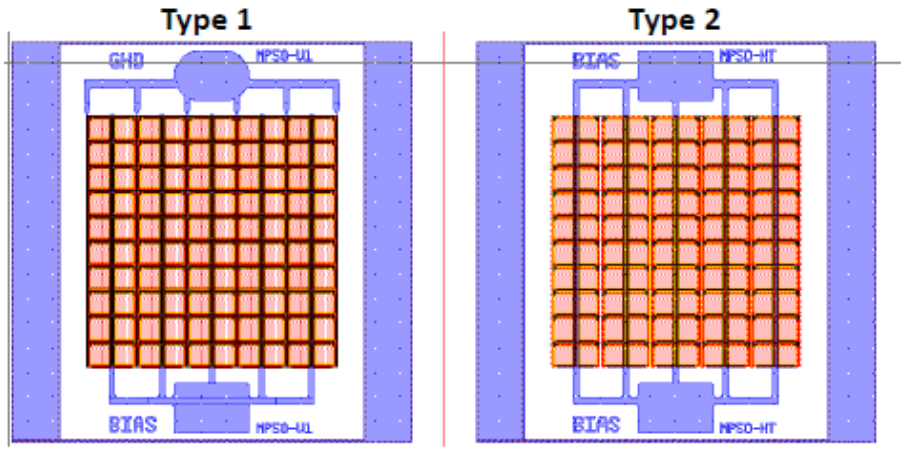

Figure 4.6 Design of KETEK SiPM chips of 0.5 × 0.5 mm^2 size with 50 × 50 μm^2 µcell size dedicated to our beta probe: type 1 with trenches, type 2 without trenches (by courtesy of KETEK Company)

For simplicity, the KETEK devices presented in this chapter have the same label like those presented in the Chapter 3 "Investigation of SiPM parameters down to cryogenic temperature", particularly because they are coming from the same production runs and wafers like the precedents ones. However, they were mounted on a different package (see Figure 4.8), allowing to perform optical tests in a mechanical configuration very close to the final beta probe.

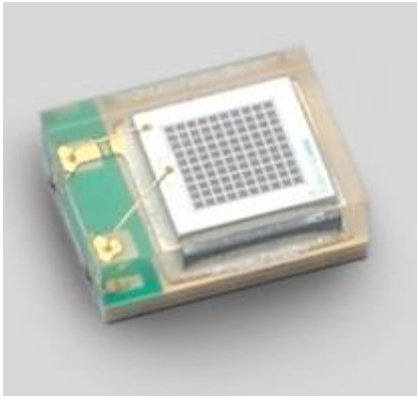

Figure 4.7 General view of the Hamamatsu device of 1.3×1.3 mm^2 size with 50 × 50 µm^2 µcell size [79]

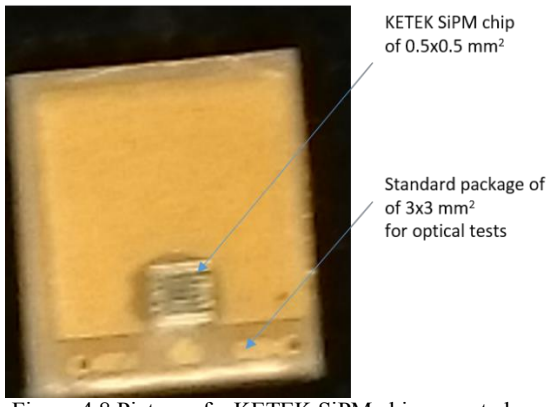

Figure 4.8 Picture of a KETEK SiPM chip mounted on a package adapted for optical tests

Each SiPM device has been coupled to a scintillating fiber and read-out by a dedicated miniaturized low-power consumption electronics and the gain, dark count rate and beta sensitivity were measured as a function of bias voltage and temperature. The setup developed for these tests in collaboration with our colleagues from the Laboratory of "Imagerie et Modelisation en Neurobiologie et Cancerologie (IMNC)" as well as the experimental results are presented in the following.

4.2.2. **Experimental setup**

The experimental measurements were performed at IMNC laboratory using the setup presented in Figure 4.9. A ^{204}Tl source was used to simulate the β^- emitter tracer (mean energy of 243 keV). The source was fixed in front of a scintillating fiber (0.5 mm diameter and 5 mm length) thermally fused to a clear optical fiber (0.5 mm diameter and 10 mm length) coupled to a SiPM. A detailed schematics of the SiPM mounting, together with the ^{204}Tl source and the optical fiber is presented in Figure 4.10. The SiPM was biased by a Keithley 2611 source-meter and read-out by a dedicated miniaturized electronics developed at LAL followed by a counter (more details about read-out electronics will be given in the next Section "*Miniaturized electronics*"). The measurements were performed inside a climatic chamber, at two temperatures of +25 ^{0}C and +35 ^{0}C.

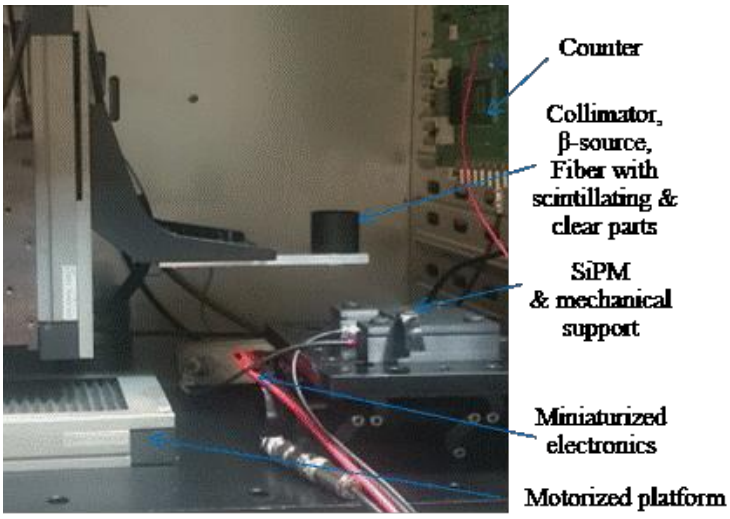

Figure 4.9 Experimental setup developed at IMNC for the characterization of SiPM devices dedicated to SONIM project

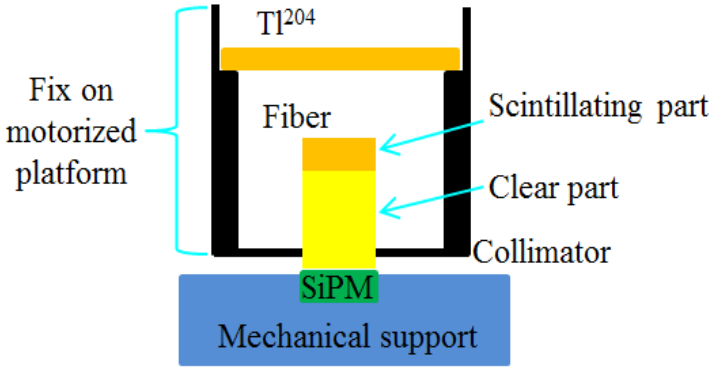

Figure 4.10 Detailed schematics of the SiPM mounting, together with the ^{204}Tl source and the optical fiber

Miniaturized electronics

To fit the requirements of the final application (e.g. small size and low-power consumption and noise) and to reach the best performance, a dedicated miniaturized electronics was developed at LAL by Dominique Breton. The electrical schematic of this dedicated miniaturized electronics is presented in Figure 4.11. We can observe that the miniaturized electronics is composed by a block for shaping and amplification of SiPM signals (i.e. operational amplifier OPA890) and a comparator block for generating TTL signals when the SiPM signal exceeds a given input threshold $V_{threshold}$ (i.e. comparator MAX9011). The dedicated miniaturized electronics has two outputs: the digital one for TTL signal and an analog one for AC measurements.

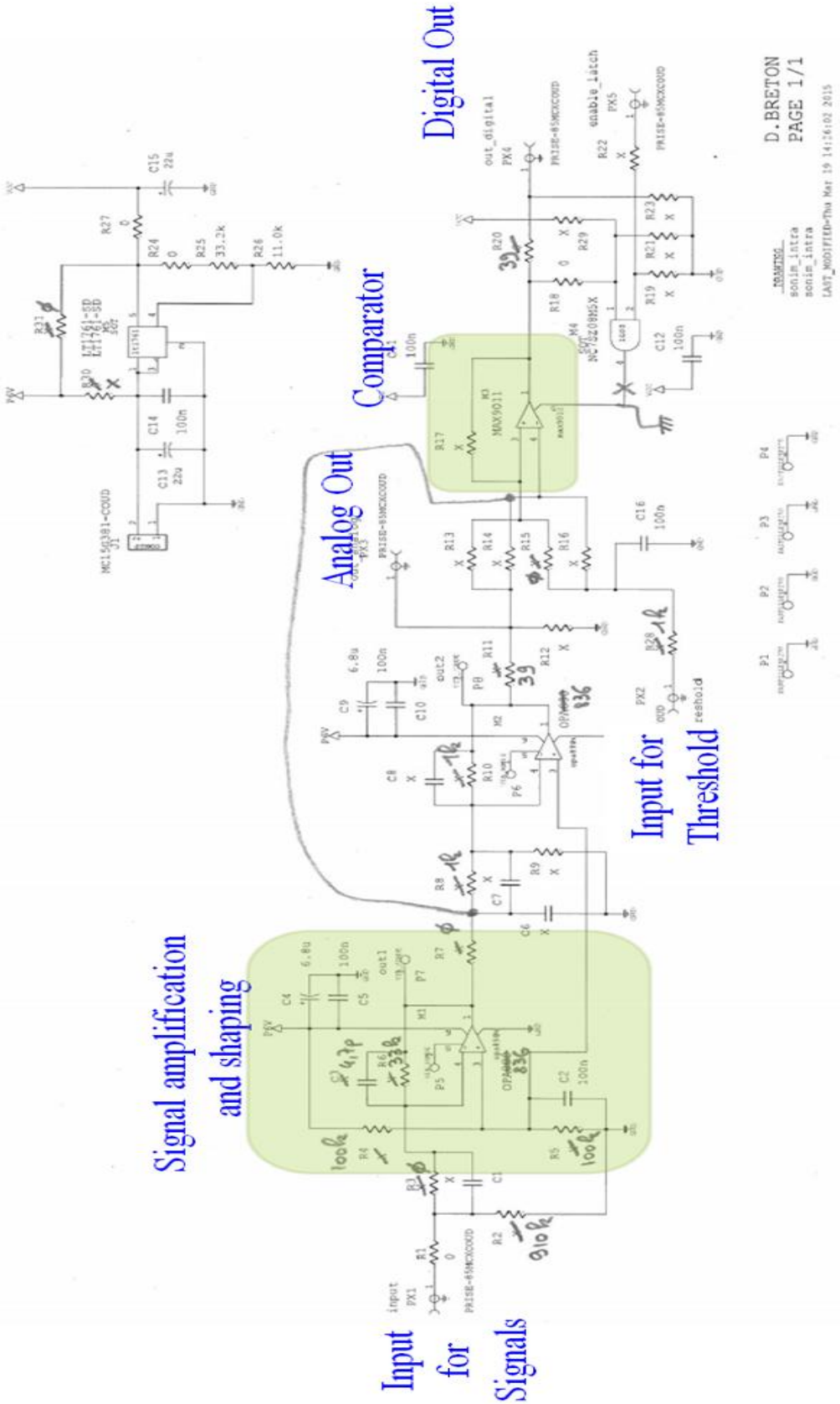

Figure 4.11 Electrical schematic of the dedicated miniaturized electronics

Typical output signals from both analog and digital outputs are presented in Figure 4.12. The digital output has been connected to the counter for counting TTL signals, while the analog output has been connected to a Tektronix TDS5054 oscilloscope for waveform acquisition.

Figure 4.12 Typical digital (red line) and analog (blue line) output signals from the dedicated miniaturized electronics

It should be pointed out that before the analog output, the SiPM signals are passing through an additional inverting stage (reserved for additional amplification stage), whereas in case of digital output the SiPM signals are passing directly to the comparator`s input. Therefore, we should keep in mind that the SiPM signals seen from the analog output are inversed with respect to the signals which are passing through the comparator and compared with a given threshold. Also, after the signal amplification and shaping, the SiPM signals have negative polarity and they are sitting on a constant DC offset of DC_{offset} = 1.746 V. Therefore the $V_{Threshold}$ is ranging from DC_{offset} = 1.746 V to 0 V. The $V_{Threshold}$ = 1.746 V is related to a situation when everything is crossing the threshold, while the $V_{Threshold}$ = 0 V is related to a situation when SiPM signals with amplitude bigger than 1.746 V are crossing the threshold. This DC_{offset} also affects the bias voltage of the SiPM. Therefore, the effective bias voltage applied to the SiPM is:

$$V_{bias}^{SiPM} = V_{bias} - DC_{offset} \qquad 4.1$$

where V_{bias}^{SiPM} – is the effective bias voltage applied to the SiPM and V_{bias} – is the instrumental bias voltage set by the Keithley 2611. For simplification, all values of the bias voltages in this Chapter will be presented as V_{bias}. Therefore, we should keep in mind that the real bias voltage of all measured devices is 1.746 V smaller.

4.2.3. **Test procedure**

Before acquiring a full set of data for all devices, the measurements performed with the SiPM connected to the custom read-out electronics and mounted on the IMNC experimental setup were calibrated with respect to the measurements carried out using the LAL cryogenic setup (detailed given in Chapter 3, Section 3.1). This calibration consisted of following steps:

- each SiPM was tested at 25 °C, using LAL cryogenic setup and analyzed by the automatic procedure (see Section 3.4). The measurements, were performed with blue laser light (λ = 467 nm). The laser trigger signal was positioned at 1.55 µs later with respect to the waveform beginning. These tests were aimed to determine the main SiPM parameters like working range, breakdown voltage V_{BD}, gain G and in the same time use the property of Poisson statistics (see Section 3.4.2 "Properties of Poisson statistics for DCR & P_{Geiger} calculation") to calculate the Geiger triggering probability P_{Geiger} and dark count rate DCR from the same set of data;

- the dark count rate DCR_{TTL} of SiPM with an amplitude exceeding a given comparator threshold $V_{Threshold}$ (i.e. counting the TTL signals from digital output) was tested using the IMNC setup. In the same time, the experimental waveforms were acquired from analog output. Therefore, the dark count rate DCR_{analog} of SiPM as a function of threshold was also calculated from the waveform analysis by applying the automatic procedure (detailed given in Chapter 3, Section 3.4.1). The DCR_{TTL} and DCR_{analog} were compared;
- the most adapted position of SiPM with respect to the optical fiber was determined, aiming to fix the SiPM in a position with maximum light collection.

For simplicity, the calibration procedure and the obtained results will be presented in this Section only for one SiPM device, namely for SIPM19-W3-TS-MP50-V1 from KETEK company.

SiPM characterization using LAL cryogenic setup

As it was already mentioned, the measurements were performed by using the LAL cryogenic setup (detailed given in Chapter 3, Section 3.1). The developed automatic procedure has been applied to experimental data to calculate the main SiPM parameters like breakdown voltage V_{BD}, gain G, P_{Geiger} and DCR.

The V_{BD} of 24.44 V has been obtained for SIPM19-W3-TS-MP50-V1 KETEK device at +25 °C. The G and 1 p.e. amplitudes as a function of overvoltage ΔV ($\Delta V = V_{bisa} - V_{BD}$) of SIPM19-W3-TS-MP50-V1 KETEK device are presented in Figure 4.13 and Figure 4.14 respectively. We can observe that this device can be operated at overvoltage range from ΔV = 0.3 V up to 9.5 V.

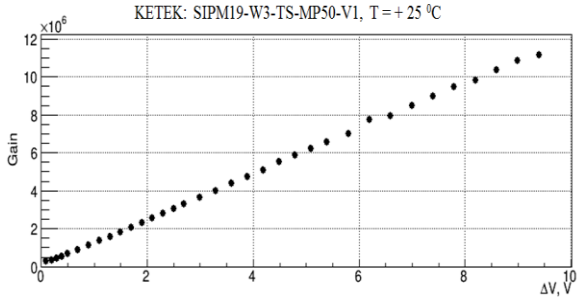

Figure 4.13 G vs. ΔV for the SIPM19-W3-TS-MP50-V1 produced by KETEK

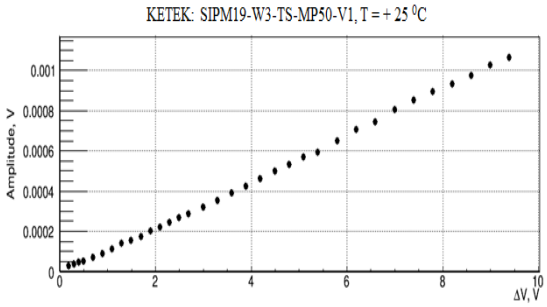

Figure 4.14 1 p.e. amplitude vs. ΔV for the SIPM19-W3-TS-MP50-V1 produced by KETEK

The DCR was calculated at 0.5 p.e. amplitude threshold and normalized to the device active area and it presented as a function of ΔV in Figure 4.15 a). The function with an exponential form (e.g. $f(\Delta V) = exp(a + b \times \Delta V)$, where a and b are free parameters) was used to approximate the experimental data and calculate the derivative $\frac{d(DCR)}{d(\Delta V)}$ which is presented in Figure 4.15 b). The $\frac{d(DCR)}{d(\Delta V)}$ indicates the speed of DCR increase with increasing ΔV. We can observe that the $\frac{d(DCR)}{d(\Delta V)}$ significantly increases from ΔV = 5 ÷ 6 V. Moreover, the total number of noise events will be enhanced by correlated noise which is presented by afterpulses and cross talk probabilities.

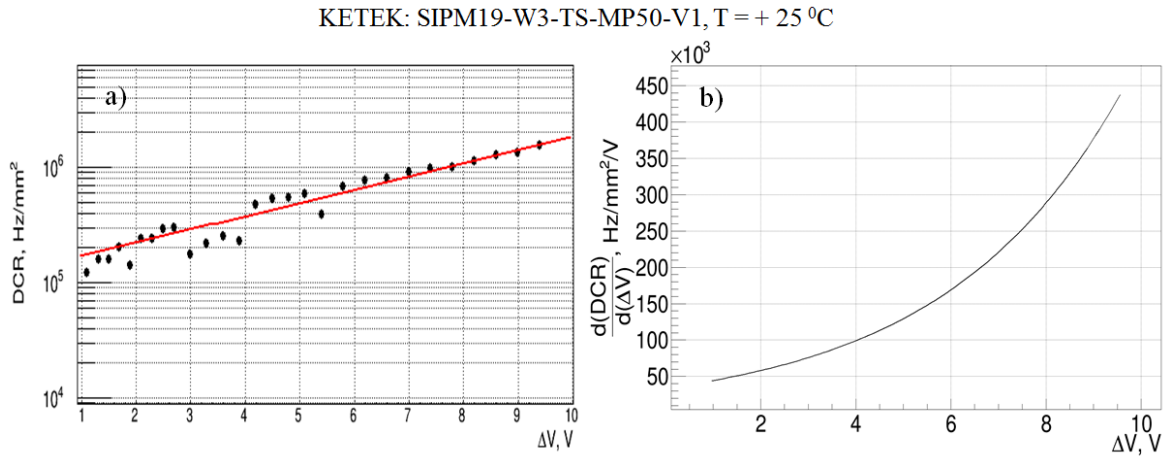

Figure 4.15 a) the normalized DCR to the device active area and b) its derivative $\frac{d(DCR)}{d(\Delta V)}$ as a function of ΔV for the SIPM19-W3-TS-MP50-V1 produced by KETEK

The cross talk probability as a function of ΔV is presented in Figure 4.16.

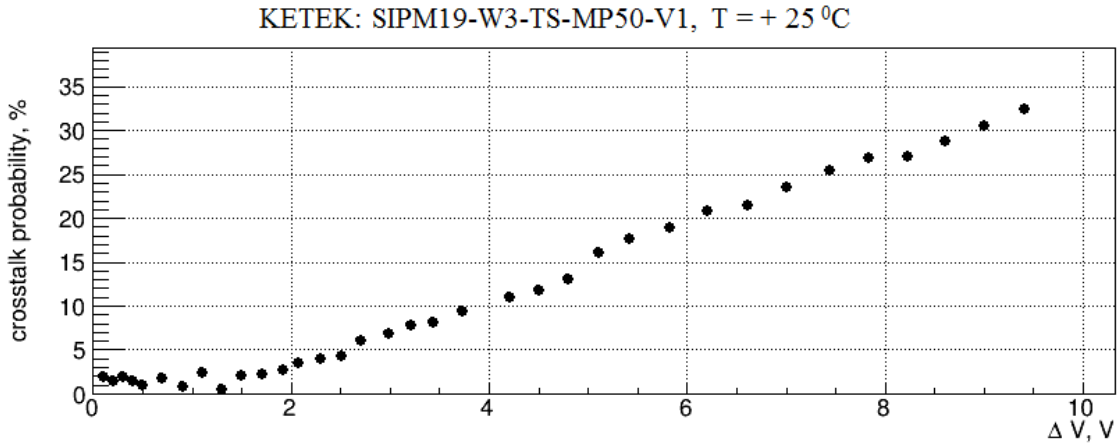

Figure 4.16) Cross talk probability as a function of ΔV for the SIPM19-W3-TS-MP50-V1 produced by KETEK

The P_{Geiger} as a function of ΔV is presented in Figure 4.17 a). The function with form presented by Eq. 3.67 has been used to fit the experimental data and calculate the derivative $\frac{d(P_{Geiger})}{d(\Delta V)}$ which is presented in Figure 4.17 b). The $\frac{d(P_{Geiger})}{d(\Delta V)}$ indicates the speed of P_{Geiger} increase with increasing the ΔV. We can observe that P_{Geiger} increases significantly with the increasing ΔV up to ~4 V. The further increasing of ΔV would not significantly increases the P_{Geiger} but dramatically increases the *DCR* and correlated noise (e.g. afterpulses and cross talk).

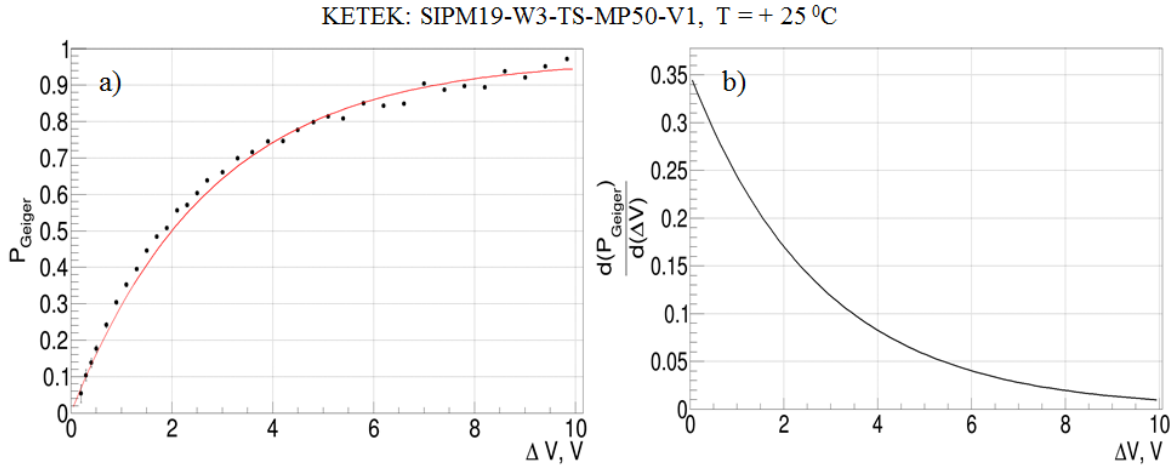

Figure 4.17 a) P_{Geiger} and b) its derivative $\frac{d(P_{Geiger})}{d(\Delta V)}$ measured for blue light λ = 467 nm as a function of ΔV for the SIPM19-W3-TS-MP50-V1 produced by KETEK

From these preliminary tests, we can expect the optimal working range for SIPM19-W3-TS-MP50-V1 KETEK device near $\Delta V = 4$ V. However, to make the final conclusions about optimal working range the measurements of the SiPM coupled to beta sensitive probe and read out by dedicated miniaturized electronics are required and will be presented in the Section 4.2.4 "Experimental results".

Calibration of DCR measured using the LAL and IMNC setups

The dark rate of SiPM pulses N_{pulses} with an amplitude exceeding a given comparator threshold $V_{Threshold}$ has been measured by counting the TTL signals. The measurements were performed as a function of $V_{Threshold}$ at different V_{bias} and two temperatures of +25 °C and +35 °C.

The variation of N_{pulses} with $V_{Threshold}$ corresponding to SIPM19-W3-TS-MP50-V1 KETEK device at +25 °C and a V_{bias} corresponding to an overvoltage of 3.78 V is presented in Figure 4.18 a). We can distinguish the stairs which are related to N_{pulses} at a $V_{Threshold}$ of 0.5, 1.5 and 2.5 p.e amplitude. From these stairs, the 1 p.e. amplitude was calculated as a difference between the second and first peaks of $\frac{\partial N_{pulses}}{\partial V_{Threshold}}$ spectrum (see Figure 4.18 b). The value of 1 p.e. amplitude will be used further to express the $V_{Threshold}$ in value of p.e. to be able to compare the experimental results at different V_{bias}.

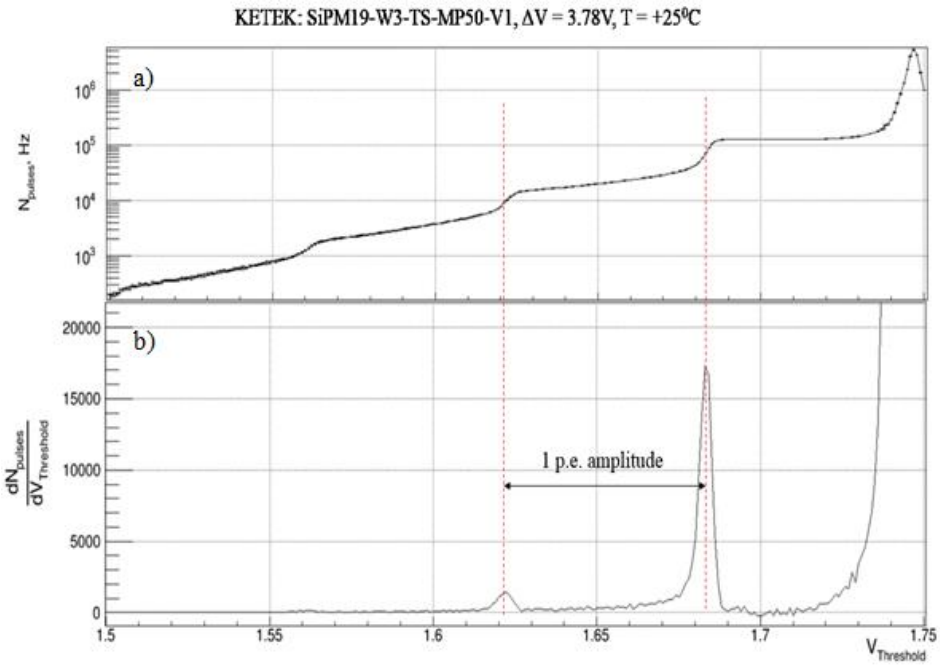

Figure 4.18 a) N_{pulses} and b) $\frac{\partial N_{pulses}}{\partial V_{Threshold}}$ as a function of $V_{Threshold}$ of SiPM19-W3-TS-MP50-V1 produced by KETEK, at ΔV = 3.78 V and T = 25 ^{0}C

We compared the N_{pulses} as a function of $V_{Threshold}$ at a given V_{bias} and T = 25 ^{0}C counted by the counter (digital output) and calculated from the waveform analysis using developed automatic analysis procedure[7] (analog output). Both measurements are presented in Figure 4.19 a), while a zoom near $V_{Threshold}$ of 1 p.e. amplitude is presented in Figure 4.19 b). A difference between the two measurements can be observed: in the range of $V_{Threshold}$ higher than 1 p.e., the N_{pulses} measured by counter (red line) shows slightly higher values with respect to measurements done with automatic analysis procedure (black line), whereas in the range of $V_{Threshold}$ smaller than 1 p.e., the opposite results can be seen. This difference is related to the presence of train of SiPM pulses, in particular to distinctive interpretation of their shapes given by the two used methods.

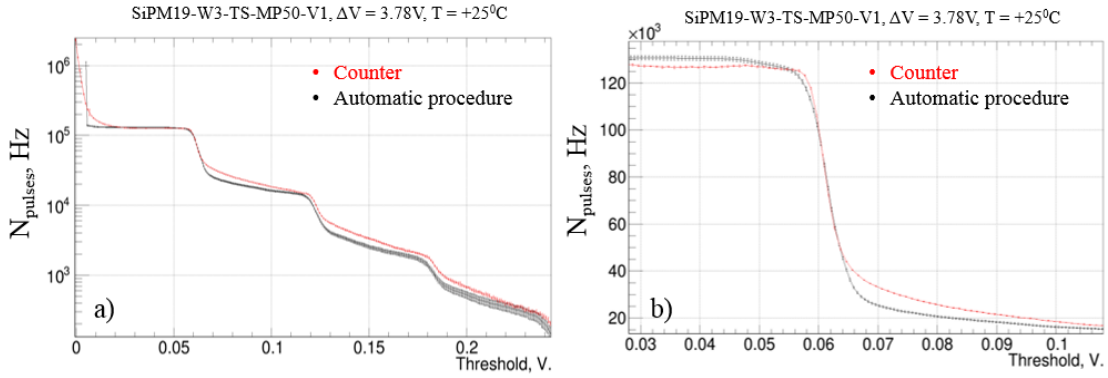

Figure 4.19 N_{pulses} as a function of $V_{Thresold}$. N_{pulses} has been measured with our readout electronics followed by the counter (red line) and with the automatic analysis procedure (black line), a) full spectrum b) zoom near $V_{Thresold}$ of 1 p.e. amplitude

As an example, let's take a typical train of pulses which consists of primary 1 p.e. pulse and secondary pulse represented by an afterpulse (see Figure 4.20, blue pulse). Our miniaturized read-out electronics followed by the counter will count such situation like a single event with

[7] Automatic procedure has been presented in the Section 3.4.1 "Automatic analysis procedure"

the amplitude of 80 mV. However, we can observe that developed automatic procedure decomposes the train of pulses into a primary pulse (orange line in Figure 4.20) and a secondary pulse (black line in Figure 4.20). Therefore, the automatic procedure will count such situation like two independent events, first with the amplitude of 58 mV and second with 42 mV. This situation explains exactly the difference which is observed in Figure 4.19 (a and b) between the two measurements.

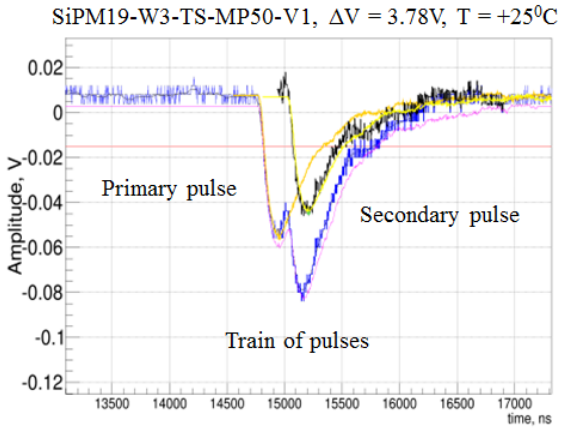

Figure 4.20 Typical SiPM train of pulses (blue line) decomposed in a primary pulse (orange line) and a secondary pulse (black line) by the automatic analysis procedure

We can conclude that the slow shaping time of miniaturized read out electronics enhanced the contribution of afterpulses phenomena into a total N_{pulses}. Nevertheless, this slow shaping time of miniaturized read out electronics allows to significantly reduce high frequency electronic noise and power consumption which are also the key requirements.

Determination of SiPM position for light collection optimization

As it was already pointed out before, the beta sensitivity is one of the most important parameters for our application. Therefore, to achieve the highest sensitivity and to optimize the light collection, the measured SiPM device has to be positioned in front of the optical fiber, as shown in Figure 4.10. To find this position, the collimator has been fixed on a micrometric motorized stages and its position has been varied in both *X* and *Y* directions. At each (*X*, *Y*) position the amplitude of the SiPM signals from the analog output has been measured and the corresponding 3D plot is shown in Figure 4.21.

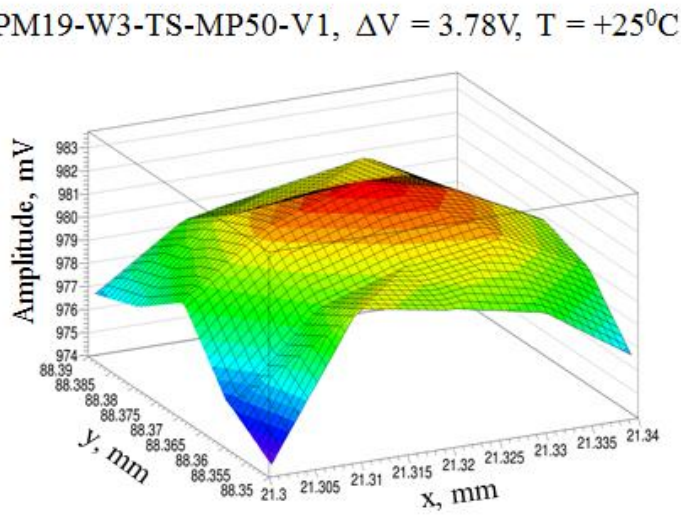

Figure 4.21 SiPM signals amplitude as a function of collimator position

Figure 4.21 shows that significant variation of ~20 μm of the collimator position (which is 4% of the SiPM size) is leading to a minor variation of ~0.5% for the sensitivity. This behavior can be related to the fact that the diameter of the light spot at the output of the fiber is bigger than SiPM sensitive area. The light spot diameter can be calculated as:

$$d = d_0 + 2 \times l \times \frac{NA}{\sqrt{1 - NA^2}} \qquad 4.2$$

where d_0 – is the fiber diameter, l – is the distance between the end of fiber and the SiPM sensitive area, defined by the thickness of the epoxy resin on the top of SiPM, NA – is the numerical aperture of the plastic fiber. For the typical values of l = 0.5 mm and NA = 0.6, d ~0.98 mm. Moreover, this increase of the light spot`s diameter leads to the fact that only a part P of the scintillating photons will reach the SiPM device. P can be calculated as:

$$P = \frac{S_{SiPM}}{S} \times 100\% = \frac{a_{SiPM}^2}{\pi r^2} \times 100\% = \frac{4 \cdot a_{SiPM}^2}{\pi d^2} \times 100\% = 65\% \qquad 4.3$$

where S_{SiPM} – is the SiPM active area, S – is the light spot area, a – is the SiPM`s lateral size. Therefore, for the typical values of l = 0.5 mm and NA = 0.6 only 33% of scintillating photons will reach the SiPM active area.

The experimental results presented later in the chapter were obtained with the collimator located on the position where the highest amplitude was observed. It should be pointed out that, to reach the higher number of events per unit of time and therefore to speed-up the defining of the SiPM position, the ^{204}Tl and the fiber have been replaced by a LED.

4.2.4. **Experimental results**

For each SiPM device, the N_{pulses} has been measured as a function of $V_{Threshold}$ with and without ^{204}Tl source at different V_{bias} and two T (+25 ^{0}C and +35 ^{0}C). Typical results obtained at +25 °C for SIPM19-W3-TS-MP50-V1 KETEK device are presented in Figure 4.15. At each V_{bias} and T, three parameters were calculated:

- E_{max} – the energy spectrum endpoint, calibrated in photoelectrons;
- $V_{Threshold}^{DCR=1Hz}$ – the value of the threshold, expressed in photoelectrons, which should be applied to remove the thermal (*DCR*) and correlated (cross-talk and afterpulses) noise down to 1 Hz;
- N_{beta} – the number of pulses, which is counted at $V_{Threshold} = V_{Threshold}^{DCR=1Hz}$.

The values of E_{max}, $V_{Threshold}^{DCR=1Hz}$ and N_{beta} at +25 °C and a given bias voltage are presented in Figure 4.16.

The aim of the final test is to compare the N_{beta} from the different SiPM devices at $V_{Threshold} = V_{Threshold}^{DCR=1Hz}$. The $V_{Threshold}^{DCR=1Hz}$ is mostly defined by cross-talk probability which enhances the amplitude distribution of the dark count signal well above the 1 p.e. level. Since the cross talk probability is related to a number of charges created in one avalanche (i.e. SiPM gain) the experimental results for different devices should be compared at the same gain G.

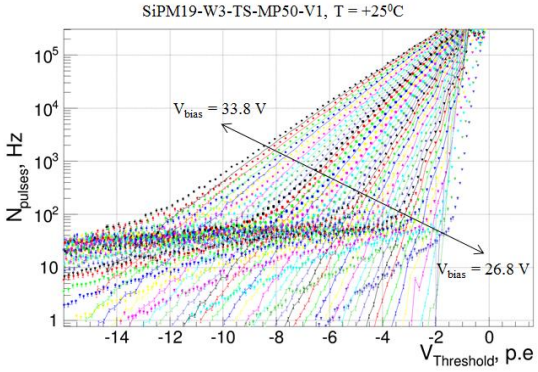

Figure 4.15 N_{pulses} as a function of $V_{Threshold}$ measured in dark conditions (lines) and with ^{204}Tl source (dots) at different V_{bias}

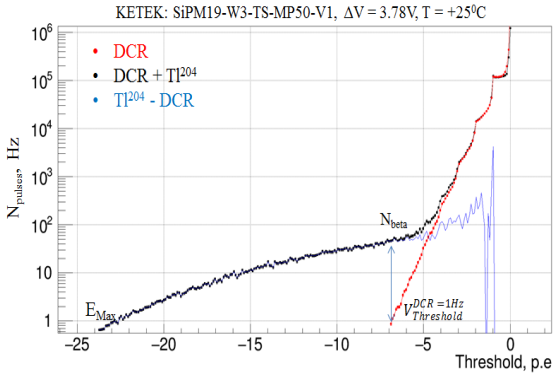

Figure 4.16 N_{pulses} as a function of $V_{Threshold}$ expressed in photoelectrons measured in dark condition (red line), with Tl^{204} source (black line) and the difference between them (blue line). The parameters E_{max}, $V_{Threshold}^{DCR=1Hz}$ and N_{beta} are presented too

The $V_{Threshold}^{DCR=1Hz}$ and E_{max} calibrated in photoelectrons number are presented in Figure 4.17 (a and b) and Figure 4.18 (a and b) respectively as a function of SiPM gain for all measured devices. From the Figure 4.17 we can observe that to achieve the thermal (*DCR*) and correlated (cross-talk and afterpulses) noise level of 1 Hz, the SiPM devices produced by KETEK require two times lower threshold with respect to the Hamamatsu device. This observation was expected due to the small active area (field of view) of the KETEK devices. Conversely, their small field of view impacts the scintillation light collection, as can be observed in Figure 4.18. We can observe a ~70% decrease between the E_{max} of the spectra measured with the Hamamatsu and the KETEK devices. This light loss is related to the enlarge size of the light spot due to the thickness of the protective epoxy resin and the acceptance angle of the fiber, as it was already shown in the previous Section.

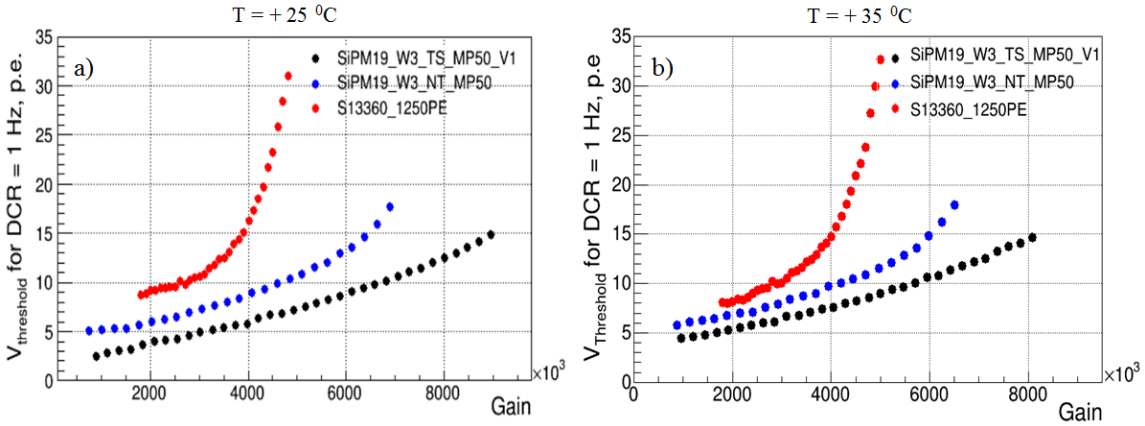

Figure 4.17 $V_{Threshold}^{DCR=1Hz}$ as a function of SiPM gain for all measured devices: a) at + 25 °C and b) + 35 °C

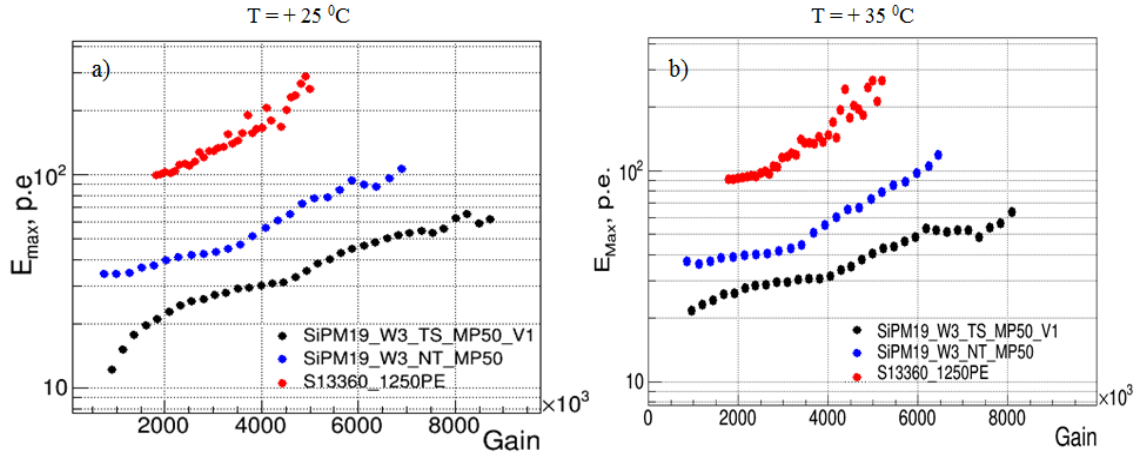

Figure 4.18 E_{max} as a function of SiPM gain for all measured devices: a) at + 25 °C and b) + 35 °C

The N_{beta} as a function of SiPM gain for all measured devices at both T is presented in Figure 4.19 (a and b). For all measured devices and both T we can distinguish a similar behavior of N_{beta} with SiPM gain. We can observe that the KETEK device SiPM19-W3-TS-MP50-V1 shows the lowest noise (e.g. $V_{Threshold}$ for DCR = 1 Hz) and highest possible gain (e.g. working range) due to reduced cross talk probability because of trench technology. However, this technology cost the geometrical fill factor (detailed given in Chapter 2, Section 2.2.4 "Photon detection efficiency (PDE)") which leads to the lowest light collection, as illustrated by the E_{max} values, and thus, the lowest final beta sensitivity N_{beta}. Since the beta sensitivity is a tradeoff between PDE and noise (e.g. DCR, cross-talk and afterpulses), the SiPM device without tranches and produced by KETEK (SiPM19-W3-NT-MP50) shows similar performances at both T as the SiPM device produced by Hamamatsu, despite an amount of scintillation light three times smaller. Therefore, we can expect that an improvement of the light collection efficiency by using focusing lens between the fiber and the SiPM should significantly improve the beta sensitivity of future intracerebral probes based on SiPM SiPM19-W3-TS-MP50 device.

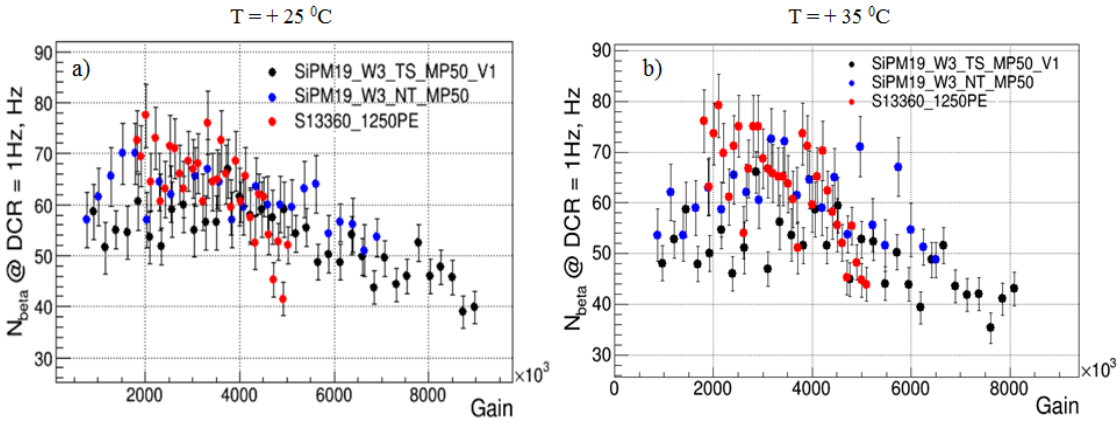

Figure 4.19 N_{beta} as a function of SiPM gain for all measured devices: a) at + 25 ^{0}C and b) + 35 ^{0}C

5. Summary of SiPM parameters investigations and perspectives

5.1. Summary

The main scope of this thesis was the investigation of SiPM physics parameters in the context of temperature and bias voltage variation and for a biomedical application.

To provide these researches, in a first step I took part to the full spectrum of experimental an work like:

- the design, installation, commissioning and calibration of a cryogenic experimental setup dedicated for electrical, optical and temperature characterizations of SiPM devices. The measurements can be performed in dark or light conditions (LED or pulsed laser diode) at different temperatures from 350 K down to 14 K;
- software development to provide automatic:
    - Dynamic and static measurements of various SiPM devices as a function of bias voltage, temperature and intensity of light sources (e.g. LED or pulsed laser diode);
    - Acquisition and analysis of huge amount of experimental data (tens of Gb/device).

As a result, the automatic analysis procedure developed initially for experimental data analysis and based on ROOT data Analysis Framework, grown subsequently into an independent software which can be used beyond the analysis of SiPM parameters. In particular, to calculate the general characteristics of output pulses from various detectors types, like charge, amplitude, signal shapes (e.g. leading edge and falling edge), etc. Moreover, the algorithm of baseline restoration, developed as part of the software, can be of very good utility in all applications with AC-coupled readout systems.

Once the experimental setup and the analysis procedure were calibrated and running, I have used them to study the physics parameters of various SiPM devices from 2015 production year:

- with different technological characteristics like p/n and n/p junctions, with and without trench technology, and different widths of epitaxial layer produced by KETEK company; these devices were tested in a temperature range from 308.15 K (+35 °C) down to 238.15 K (-35 °C).
- with improved technological characteristics inducing a reduced noise produced by Hamamatsu company; these devices were tested in a wider temperature range from 318.15 K (+45 °C) down to 98.15 K (-175 °C); for calibration and comparison purposes, an old Hamamatsu device from 2011 production run was also tested in the same conditions.

From these investigations, a complete set of AC electrical parameters like gain G, breakdown voltage V_{BD}, microcell capacitance $C_{\mu cell}$, pulse shape, quenching resistance R_q, dark count rate DCR and cross talk probability were calculated as a function of temperature. From the variation of DCR with temperature, the activation energy E_{act} for each SiPM device has been also calculated. The activation energy E_{act} gives us an indication to the dominant source of carrier generation (e.g. Shockley-Read-Hall, injection from neutral region, trap-assisted tunneling or Band-to-band tunneling) determining the dark count rate DCR and consequently leading to the

limitation of use the SiPM detectors as single photon detector at room temperature. Also, it has been shown that the value of microcell capacitance $C_{\mu cell}$ can be used to calculate the structure parameter like thickness of epitaxial layer. Detector properties like photon detection efficiency *PDE* and associated Geiger triggering probability P_{Geiger} were also be evaluated.

Further on, based on the knowledge obtained from the investigations of SiPM electrical and optical parameters described previously, the main physical mechanisms contributing to the shape of the reverse IV characteristic have been defined, namely the bulk thermal generated carriers enhanced by SiPM gain, Geiger triggering probability P_{Geiger} and afterpulsing probability. These mechanisms have been used to develop a physical model describing the SiPM IV shapes over full device working range. The proposed model has been tested on SiPM devices mentioned previously, in dark conditions from 308.15 K (+35 °C) down to 238.15 K (-35 °C) and in addition, illuminated by blue (λ = 467 nm) and red (λ = 635 nm) laser light from 318.15 K (+45 °C) down to 98.15 K (-175 °C). It has been shown that the proposed model fits well the shape of IV curve in a very large currents range from 10^{-12} A up to 10^{-5} A over the full working range of various devices. Consequently, the IV model can be used as a simple and fast method for determination of SiPM parameters like breakdown voltage V_{BD}, the shape of Geiger triggering probability P_{Geiger} as a function of V_{bias} as well as the V_{bias} working range and their variation with temperature. It has been found that the shape of Geiger triggering probability P_{Geiger} changes with changing the temperature in given conditions of light wavelength and device technological structure (p/n or n/p junction).

To confirm that the proposed IV model can be used as a simple and fast method for determination of SiPM parameters (in particular in the applications where huge numbers of the detectors are used and need to be characterized) the obtained results have been compared with those calculated from AC measurements. It has been found that, for all studied devices and temperatures, the breakdown voltage calculated from IV model has slightly higher value (~100 mV) with respect to one calculated from AC measurements. This discrepancy reflects the fundamental difference in the physical significance of the "breakdown" voltage determined by these two methods. The "IV-based" measurement is sensitive to the avalanche phenomenon and it determines the "breakdown" as defined by fundamental papers of McIntyre. The AC/Gain linearity method determines the voltage to which the voltage across the diode is reduced to quench the avalanche. The latter is naturally lower than the former and our results are consistent with this expectation.

In the second part of my thesis I took part to the investigation of SiPM devices and their physical parameters required to build a prototype of beta-sensitive intracerebral probe dedicated to neurocerebral studies. In particular, three SiPM devices of 50 × 50 μm^2 μcell size have been chosen as the most adapted for our application:

- two small devices of 0.5 × 0.5 mm^2 size, with and without optical trenches, specially developed by KETEK company to fulfill our requirements;
- one standard Hamamatsu device of 1.3 × 1.3 mm^2 size.

To study these devices in the context of our application, I participated to the development of an experimental setup based on a beta radioactive source (^{204}Tl), a scintillating fiber coupled to the SiPM and a miniaturized read-out electronics. In particular, I contributed to setup installation and commissioning as well as to the development of the data acquisition software. Subsequently, I have performed measurements of the SiPM gain *G*, the dark count rate *DCR*

and the beta sensitivity as a function of V_{bias} at two temperatures: 298.15 K (+25 ^{0}C) and 308.15 K (+35 ^{0}C).

For calibration purposes, I compared the *DCR* values with those measured with the cryogenic setup and analyzed by the automatic developed procedure and I demonstrated that, based on the used readout electronics and data analysis method, small differences can be found.

From the application point of view, the obtained results showed that the small field of view and newly developed structure of the KETEK devices allow a large decrease of the dark count rate *DCR*. However, this small field of view also leads to a reduced light collection due to the thickness of the epoxy protection resin on top of the SiPM and the acceptance angle of the fiber. Since the beta sensitivity represents a tradeoff between photon detection efficiency *PDE* and dark count rate *DCR*, KETEK SiPMs exhibit similar performances in comparison with the Hamamatsu device. Preliminary results demonstrate that the beta sensitivity of KETEK devices can be significantly improved by using focusing lens between the scintillating fiber and the SiPM or by reducing the thickness of the epoxy protection resin.

5.2.Perspectives

The experimental data acquired during my thesis include much more information than has been possible to extract up today due to limited time. In particular, the probability of afterpulses and their lifetime temperature dependence, and the physics of non-quenched pulses can be studied. Moreover, these phenomena have not been yet studied in such wide temperature range and the developed automatic procedure has enough capacity for such investigation. In particular, the developed analysis procedure includes an algorithm to separate and reconstruct the shapes of primary pulses and afterpulses if the time interval between them is at least equal to SiPM rise time (~10 ns for our read-out chain).

It has been observed that the shape of Geiger triggering probability of Hamamatsu devices (p/n structure) shows much stronger variation with temperature for red light (λ = 635 nm) with respect to blue light (λ = 467 nm). However, measurements with only two different wavelengths are not enough to quantify such phenomena. Therefore, additional measurements (AC and DC) with at least one short wavelength (λ = 300 ÷ 400 nm.) and one long wavelength (λ = 800 ÷ 1000 nm.) would be extremely useful to complete these studies.

Also, to conclude the part related to bio-medical investigation, it would be very nice to do the measurements with focusing lens between the scintillating fiber and the SiPM.

Last but not the least, would be work to finalize/prepare a user-friendly interface for automatic procedure for data analysis and for developed reverse IV model. This work will allow to share these programs with another scientists.

A. Resume

Le photomultiplicateur en silicium (SiPM) est devenu un détecteur de lumière / photon adapté à de nombreuses applications telles que les expérimentations en physique de haute énergie et les expériences neutrinos, la détection de la fluorescence, la biophotonique et l'imagerie médicale. Les principaux avantages de ces composants tiennent dans leur compacité (épaisseur des plaquettes de Si ~300µm), une surface de détection ajustable (de un à plusieurs centaines de canaux de lecture), un fonctionnement à faible tension de polarisation (c.-à-d. Vbias< 80 V), un gain élevé (G~105÷107), une réponse rapide (quelques dizaines de picosecondes de résolution temporelle pour un photon), et une insensibilité aux champs magnétiques (jusqu'à 7 T).

Pour obtenir les meilleures performances pour une application donnée, il faut considérer deux points importants : (1) Les paramètres physiques comme le gain G, la tension de claquage Vbd, la forme du signal, la capacité de la µ-cellule Cµcell, la résistance d'amortissement Rq, le taux de bruits de comptage DCR (c.-à-d.: bruit thermique, postimpulsion, perturbations de diaphonie) ainsi que leurs variations en fonction de la température doivent être connus, mais également leur impact sur la qualité de la mesure doit être comprise ; (2) Le composant SiPM doit être sélectionné sur certains critères technologiques et sur l'adéquation de ses paramètres géométriques à l'application.

Pendant la préparation de ma thèse j'ai étudié plusieurs types de SiPM de même taille de µ-cellule (50×50µm2) produits par deux sociétés (KETEK et HAMAMATSU), et j'ai concentré mes analyses sur l'amélioration de nos connaissances concernant les paramètres mentionnés précédemment.

La première partie de ma thèse concerne l'étude des divers paramètres physiques des SiPM en fonction de température T. En particulier, des composants récents (2015) de KETEK ayant diverses caractéristiques technologiques comme des jonctions p/n ou n/p, avec ou sans technologie de rainure, différentes épaisseurs de couches épitaxiales, etc. ont été étudiés dans la gamme de T de 308.15 K (+35°C) à 238.15 K (-35°C). En plus, des composants Hamamatsu de production 2011, ainsi que de production 2015 avec des caractéristiques technologiques améliorées (faible bruit), ont été testés dans la gamme 318.15K (+45°C) à 98.15K (-175°C).

Dans le cadre de ma thèse, j'ai participé à la conception, l'installation et l'étalonnage d'un dispositif expérimental dédié à la caractérisation électrique et optique ainsi qu'à la caractérisation de T des appareils SiPM. Les mesures peuvent être effectuées dans les conditions sombres ou claires (diode laser à LED ou à impulsions) à différentes T de 350 K à 14 K.

Une vue générale du dispositif expérimental est présenté sur la Figure 1. Le dispositif est équipé d'un cryoréfrigérateur He à cycle fermé d'Advanced Research System qui fonctionne selon le principe thermodynamique de Gifford McMahon. Le dispositif est composé d'un compresseur, des conduites de gaz et d'une soudure froide située à l'intérieur de la chambre climatique. Pour réduire l'échange thermique avec la température ambiante la chambre climatique a été réalisée dans des conditions de vide à P <10-4 mbar assurée par des pompes primaires et turbo-moléculaires.

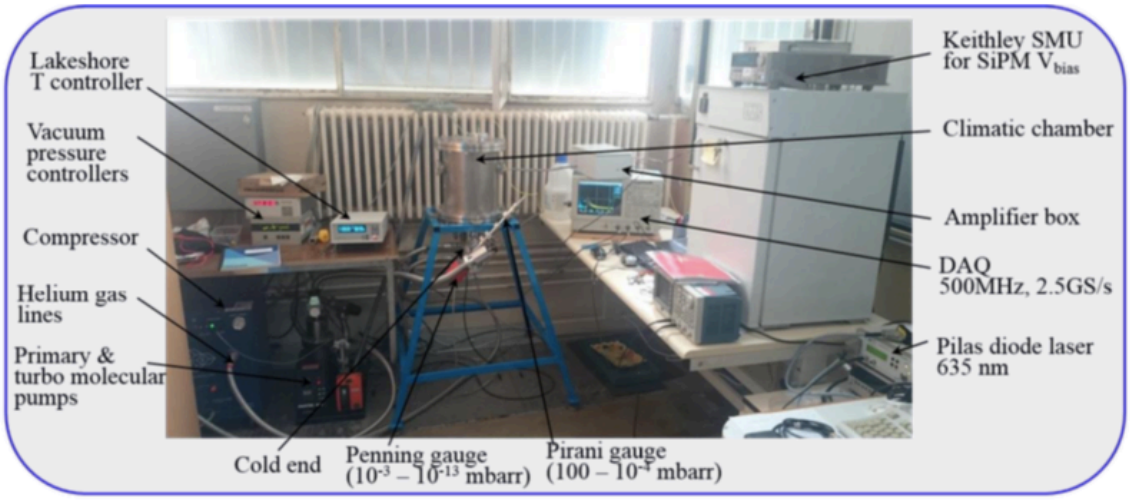

Figure A.1 *Dispositif expérimental développé au LAL pour la caractérisation des dispositifs SiPM dans une plage de T de 14 K à 350 K*

En utilisant le dispositif développé on a réalisé deux séries de mesures de courant AC et DC :

- La première série de mesures a été effectuée dans la plage T de 238,15 K à 308,15 K, par pas de 10 K. Lors des mesures en continu (avant et arrière), les dispositifs de SiPM ont été opérés dans un état sombre. Tandis que lors de la mesure en courant alternatif des dispositifs de SiPM ont été illuminés par des impulsions laser de la lumière de faible intensité de longueur d'onde différente (par exemple. 467 nm, 523 nm et 635 nm). Lors de cette série de mesures, sept appareils SiPM ont été testés :
  - Trois appareils produits par Hamamatsu, d'une superficie totale de 3 × 3 mm2 et d'une taille de celluleμ de 50 × 50 μm2 (N μcellules = 3600) :
    - S10931-050P, cet appareil a déjà été étudié avec l'utilisation de l'installation FermiLab (Dinu, Nagai et Para, études de détecteurs MPPC à des températures cryogéniques 2015) et il sert de référence pour l'étalonnage de comparaison entre les configurations LAL et Fermilab; il faut noter que cet appareil provient d'une production de 2011 ;
    - S13082-050CS(X), cet appareil vient d'une production de 2015 et a une faible probabilité de post-pulsation comme indiqué dans la fiche technique Hamamatsu;
    - S13360-3050CS, cet appareil vient également d'une production de 2015 et en plus d'une faible probabilité de post-impulsion, il a une faible probabilité d'interférence ;
  - Quatre dispositifs produits par KETEK, d'une surface totale de 0,5 × 0,5 mm2 et d'une taille de μcellule de 50 × 50 μm2 (Nμcellules = 100). Tous les appareils proviennent d'une production de 2015.
    - Deux appareils à structure P-sur-N :
      - SiPM19-W3-MP50-NT, sans tranchées (rainures) ;
      - SiPM19-W3-MP50-V1, avec tranchées (rainures) ;
    - Deux appareils à structure P-sur-N et sans tranchées (rainures) :
      - SiPM20-W4-50NT, avec la couche épitaxiale de type p plus mince avec la profondeur de 2,0 μm ;

- SiPM20-W5-50NT, avec la couche épitaxiale de type p plus épaisse avec la profondeur de 2,4 μm.

- La deuxième série de mesures a été effectuée dans la plage T de 98,15 K à 318,15 K par pas de 20 K. Pendant les mesures en courant DC, les dispositifs SiPM étaient utilisés dans des conditions sombres, alors que les mesures en courant AC étaient effectuées dans des conditions différentes : sombre et éclairé par trois intensités différentes (faible, moyenne et élevée) d'impulsions laser de lumière de deux longueurs d'onde différentes (par exemple 467 nm, 635 nm). Pendant les mesures en courant alternatif, les dispositifs de SiPM ont été illuminés par des impulsions laser de lumière d'intensité faible de deux longueurs d'onde différentes (par exemple 467 nm et 635 nm). Lors de cette série de mesures, trois appareils SiPM produits par Hamamatsu ont été testés: S10931-050P, S13082-050CS (X) et S13360-3050CS (plus de détails sur ces dispositifs sont donnés ci-dessus).

Pour chaque appareil étudié, les mesures en courant continu ont été effectuées avant celles en courant alternatif car elles sont beaucoup plus simples, plus rapides et la plage de fonctionnement du dispositif peut être déterminée. A partir de ces mesures, la tension de claquage VBD pour chaque appareil à T donnée a été déterminée et utilisée dans d'autres mesures en courant alternatif.

Au cours des mesures AC, à chaque T 10000 formes d'onde de 2 μs de longueur (la première série de mesures) et 4 μs de longueur (deuxième série de mesures) ont été acquises à différents Vbias. La collecte de données a été déclenchée par le laser avec le signal laser positionné à 1,55 μs après le début de la forme d'onde. La tension de claquage V_{BD} de SiPM se modifie avec T. Par conséquent, pour mesurer les dispositifs dans des conditions de fonctionnement comparables indépendantes de T, chaque Vbias a été sélectionné pour obtenir le même ΔV par rapport à V_{BD}. Le modèle de Hamamatsu SiPM de 2011 a été mesuré dans une plage ΔV de 0,4 V <ΔV <2,7 V, tandis que les modèles Hamamatsu et KETEK SiPM de 2015 ont été mesurés dans une plage ΔV de 0,4 V <ΔV <10 V. La limite supérieure de la plage de tension de polarisation est imposée par l'apparition d'une forte post-pulsation conduisant à la saturation de l'amplificateur et aux décalages de la ligne de base. Les appareils Hamamatsu de 2011 ont une plage de fonctionnement ΔV de seulement 2,7 V, tandis que la dernière génération des deux fournisseurs a un ΔV ~ 10 V supérieur, ce qui montre une amélioration considérable de la technologie SiPM.

Les caractéristiques dynamiques conduisent à une quantité énorme de données expérimentales (des dizaines de Go / dispositif). Par conséquent, une procédure automatique pour l'analyse des données, basée sur le cadre d'analyse des données ROOT, a été développée. Cette procédure utilise des formes d'onde expérimentales de l'oscilloscope comme fichiers d'entrée et crée des fichiers N-tuples de sortie avec des caractéristiques d'impulsions SiPM pour chaque condition expérimentale (T et Vbias). Les principales étapes de l'algorithme développé sont les suivantes :

- Analyse de forme d'onde pour éliminer la différenciation de la forme d'onde déterminée par l'électronique de lecture (readout-electronics) et pour rétablir sa base zéro ;
- Procédure de recherche d'impulsions pour déterminer les intervalles de temps contenant des impulsions SiPM ;

- Analyse des caractéristiques de l'impulsion SiPM pour calculer les principaux paramètres SiPM.

Le développement et l'étalonnage de la procédure automatique ont été réalisés d'après des données expérimentales de deux appareils Hamamatsu : S10362-11-050U et S10931-050P mesurés antérieurement pour ma thèse (travaux effectués par A. Para, N. Dinu et l'équipe technique de Fermilab). Cette procédure a fonctionné avec succès et par conséquent, elle a été utilisée pour les analyses des appareils SiPM les plus récents mesurés par moi-même avec l'utilisation de l'installation cryogénique LAL. En particulier, un ensemble complet de paramètres électriques alternatifs tels que le gain G, la tension de claquage V_{BD}, la capacité microcellulaire Cμcell, la forme des impulsions, la résistance d'amortissement Rq, le taux de bruits de comptage DCR et la diaphonie optique ont été calculés. Les propriétés du détecteur telles que l'efficacité de détection des photons EDP et la probabilité de déclenchement Geiger associée PGeiger ont également été évaluées. Certains résultats typiques sont présentés sur la figure 2, Figure 3, Figure 4, Figure 5 et Figure 6.

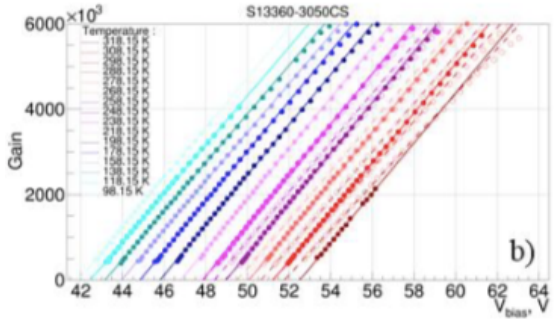

Figure A.2 Gain vs. V_{bias}

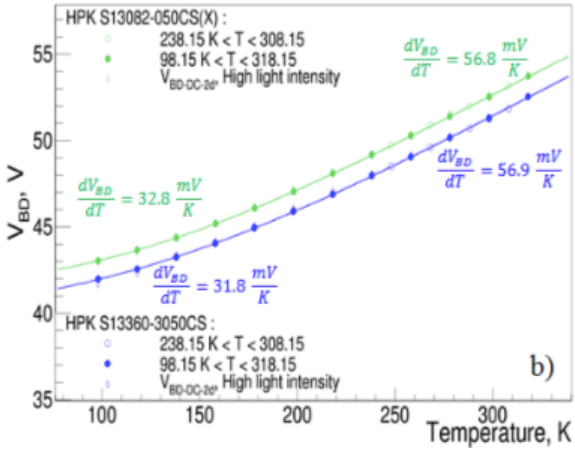

Figure A.3 V_{BD} vs. Température

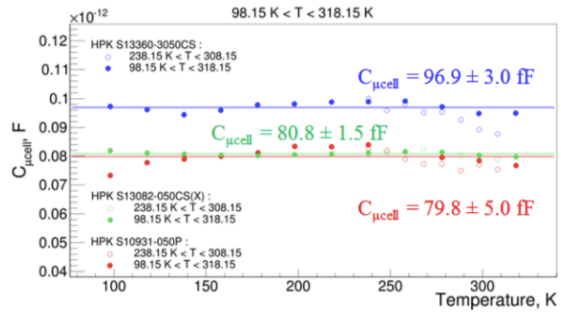

Figure A.4 Capacité vs. Température

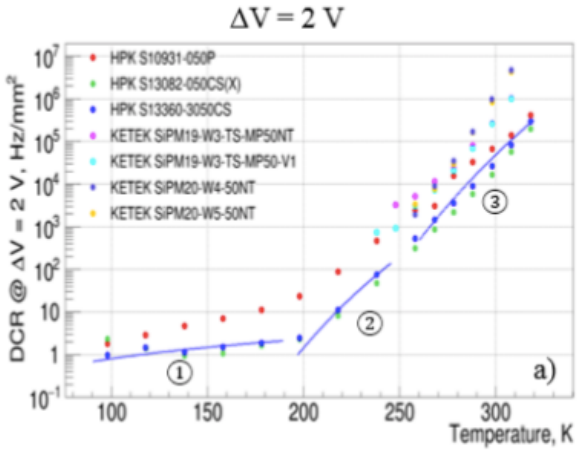

Figure A.5 DCR vs. Température

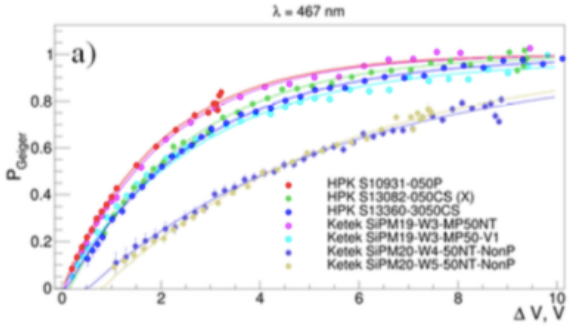

Figure A.6 Probabilité Geiger en fonction de la surtension

J'ai également développé un modèle physique décrivant les courbes DC I-V des détecteurs SiPM à différentes températures. Le modèle proposé s'adapte bien à la forme de la courbe IV dans une très grande gamme de courants allant de 10-12 A à 10-5 A sur toute la plage de fonctionnement de divers dispositifs (voir la Figure 7). Par conséquent, le modèle IV peut être utilisé comme méthode simple et rapide pour déterminer les paramètres SiPM tels que la tension de claquage V_{BD}, la forme de la probabilité de déclenchement Geiger en fonction de Vbias ainsi que la plage de travail Vbias. La comparaison de ces paramètres avec ceux calculés à partir des mesures en courant alternatif et analysés par la procédure automatique montre un bon accord.

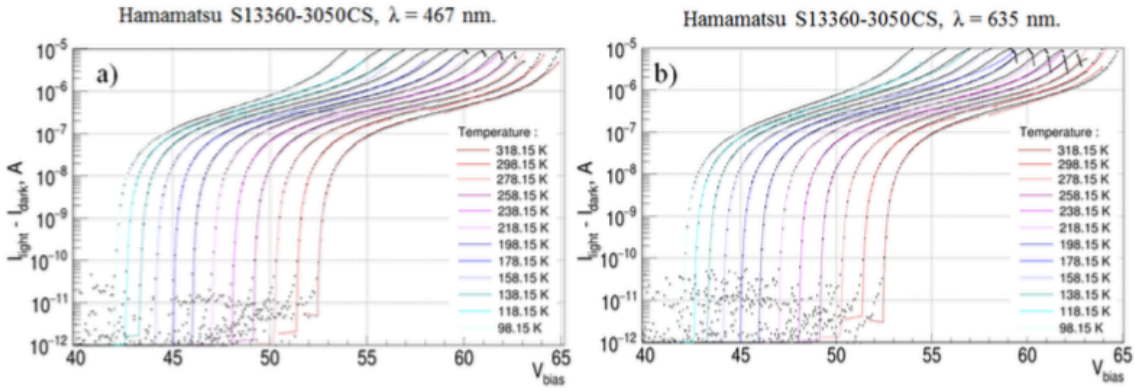

Figure A.7 Exemple de courbes IV inversées adaptées au modèle IV développé

La deuxième partie de ma thèse a été orientée vers l'étude des dispositifs SIPM et leurs paramètres physiques nécessaires à la construction d'un prototype de sonde intracérébrale bêta-sensible. Cette sonde est dédiée à la mesure de la concentration locale de molécules radiomarquées sur des animaux éveillés et en liberté et à l'étude de nouveaux modèles animaux de pathologies humaines (maladies neurodégénératives, croissance tumorale et troubles neuropsychiatriques). La sonde intracérébrale bêta-sensible est composée d'un appareil SiPM de petite taille et à faible bruit couplé à une fibre scintillante et est lu par une électronique à faible consommation d'énergie miniaturisée (voir la Figure 8). Trois appareils SiPM ont été choisis comme les plus adaptés à notre application :

- deux petits appareils KETEK de taille 0,5 × 0,5 mm2 (avec et sans tranchées (rainures) optiques, spécialement développés par KETEK pour répondre à nos exigences) ;
- appareil Hamamatsu standard de taille 1,3 × 1,3 mm2, tous les appareils ayant une taille de cellule de 50 × 50 μm2μ.

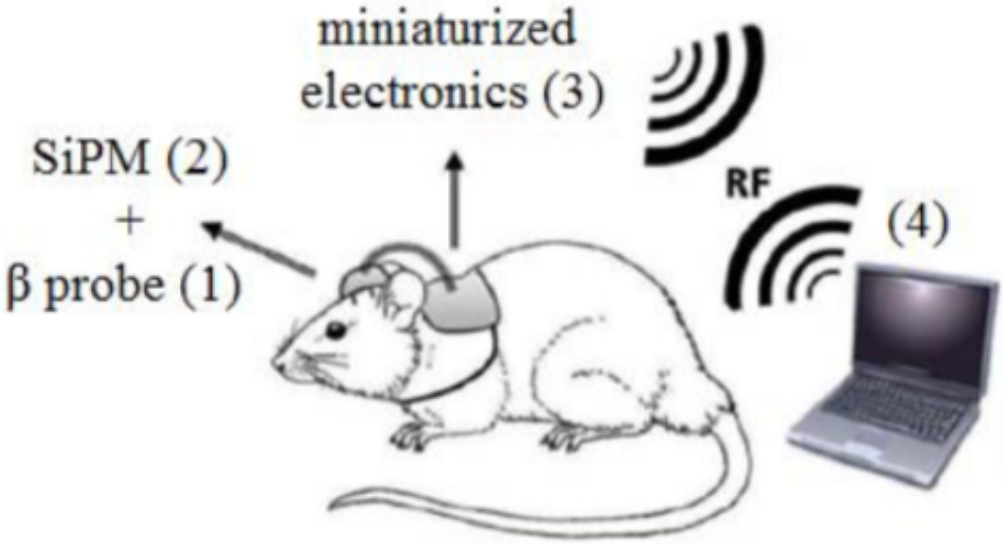

Figure A.8 *Architecture générale de SONIM. (1) Sonde sensible β + implantée dans un cerveau du rat sur un côté et couplée à un petit dispositif SiPM (2) à faible bruit sur un autre. Les signaux SiPM sont lus par l'électronique dédiée à faible consommation (3) qui transmet également les données expérimentales au PC (4)*

Pour chaque SiPM le gain G, le taux de bruits de comptage DCR et la sensibilité bêta (voir la Figure 9) ont été mesurés en fonction de Vbias et de la température. Les résultats obtenus ont montré que le petit champ de vision et la structure nouvellement développée des dispositifs KETEK permettent une forte diminution du taux de bruits de comptage DCR. Cependant, ce petit champ de vision conduit également à une collection de lumière réduite en raison de l'épaisseur de la résine de protection époxy au-dessus du SiPM et de l'angle d'acceptation de la fibre. Étant donné que la sensibilité bêta représente un compromis entre l'efficacité de détection de photons PDE et le taux de bruits de comptage DCR, les SiPM KETEK présentent des performances similaires à celles du dispositif Hamamatsu. Les résultats préliminaires démontrent que la sensibilité bêta des dispositifs KETEK peut être considérablement améliorée avec l'utilisaton d'une lentille de focalisation entre la fibre scintillante et le SiPM ou avec la réduction de l'épaisseur de sa résine de protection époxy.

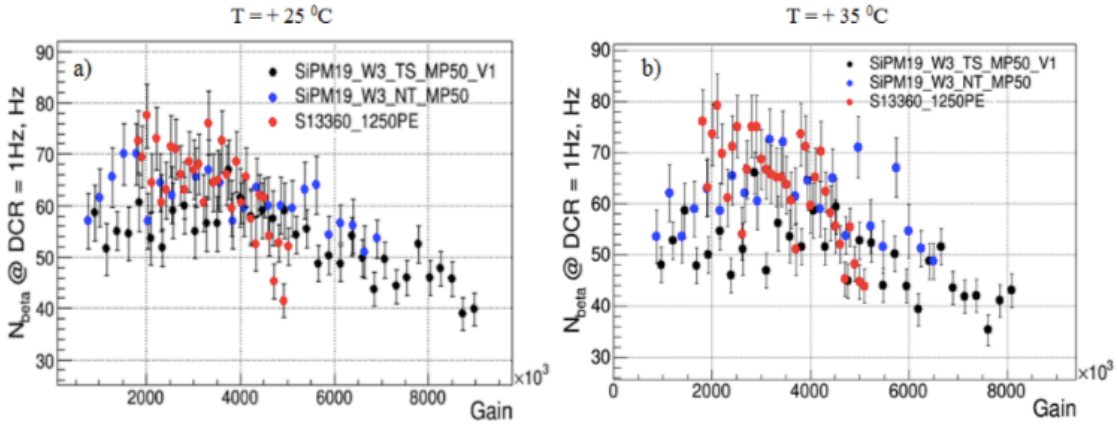

Figure A.9 Sensibilité bêta en fonction du Gain pour 3 appareils SiPM à 25 et 35 C

Annex 1 – Static measurements

This annex complements the full view of acquired static measurements: forward and reverse current – voltage IV measurements. All the physics related to these data has been already presented in the Chapter 3, Sections 3.3 “Static characterizations” and 3.5 “Physical model of the reverse IV characteristic”.

Forward measurements

The collection of forward IV characteristics of SiPM devices produced by KETEK and Hamamatsu measured in T range from 308.15 K down to 238.15 K is presented in Figure A. 1 (a, b, c and d) and Figure A. 2 (a, b and c) respectively. The forward IV characteristics of Hamamatsu SiPM devices measured in wider T range from 318.15 K down to 98.15 K is presented in Figure A. 3 (a, b and c).

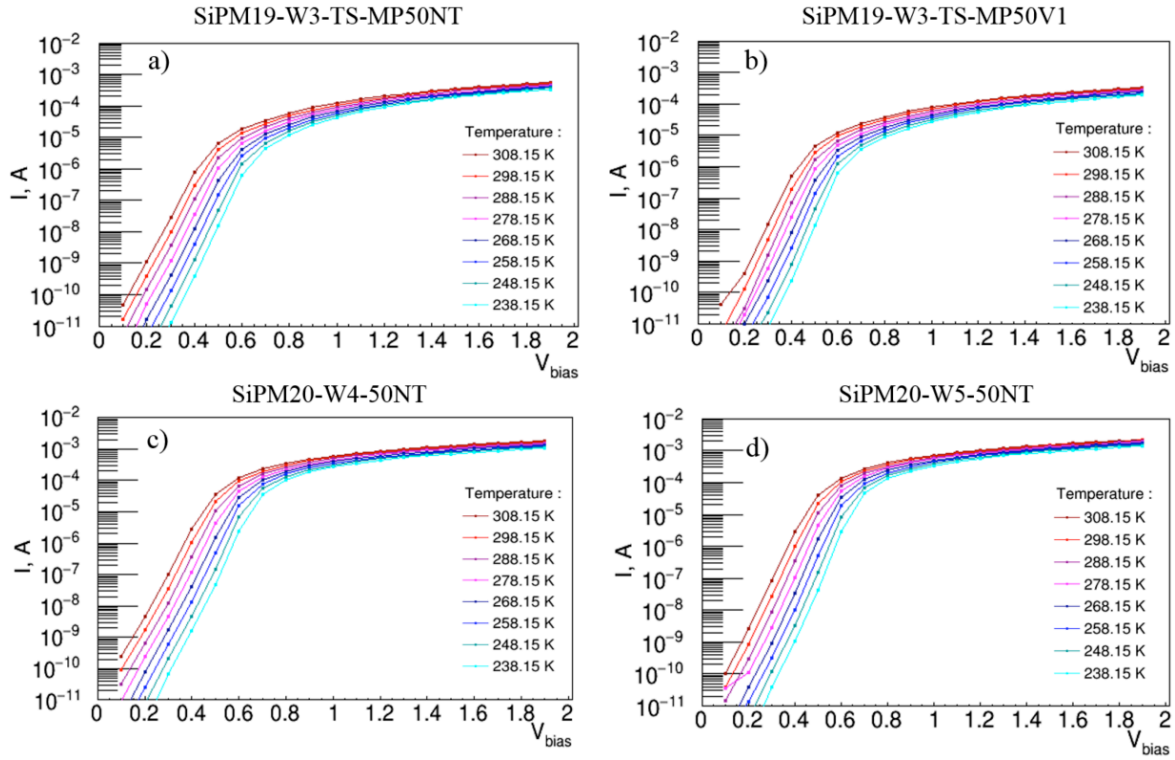

Figure A. 1 Forward IV characteristics of KETEK devices a) SiPM19-W3-MP50-NT, b) SiPM19-W3-MP50V1, c) SiPM20-W4-50NT and d) SiPM20-W5-50NT measured in T range from 308.15 K down to 248.15 K

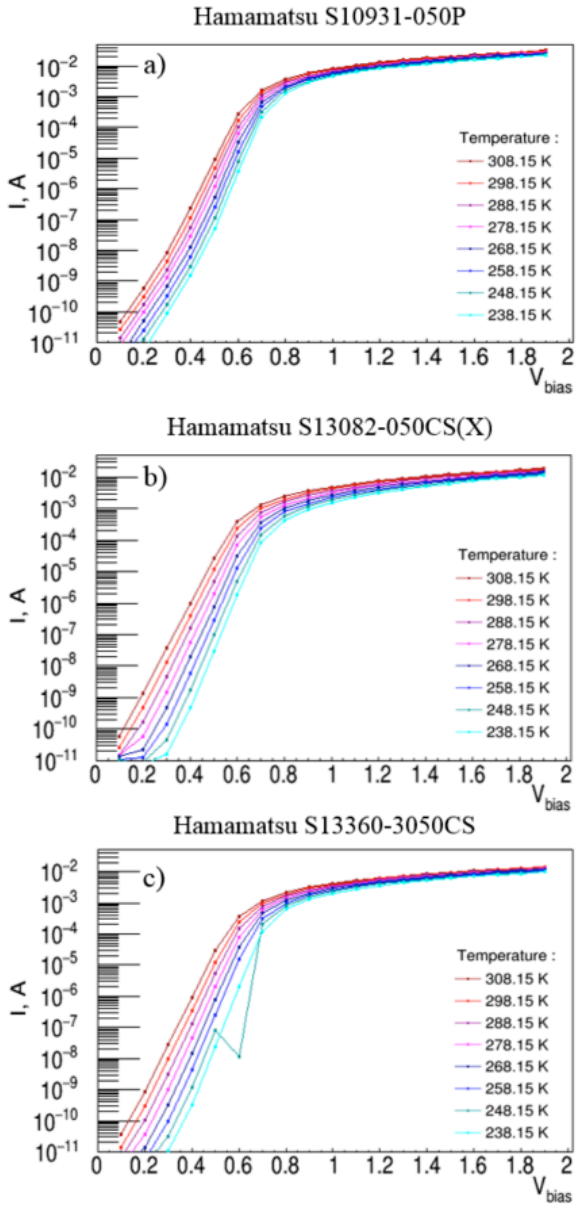

Figure A. 2 Forward IV characteristics of Hamamatsu devices a) S10931-050P, b) S13082-050CS(X) and c) S13360-3050CS measured in T range from 308.15 K down to 248.15 K

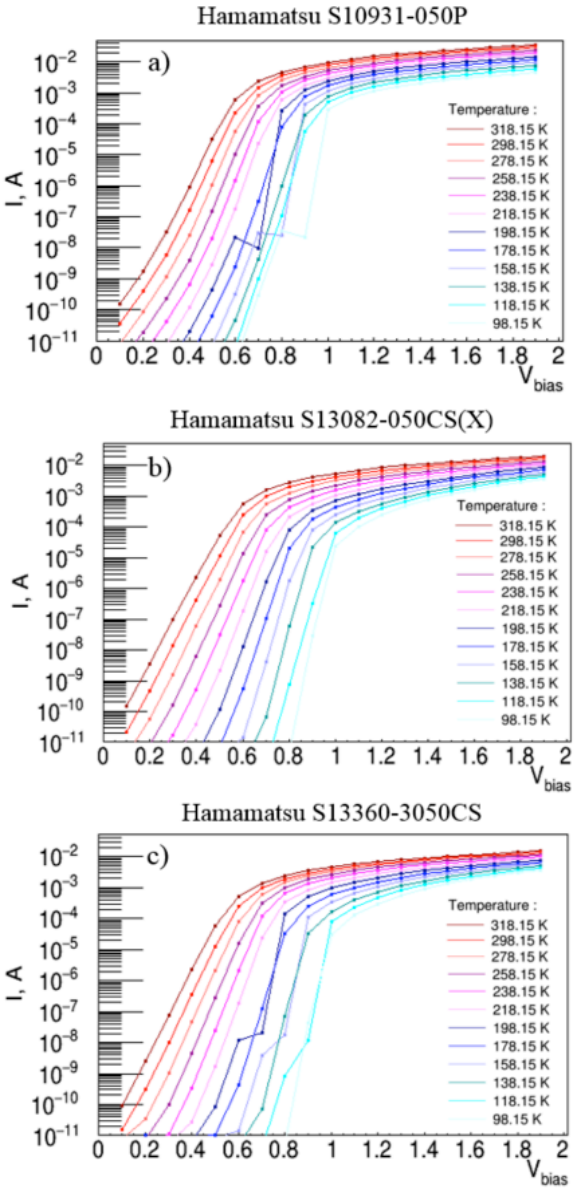

Figure A. 3 Forward IV characteristics of Hamamatsu devices a) S10931-050P, b) S13082-050CS(X) and c) S13360-3050CS measured in T range from 318.15 K down to 98.15 K

Reverse measurements

The collection of reverse IV characteristics of SiPM devices produced by KETEK and Hamamatsu measured in T range from 308.15 K down to 238.15 K and dark conditions is presented in Figure A. 4 (a, b, c and d) and Figure A. 5 (a, b and c) respectively. The reverse IV characteristics of Hamamatsu SiPM devices measured in T range from 318.15 K down to 98.15 K in dark conditions is presented in Figure A. 6 (a, b and c), while the measurements with blue (λ = 467 nm) and red light (λ = 635 nm) of three intensities (low, middle and high) is presented in Figure A. 7 (a, b and c), Figure A. 8 (a, b and c) and Figure A. 9 (a, b and c).

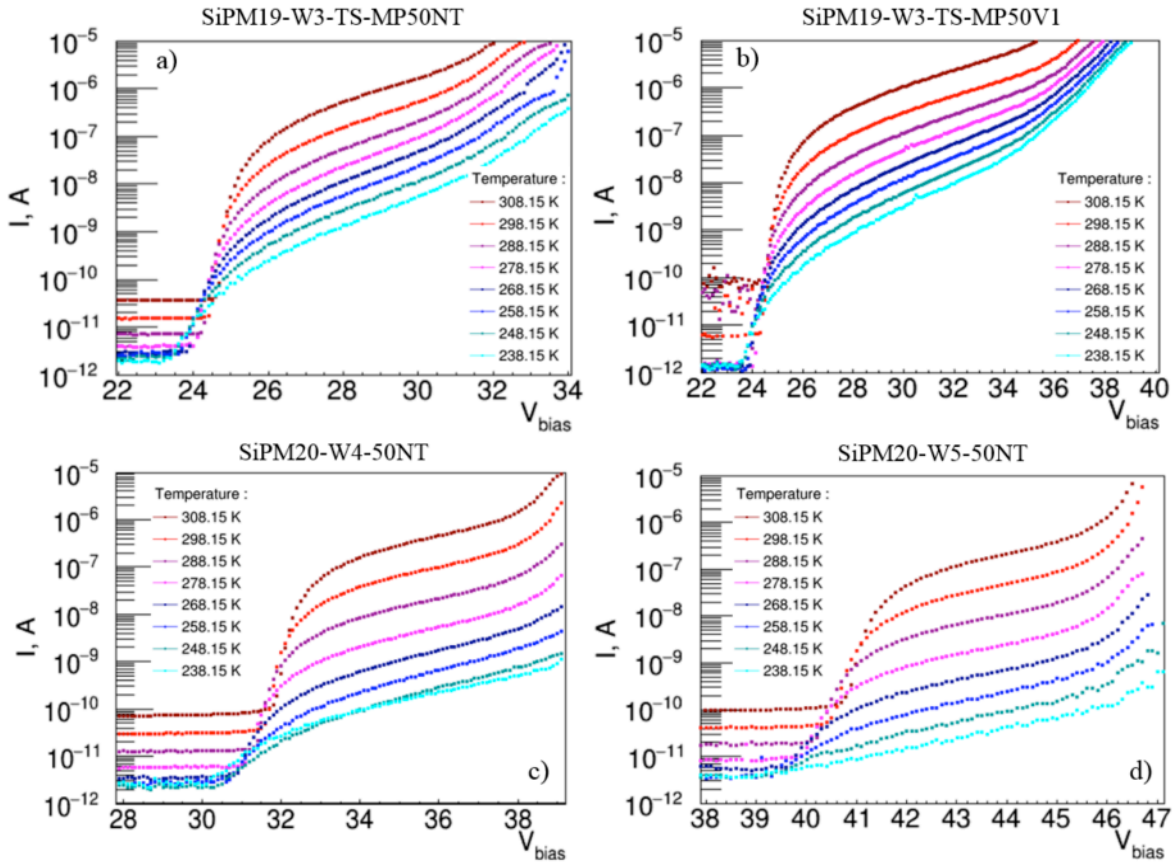

Figure A. 4 Reverse IV characteristics of KETEK devices a) SiPM19-W3-MP50-NT, b) SiPM19-W3-MP50V1, c) SiPM20-W4-50NT and d) SiPM20-W5-50NT measured in T range from 308.15 K down to 248.15 K and dark conditions

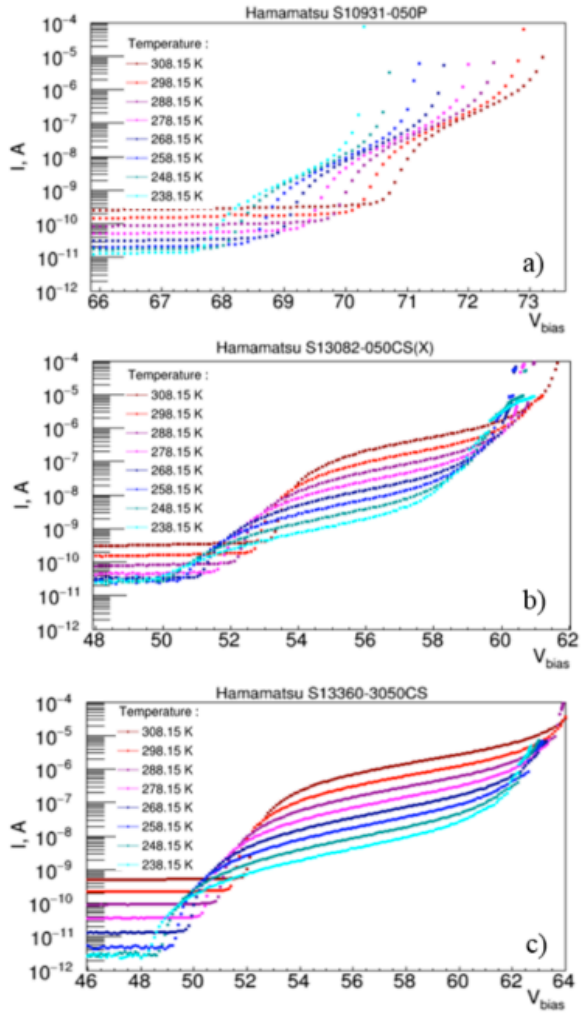

Figure A. 5 Reverse IV characteristics of Hamamatsu devices a) S10931-050P, b) S13082-050CS(X) and c) S13360-3050CS measured in T range from 308.15 K down to 248.15 K and dark conditions

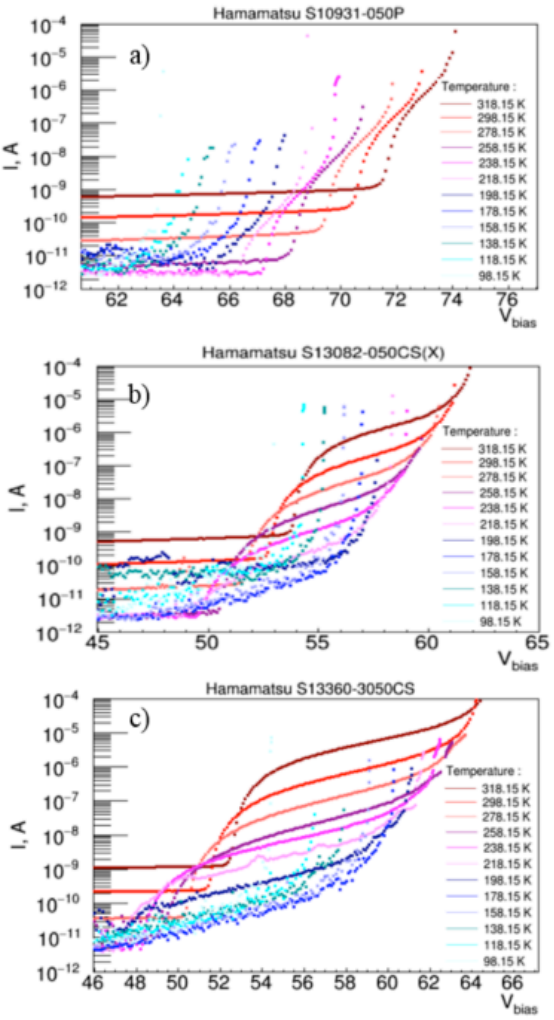

Figure A. 6 Reverse IV characteristics of Hamamatsu devices a) S10931-050P, b) S13082-050CS(X) and c) S13360-3050CS measured in T range from 318.15 K down to 98.15 K and dark conditions

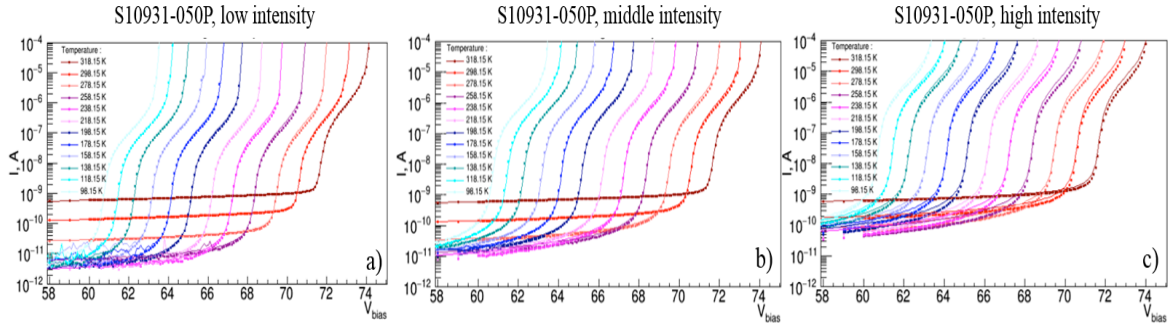

Figure A. 7 Reverse IV characteristics of Hamamatsu S10931-050P device measured in T range from 318.15K down to 98.15 K with a) low, b) middle and c) high light intensity and measured with blue $\lambda = 467$ (lines) nm and red $\lambda = 635$ nm (dots) laser light

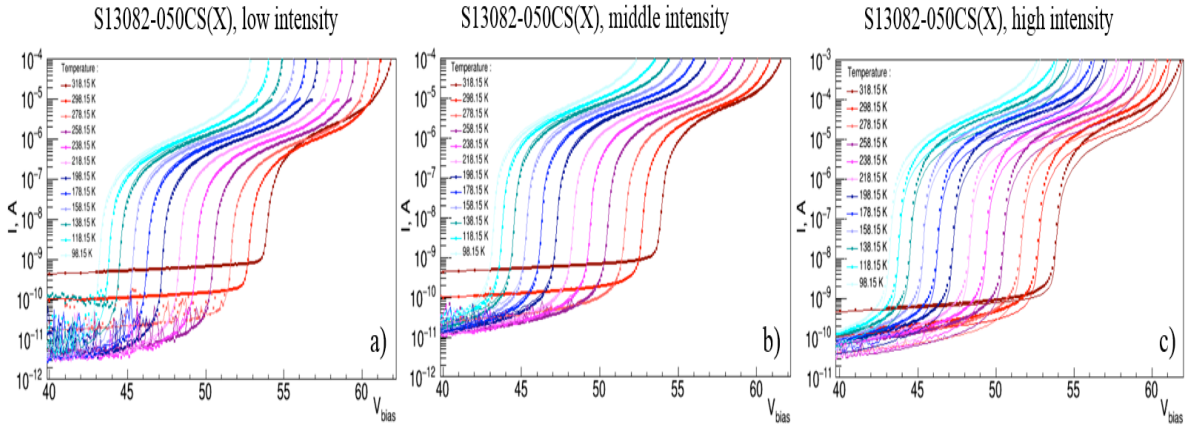

Figure A. 8 Reverse IV characteristics of Hamamatsu S13082-050CS(X) device measured in T range from 318.15 K down to 98.15 K with a) low, b) middle and c) high light intensity and measured with blue λ = 467 (lines) nm and red λ = 635 nm (dots) laser light

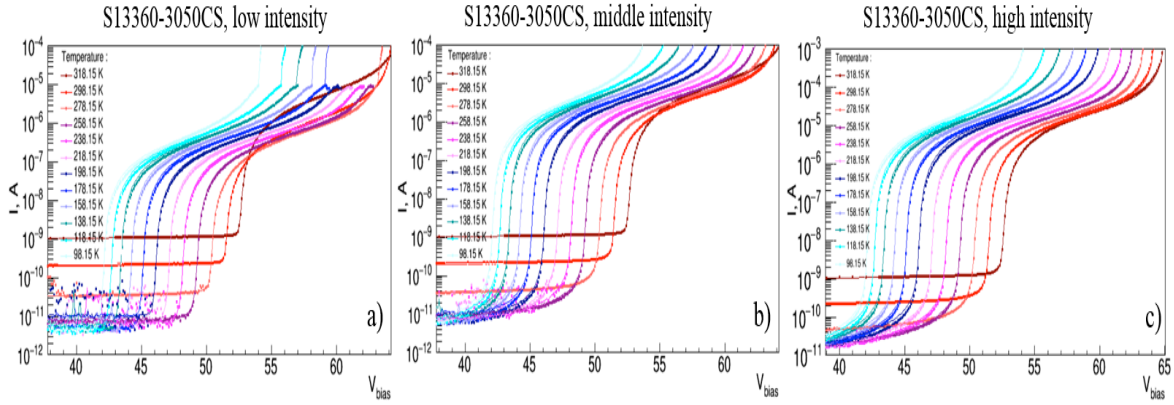

Figure A. 9 Reverse IV characteristics of Hamamatsu S13360-3050CS device measured in T range from 318.15 K down to 98.15 K with a) low, b) middle and c) high light intensity and measured with blue λ = 467 (lines) nm and red λ = 635 nm (dots) laser light

Annex 2 - P_{Geiger} measurements

This annex complements the full view of calculated Geiger triggering probability $P_{Geiger\text{-}AC}$ from AC measurements as a function of ΔV at different temperatures T. All the physics related to these data has been already presented in the Chapter 3, Sections 3.4.3.h "*P_{Geiger} vs. ΔV vs. T*".

The $P_{Geiger\text{-}AC}$ vs. ΔV of SiPM devices produced by KETEK and calculated in T range from 308.15 K down to 248.15 for three different light wavelengths (e.g. λ = 467 nm, λ = 523 nm and λ = 635 nm) are presented in Figure A. 10 (a, b and c), Figure A. 11 (a, b and c), Figure A. 12 (a, b and c) and Figure A. 13 (a, b and c). The $P_{Geiger\text{-}AC}$ vs. ΔV for Hamamatsu devices calculated in T range from 318.15 K down to 98.15 for two light wavelengths (e.g. λ = 467 nm and λ = 635 nm) is presented in Figure A. 14 (a and b), Figure A. 15 (a and b) and Figure A. 16 (a and b).

It should be pointed out that $P_{Geiger\text{-}AC}$ (dots) was parameterized by the Eq. 3.67 (continuous lines). Moreover, the $P_{Geiger\text{-}AC}$ was normalized by *p* at 298.15 K (for more details see the Eq. 3.67).

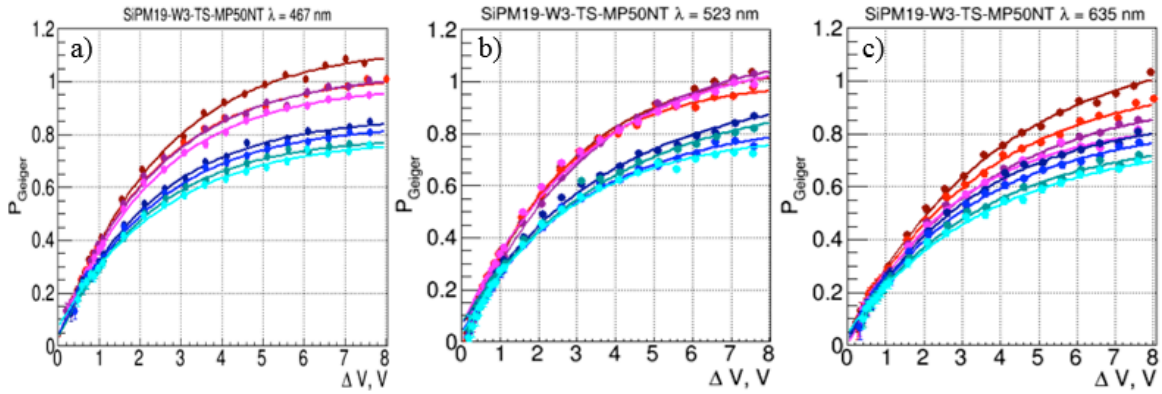

Figure A. 10 $P_{Geiger\text{-}AC}$ vs. ΔV at T range from 308.15 K down to 238.15 K for SiPM19-W3-TS-MP50NT and measured with a) blue λ = 467 nm, b) green λ = 523 nm and c) red λ = 635 nm laser light

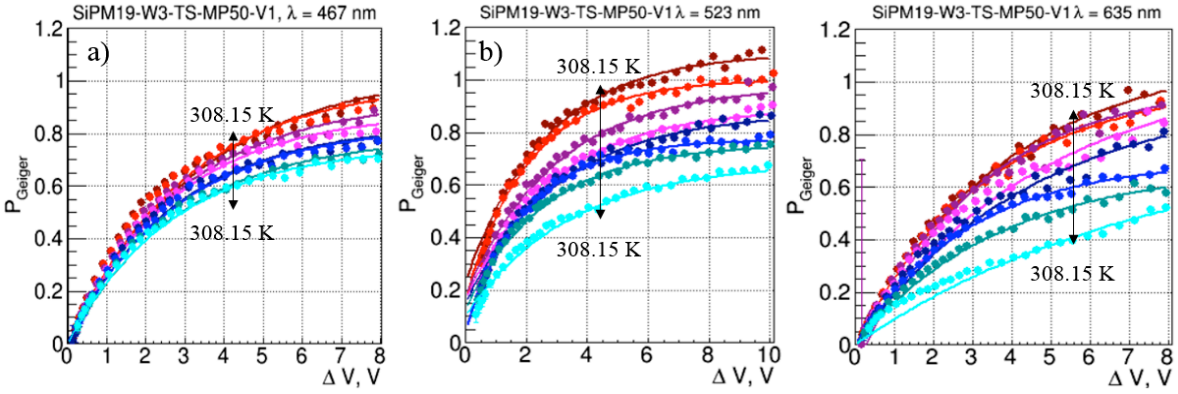

Figure A. 11 $P_{Geiger\text{-}AC}$ vs. ΔV at T range from 308.15 K down to 238.15 K for SiPM19-W3-TS-MP50-V1 and measured with a) blue λ = 467 nm, b) green λ = 523 nm and c) red λ = 635 nm laser light

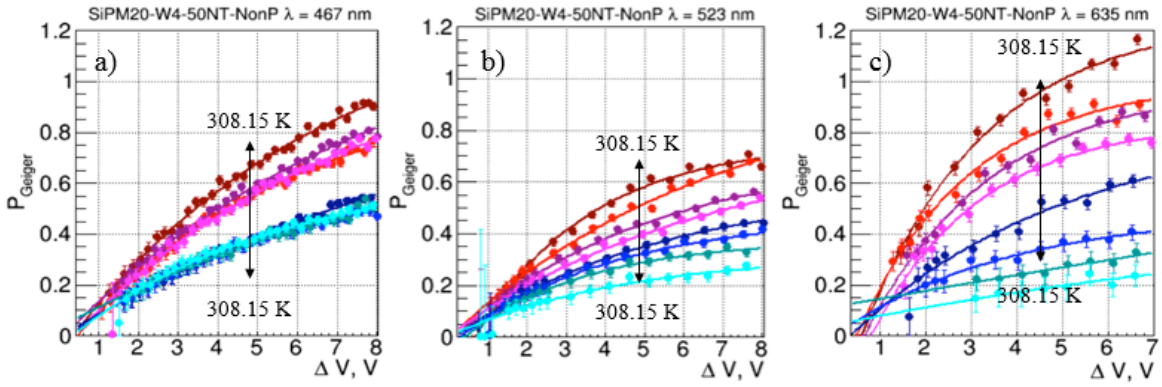

Figure A. 12 $P_{Geiger-AC}$ vs. ΔV at T range from 308.15 K down to 238.15 K for SiPM20-W4-50NT and measured with a) blue λ = 467 nm, b) green λ = 523 nm and c) red λ = 635 nm laser light

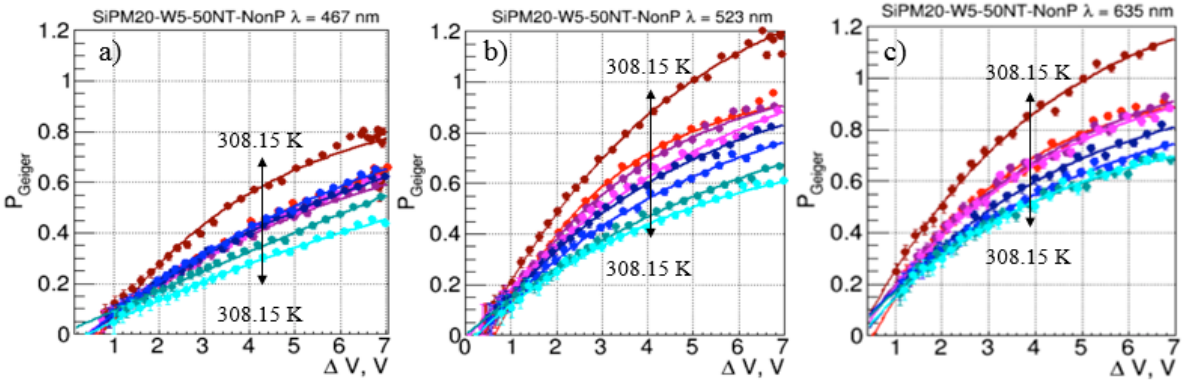

Figure A. 13 $P_{Geiger-AC}$ vs. ΔV at T range from 308.15 K down to 238.15 K for SiPM20-W5-50NT and measured with a) blue λ = 467 nm, b) green λ = 523 nm and c) red λ = 635 nm laser light

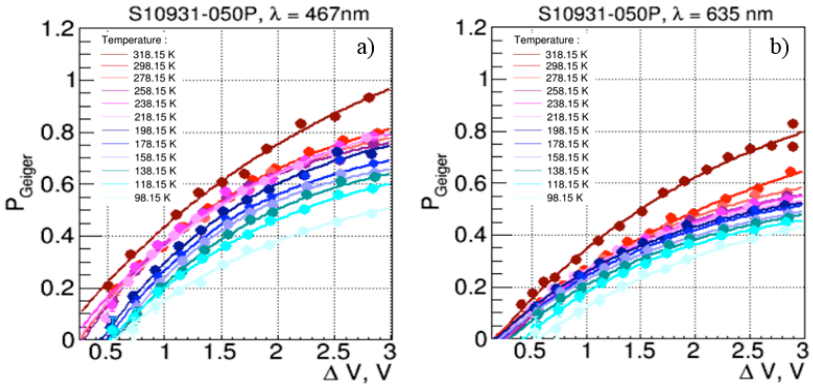

Figure A. 14 $P_{Geiger-AC}$ vs. ΔV at T range from 318.15 K down to 98.15 K for S10931-050P and measured with a) blue λ = 467 nm and b) red λ = 635 nm laser light

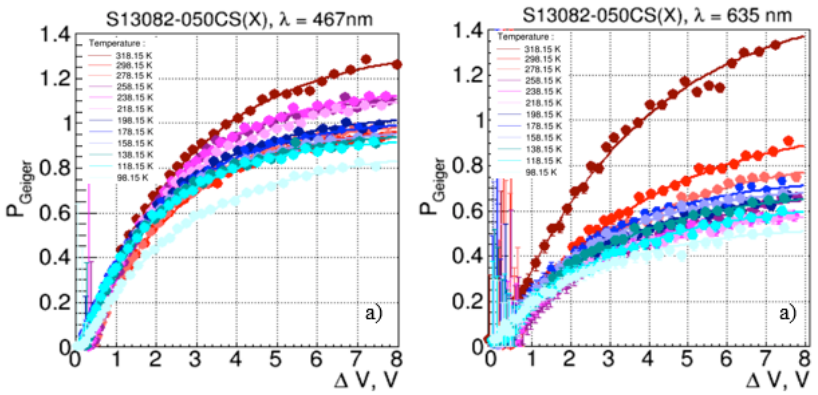

Figure A. 15 $P_{Geiger\text{-}AC}$ vs. ΔV at T range from 318.15 K down to 98.15 K for S13082-050CS(X) and measured with a) blue λ = 467 nm and b) red λ = 635 nm laser light

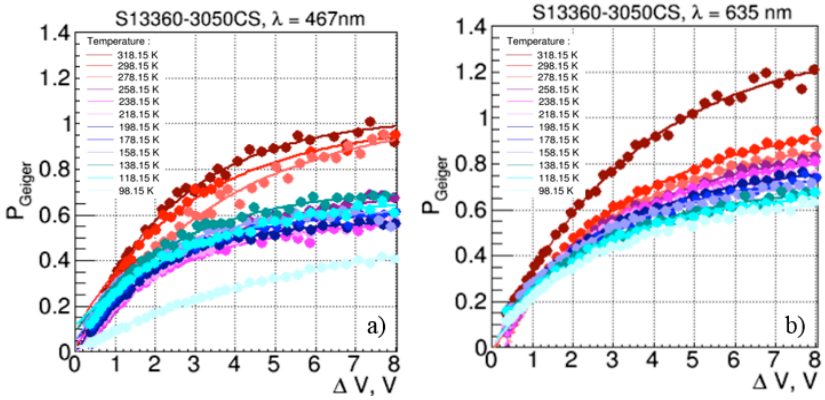

Figure A. 16 $P_{Geiger\text{-}AC}$ vs. ΔV at T range from 318.15 K down to 98.15 K for S13360-3050CS and measured with a) blue λ = 467 nm and b) red λ = 635 nm laser light

Annex 3 – Numerical TCAD C-V simulation

The relationship between µcell capacitance $C_{\mu cell}$, thickness of epitaxial layer and depletion region was studied from TCAD [80] simulation and will be presented in the following.

The C-V characteristic of a 2D diode structure similar to the SiPM µcell of 25 µm size (i.e. $n^+/p/\pi/p^+$ structure with 2 µm epitaxial layer thickness) was done. The simulated doping profile is presented in Figure A. 17, while the simulated C-V measurements is presented in Figure A. 18. We can observe that the capacitance drops rapidly with voltage down to 15 V, which corresponds to the full depletion of the simulated diode. The capacitance was found to be mostly constant ~1.33 fF/µm when the simulated voltage is higher than 15 V. It should be pointed out that the simulation was done for 2D structure. Therefore to obtain the correct capacitance for real 3D diode, the simulated value should be multiplied to the dimension of the third axes (25 µm for our case):

$$C_{cell}^{TCAD} = 25\ \ m \cdot 1.33\,fF/\ \ m = 33.25\,fF \qquad \text{A. 1}$$

where $C_{\mu cell}^{TCAD}$ – is the µcell capacitance from the numerical TCAD C-V simulation. The concentration of electrons and holes (after full depletion) across the epitaxial layer of simulated diode is presorted in Figure A. 19. We can observe the thickness of depletion region of 1.89 µm.

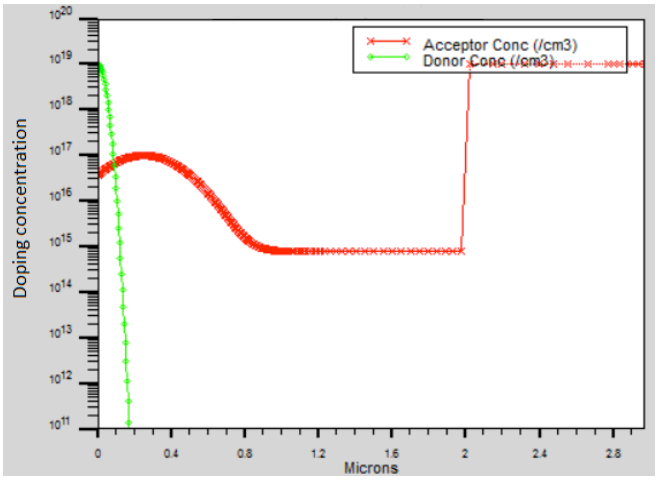

Figure A. 17 Simulated doping profile for the diode structure similar to the SiPM µcell

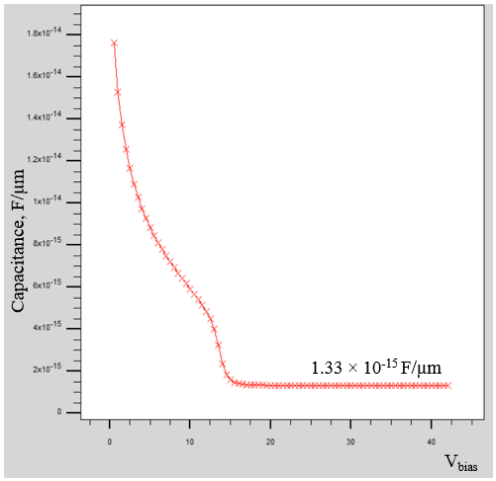

Figure A. 18 Simulated C-V measurements for the diode structure similar to the SiPM µcell. It should be pointed out, that simulation was done for 2D structure. Therefore to obtain the total capacitance the simulated value should be multiplied to the dimension of third axes (25 µm for our case)

As it was already shown in the Chapter 3, Section 3.4.3.d "$C_{\mu cell}$ *vs.* T" the thickness of depleted region d can be also calculated from the Eq. 3.53 (plane parallel capacitance equation) as:

$$d = {}_0\ {}_{Si} \cdot \frac{A}{C_{cell}^{TCAD}} = 8.854 \cdot 10^{-14}\,F/cm \cdot 11.9 \cdot \frac{25 \cdot 25\ m^2}{33.25\,fF} = 1.98\ \ m \qquad \text{A. 2}$$

We can observe that the value of d calculated from the Eq. A. 2 is between the observed thicknesses of depleted region (i.e. 1.89 µm) and epitaxial layer (i.e 2 µm). Therefore, we can

conclude, that the plane parallel capacitance equation (Eq. 3.53) can be used to calculate the thickness of depleted region and epitaxial layer from the $C_{\mu cell}$ with a good precision of ±0.1 µm.

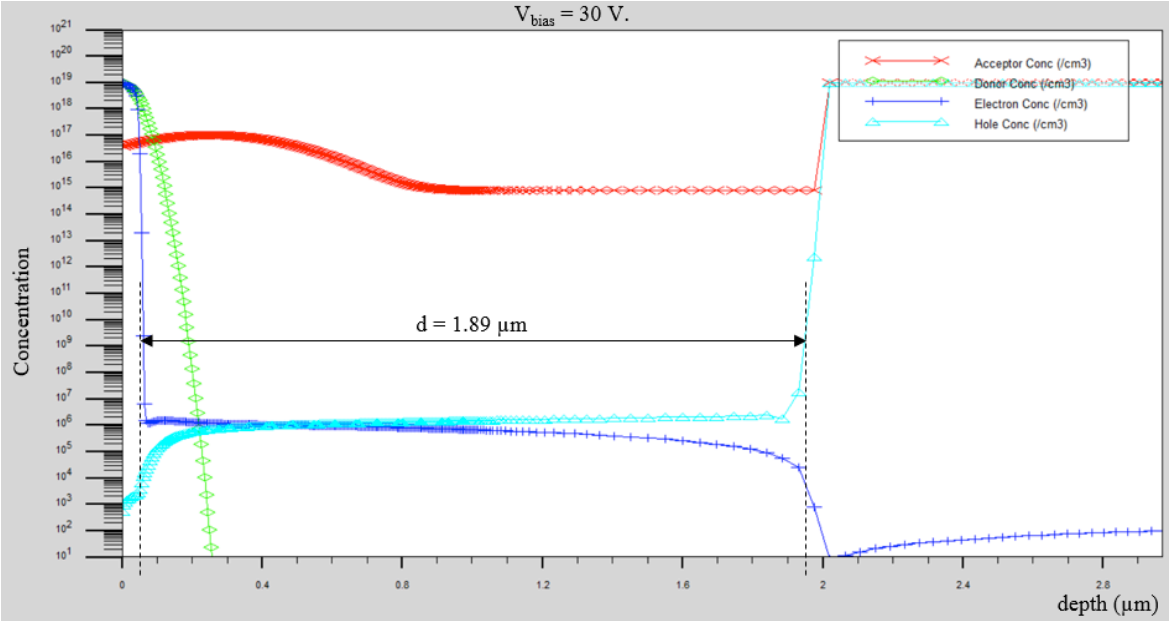

Figure A. 19 Simulated concentration of electrons and holes across the diode with structure similar to the SiPM µcell biased (V_{bias} = 30 V) above the full depletion voltage. The thickness of depletion region of 1.89 µm can be observed

Annex 4 - P_{Geiger} parameterization

The triggering probability, also well known as Geiger probability, represents the probability that a carrier reaching the high field region will trigger an avalanche. The pioneering studding of triggering probability in avalanche diodes was done by Oldham [42] and McIntyre [43]. It was shown that the triggering probability is increases with increasing the overvoltage ΔV. In this Section the studies of a possible parameterization of the shapes of P_{Geiger} as a function of ΔV will be presented.

Following the Oldham [42] the triggering probability can be calculated from:

$$\frac{dP_e}{dx} = (1 \quad P_e) \quad {}_e\left[P_e + P_h \quad P_e P_h\right] \qquad \text{A. 3}$$

$$\frac{dP_h}{dx} = (1 \quad P_h) \quad {}_h\left[P_e + P_h \quad P_e P_h\right] \qquad \text{A. 4}$$

where $P_e(x)$– is the probability that an electron starting at position x in the depletion layer will trigger an avalanche, $P_h(x)$ – is defined analogously for holes, and α_e and α_h – are the electrons and holes ionization rates respectively. The McIntyre [43] has shown that in approximation:

$${}_h = k \cdot \quad {}_e \qquad \text{A. 5}$$

where k – is a constant independent of electrical field, the probability for initiation of an avalanche by a hole $P_h(0)$ or electron $P_e(W)$ generated at position 0 and W respectively in the depletion layer (x = 0 and x = W are the extremities of the depletion layer, in the n and p regions respectively) of an avalanche diode biased above the breakdown voltage can be calculated numerically from:

$$\log\left[1 \quad P_h(0)\right] = \frac{k}{1 \quad k}\log\left[P_h(0) f(W) + 1 \quad P_h(0)\right] \qquad \text{A. 6}$$

$$1 \quad P_h(0) = \left[1 \quad P_e(W)\right]^k \qquad \text{A. 7}$$

$$f(W) = \exp\left[(1 \quad k) \quad \right] \qquad \text{A. 8}$$

as a function of two parameters δ and k, where δ is defined as:

$$= \int_0^W {}_e dx \qquad \text{A. 9}$$

The results of a numerical calculation of $P_h(0)$ and $P_e(W)$ as a function of k and δ are presented in Figure A. 20 a) [43]. The same results were obtained after solving the Eq. A. 6 ÷ Eq. A. 8

numerical by applying the Newton`s method [81]. The results are presented in Figure A. 20 b) for k = 0.999, 0.5, 0.2, 0.1, 0.05, 0.02, 0.01.

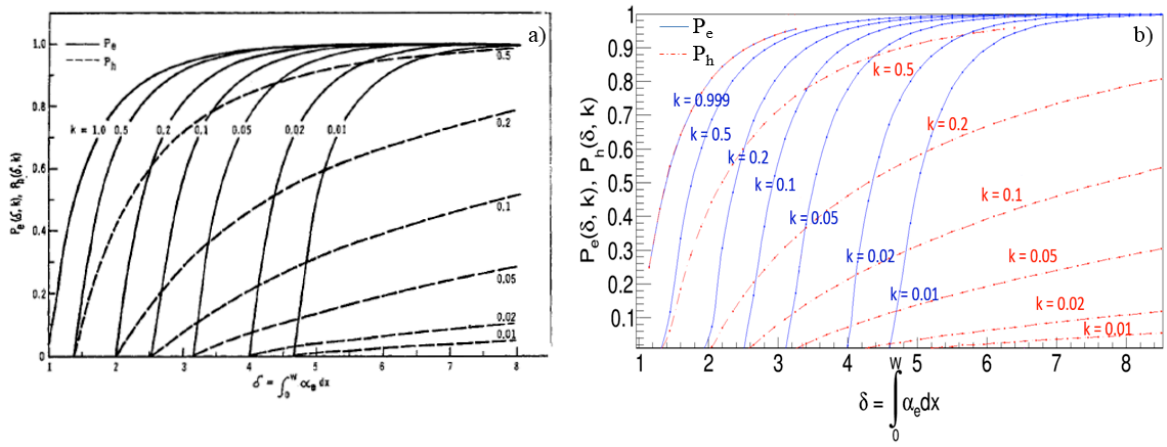

Figure A. 20 Numerical calculation of $P_e(W)$ and $P_h(0)$ as a function of two parameters k and δ a) calculated by McIntyre [43] and b) from Newton`s method

The α_e increases with increasing the internal electrical field inside the junction [53], [82] and [24]. Since, the electrical field increase with increasing the applied voltage [83], the α_e will increase with increasing the applied voltage/overvoltage too. Therefore, we can expect that $= \int_0^W {}_e dx$ will be proportional to the overvoltage ΔV:

$$= \int_0^W {}_e dx = C \cdot \quad V \qquad \text{A. 10}$$

where C – is the coefficient of proportionality. Therefore the Eq. 3.67 can be expressed in δ as:

$$P_{Geiger}(\ ) = 1 \quad \exp \ p \ \frac{}{C} \ = 1 \quad \exp(p \quad) \qquad \text{A. 11}$$

where $\acute{p} = \frac{p}{C}$ – is the free parameter. The Eq. A. 11 (solid lines) was used to parameterize the numerically calculated P_h and P_e (See the Figure A. 21). We can observe that the Eq. A. 11 is

providing a good description of experimental data. Therefore, we can conclude that the shapes of P_{Geiger} can be parameterized as a function of ΔV:

$$P_{Geiger}(\ V) = 1 \quad \exp(p \quad V) \qquad \text{A. 12}$$

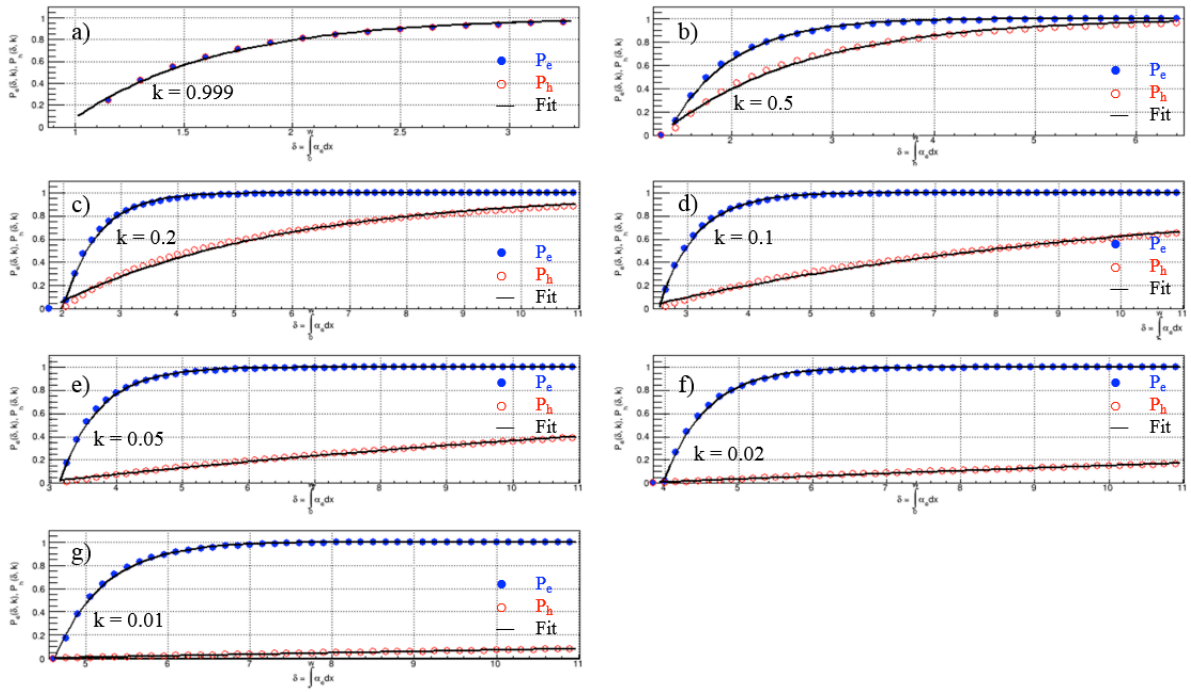

Figure A. 21 Numerical calculation of $P_e(W)$ and $P_h(0)$ as a function of δ for different k, a) k = 0.999, b) k = 0.5, c) k = 0.2, d) k = 0.1, e) k = 0.05, f) k = 0.02 and g) k = 0.01. Data have been fitted by Eq. A. 12

Thesis results

List of the papers published on the thesis results

- N. Dinu, A. Nagai, A. Para, "Breakdown voltage and triggering probability of SiPM from IV curves at different temperatures", NIM A, Available online 30 May 2016
- A. Nagai, N. Dinu, A. Para, "Breakdown voltage and triggering probability of SiPM from IV curves", submitted to the Conference Record of IEEE NSS 2015
- N. Dinu, A. Nagai, A. Para, "Studies of MPPC detectors down to cryogenic temperatures", NIM A, Volume 787, 2015, Pages 275-279.
- N. Dinu, T. Ait Imando, A. Nagai & al., "SiPM arrays and miniaturized readout electronics for compact gamma camera", NIM A, Volume 787, 2015, Pages 367-372.
- A. Nagai, "Silicon Photomultiplier for Medical Imaging –Analysis of SiPM characteristics-", Proceedings of Journées de Rencontre Jeunes Chercheurs, 2013, Page 43- 46.

List of the conferences attended presenting the results of the thesis

- *Breakdown voltage and triggering probability of SiPM from IV curves*, 14th Vienna Conference on Instrumentation – VCI2016. Austria, Vienna, 15-19 February 2016
- *Studies of MPPC detectors down to cryogenic temperatures*, 7th International Conference on New Developments in Photodetection – NDIP 2014. France, Tours, 30 June - 4 July 2014
- *Silicon Photomultiplier for Medical Imaging – Analysis of SiPM characteristics* -, Journées de Rencontre des Jeunes Chercheurs – JRJC2013. France, Barbaste, 1 - 7 December 2013

References

[1] D. Jeans, "Results of the Calice scintillator ECAL beam test at Desy," *Journal of Physics: Conference Series,* vol. 160, no. 01026, 2009.

[2] A. Vacheret, G. J. Barker, M. Dziewiecki, P. Guzowski, M. D. Haigh, B. Hartfiel, A. Izmaylov, W. Johnston, M. Khabibullin, A. Khotjantsev, Y. Kudenko, R. Kurjata, T. Kutter, T. Lindner, P. Masliah, J. Marzec, O. Mineev and Y. Musienko, "Characterization and Simulation of the Response of Multi Pixel Photon Counters to Low Light Levels," *Nuclear Instruments and Methods in Physics Research Section A,* pp. 69-83, 11 November 2011.

[3] Ł. Mik, W. Kucewicz, J. Barszcz, M. Sapor and S. Głąb, "Silicon photomultiplier as fluorescence light detector," *Mixed Design of Integrated Circuits and Systems (MIXDES), 2011 Proceedings of the 18th International Conference,* pp. 663-666, 2011.

[4] H. Li, N. Lopes, S. Moser, G. Sayler and S. Ripp, "Silicon photomultiplier (SPM) detection of low-level bioluminescence for the development of deployable whole-cell biosensors: Possibilities and limitations," *Biosensors and Bioelectrinics,* vol. 33, no. 1, pp. 299 - 303, 2012.

[5] G. Llosá, N. Belcar, M. Bisogni, G. Collazuol, S. Marcatili, M. Boscardin, M. Melchiorr, A. Tarolli, C. Piemonte, N. Zorzi, P. Barrillon, S. Bondil-Blin, V. Chaumat, C. de La Taille, N. Dinu, V. Puill, J.-F. Vagnucci and A. Del Guerra, "First results in the application of silicon photomultiplier matrices to small animal PET," *Nuclear Instruments and Methods in Physics Research Section A: Accelerators, Spectrometers, Detectors and Associated Equipment,* vol. 610, no. 1, pp. 196 - 199, 2009.

[6] N. Dinu, T. Ait Imando, A. Nagai, L. Pinot, V. Puill, S. Callier, B. Janvier, C. Esnault, M.-A. Verdier, L. Raux, V. Vandenbussche, Y. Charon and L. Menard, "SiPM arrays and miniaturized readout electronics for compact gamma camera," *Nuclear Instruments and Methods in Physics Research Section A, Vol. 787,* pp. 367-372, 1 July 2015.

[7] K. K. Hamamatsu Photonics, Opto-semiconductor Handbook, Hamamatsu Photonics K.K. Solid State Division, 2014.

[8] S. Cova, M. Ghioni, A. Lacaita, C. Samori and F. Zappa, "Avalanche photodiodes and quenching cirquits for single-photon detector," *Applied Optics, Vol. 35, No 12,* vol. 35, pp. 1956-1976, 1996.

[9] R. H. Haitz, "Model for the electrical behavior of the micro-plasma," *Journal of Applied Physics,* vol. 35, no. 5, pp. 1370-1376, 1964.

[10] B. Senitzky and J. Moll, "Breakdown in silicon," *Physical Review, Vol. 110, Issue 3,* 1958.

[11] S. Cova, M. Ghioni, A. Lotito, I. Rech and F. Zappa, "Evolution and prospects for single-photon avalanche diodes and quenching circuits," *journal of modern optics,* pp. 1267-1288, 15 June 2004.

[12] V. M. Golovin, M. L. Tarasov and G. B. Bondarenko, "Avalanche photodetector". Russia Patent 2142175, 27 11 1999.

[13] Sadygov, Ziraddin and Jaub-ogli, "Avalanche Photodetector". Russia Patent 2086047, 27 07 1997.

[14] N. Dinu, "Instrumentation on Silicon Detector: from properties characterization to applications," *LAL-13-192,* 2013.

[15] N. Dinu, Z. Amara, C. Bazin, V. Chaumat, C. Cheikali, G. Guilhem, V. Puill, C. Sylvia and J. Vagnucci, "Electro-optical characterization of SiPM: A comparative study," *Nuclear Instruments and Methods in Physics Research A 610,* pp. 423-426, 2009.

[16] F. R. Schneider, T. R. Ganka, G. Seker, E. Engelmann, D. Renker, S. Paul, W. Hansch and S. Ziegler, "Characterization of blue sensitive 3x3mm2 SiPMs and their use in PET," *Journal of Instrumentation,* vol. 9, no. 7, p. 07027, 2014.

[17] C. Piemonte, "Characterization of the First Prototypes of Silicon Photomultiplier Fabricated at ITC-irst," *IEEE Transactions on Nuclear Science,* vol. 54, no. 1, pp. 238-244, 2007.

[18] N. Serra, G. Giacomini, A. Piazza, C. Piemonte, A. Tarolli and N. Zorzi, "Experimental and TCAD study of breakdown voltage temperature behavior in n+/p SiPM's," *IEEE Transactions on Nuclear Science,* vol. 58, no. 3, pp. 1233-1240, 2011.

[19] E. Garutti, M. Ramilli, C. Xu, H. W. L. and R. Klanner, "Characterization and X-ray damage of Silicon Photomultipliers," *Proceedings, 3rd International Conference on Technology and Instrumentation in Particle Physics,* p. 70, 2014.

[20] S. Seifert, H. T. Van Dam, J. Huizenga, R. Vinke, P. Dendooven, H. Löhner and D. R. Schaart, "Simulation of Silicon Photomultiplier Signals," *IEEE Transactions on Nuclear Science,* vol. 56, no. 6, pp. 3726-3733, 2009.

[21] F. Corsi, C. Marzocca, A. Perrota, A. Dragone, M. Foresta, A. Del Guerra, S. Marcatili, G. Llosa, G. Collazoul, D. B. G.F., N. Dinu, P. C., G. Pignatel and G. Levi, "Electrical characterization of Silicon Photomultipliers detectors for optical front-end design," *IEEE Nuclear Science Symposium Conference Record, N30-222,* pp. 1276-1280, 2006.

[22] F. Corsi, A. Dragone, C. Marzocca, A. Del Guerra, D. P., N. Dinu, P. C., B. M. and D. B. G.F., "Modeling a silicon photomultiplier (SiPM) as a single source for optimum front-end design," *Nuclear Instruments and Methods A, Vol. 572,* pp. 416-418, 2007.

[23] F. Wiest, "SiPM Development at KETEK -A short introduction to KETEK SiPM Products and Status with focus on small microcell SiPMs -," 2013.

[24] S. M. Sze, Physics of semiconductor devices, 2nd edition, John Willey & Sons, 1981.

[25] C. A. Lee, R. A. Logan, R. L. Batdorf, J. J. Kleimack and W. Wiegmann, "Ionization rates of holes and electrons in silicon," *Physical Review,* vol. 134, no. 3A, pp. A761-A773, May 1964.

[26] R. van Overstraeten and H. DeMan, "Measurement of the lonization Rates in Diffused Silicon p-n Junctions," *Solid-St. Electron.,* vol. 13, pp. 583-608, 1970.

[27] W. Shockley and W. T. Read, "Statistics of the Recombination of Holes and Electrons," *Physical Review,* vol. 87, pp. 835-842, 1952.

[28] R. N. Hall, "Electron Hole Recombination in Germanium," *Physical Review,* vol. 87, p. 387, 1952.

[29] O. K. B. Lui and P. Migliorato, "A New Generation-Recombination Model For Device Simulation Including The Poole-Frenkel Effect And Phonon-Assisted Tunneling," *Solid-State Electronics,* vol. 41, no. 4, pp. 575-583, 1997.

[30] G. A. M. Hurkx, H. C. de Graaff, W. J. Kloosterman and M. P. G. Knuvers, "A Novel Compact Model Description of Reverse Biase Diode Characteristics including Tunneling," *ESSDERC '90: 20th European Solid State Device Research Conference,* pp. 49-52, 1990.

[31] R. Pagano, Operative parameters of Silicon Photomultipliers, 2011.

[32] P. Eckert, S.-C. H. C., W. Shen, R. Stamen and T. A., "Characterisation studies of silicon photomultipliers," *Nuclear Instruments and Methods in Physics Research Section A,* pp. 217-226, 2010.

[33] M. De Gerone, G. F., Y. Ootani, M. Uchiyama, M. Nishimura, S. Shirabe, P. Cattaneo and M. Rossella, "Design and test of an extremely high resolution Timing Counter for the MEG II experiment: preliminary results," *arXiv:1312.0871v1 [physics.ins-det],* 2013.

[34] S. Piatek, "Optical crosstalk in a silicon photomultiplier," Hamamatsu Corporation & New Jersey Institute of Technology, 2016.

[35] A. Lacaita, F. Zappa, S. Bigliradi and M. Manfredi, "On the breamsstrahlung origin of hot-carrier-induced photons in silicon devices," *IEEE Transactions on Electron devices, Vol. 40, Issue 5,,* pp. 577-582, 1993.

[36] I. Prochazka, K. Hamal, L. Kral and J. Blazej, "Silicon photon counting detector optical cross-talk effect," *5th International Conferance on Photonics, Devices and Systems, Prague,* pp. 618001-618001-6, 2006.

[37] W. J. Kindt, H. W. van Zeijl and S. Middelhoek, "Optical cross-talk in Geiger mode avalanche photodiodes arrayes: modeling, prevention and measurement," in *Solid-State Device research Conferance, Proceedings of the 28th European*, 1998.

[38] I. Rech, A. Ingargiola, R. Spinelli, I. Labanca, S. Marangoni, M. Ghioni and S. Cova, "Optical crosstalk in single photon avalanche diode arrays: a new complete model," *Optics Express, Vol. 16, Issue 12,* pp. 8381-8394, 2008.

[39] K. K. Hamamatsu Photonics, "MPPC and MPPC module for precision measurement," March 2016. [Online].

[40] A. Para, "Afterpulsing in Silicon Photomultipliers: Impact on the Photodetectors Characterization," *arXiv:1503.01525v1 [physics.ins-det],* 5 March 2015.

[41] M. S. Tyagi, Introduction to semiconductor materials and devices, John Wiley & Sons, Inc., 1991.

[42] W. G. Oldham, R. R. Samuelson and P. Antognetti, "Triggering Phenomena in Avalanche Diodes," *IEEE Transactions on Electron Devices,* vol. 19, no. 9, pp. 1056-1060, September 1972.

[43] R. J. McIntyre, "On the Avalanche Initiation Probability of Avalanche Diodes Above the Breakdown Voltage," *IEEE Transactions on Electron Devices,* vol. 20, no. 7, pp. 637-641, July 1973.

[44] V. Chaumat, C. Bazin, N. Dinu, P. V. and V. J-F., "Absolute Photo Detection Efficiency measurement of Silicon PhotoMultipliers," *Proceeding of Science, in press,* 2013.

[45] R. Pagano, S. Libertino, D. Corso, L. S., G. Valvo, D. Sanfilippo, G. Condorelli, M. Mazzillo, A. Piana, B. Carbone and G. Fallica, "Improvement of the Diffusive Component of Dark Current in Silicon Photomultiplier Pixels," *SENSORDEVICES 2012 : The Third International Conference on Sensor Device Technologies and Applications,* 2012.

[46] E. Roncali and C. S. R., "Application of Silicon Photomultipliers to Positron Emission Tomography," *Annals of Biomedical Engineering,* vol. 39, no. 4, p. 1358–1377, April 2011.

[47] A. Cardini, V. Fanti and A. Lai, "Performance of avalanche photodetectors at cryogenic temperatures: Operations of MPPCs at temperatures below 77 K," *2013 IEEE Nuclear Science Symposium and Medical Imaging Conference,* pp. 1 - 6, 2013.

[48] G. Collazuol, M. Bisogni, S. Marcatili, C. Piemonte and A. Del Guerra, "studies of silicon photomultipliers at cryogenic temperatures," *Nuclear Instruments and Methods in Physics Research Section A, Vol. 628, Issue 1,* pp. 389-392, 2011.

[49] N. Dinu, C. Bazin, V. Chaumat, C. Cheikali, A. Para, V. Puill, C. Sylvia and J. Vagnucci, "Temperature and Bias Voltage Dependence of the MPPC Detectors," *IEEE Nuclear Science Symposuim & Medical Imaging Conference Record,* pp. 215-219, 2010.

[50] P. K. Lightfoot, G. J. Barker, K. Mavrokoridis, Y. Ramachers and N. J. C. Spooner, "Characterisation of a silicon photomultiplier device for applications in liquid argon based neutrino physics and dark matter searches," *Journal of Instrumentation,* vol. 3, p. P10001, 2008.

[51] G. Collazuol, "The SiPM Physics and Technology - a Review -," *Presentation at PhotoDet 2012, LAL Orsay,* 2012.

[52] A. Para, "Detection Efficiency, Cross Talk and Afterpulsing in Silicon Photomultipliers," *LIGHT 2011,* 2011.

[53] C. R. Crowell and S. M. Sze, "Temperature dependence of avalanche multiplication in semiconductors," *Applied Physics Letters,* vol. 9, no. 6, pp. 242-244, 1966.

[54] C. Y. Chang, S. S. Chiu and L. P. Hsu, "Temperature dependence of breakdown voltage in silicon abrupt pn junction," *IEEE Transactions on Electron Devices,* vol. 18, no. 6, pp. 391-393, 1971.

[55] L. Pancheri, P. Brogi, G. Collazuol, G.-F. Dalla Betta, A. Ficorella, P. Marrocchesi, F. Morsani, L. Ratti and S.-N. A., "First prototypes of two-tier avalanche pixel sensors for particle detection," *Vienna Conference on Instrumentation,* 2016.

[56] A. Bouvier, L. Gebremedhin, C. Johnson, K. A., D. A. Williams, N. Otte, R. Strausbaugh, N. Hidaka, H. Tajima, J. Hinton, R. White, M. Errando and R. Mukherjee, "Photosensor Characterization for the Cherenkov Telescope Array: Silicon Photomultiplier versus Multi-Anode Photomultiplier Tube," *arXiv:1308.1390v1 [astro-ph.IM],* 2013.

[57] W. Gifford, "The Gifford-McMahon on cycle," *Adv. Cryog. Eng.,* 1966.

[58] I. Lake Shore Cryotronics, "www.lakeshore.com," [Online].

[59] I. Lake Shore Cryotronics, "User`s Manual Model 335 Temperature Controller," 2014.

[60] N. Dinu, A. Nagai and A. Para, "Studies of MPPC detectors down to cryogenic temperatures," *Nuclear Instruments and Methods in Physics Research Section A, Volume 787,* p. 275–279, 1 July 2015.

[61] N. C. C. Lu, L. Gerzberg, C. Y. Lu and J. D. Meindl, "Modeling and optimization of monolithic polycrystalline silicon resistors," *IEEE Transactions on Electron Devices,* vol. 28, no. 7, pp. 818-830, 1981.

[62] CERN, "https://root.cern.ch/," 2014. [Online].

[63] A. Nagai, "Silicon Photomultiplier for Medical Imaging - Analysis of SiPM characteristics -," *Proceedings of Journees de Rencontre Jeuntre Jeunes Chercheurs,* pp. 43-46, 2013.

[64] L. Technology, "Linear Technology," http://www.linear.com/designtools/software/. [Online].

[65] P. Hough, "Method and means for recognizing complex patterns". U.S. Patent 3,069,654 18 Dec. 1962.

[66] R. L. Burden and J. D. Faires, Numerical Analysis, 6th Edition, Brooks Cole, 1996.

[67] I. Tektronix, "User Manual TDS5000 Series Digital Phosphor Oscilloscopes".

[68] R. J. McIntyre, "Theory of micro-plasma instability in silicon," *Journal of Applied Physics,* vol. 32, no. 6, pp. 983-995, 1961.

[69] R. J. McIntyre, "Multiplication noise in uniform avalanche diodes," *IEEE Transactions on Electron Devices,* vol. 13, no. 1, pp. 164-168, 1966.

[70] D. Schulz and P. Vaska, "Integrating PET with behavioral neuroscience using RatCAP tomography," *Reviews in the neurosciences,* vol. 22, no. 6, pp. 647-655, 18 Nov. 2011.

[71] V. Patel, D. Lee, D. Alexoff, S. Dewey and W. Schiffer, "Imaging dopamine release with Positron Emission Tomography (PET) and 11C-raclopride in freely moving animals," *Neuroimage,* vol. 41, no. 3, pp. 1051-1066, 2008.

[72] D. Schulz, S. Southekal, S. Junnarkar, J. Pratte, M. Purschke, S. Stoll, B. Ravindranath, S. Maramraju, S. Krishnamoorthy, F. Henn, P. O'Connor, C. Woody, D. Schlyer and P. Vaska, "Simultaneous assessment of rodent behavior and neurochemistry using a miniature positron emission tomograph," *Nat Methods.,* vol. 8(4), pp. 347-352, 2011.

[73] A. Kyme, V. Zhou, S. Meikle and R. Fulton, "Real-time 3D motion tracking for small animal brain PET," *Phys Med Biol.,* vol. 53(10), pp. 2651-2666, 2008.

[74] P. Delpierre, B. Dinkespiler, J. Godart, P. Laniece and L. Pinot, "Dispositif de détection de la désintegration de radioisotopes dans un tissu biologique". 2009.

[75] F. Pain, P. Laniece, R. Mastrippolito, Y. Charon, D. Comar, V. Leviel, J. F. Pujol and L. Valentin, "SIC, an intracerebral radiosensitive probe for in vivo neuropharmacology investigations in small laboratory animals: theoretical considerations and practical characteristics," *IEEE Transactions on Nuclear Science,* vol. 47, pp. 25-32, 2000.

[76] F. Pain, P. Laniece, R. Mastrippolito, L. Pinot, Y. Charon, A. Glatigny, M. Guillemin, P. Hantraye, V. Leviel, L. Menard and L. Valentin, "SIC: An Intracerebral Radiosensitive Probe for In Vivo Neuropharmacology Investigations in Small Laboratory Animals: Prototype Design, Characterization, and In Vivo Evaluation," *IEEE TRANSACTIONS ON NUCLEAR SCIENCE,* vol. 49, no. 3, 2002.

[77] J. Maerk, D. Benoit, L. Balasse, M. Benoit, J. Clémens, S. Fieux, D. Fougeron, J. Graber-Bolis, B. Janvier, M. Jevaud, A. Genoux, P. Gisquet-Verrier, M. Menouni, F. Pain, L. Pinot, C. Tourvielle, L. Zimmer, C. Morel and P. Laniece, "A wireless beta-microprobe based on pixelated silicon for in vivo brain studies in freely moving rats," *Phys Med Biol.,* vol. 58(13), pp. 4483-4500, 2013.

[78] L. Balasse, J. Maerk, F. Pain, A. Genoux, S. Fieux, C. Morel, P. Gisquet-Verrier, L. Zimmer and P. Laniece, "PIXSIC, a wireless β+-sensitive probe for radiopharmacological investigations in rat brain: binding studies with 18F-MPPF," *Mol Imaging and Biology,* vol. 17(2), pp. 163-167, 2015.

[79] K. K. Hamamatsu Photonics, "http://www.hamamatsu.com/eu/en/product/category/3100/4004/4113/S13360-1350PE/index.html," [Online].

[80] I. Silvaco, "http://www.silvaco.com/products/tcad.html," 1984-2016. [Online].

[81] K. E. Atkinson, An Introduction to Numerical Analysis, John Wiley & Sons, Inc, 1989.

[82] P. Mars, "Temperature dependence of avalanche breakdown voltage in p-n junction," *Int. J. Electronics,* vol. 32, pp. 23-37, 1971.

[83] W. N. Grant, "Electron and hole ionization rates in epitaxial silicon at high electric field," *Solid-State Electronics,* vol. 16, pp. 1189-1203, 1973.

[84] R. H. Haitz, "Mechanisms contributing to the noise pulse rate of avalanche diodes," *Journal of Applied Physics,* vol. 36, no. 10, pp. 3123-3130, 1965.

université PARIS-SACLAY | ÉCOLE DOCTORALE PHENIICS

Titre : Etude des détecteurs SiPM jusqu'aux températures cryogéniques et pour une application biomédicale

Mots clés : SiPM, cryogéniques, application biomédicale, IV modèle

Résumé : Les Photomultiplicateurs Silicium (SiPM) sont devenus aujourd'hui des détecteurs de lumière visible, applicables dans de nombreux domaines comme la Physique des Hautes Énergies, les expériences Neutrinos, la détection de fluorescence, pour des applications de bio-photonique ou d'imagerie médicale.

La première partie de ma Thèse concerne l'étude des divers paramètres physiques des SiPM en fonction de température T. En particulier, des composants récents (2015) de KETEK ayant diverses caractéristiques technologiques comme des jonctions p/n ou n/p, avec ou sans ″trench″ entre cellules, différentes épaisseurs de couches épitaxiales, etc … ont été étudiés dans la gamme de T de 308.15 K (+35 °C) à 238.15 K (-35 °C). En plus, des composants Hamamatsu de production 2011, ainsi que de production 2015 avec des caractéristiques technologiques améliorées (faible bruit), ont été testés dans la gamme 318.15 K (+45 °C) à 98.15 K (-175 °C).

Pour ces études, j'ai participé à la conception, l'installation, la mise en service et la calibration d'un banc cryogénique destiné aux caractérisations électriques, optiques, et en température, des SiPM. J'ai développé une procédure d'analyse automatisée, capable de traiter en un temps très court une énorme quantité de données expérimentales (i.e. dizaines de Gb/détecteur), et de fournir une information rapide et précise sur les principaux paramètres et leur dépendance en T.

J'ai développé un modèle physique décrivant les courbes IV en DC pour différentes T. Ce modèle proposé reproduit bien la forme de la courbe IV dans une large gamme de courants allant de 10^{-12} à 10^{-5} A sur toute la zone de fonctionnement des divers détecteurs. Ainsi, le modèle IV peut être utilisé comme un outil simple et rapide pour déterminer les paramètres du SiPM comme le V_{BD}, la forme de la courbe P_{Geiger} en fonction de V_{bias}, ainsi que la plage des tensions de fonctionnement. La comparaison de ces paramètres avec ceux obtenus en mesure AC, et analysés par la procédure automatisée, sont en bonne concordance.

La seconde partie de ma Thèse a porté sur l'étude de composants SiPM spécialement adaptés à une application biomédicale. Il s'agit d'une sonde intracérébrale, sensible à l'émission β (N_β) de molécules marquées par un traceur radioactif, injectées dans le cerveau d'un animal vivant. Le but étant de construire un nouveau ″modèle animal″ de maladies humaines telles que les maladies neuro-dégénératives ou neuropsychiatriques et la croissance de tumeurs. Cette sonde se compose d'un SiPM de très petite taille, bas bruit, couplé à une fibre scintillante, suivie d'une électronique de lecture spécifique, miniaturisée, à faible consommation. Ces SiPM ont été choisis comme les plus adaptés à notre application : deux SiPM de KETEK de 0.5x0.5 mm^2 (spécialement développés par cette compagnie pour nos besoins), et un SiPM standard de 1.3x1.3 mm^2 de Hamamatsu, tous ayant des µ-cellules de 50 × 50 μm^2. Pour chaque composant, les paramètres G, DCR et la sensibilité β ont été mesurés en fonction de V_{bias} et T. Les résultats obtenus montrent que le faible champ de vue des nouvelles structures KETEK permet une bonne amélioration du DCR. Cependant ce faible champ de vue entraîne une perte de collection de lumière due à l'épaisseur de la couche de résine époxy de protection, et à l'angle d'acceptante de la fibre.

Comme la sensibilité β est un compromis entre le PDE et le DCR, les SiPM de KETEK montrent au final des performances voisines de celles de Hamamatsu. Les résultats préliminaires démontrent que la sensibilité β de KETEK peut être améliorée significativement en utilisant une lentille de focalisation entre la fibre scintillante et le SiPM, ou en diminuant l'épaisseur de la couche de résine époxy de protection.

Université Paris-Saclay
Espace Technologique / Immeuble Discovery
Route de l'Orme aux Merisiers RD 128 / 91190 Saint-Aubin, France

université PARIS-SACLAY | ÉCOLE DOCTORALE PHENIICS

Title : Investigation of SiPM physics parameters down to cryogenic temperatures and for a bio-medical application

Keywords : SiPM, Cryogenic, biomedical application, IV Model

Abstract : Silicon PhotoMultiplier (SiPM) detector has become a suitable visible light/photon detector for many applications like high energy physics and neutrino experiments, fluorescence detection, bio-photonics and medical imaging.

The first part of my thesis was oriented to the studies of SiPM physics parameters as a function of temperature. Particularly, recent KETEK devices (year 2015) with different technological characteristics like p/n and n/p junctions, with and without trench technology, and different widths of epitaxial layer were studied in the temperature range from 308.15 K (+35 °C) down to 238.15 K (-35 °C). In addition, the Hamamatsu devices from 2011 production run as well as new devices from 2015 year, with improved technological characteristics inducing a reduced noise, were investigated in a wider temperature range from 318.15 K (+45 °C) down to 98.15 K (-175 °C).

For these purposes, I participated to the design, installation, commissioning and calibration of a cryogenic experimental setup dedicated to electrical, optical and temperature studies of SiPM devices. Also, I have developed an automatic analysis procedure able to handle in a short time an impressive quantity of experimental data (i.e. tens of Gb/device) and to give a precise and fast information on main SiPM parameters and their temperature dependence.

I have also developed a physical model describing the DC I-V curves of SiPM detectors at different temperatures. The proposed model fits well the shape of IV curve in a very large currents range from 10^{-12} A up to 10^{-5} A over the full working range of various devices. Consequently, the IV model can be used as a simple and fast method for determination of SiPM parameters like breakdown voltage V_{BD}, the shape of Geiger triggering probability P_{Geiger} as a function of V_{bias} as well as the V_{bias} working range. The comparison of these parameters with those calculated from AC measurements and analyzed by the automatic procedure showed a good agreement.

The second part of my thesis was oriented to the study of SiPM devices and their physical parameters required to build a prototype of beta-sensitive intracerebral probe. Such probe is dedicated to measure the local concentration of radiolabeled molecules on awake and freely moving animal and to study new animal models of human disorders (neurodegenerative diseases, tumor growth, and neuropsychiatric disorders). It is composed of small size, low-noise SiPM device coupled to a scintillating fiber and read-out by a dedicated miniaturized low-power consumption electronics. Three SiPM devices have been chosen as the most adapted for our application: two small KETEK devices of 0.5×0.5 mm^2 size (with and without optical trenches, specially developed by KETEK to fulfill our requirements) and a standard Hamamatsu device of 1.3×1.3 mm^2 size, all devices having 50 × 50 μm^2 µcell size. For each SiPM the gain G, dark count rate DCR and beta sensitivity were measured as a function of V_{bias} and temperature. The obtained results showed that the small field of view and newly developed structure of the KETEK devices allow a large decrease of the dark count rate DCR. However, this small field of view also leads to a reduced light collection due to the thickness of the epoxy protection resin on top of the SiPM and the acceptance angle of the fiber. Since the beta sensitivity represents a tradeoff between photon detection efficiency PDE and dark count rate DCR, KETEK SiPMs exhibit similar performances in comparison with the Hamamatsu device. Preliminary results demonstrate that the beta sensitivity of KETEK devices can be significantly improved by using focusing lens between the scintillating fiber and the SiPM or by reducing the thickness of its epoxy protection resin.

Université Paris-Saclay
Espace Technologique / Immeuble Discovery
Route de l'Orme aux Merisiers RD 128 / 91190 Saint-Aubin, France